Disorder and topology in strongly coupled light-matter systems

Thomas Allard

To cite this version:

Thomas Allard. Disorder and topology in strongly coupled light-matter systems. Condensed Matter [cond-mat]. Université de Strasbourg, 2023. English. NNT : 2023STRAE031 . tel-04586338

HAL Id: tel-04586338
https://theses.hal.science/tel-04586338v1
Submitted on 24 May 2024

UNIVERSITÉ DE STRASBOURG

ÉCOLE DOCTORALE DE PHYSIQUE ET CHIMIE PHYSIQUE

Institut de Physique et Chimie des Matériaux de Strasbourg

THÈSE

présentée par :

Thomas Allard

soutenue le : **27 septembre 2023**

pour obtenir le grade de : **Docteur de l'Université de Strasbourg**
Discipline : Physique de la Matière Condensée

Disorder and topology in strongly coupled light-matter systems

Effets du couplage fort lumière-matière sur les systèmes désordonnés ou topologiques unidimensionnels

THÈSE dirigée par :

M. WEICK Guillaume	Dr., IPCMS, Université de Strasbourg

RAPPORTEURS :

M. BASKO Denis	Dr., LPMMC, Université Grenoble Alpes
M. FUCHS Jean-Noël	Dr., LPTMC, Sorbonne Université

AUTRES MEMBRES DU JURY :

Mme ARROYO HUIDOBRO Paloma	Dr., IFIMAC, Université autonome de Madrid
M. GENET Cyriaque	Dr., ISIS, Université de Strasbourg
M. HAGENMULLER David	Dr., CESQ, Université de Strasbourg

À Juliette

CONTENTS

REMERCIEMENTS

L’après-soutenance de thèse et le peaufinage du manuscrit sont de ces instants qui, achevant de manière nette une importante période de vie – la vie étudiante –, amènent à prendre du recul, et à questionner ce qui permit le déroulement sans encombre de ladite période. L’introspection amène alors naturellement aux remerciements.

Je commencerai tout d’abord par exprimer ma gratitude aux membres du jury, qui ont accepté d’étudier et de juger ce travail de thèse. Merci à Paloma Arroyo Huidobro, Denis Basko, Jean-Noël Fuchs, Cyriaque Genet et David Hagenmuller.

Je remercie ensuite tout particulièrement mon directeur de thèse, Guillaume Weick, qui, bien plus qu’un simple directeur (ou comme tu dirais, “advisor” !) est très rapidement devenu un collègue avec qui une véritable relation amicale s’est construite. Merci à toi Guillaume pour ta bienveillance, pour m’avoir poussé à prendre confiance en moi, et pour m’avoir partagé ton éthique irréprochable de l’enseignement et de la recherche.

Merci également à Clément Tauber pour nos discussions de physique topologique, ainsi qu’à David Hagenmuller, cette fois non pour son rôle de membre du jury, mais pour nos discussions de polaritonique désordonnée.

Merci à mes collègues de la Faculté de Physique et de Télécom Physique, avec qui j’ai pu enseigner durant ces 3 années de thèse et ainsi valider mon agrégation, notamment Olivier Bengone, Guillaume Weick (encore !), et Yann Leroy.

A l’IPCMS, merci à toute l’équipe Méso et notamment à Rodolfo Jalabert, Dietmar Weinmann, Mauricio Gómez Viloria et Nico Leumer pour tous ces repas et cafés partagés dans la bonne humeur autour de belles discussions. Merci aussi aux autres collègues du DMONS que j’ai pu cotoyer, notamment Stéphane Berciaud, Arnaud Gloppe, Joanna Wolff et Loïc Moczko pour la machine à café indispensable.

Je remercie aussi bien entendu mon d'abord collègue, puis rapidement cobureau et ami Gaëtan Percebois, sans qui cette thèse n'aurait vraisemblablement pas du tout été la même. Merci pour ces bavardages interminables à propos de tout et de rien, entrecoupés tout de même parfois de discussions de physique.

J'aimerai également remercier le soutien financier de l'ITI QMAT de l'Université de Strasbourg, qui m'a permis de participer à des écoles et conférences à Paris, Cargèse, Aussois, San-Sebastián, Straubing ou encore Madrid. Ces expériences ont été indispensables à ma formation scientifique et au bon déroulé de ma thèse, m'offrant des semaines de coupures et m'amenant à faire de belles rencontres.

Je tiens ensuite à exprimer toute ma gratitude à mes proches amis, qui m'accompagnent pour beaucoup depuis 10 voir 20 ans. Sans leur soutien infaillible toutes ces années je n'aurais pu en arriver là. Il en est de même pour ma famille, dont je remercie tout particulièrement mon frère, ma marraine, mes parents et mes grands-parents, pour avoir fait de moi ce que je suis aujourd'hui.

Pour finir, je remercie évidemment Juliette, qui partage ma vie et m'apporta tout au long de ces 3 années l'amour et le bonheur indispensables au bon déroulement de ce doctorat. Il me tarde désormais d'explorer de nouvelles opportunités à tes côtés !

LIST OF FIGURES

INTRODUCTION

Condensed matter physics, whose modern origin can be attributed to Einstein's seminal works on the photoelectric effect [1] and on the heat capacity of solids [2], aims to investigate both the microscopic and macroscopic properties of matter from the collective effects of a large number of particles, and notably to study the different *phases* of matter in the broadest sense. Throughout the twentieth century, it became one of the most prolific field of physics, and as a matter of fact, the subsection "cond-mat" on the arXiv prepublication platform is today the most popular physics category.

Within the field of condensed matter, two branches have especially attracted a lot of attention in the past fifty years. The first one is the field of disordered systems, in which the effect of Anderson localization unveiled the fact that a piece of metallic material can be turned into an insulating one by microscopic disorder, the latter leading the electron wavefunctions to localize. The second one is the physics of topological matter, which encompasses notably the emblematic integer quantum Hall effect. In particular, it allows to rigorously classify physical materials than can behave as insulating in their bulk, but metallic on their surfaces or edges, thanks to symmetry protected topological surface or edge states, and to explain these intriguing new states of matter through concepts borrowed from topology.

Interestingly, both Anderson localization and topological phases of matter have the peculiarity, although developed in the context of condensed matter quantum electronic systems, of originating from wave phenomena [3, 4]. The emergence of these effects in solid-state physics is therefore solely the result of the quantum wave-particle duality of electrons. Indeed, Anderson localization and topological physics have been studied in fields far beyond electronic systems, and as varied as acoustics [3, 5], shallow water waves [6–8], cold atoms [9, 10] or photonics [11–15].

Another field which has been rapidly expanding in the past few decades is the physics of strong light-matter coupling, which addresses the behavior of collective hybrid light-matter excitations known as polaritons. Whereas matter ordinarily weakly couples to the electromagnetic vacuum, the use of optical cavities, i.e., of confined electromagnetic modes, allows one to enhance the light-matter interaction. Once in what is known as the strong-coupling regime, the hybridization of matter excitations with photons has been shown to significantly modify material properties, in particular through a photon-induced long-range coupling between matter degrees of freedom [16]. As wave-like collective excitations, polaritons could in principle be subject to the above-mentioned Anderson localization and topological phenomena.

The goal of the present thesis work is to combine these three active fields of study by investigating the fate of Anderson localization as well as of topological phases of matter and their related topological edge states, in the context of strongly-coupled light-matter systems. A unique feature of our theoretical approach is to focus on one-dimensional structures, and to model the light-matter coupling through a microscopically derived Hamiltonian, which describes realistic multimode optical cavities.

With the aim of addressing this objective, we organized the remainder of the manuscript as follows:

- Chap. 1 serves to provide a preliminary introduction to the different fields of study under consideration in this manuscript, namely, Anderson localization in disordered systems, the concept of topological phases of matter, and the physics of strong-light matter coupling.

- Chap. 2 is dedicated to the theoretical framework we employ to model the light-matter coupling. Through a Hamiltonian approach in the Coulomb gauge, we derive a general model of a one-dimensional array of dipolar emitters coupled to the confined electromagnetic modes of an optical cavity.

- Chap. 3 contains our investigations on the fate of Anderson localization in one dimension in the strong light-matter coupling regime. With the help of the model developed in Chap. 2, we study both the eigenspectrum and the driven dissipative transport properties of a disordered chain of dipoles strongly-coupled to a multimode cavity. An important result of this chapter is the emergence of disorder-enhanced transport, a phenomenon originating from the disorder-induced hybridization of dark states into polaritons.

- Chap. 4 concerns our study of the interplay between topological phenomena and strong light-matter coupling. Relying on the theory developed in Chap. 2, we analyze the properties of a dimerized chain of dipolar emitters strongly-coupled to cavity photons. Such a system represents a variation of the Su-Schrieffer-Heeger model of polyacetylene – a textbook model of a one-dimensional topological system – with the addition of an effective, photon-mediated, dipole-dipole coupling. We study the eigenspectrum of the system, its driven-dissipative transport properties, and in particular the fate of its topological features.

An important result of this chapter is the hybridization of the original topological edge states into what we coin polaritonic edge states, which present unusual properties, and emerge in the strong-coupling regime only.

- Eventually, we draw conclusions on the effects of disorder and topology in strongly coupled light-matter systems, and we place our work in perspectives, discussing its limitations and proposing further studies on the topic.

The results that we present, respectively, in the third and fourth chapters of this manuscript have been published in the following articles:

- T.F. Allard, G. Weick, *Disorder-enhanced transport in a chain of lossy dipoles strongly coupled to cavity photons*, Physical Review B **106**, 245424 (2022) [17]
- T.F. Allard, G. Weick, *Multiple polaritonic edge states in a Su-Schrieffer-Heeger chain strongly coupled to a multimode cavity*, Physical Review B **108**, 245417 (2023) [18]

During the time of the PhD, the following work, containing results which are not presented in this manuscript, has also been published as a journal article:

- T.F. Allard, G. Weick, *Quantum theory of plasmon polaritons in chains of metallic nanoparticles: From near- to far-field coupling regime*, Physical Review B **104**, 125434 (2021) [19].

CHAPTER 1

PRELIMINARIES

In this preliminary chapter, we give a concise overview of the specific topics addressed in this thesis. First, we introduce the fields of Anderson localization and topological phases of matter. We note that a complementary practical introduction to these two topics, based on a hands-on examination of celebrated toy models, will also be provided, respectively, in the beginning of Chaps. 3 and 4. Then, the physics of strong light-matter coupling, with the emergence of polaritonic hybrid states, is presented.

1.1 Disordered systems and Anderson localization

From inevitable impurities, inhomogeneities or irregularities, disorder is ubiquitous in nature. This makes the perfect crystalline structure the exception rather than the rule, and in most realistic cases, one has to deal with a certain amount of randomness and disorder in its experiment. This naturally led to a profound interest in the study of disordered systems. Among many fascinating phenomena induced by the presence of disorder, such as the Griffiths phase, glassy behavior, amorphous solids or the liquid-solid transition, one of them, the effect of Anderson localization, is particularly universal and has led to its own active field of research.[1]

In his seminal work published in 1958 [25], Anderson considered a tight-binding model of an electron hopping in a three-dimensional (3d) disordered lattice in the thermodynamic limit, so that on each site of the lattice the electron experiences a random potential energy, chosen within an interval of width W. Once trapped on a lattice site, the electron can hop to the nearest neighboring site through tunnelling.[2]

Such a system is sketched in Fig. 1.1(a), first in the case of no disorder on the top panel. In that case, the electron wavefunction is a Bloch wave that is extended in the lattice. What Anderson demonstrated is that if the disorder strength W is large enough, the electron wavefunction becomes exponentially confined to small regions of space, leading to a lack of diffusion and a complete localization, as sketched in the bottom panel. Therefore, in that case, the conduction of the system is not only diminished, but totally suppressed.

While the decrease of conduction due to impurities can be intuitive, the possibility of a complete suppression is less. In particular, Anderson's picture of the behavior of an electron in a random potential dramatically contrast with the one of small classical particles, for which it is well known, for instance from Jean Perrin's experiments, that disorder leads to diffusive motion [29].

The phenomenon is in fact even more striking in systems of smaller dimensionality. Indeed, while a disorder-induced metal-to-insulator transition occurs at a finite value of W in 3d systems, it has been shown that any infinitesimal value of W leads, at the thermodynamic limit, to the exponential localization of the wavefunction in both 1d [30] and 2d [31] systems.[3] In Chap. 3, we will conduct a comprehensive study of the 1d Anderson model.

---

[1] For a complete review, see, e.g., Refs. [20–23], while for a comprehensive historical review see Ref. [24].

[2] It is noteworthy to mention that Anderson's model only account for noninteracting, short-ranged Hamiltonians. The inclusion of interactions [26] or of long-range couplings [27] considerably modify the standard theory of Anderson localization.

[3] This dimensionality dependence can be phenomenologically understood from a naive analogy with a classical random walk. Indeed, on one- and two-dimensional lattices, the return probability ρ of a particle with random equiprobable hopping is 1 in the thermodynamic limit. In contrast, in a three-dimensional random walk, one always has $\rho < 1$ [32].

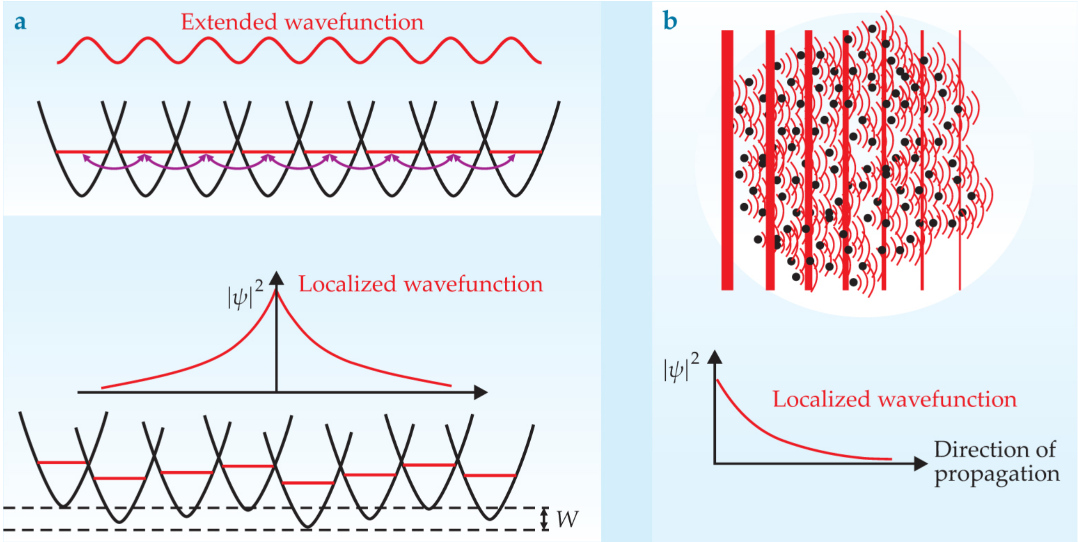

Figure 1.1: Anderson localization. (a) Sketch of the Anderson model. Top panel: the lattice has a crystalline structure, so that the electron propagation is governed by Bloch's theorem and the wavefunction is extended. Bottom panel: When the potential landscape felt by the electron is disordered and the disorder strength W is large enough, the wave function localizes exponentially in space. (b) Sketch of the interference phenomenon underlying Anderson localization. The vertical red lines represent the wavefront of a plane wave propagating in a medium with many impurities or defects, depicted as black dots. Once the plane wave scatters on impurities, the rescattered wavelets interfere coherently with each other. For a large enough amount of impurities, the interference is destructive in the direction of propagation so that the wavefunction amplitude decreases exponentially. Figure reproduced from Ref. [28].

It was later realized that Anderson localization arises solely from a subtle wave interference mechanism, so that it is a universal effect that applies to any wave propagating through a disordered medium. In the case of electrons in solids, the interferences occur between multiple scattering paths of the electrons. When these paths have widely separated initial and final positions, destructive interferences occur, trapping the electron in its initial position.

A qualitative illustration of this phenomenon in a two-dimensional (2d) scenario is depicted in Fig. 1.1(b). It presents a plane wave – the vertical red lines denoting the wavefronts – propagating through a medium containing numerous impurities or defects represented by black dots. As the wave propagates through the medium, it scatters off the impurities, breaking into wavelets. These wavelets then interfere destructively with each other in the direction of propagation, leading to an exponential decay of the wave amplitude, which characterizes Anderson localization.

The universality of Anderson localization in wave physics has sparked renewed interest in its investigation over the past few decades. It has proven to be relevant in a variety of classical physics fields, from acoustics [3] to oceanography [6], photonics [11], or even geology [33].

The study of Anderson localization in these classical application domains may necessitate new theoretical considerations. Indeed, while electrons in solids can be modeled under certain approximations with nearest-neighbor couplings only, systems involving for instance polaritonic excitations naturally give rise to longer-range coupling. This could possibly render the standard theory of Anderson localization inadequate, and it is partly what we will endeavor to do in Chap. 3, where the focus will be on the interplay between disorder and polaritons.

1.2 Topological phases of matter

The second subject we will encounter in this manuscript is the physics of topological phases of matter.[4] In 1980, an experimental discovery by von Klitzing, Dorda, and Pepper of a phenomenon which is now known as the integer quantum Hall effect (IQHE), revealed that a 2d electron gas exposed to a low temperature and a strong perpendicular magnetic field exhibits a Hall conductance characterized by extremely precise quantized plateaus, so precise that their value was until recently used for metrological purpose [42]. At the boundaries of this 2d electron gas, chiral edge states were predicted, causing the material to be insulating within its bulk but metallic on its edges [43]. Remarkably, both of these features, namely, the presence of an integer invariant originating from bulk properties, and the presence of chiral edge states, were found to exhibit an intriguing robustness against material imperfections, and there was in fact a deep connection between them, known as the bulk-edge correspondence [44].

The investigation of the integer quantum Hall effect marked the beginning of what would later be termed – in the broadest sense – as topological insulators, a significantly larger concept that paved the way for an entirely new branch of physics [36, 37]. A topological insulator is distinguished by its peculiar behavior as an insulating material in the bulk which exhibits conducting surface or edge states when placed in contact with a conventional insulator, e.g., the vacuum. Here, the terminology "topological" originates from the mathematical discipline of topology, which notably classifies objects that remain unchanged under continuous deformations. For instance, a sphere and a cube can be smoothly deformed into each other, rendering them topologically equivalent. Conversely, a sphere and a torus cannot undergo such continuous deformations, establishing them as topologically distinct. To transition between these topologically distinct objects, a topological phase transition, such as puncturing the sphere or filling the torus, has to take place. Within this context, a global property characterizing the topology

---

[4] For a comprehensive introduction to the field, see, e.g., Refs. [34, 35]. For a more complete review, see Refs. [36, 37], while for a concise introduction, we suggest the reader to have a look at Refs. [38–41].

of such geometric objects is their genus $\mathcal{G}$, which takes a value of 0 for the sphere and the cube, but of 1 for the torus. The quantity $\mathcal{G}$ serves as the topological invariant of the system, and thus manifests by definition robustness against continuous deformations. In the case of topological phases of matter, rather than geometric objects, it is Hamiltonians that are to be classified, and their band structures – which originate typically from electrons propagating in crystals – that undergo deformations. Following the previous discussion, the IQHE phase discovered in 1980 can therefore be regarded as topologically distinct from all previously recognized phases of matter [39].

To study topological insulators, we focus on Hamiltonians that exhibit a gapped spectrum (there are also topological superconductors, for which the band gap refers to the superconducting gap). The system's topological invariant, computed from electron wavefunction properties, will then remains robust under any changes to the band structure that do not close the gap. In other words, the topological invariant remains unchanged as long as the material remains insulating. Consequently, the edge or surface states associated with the nontrivial topological phase are also robust against any continuous deformation of the Hamiltonian band structure. In practice, this robustness manifests as resistance against disorder, sometimes provided certain types of symmetries of the system are preserved. Such a robustness of boundary states is one of the compelling reasons why the physics of topological phases draws significant attention from the community. Indeed, topological insulators are sought after for numerous potential applications, particularly in quantum or photonic technologies, such as lasing, spintronics, or quantum computing.

An important breakthrough in the field of topological phases of matter has been the complete classification of all phases in any dimension, achieved through certain internal discrete symmetries of the Hamiltonian [45, 46]. This classification of topological insulators, known as the "tenfold way", is depicted in Tab. 1.1, which we will now briefly introduce.[5]

In 1996, Altland and Zirnbauer demonstrated that all Hamiltonians can be classified according to two fundamental symmetries: time-reversal symmetry ($\mathcal{T}$) and charge conjugation symmetry ($\mathcal{C}$), the latter being also known as "particle-hole" symmetry [55]. These two symmetries correspond to anti-unitary transformations, meaning that they can be expressed as the product of a unitary matrix U and of the complex conjugation operator $\mathcal{K}$, and therefore that, importantly, they can take values of +1 or -1 once squared. To better understand the meaning of these discrete symmetries, one can examine their effect on the band structure of a Hamiltonian. On such a band structure, time-reversal symmetry reverses the momentum of an eigenstate, implying

---

[5] We note that such a periodic table of topological phases has been originally introduced for free fermions. Moreover, it only concerns short-ranged, non-interacting, Hermitian Hamiltonians, but a number of investigations are currently underway to overcome these limitations [47–49]. Finally, it does not either take into account crystalline symmetries [50–52], which can lead to what is called higher order topological insulators [53], and notably allowed the investigation of topological phases in thousands of crystals [54].

Symmetry				**Dimension**							
AZ class	$\mathcal{T}$	$\mathcal{C}$	$\mathcal{S}$	**1**	**2**	**3**	**4**	**5**	**6**	**7**	**8**
A	0	0	0	0	$\mathbb{Z}$	0	$\mathbb{Z}$	0	$\mathbb{Z}$	0	$\mathbb{Z}$
AIII	0	0	+1	$\mathbb{Z}$	0	$\mathbb{Z}$	0	$\mathbb{Z}$	0	$\mathbb{Z}$	0
AI	+1	0	0	0	0	0	$\mathbb{Z}$	0	$\mathbb{Z}_2$	$\mathbb{Z}_2$	$\mathbb{Z}$
BDI	+1	+1	+1	$\mathbb{Z}$	0	0	0	$\mathbb{Z}$	0	$\mathbb{Z}_2$	$\mathbb{Z}_2$
D	0	+1	0	$\mathbb{Z}_2$	$\mathbb{Z}$	0	0	0	$\mathbb{Z}$	0	$\mathbb{Z}_2$
DIII	-1	+1	+1	$\mathbb{Z}_2$	$\mathbb{Z}_2$	$\mathbb{Z}$	0	0	0	$\mathbb{Z}$	0
AII	-1	0	0	0	$\mathbb{Z}_2$	$\mathbb{Z}_2$	$\mathbb{Z}$	0	0	0	$\mathbb{Z}$
CII	-1	-1	+1	$\mathbb{Z}$	0	$\mathbb{Z}_2$	$\mathbb{Z}_2$	$\mathbb{Z}$	0	0	0
C	0	-1	0	0	$\mathbb{Z}$	0	$\mathbb{Z}_2$	$\mathbb{Z}_2$	$\mathbb{Z}$	0	0
CI	+1	-1	+1	0	0	$\mathbb{Z}$	0	$\mathbb{Z}_2$	$\mathbb{Z}_2$	$\mathbb{Z}$	0

Table 1.1: The tenfold way. Altland-Zirnbauer (AZ) periodic table of topological insulators (and superconductors) [45, 46]. The ten lines in the table represent the ten different Altland-Zirnbauer (AZ) classes of Hamiltonian, labeled by their Cartan's index. These classes are determined based on the presence of time-reversal ($\mathcal{T}$), charge ($\mathcal{C}$), and sublattice ($\mathcal{S}$) symmetries. The right part of the table presents the classification itself for the first eight dimensions. In the table, a 0 entry indicates the absence of a nontrivial topological phase for the given Hamiltonian class and dimension. On the other hand, a $\mathbb{Z}$ or $\mathbb{Z}_2$ entry indicates the ensemble to which the topological invariant of the system can belong.

a symmetry around momentum 0, while particle-hole symmetry, on the other hand, reverses the momentum but also leads to a mirror symmetry between the filled and empty bands. Those two symmetries, when distinguishing between the positive or negative sign of their square, leads to 9 different classes of Hamiltonians. However, a last case is possible. Indeed, some Hamiltonians may possess neither $\mathcal{T}$ nor $\mathcal{C}$ symmetry independently, but instead a combination of the two – known as chiral, or sublattice symmetry ($\mathcal{S} = \mathcal{C}\mathcal{T}$) – leading to a third symmetry, and to a tenth class of Hamiltonians. These 10 classes, known as Altland-Zirnbauer (AZ) classes, divide matter in 10 fundamentally different kinds. They are represented in the second, third, and fourth columns of Tab. 1.1, in which in each cell a 0 signifies the absence of a particular symmetry, and a 1 its presence, with $+$ or $-$ representing the sign of the square of the latter symmetry.

To classify these Hamiltonians whether or not they may exhibit nontrivial topology, Schnyder, Ryu, Furusaki, and Ludwig noticed that a topological phase is a phase in which there exists boundary states that precisely do not undergo Anderson localization [46, 56]. Indeed, edge or surface states being conducting, i.e. delocalized, and presenting robustness against disorder, they avoid localization, so that topological phases in dimension d can be classified as phases in dimension $d-1$ avoiding Anderson localization.[6] It is following this approach that the filling of Tab. 1.1 has first been made possible [56], and the result is presented in the right part of the latter table, where the 8 columns indicate the considered dimension. On the one hand, a 0 entry denotes the absence of a topological phase for the Hamiltonian in a given class and dimension. On the other hand, when a topological phase is present, it is indicated by the set to which its topological invariant belongs. Only two types of topological invariants exist: $\mathbb{Z}$ invariants, which can take any integer values, and $\mathbb{Z}_2$ invariant, which are restricted to 0 or 1. It is worth noting that the table exhibits a periodicity of dimension 8, a phenomenon known as the "Bott Clock", which explains why only the first 8 dimensions are represented. A Hamiltonian of a given AZ class presenting a topological phase in dimension 1 will thus also present one – with the same type of invariant – in dimension 9. This curious periodicity stems from the deep mathematical structure underlying the classification [45].

Remarkably, one concludes from this analysis that topological phases are characterized by the *preservation* – rather than by the *breaking* – of specific symmetries. This is in stark contrast to non topological phases of matter, where transitions, such as, e.g., the paramagnetic-ferromagnetic transition, or the liquid-solid transition, can be described using Landau's approach, in which spontaneous symmetry breaking occurs [39].

To give some examples of the topological phases presented in Tab. 1.1, the integer quantum Hall effect appears in dimension 2 and belongs to the class A (no symmetries other than the unitarity of the Hamiltonian). Its edge states are thus robust against any form of disorder, and its topological invariant, the Hall conductance, can take any integer value, making it a $\mathbb{Z}$ topological invariant. Another example is the quantum spin Hall effect [60], which falls under class AII by possessing a fermionic time-reversal symmetry ($\mathcal{T}^2 = -1$). It has a $\mathbb{Z}_2$ topological invariant, and its topological properties remain robust against perturbations that preserve the Hamiltonian within this class, therefore, it is for instance not robust against a magnetic field which would destroy $\mathcal{T}$ symmetry.

In this manuscript, importantly, we will focus specifically on one-dimensional (1d) topological physics, leaving the cases of larger dimensionality for future research. In particular, our study will revolve around the Su-Schrieffer-Heeger (SSH) model of polyacetylene [61], which exhibits all the three $\mathcal{T}$, $\mathcal{C}$, and $\mathcal{S}$ symmetries. Depending on which symmetries we enforce, i.e., which symmetries we consider to ensure the robustness of topological properties,

---

[6] Interestingly, this highlights the intricate interplay between the physics of Anderson localization and topological phases. Another example is the fundamental role played by disorder in the emergence of the IQHE, through the broadening of Landau levels. Moreover, it has been shown that topological phases in the absence of crystalline and sublattice symmetries, such as the integer and spin quantum Hall effects, also have an obstruction to the full localization of their bulk spectrum, leading to extended *bulk* states being robust to Anderson localization [57]. Finally, we note that other intriguing features of this interplay also include disorder-induced topological transitions [58], as well as topological phases characterized by a fully localized bulk in the presence of disorder [59].

the SSH model can thus belong to the classes AIII or BDI (the D class representing the Kitaev chain, a topological superconductor), leading to the presence of a $\mathbb{Z}$ topological invariant. The SSH model frequently serves as a typical textbook example of 1d topology and will be thoroughly introduced in Chap. 4.

Interestingly, much like Anderson localization, many topological phenomena in physics have their underlying source in non-quantum phenomena. More precisely, topological properties originate from geometric phase effects, which can notably be found in numerous wave physics systems, particularly those propagating through periodic media in which a well-defined band structure exists [4]. Indeed, numerous classical systems exhibit properties which are analogous to those of certain electronic topological insulators, so that the observation of topological edge states has spanned a wide range of diverse fields, including acoustics [5], mechanics [62], active matter [63], oceanographic waves [7], coordinated human movements (such as dance) [64], cold atoms [10], photonics [14], and also polaritonics [65, 66], the latter of which we will introduce in the following section.

1.3 Strong light-matter coupling

The interaction between light and matter, as we constantly experience it, has been a subject of scientific research since the very beginning of the scientific method, many centuries ago. An important milestone in the understanding of the light-matter interaction came in the 1930s, with the establishment of the theory of quantum electrodynamics (QED), which offered a comprehensive and precise theoretical framework for explaining its subtleties at the most fundamental level. In particular, QED has notably elucidated phenomena as important as the one of spontaneous emission, the latter playing a crucial role in being at the origin of the vast majority of the light that surrounds us every day [67].

While light and matter may initially appear as totally separate entities, there is a situation in which they have a closely related behavior, known as the strong light-matter coupling regime. In this regime, light and matter excitations become indistinguishable, and behave as hybrid excitations, or quasiparticles, known as polaritons. These quasiparticles, linear combination of light and matter, were first introduced in the 1950s in the context of strong-coupling of light with vibrational excitations, namely phonons, resulting in phonon-polaritons [68, 69]. Subsequently, similar characteristics were predicted in the coupling of light with electronic degrees of freedom such as excitons – a combination of an electron and a hole bound by the Coulomb force – giving rise to exciton-polaritons [70, 71]. Since then, the field has not stopped growing, with today the confirmed identification of over 70 different types of polaritonic excitations [72]. Among them, plasmon-polaritons, excitations at a metal-insulator interface, have attracted significant attention, as well as exciton-polaritons, the latter having been extensively studied in the context of quantum wells embedded in microcavities [73], and of molecular semiconductor films in optical resonators [74].

The mechanism underlying the existence of polaritons can be roughly understood from a simple classical perspective [75], notably by means of the coupled oscillators analogy illustrated in Fig. 1.2(a). In this analogy, detailed in Ref. [76], we consider two mechanical oscillators modeled as mass-spring systems, each with a different resonance frequency ω_A and ω_B. Once linearly coupled with a coupling strength $g/2$, the bare modes of the two oscillators are renormalized into two new eigenexcitations of the combined system: an anti-phase excitation, with frequency ω_+, and an in-phase excitation, with frequency ω_-. In the context of the strong light-matter coupling, oscillator A and B correspond, for instance, respectively, to photonic and matter excitations, while the coupling $g/2$ denotes the rate of energy exchange between them. The two new eigenmodes, which can be viewed as hybrid excitations made of the bare oscillators A and B, are then referred to as polaritons. Interestingly, in many scenarios, both light and matter excitations can actually be modeled as harmonic oscillators, and the light-matter coupling is linear, rendering this naive analogy pretty realistic [76].

If we now look at the variation of the renormalized frequencies, ω_+ and ω_-, as a function of the detuning between the two bare frequencies $\Delta\omega = \omega_A - \omega_B$, we obtain the red curves shown in Fig. 1.2(b). In the latter figure, the two light blue straight dashed lines, on the other hand, represent the bare frequencies. We observe in such a plot what is known as an avoided crossing, namely, the splitting of the two intersecting blue dashed lines into the two red curves, a typical phenomenon of the physics of strongly-coupled systems, commonly observed in the polaritonic band structure. Notably, when the detuning $\Delta\omega = 0$, i.e., when the two resonators enter in resonance, the gap between the two renormalized frequencies amounts exactly to g, twice the coupling strength. In the context of polaritons, such a gap is known as the Rabi splitting.

In order to properly describe a physical system, it is necessary to take into account the effect of losses, which leads to consider the finite lifetimes of the excitations. These loss rates, which we denote as κ for the photon (oscillator A), and γ for the matter excitation (oscillator B), induce a linewidth to the excitation, which is represented in Fig. 1.2(b) as a red blur surrounding the lines. Then, in order to establish a well-defined strong-coupling regime, it is essential for the energy exchange rate between the two oscillators to exceeds the loss rates of the excitations, so that a coherent energy transfer between the oscillators can take place. In other words, the linewidth of the excitations must be smaller than the Rabi splitting, so that the two blurred red eigenmodes in Fig. 1.2(b) must remain distinguishable from each other. This leads one to commonly define the strong-coupling regime through the criterion $g > \kappa, \gamma$.

In Fig. 1.2(c), we then illustrate the case of a more lossy system, with $g < \kappa, \gamma$. In that case, the system is in the weak-coupling regime, the excitations

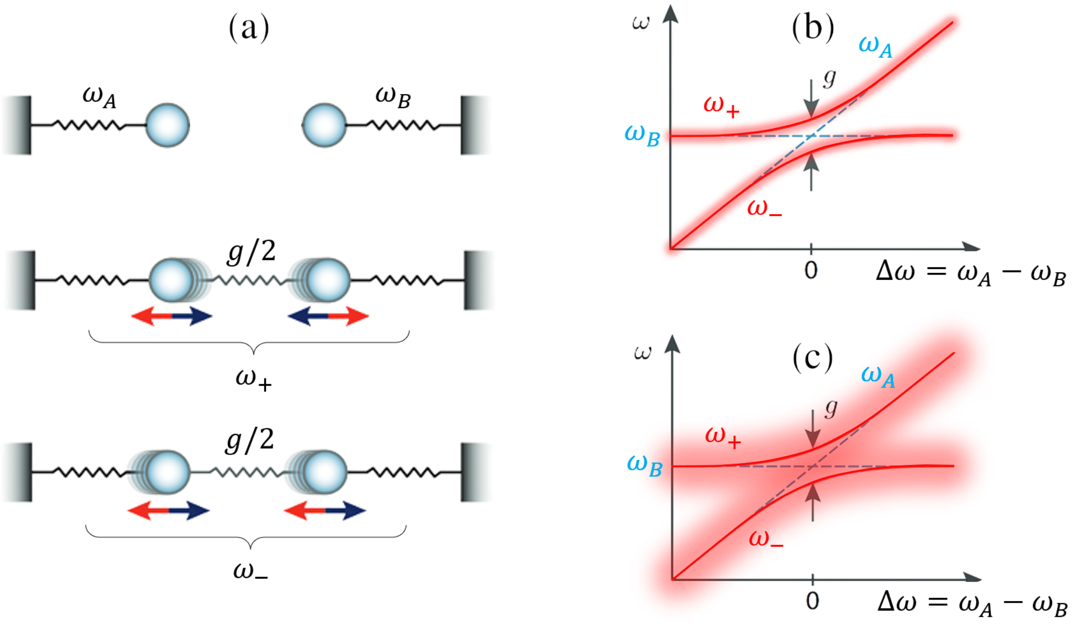

Figure 1.2: Coupled oscillators analogy. (a) Sketch of two mass-spring oscillators with frequency ω_A and ω_B, representing photonic and matter degrees of freedom. Once linearly coupled through the coupling constant $g/2$, the combined system hosts two eigenmodes: an anti-phase one, of frequency ω_+, and an in-phase one, of frequency ω_-. They constitute hybrid excitations made of a combination of the two bare modes, just as polaritons that are hybrid light-matter excitations. (b)-(c) Frequencies of the system as a function of the detuning between the bare oscillators $\Delta\omega = \omega_A - \omega_B$. The splitting at zero-detuning, g, is the Rabi splitting, and the blur surrounding the red lines represents the excitation linewidths. While panel (b) represents a scenario of strong-coupling, with a Rabi splitting larger than the linewidths, (c) shows the weak-coupling regime, with linewidths broader than the splitting, so that the two polaritons are no longer distinguishable. Figures adapted from Ref. [77].

being lost before they can hybridize. We note that when the Rabi splitting g becomes large enough, typically on the order of a non-negligible fraction of the bare matter excitation frequency, the system enters the so-called ultra-strong coupling regime. In that regime, this classical analogy is no longer appropriate, as purely quantum phenomena, such as the population of the ground state by virtual photons, may become relevant. In this manuscript, we will not explore such an ultra-strong coupling regime, as we consider it beyond the scope of our study, but we leave it for future investigations.

In order to experimentally reach the strong-coupling regime, physicists frequently employ Fabry-Pérot-type mirror cavities to confine electromagnetic modes within a finite volume. The mirrors reflect photons, enhancing their interaction with the material inside the cavity and consequently increasing their effect on matter excitations. Through a fine-tuning of the cavity, it is possible to select the resonant frequency of the cavity photons inside, so that the detuning approaches 0, and to optimize the photon lifetime by increasing the quality factor of the mirrors. The development of such cavity QED as a field led notably to the study of polaritons in atomic and molecular systems. This is also the approach we will consider in this thesis, as it will be theoretically introduced in detail in Chap. 2.

Polaritons offer significant advantages and are highly sought-after due to their combination of photon and matter excitation properties. In particular, they promise technological and fundamental advances in various fields, allowing notably for polariton Bose-Einstein condensation [78], the study of out-of-equilibrium universal behaviors [79], room temperature lasing [80], superfluidity [81] or the manipulation and improvement of chemical reactions [82]. Beside that, one of the key features of polaritons is their capability for long-range transport with ballistic propagation.

This led a large amount of theoretical proposals [83–95] as well as experiments using organic molecular semiconductors [96–110], quantum well semiconductors [111], plexcitons in arrays of plasmonic nanoparticles [112], or transition-metal-dichalcogenides [113–115], to use strong light-matter coupling in order to enhance energy and charge transport properties in matter, such as electrical conductivity or photoconductivity [106], the latter being of particular interest for photovoltaic solar-cell technologies. Interestingly, dark states, i.e., matter states that are only weakly hybridized to photonic degrees of freedom, can also show nontrivial transport properties induced by the strong-coupling regime [87, 90, 91, 107].

These enhancements are directly attributed to the hybrid nature of collective polaritonic excitations, enabling their delocalization throughout the system, with strong coupling inducing an effective, photon-mediated long-range coupling between matter excitations. Such a cavity-enhanced transport can be particularly interesting when applied to disordered systems, a scenario we will study extensively in Chap. 3.

Very recently, experimental studies have notably achieved to precisely track polariton long-range transport using real-space time-resolved microscopy techniques [109, 110]. We present these results in Figs. 1.3(a)-(b), which have the advantage to offer clear visualizations of the phenomenon of cavity-enhanced transport. These experiments have been conducted at room temperature using 2d films of excitonic materials, embedded between distributed Bragg reflectors (DBR), which are Fabry-Pérot-like cavities made of alternating layers of material with different refractive indices. Using a pump-probe setup, the difference of reflectivity intensity between the pumped and unpumped signals, ΔR, has been measured, and then normalized by the unpumped signal, R. Different pump-probe delay times have been used to track the temporal evolution of the excitation.

In Fig. 1.3(a), dye molecular J-aggregates, an organic semiconductor, has been used. We clearly observe the fast propagation of the polaritonic excitation, travelling dozens of micrometers in a picosecond. In Fig. 1.3(b),

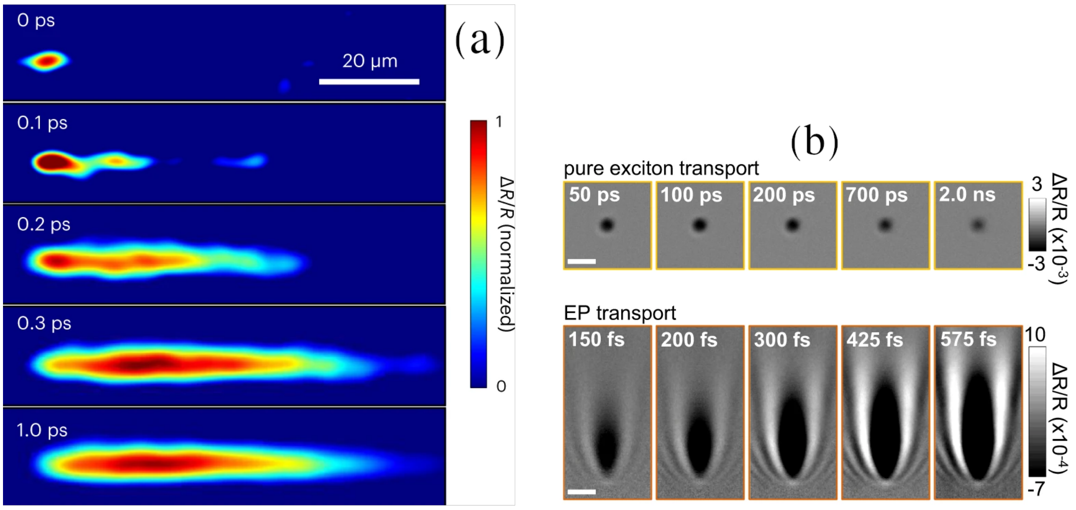

Figure 1.3: Polaritons transport. Real-space time-resolved imaging of polariton transport, through differential reflectivity measurements of pump-probe experiments. (a) Fast-propagating exciton-polariton (EP) in a dye molecular film embedded in a mirror cavity, reproduced from Ref. [109]. (b) Comparison between pure exciton and EP transports in a slab of layered halide perovskite embedded in a mirror cavity, reproduced from Ref. [110].

layered halide perovskite, a particularly photosensitive semiconductor, has been utilized. A comparison between bare exciton (top panels) and exciton-polariton (bottom panels) propagations allow to clearly visualize polariton advantages. Interestingly, as these molecular films are amorphous in nature and hence highly disordered, they permit the study of disordered polaritons, so that we will briefly come back to these type of experiments at the beginning of Chap. 3.

In the study presented throughout the remaining of this manuscript, we will demonstrate that such long-distance propagation features of polaritonic excitations may hold significant potential in both disordered and topological systems.

CHAPTER 2

MODELLING THE LIGHT-MATTER COUPLING

In this chapter, we develop a fully microscopic quantum theory of a one-dimensional array of dipolar emitters coupled to confined electromagnetic modes. More precisely, after reviewing the quantization of the electromagnetic field in the Coulomb gauge and its coupling to dipolar emitters, we present our model of light-matter coupling in an optical cavity. Both the cases of an infinite waveguide cavity and of a finite cuboidal cavity are examined. In particular, we present the approximations that allow us to simplify the model and handle the physical systems under study in Chaps. 3 and 4.

While Maxwell's equations are basically sufficient to describe the light-matter interaction in classical systems, including the strong light-matter coupling regime, it is convenient to construct quantum mechanical models based on the Hamiltonian formalism. It enables the use of quantum optics tools and facilitates the gain of analytical insights into the problem, whereas solving Maxwell's equations usually requires complex numerical algorithms. Therefore, we emphasize that although we present here a fully quantum theory, the system under study – dipolar emitters (strongly) coupled to the electromagnetic field – remains of purely classical nature, and no quantum effects are considered. Although a classical formalism could have been employed, the quantum Hamiltonian approach provides, in our view, greater transparency and ease of implementation [19, 116–118].

2.1 Quantization of the electromagnetic field in the Coulomb gauge

In the entire manuscript, we work in the Coulomb gauge, where the vector potential $\mathbf{A}$ of the considered electromagnetic field is such that

$$\nabla \cdot \mathbf{A} = 0. \tag{2.1}$$

Such gauge choice, common in quantum optics, notably implies that the vector potential, as well as the magnetic field, is purely transverse. Then, the electric field $\mathbf{E} = -(1/c)\partial_t \mathbf{A} - \nabla\phi$, where c is the speed of light in vacuum, has a longitudinal part arising from the scalar potential ϕ, i.e., the source charges only.[1] Hence, the Helmholtz decomposition theorem is trivially verified [119]. Interestingly, this leads the scalar potential to be instantaneous, i.e., static, and entirely contained in the electromagnetic field Hamiltonian. The light-matter coupling is then described solely through the vector potential $\mathbf{A}$, and contains all the retardation effects of the radiation field.

The quantization of the electromagnetic field follows from the fact that photonic modes can be seen as harmonic oscillators. Indeed, a Fourier expansion of the vector potential, and the substitution of the Fourier coefficients by second quantized, bosonic ladder operators, lead to [120–122]

$$\mathbf{A}(\mathbf{r}) = \sum_{\mathbf{k},\hat{\lambda}_\mathbf{k}} \sqrt{\frac{2\pi\hbar c^2}{\omega_\mathbf{k}^{\mathrm{ph}}}} \left[\mathbf{f}_\mathbf{k}^{\hat{\lambda}_\mathbf{k}}(\mathbf{r}) c_\mathbf{k}^{\hat{\lambda}_\mathbf{k}} + \mathbf{f}_\mathbf{k}^{\hat{\lambda}_\mathbf{k}\,*}(\mathbf{r}) c_\mathbf{k}^{\hat{\lambda}_\mathbf{k}\,\dagger} \right]. \tag{2.2}$$

In the above equation, $\omega_\mathbf{k}^{\mathrm{ph}} = c|\mathbf{k}|$ represents the photonic dispersion and $\mathbf{f}_\mathbf{k}^{\hat{\lambda}_\mathbf{k}}(\mathbf{r})$ corresponds to the mode functions of the electromagnetic field, evaluated at the position $\mathbf{r} = x\hat{x} + y\hat{y} + z\hat{z}$.[2] The mode functions $\mathbf{f}_\mathbf{k}^{\hat{\lambda}_\mathbf{k}}(\mathbf{r})$ contain the

---

[1] Throughout the manuscript, we use cgs units.

[2] Throughout the manuscript, hats designate unit vectors.

spatial dependence of the field mode with wavevector $\mathbf{k}$ and polarization $\hat{\lambda}_{\mathbf{k}}$, and therefore depend on the space geometry in which the field is quantized. We recall that due to the massless nature of the electromagnetic field, there are only two distinct photonic polarizations $\hat{\lambda}_{\mathbf{k}} = \{\hat{1}_{\mathbf{k}}, \hat{2}_{\mathbf{k}}\}$. These polarizations follow the transverse conditions $\hat{1}_{\mathbf{k}} \cdot \mathbf{k} = \hat{2}_{\mathbf{k}} \cdot \mathbf{k} = 0$ and $\hat{1}_{\mathbf{k}} \cdot \hat{2}_{\mathbf{k}} = 0$. The bosonic field operators $c_{\mathbf{k}}^{\hat{\lambda}_{\mathbf{k}}}$ and $c_{\mathbf{k}}^{\hat{\lambda}_{\mathbf{k}}\dagger}$ appearing in Eq. (2.2) respectively annihilate and create a photon with wavevector $\mathbf{k}$ and polarization $\hat{\lambda}_{\mathbf{k}}$. These operators obey the bosonic commutation relations

$$\left[c_{\mathbf{k}}^{\hat{\lambda}_{\mathbf{k}}}, c_{\mathbf{k}'}^{\hat{\lambda}'_{\mathbf{k}'}\dagger} \right] = \delta_{\mathbf{k},\mathbf{k}'} \delta_{\hat{\lambda}_{\mathbf{k}}, \hat{\lambda}'_{\mathbf{k}'}}, \tag{2.3}$$

where $\delta_{i,j}$ denotes the Kronecker delta.

Importantly, in our present analysis, we are considering the quantization of the electromagnetic field in a charge-free space. Under such a condition, both the electric and magnetic fields are divergence-free and thus have no longitudinal part, so that they can be written as $\mathbf{E} = \mathbf{E}_{\perp}$ and $\mathbf{B} = \mathbf{B}_{\perp}$. Therefore, from the relations $\mathbf{B} = \nabla \times \mathbf{A}$ and $\mathbf{E}_{\perp} = -(1/c)\partial_t \mathbf{A}$, the (source-free) quantized electromagnetic field reads

$$\mathbf{E}(\mathbf{r}) = \mathrm{i} \sum_{\mathbf{k},\hat{\lambda}_{\mathbf{k}}} \sqrt{2\pi\hbar\omega_{\mathbf{k}}^{\mathrm{ph}}} \left[\mathbf{f}_{\mathbf{k}}^{\hat{\lambda}_{\mathbf{k}}}(\mathbf{r}) c_{\mathbf{k}}^{\hat{\lambda}_{\mathbf{k}}} - \mathbf{f}_{\mathbf{k}}^{\hat{\lambda}_{\mathbf{k}}*}(\mathbf{r}) c_{\mathbf{k}}^{\hat{\lambda}_{\mathbf{k}}\dagger} \right] \tag{2.4}$$

and

$$\mathbf{B}(\mathbf{r}) = \sum_{\mathbf{k},\hat{\lambda}_{\mathbf{k}}} \sqrt{\frac{2\pi\hbar c^2}{\omega_{\mathbf{k}}^{\mathrm{ph}}}} \left[\left(\nabla \times \mathbf{f}_{\mathbf{k}}^{\hat{\lambda}_{\mathbf{k}}}(\mathbf{r}) \right) c_{\mathbf{k}}^{\hat{\lambda}_{\mathbf{k}}} + \left(\nabla \times \mathbf{f}_{\mathbf{k}}^{\hat{\lambda}_{\mathbf{k}}*}(\mathbf{r}) \right) c_{\mathbf{k}}^{\hat{\lambda}_{\mathbf{k}}\dagger} \right]. \tag{2.5}$$

Within such a second-quantized framework, the photonic Hamiltonian, corresponding to the source-free electromagnetic field, reads [120–122]

$$\begin{aligned} H_{\mathrm{ph}} &= \frac{1}{8\pi} \int \mathrm{d}^3\mathbf{r} \left[|\mathbf{E}_{\perp}|^2 + |\mathbf{B}|^2 \right] \\ &= \sum_{\mathbf{k},\hat{\lambda}_{\mathbf{k}}} \hbar\omega_{\mathbf{k}}^{\mathrm{ph}} \left[c_{\mathbf{k}}^{\hat{\lambda}_{\mathbf{k}}\dagger} c_{\mathbf{k}}^{\hat{\lambda}_{\mathbf{k}}} + \frac{1}{2} \right], \end{aligned} \tag{2.6}$$

so that it has been expressed as a sum of quantum harmonic oscillator Hamiltonians, one for each photonic mode. The familiar $1/2$ term in the above photonic Hamiltonian will be left out in the remaining of this manuscript, as it merely represents a constant energy shift, thus having no incidence on the equations of motion.

In the next section, we will introduce sources, specifically dipolar emitters, into the system. Besides the minimal coupling between the emitters and the electromagnetic field, it will add a longitudinal part to the electric field (2.4),

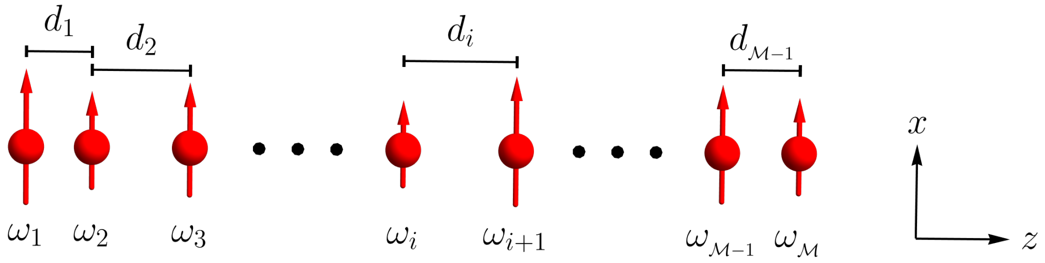

Figure 2.1: Chain of emitters. Sketch of a generic chain of $\mathcal{M}$ dipolar emitters, all polarized along the same x direction, and arranged along the z direction. Each given emitter labeled by i has a resonance frequency ω_i and is separated from its neighbor to the right by a distance d_i. The average individual resonance frequency is ω_0, and the average distance between two dipoles is d.

arising from the instantaneous scalar potential ϕ. This longitudinal part gives rise to the quasistatic coupling between the dipoles.

2.2 $\mathcal{M}$ dipolar emitters coupled to the vacuum electromagnetic field

We now consider the coupling of $\mathcal{M}$ subwavelength dipolar emitters to the vacuum electromagnetic field. Due to their subwavelength nature, we treat them as dimensionless point dipoles without considering any internal degrees of freedom, so that they behave as classical oscillating dipoles.

These point dipoles represent a large variety of physical systems whose primary coupling mechanism is dipolar in nature and is governed by classical electromagnetism. Indeed, such generic emitters model experimental platforms as diverse as subwavelength plasmonic, dielectric or SiC nanoparticles [19, 123–125], magnonic microspheres [126–128], microwave antennas [129], semiconductor excitons [130], cold atoms [131–133], or any other two-level emitters, as they behave as classical dipoles in the single excitation manifold [134].

In particular, we consider all the emitters to be polarized along the same direction $\hat{\sigma} = \hat{x}$, and to be arranged in a long but finite one-dimensional lattice along the z direction, as sketched in Fig. 2.1. Two different cases of lattice will be discussed in this thesis. First, in Chap. 3 we study a simple unipartite array of dipolar emitters, with a single dipole per unit cell. Second, in Chap. 4, a dimerized, bipartite array is considered, thus with two dipoles per unit cell. In both cases, we denote the average distance between two units cells, i.e., the lattice constant in the case of a periodic array, as d. For convenience, we present in this chapter only the simple array, therefore with d being the average distance between two dipoles. The generalization to two dipoles per unit cell is direct, and will be presented in Chap. 4.

Each dipolar emitter, labeled by i, has a single dynamical degree of freedom, its displacement vector $\mathbf{h}_i = h_i\hat{x}$. It oscillates at a resonance frequency ω_i, has an effective mass M, and its associated electric dipole moment is $\mathbf{p}_i = -Q\mathbf{h}_i$, with $-Q$ its effective charge. From these effective quantities, we define a typical dipole length scale,[3]

$$a = \left(\frac{Q^2}{M\omega_0^2}\right)^{1/3}, \tag{2.7}$$

where ω_0 denotes the average resonance frequency of the considered dipolar emitters. For the sake of simplicity, we consider in the following that all the emitters have the same length scale a, while their resonance frequencies ω_i can be different.[4]

In order for the point dipole approximation to be valid, we consider the dipole length scale to be much smaller than the average inverse wave number $k_0^{-1} = c/\omega_0$ associated with an individual dipolar mode, i.e., we require that the dimensionless dipole strength $k_0 a \ll 1$. For these emitters to interact with the electromagnetic field as point dipoles, we also need to consider the long wavelength approximation for the photons, namely that $|\mathbf{k}|a \ll 1$.

2.2.1 Quasistatic coupling between the emitters

The Hamiltonian corresponding to the set of $\mathcal{M}$ *uncoupled* dipoles reads

$$H_{\mathrm{dp}}^0 = \sum_{i=1}^{\mathcal{M}} \left[\frac{\mathbf{\Pi}_i^2}{2M} + \frac{M\omega_i \mathbf{h}_i^2}{2}\right], \tag{2.8}$$

where $\mathbf{\Pi}_i$ is the conjugate momentum to the displacement $\mathbf{h}_i$ of the ith dipole excitation.

With the addition of dipolar emitters as sources, the Hamiltonian of the electromagnetic field reads [120–122]

$$\begin{aligned} H_{\mathrm{em}} &= \frac{1}{8\pi}\int \mathrm{d}^3\mathbf{r} \left[|\mathbf{E}_\perp + \mathbf{E}_\parallel|^2 + |\mathbf{B}|^2\right] \\ &= H_{\mathrm{ph}} + \frac{1}{2}\int \mathrm{d}^3\mathbf{r}\, \rho\phi, \end{aligned} \tag{2.9}$$

where a term corresponding to the longitudinal part of the electric field has been added to the source free electromagnetic field Hamiltonian (2.6). In the

---

[3] As an example, in the case of spherical metallic nanoparticles hosting localized surface plasmons, $Q = eN_\mathrm{e}$ and $M = m_\mathrm{e}N_\mathrm{e}$, where N_e is the number of valence electrons of charge $-e < 0$ and mass m_e. The resonance frequency of the plasmon is then the Mie frequency of the nanoparticle $\omega_0 = (N_\mathrm{e}e^2/m_\mathrm{e}a^3)^{1/2}$, with the dipole length scale a being the nanoparticle radius.

[4] While considering varying effective masses M_i and charges Q_i, along with the varying resonance frequencies ω_i, is formally more accurate, it complicates the derivation of the model and does not change the physics under consideration in this manuscript.

above equation, ρ denotes the source charge density, while ϕ is the scalar potential. In the point dipole, long wavelength approximation, such an additional term corresponds to the Coulomb potential energy between the dipolar emitters [120]

$$V_{\text{Coulomb}}^{\text{dip-dip}} = \frac{1}{2} \sum_{\substack{i,j=1 \\ (i \neq j)}}^{\mathcal{M}} \frac{\mathbf{p}_i \cdot \mathbf{p}_j - 3\left(\mathbf{p}_i \cdot \hat{n}_{ij}\right)\left(\mathbf{p}_j \cdot \hat{n}_{ij}\right)}{|\mathbf{r}_i - \mathbf{r}_j|^3}, \tag{2.10}$$

where $\mathbf{r}_i$ is the location of the ith dipole, and $\hat{n}_{ij} = (\mathbf{r}_i - \mathbf{r}_j)/|\mathbf{r}_i - \mathbf{r}_j|$. Such potential energy (2.10) accounts for the quasistatic dipole-dipole coupling, decreasing with the inverse distance cubed, and solely containing dipolar degrees of freedom.

2.2.2 Minimal coupling

While the longitudinal electric part of the interaction leads to the potential energy (2.10), the transverse electric and magnetic part of the interaction enters in the kinetic energy, through the minimal substitution of the momentum [121]

$$\mathbf{\Pi}_i \rightarrow \mathbf{\Pi}_i + \frac{Q}{c}\mathbf{A}(\mathbf{r}_i). \tag{2.11}$$

It fundamentally originates from a relativistic theory by the replacement in the free Lagrangian of the usual derivatives with the covariant derivatives, $\partial_\mu \rightarrow D_\mu = \partial_\mu + (\mathrm{i}Q/c)A_\mu$, where A_μ is the four-vector gauge potential. This replacement is required to preserve the $U(1)$ gauge symmetry of electromagnetism, therefore, the light-matter coupling is fully determined by the gauge invariance of the theory itself [135].

The total Hamiltonian of the system of emitters coupled to the electromagnetic field thus read

$$H = \sum_{i=1}^{\mathcal{M}} \left[\frac{\left(\mathbf{\Pi}_i + \frac{Q}{c}\mathbf{A}(\mathbf{r}_i)\right)^2}{2M} + \frac{M\omega_i \mathbf{h}_i^2}{2} \right] + V_{\text{Coulomb}}^{\text{dip-dip}} + H_{\text{ph}}, \tag{2.12}$$

which we reorganize as

$$H = H_{\text{dp}} + H_{\text{ph}} + H_{\mathbf{\Pi}\cdot\mathbf{A}} + H_{\mathbf{A}^2}. \tag{2.13}$$

In the above Hamiltonian, the first term on the right-hand-side (r.h.s.) accounts for the dipolar degrees of freedom with quasistatic coupling and reads

$$H_{\text{dp}} = H_{\text{dp}}^0 + V_{\text{Coulomb}}^{\text{dip-dip}}, \tag{2.14}$$

while the second term is the photonic Hamiltonian given in Eq. (2.6). The third term on the r.h.s. of Eq. (2.13) is the so-called paramagnetic, $\mathbf{\Pi} \cdot \mathbf{A}$

Hamiltonian

$$H_{\mathbf{\Pi}\cdot\mathbf{A}} = \sum_{i=1}^{\mathcal{M}} \frac{Q}{Mc}\mathbf{\Pi}_i \cdot \mathbf{A}(\mathbf{r}_i), \tag{2.15}$$

which is linear in the vector potential and couples light and matter degrees of freedom. Finally, the fourth term is the so-called diamagnetic, $\mathbf{A}^2$ Hamiltonian

$$H_{\mathbf{A}^2} = \sum_{i=1}^{\mathcal{M}} \frac{Q^2}{2Mc^2}\mathbf{A}^2(\mathbf{r}_i), \tag{2.16}$$

which is quadratic in the vector potential, and contains no matter, namely, dipolar, degrees of freedom.

2.2.3 Second quantization formalism

While the electromagnetic field has been quantized in Sec. 2.1, we still need to quantize the dipolar degrees of freedom. To this end, we introduce the bosonic ladder operators

$$b_i = \sqrt{\frac{M\omega_i}{2\hbar}}\mathbf{h}_i \cdot \hat{x} + \mathrm{i}\sqrt{\frac{1}{2\hbar M\omega_i}}\mathbf{\Pi}_i \cdot \hat{x} \tag{2.17}$$

and

$$b_i^{\dagger} = \sqrt{\frac{M\omega_i}{2\hbar}}\mathbf{h}_i \cdot \hat{x} - \mathrm{i}\sqrt{\frac{1}{2\hbar M\omega_i}}\mathbf{\Pi}_i \cdot \hat{x}, \tag{2.18}$$

which, respectively, annihilates and creates a dipolar excitation with effective mass M, resonance frequency ω_i and polarized along the x direction. They obey the bosonic commutation relations

$$\left[b_i, b_j^{\dagger}\right] = \delta_{ij}. \tag{2.19}$$

The displacement coordinate of the ith dipole and its conjugate momentum thus read in second quantized form

$$\mathbf{h}_i = \sqrt{\frac{\hbar}{2M\omega_i}}\left(b_i^{\dagger} + b_i\right)\hat{x} \tag{2.20}$$

and

$$\mathbf{\Pi}_i = \mathrm{i}\sqrt{\frac{\hbar M\omega_i}{2}}\left(b_i^{\dagger} - b_i\right)\hat{x}, \tag{2.21}$$

so that the dipolar Hamiltonian (2.14) can be rewritten as

$$\begin{aligned} H_{\mathrm{dp}} = & \sum_{i=1}^{\mathcal{M}} \hbar\omega_i \left({b_i}^\dagger b_i + \frac{1}{2} \right) \\ & + \sum_{\substack{i,j=1 \\ (i \neq j)}}^{\mathcal{M}} \frac{\hbar\Omega_{ij}\eta_{ij}}{2} \left({b_i}^\dagger + b_i \right) \left({b_j}^\dagger + b_j \right) . \end{aligned} \tag{2.22}$$

The first term on the r.h.s. of Eq. (2.22) corresponds to the sum of $\mathcal{M}$ quantum harmonic oscillators. As for the photonic Hamiltonian (2.6), in the remaining of the manuscript we drop the irrelevant 1/2 term. The second term on the r.h.s. accounts for the dipole-dipole Coulomb energy, in which the quasistatic dipole coupling strength

$$\begin{aligned} \Omega_{ij} & = \frac{Q^2}{2M\sqrt{\omega_i\omega_j}|\mathbf{r}_i - \mathbf{r}_j|^3} \\ & = \frac{\omega_0^2}{2\sqrt{\omega_i\omega_j}} \left(\frac{a}{|\mathbf{r}_i - \mathbf{r}_j|} \right)^3 , \end{aligned} \tag{2.23}$$

and the polarization-dependent factor

$$\begin{aligned} \eta_{ij} & = 1 - 3\left(\hat{x} \cdot \hat{n}_{ij}\right)^2 \\ & = 1. \end{aligned} \tag{2.24}$$

Indeed, due to the transverse polarization of the dipoles, being polarized along the x direction and arranged in an array along the z direction, one has $\mathbf{r}_i - \mathbf{r}_j = r_{ij}\hat{z}$, so that $\hat{n}_{ij} = \hat{z}$.

This leads us to the total, second quantized Hamiltonian

$$\begin{aligned} H = & \sum_{i=1}^{\mathcal{M}} \hbar\omega_i {b_i}^\dagger b_i + \sum_{\mathbf{k},\hat{\lambda}_{\mathbf{k}}} \hbar\omega_{\mathbf{k}}^{\mathrm{ph}} {c_{\mathbf{k}}^{\hat{\lambda}_{\mathbf{k}}}}^\dagger c_{\mathbf{k}}^{\hat{\lambda}_{\mathbf{k}}} \\ & + \sum_{\substack{i,j=1 \\ (i \neq j)}}^{\mathcal{M}} \frac{\hbar\Omega_{ij}}{2} \left({b_i}^\dagger + b_i \right) \left({b_j}^\dagger + b_j \right) \\ & + \mathrm{i}\hbar \sum_{i=1}^{\mathcal{M}} \sum_{\mathbf{k},\hat{\lambda}_{\mathbf{k}}} \sqrt{\frac{\pi Q^2 \omega_i}{M\omega_{\mathbf{k}}^{\mathrm{ph}}}} \left({b_i}^\dagger - b_i \right) \left[\mathbf{f}_{\mathbf{k}}^{\hat{\lambda}_{\mathbf{k}}}(\mathbf{r}_i) c_{\mathbf{k}}^{\hat{\lambda}_{\mathbf{k}}} + \mathrm{H.c.} \right] \cdot \hat{x} \\ & + \sum_{i=1}^{\mathcal{M}} \sum_{\substack{\mathbf{k},\hat{\lambda}_{\mathbf{k}} \\ \mathbf{k}',\hat{\lambda}'_{\mathbf{k}'}}} \frac{\hbar\pi Q^2}{M\sqrt{\omega_{\mathbf{k}}^{\mathrm{ph}}\omega_{\mathbf{k}'}^{\mathrm{ph}}}} \left[\mathbf{f}_{\mathbf{k}}^{\hat{\lambda}_{\mathbf{k}}}(\mathbf{r}_i) c_{\mathbf{k}}^{\hat{\lambda}_{\mathbf{k}}} + \mathrm{H.c.} \right] \cdot \left[\mathbf{f}_{\mathbf{k}'}^{\hat{\lambda}'_{\mathbf{k}'}}(\mathbf{r}_i) c_{\mathbf{k}'}^{\hat{\lambda}'_{\mathbf{k}'}} + \mathrm{H.c.} \right], \end{aligned} \tag{2.25}$$

which will be at the heart of the study done throughout the manuscript.

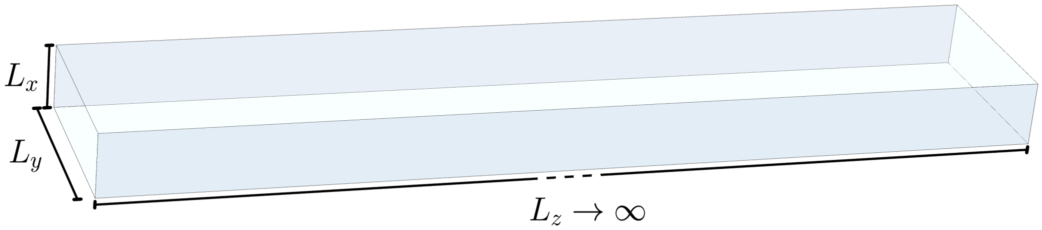

Figure 2.2: Waveguide cavity. Sketch of the waveguide cavity under consideration, with a cross section such that $L_y \gg L_x$, and a length L_z that extends to infinity. Perfectly conducting mirrors are considered in the x and y direction only, since the infinite extension in the z direction is equivalent to consider open ends.

2.3 Light-matter coupling in an infinite elongated cavity

In the remaining of this manuscript, we will be interested in the light-matter coupling of dipolar emitters placed into an elongated mirror cavity, with one spatial dimension larger than the two others. Namely, the optical structure under consideration has spatial dimensions $L_z \gg L_y \gg L_x$. From the particular shape and boundary conditions of such a photonic cavity depend the mode functions of the electromagnetic field and thus the vector potential (2.2).

In this section, we rely on Ref. [136] and consider a cavity with periodic boundary conditions in the z direction, and perfectly conducting mirror walls on the x and y sides. It leads to the photonic wavevector

$$\mathbf{k} = \begin{pmatrix} k_x \\ k_y \\ k_z \end{pmatrix} = \begin{pmatrix} \frac{\pi n_x}{L_x} \\ \frac{\pi n_y}{L_y} \\ \frac{2\pi n_z}{L_z} \end{pmatrix}, \tag{2.26}$$

with $n_x, n_y \in \mathbb{N}$, and $n_z \in \mathbb{Z}$. Moreover, we consider here the limit of an infinitely long cavity, with a longitudinal size $L_z = L_{\text{chain}} + 2d_{\text{cav}} \to \infty$, with L_{chain} the length of the chain of dipolar emitters, and d_{cav} the distance between one end of the latter chain and one end of the cavity.

This limit is equivalent to an open, *waveguide* cavity, with open boundary conditions in the z direction, as long as the distance d_{cav} between the dipolar emitters and the open ends is large enough. A sketch of such waveguide cavity is presented in Fig. 2.2. It leads to the fact that the longitudinal wavenumber k_z is continuous, allowing us to coin in the following a triplet (n_x, n_y, k_z) a cavity *mode*, and a doublet (n_x, n_y) a cavity *band*.

Importantly, and as detailed for the specific systems under study in Chaps. 3 and 4, in the case of the emitters thermodynamic limit, i.e., when dealing with an infinite chain of dipoles so that both $L_{\text{chain}} \to \infty$ and $L_z \to \infty$, and when the chain is periodic with the lattice constant d of the emitter array, the quasiwavenumber q associated with the quasimomentum of the dipolar excitation, which belongs to the first Brillouin zone $[-\pi/d, +\pi/d]$, is conserved with the longitudinal photonic wavenumber k_z. This leads us to consider here, in the case of a long but finite chain of dipole, that $k_z \in [-\pi/d, +\pi/d]$, so that the cavity modes taken into account in our finite system match the ones in the case of the above thermodynamic limit. We note that this requires the cavity length L_z to be an even multiple of the lattice constant d.

In such a context, the photonic dispersion reads

$$\omega_{\mathbf{k}}^{\mathrm{ph}} = \omega_{n_x n_y k_z}^{\mathrm{ph}} = c\sqrt{\left(\frac{\pi n_x}{L_x}\right)^2 + \left(\frac{\pi n_y}{L_y}\right)^2 + {k_z}^2}. \tag{2.27}$$

Rewriting the photonic wavevector in spherical coordinates,

$$\mathbf{k} = k \begin{pmatrix} \sin\theta_{\mathbf{k}} \cos\nu_{\mathbf{k}} \\ \sin\theta_{\mathbf{k}} \sin\nu_{\mathbf{k}} \\ \cos\theta_{\mathbf{k}} \end{pmatrix}, \tag{2.28}$$

allows one to write the two photons polarizations $\hat{\lambda}_{\mathbf{k}} = \{\hat{1}_{\mathbf{k}}, \hat{2}_{\mathbf{k}}\}$ as

$$\hat{1}_{\mathbf{k}} = \begin{pmatrix} \cos\theta_{\mathbf{k}} \cos\nu_{\mathbf{k}} \\ \cos\theta_{\mathbf{k}} \sin\nu_{\mathbf{k}} \\ -\sin\theta_{\mathbf{k}} \end{pmatrix} \quad \text{and} \quad \hat{2}_{\mathbf{k}} = \begin{pmatrix} -\sin\nu_{\mathbf{k}} \\ \cos\nu_{\mathbf{k}} \\ 0 \end{pmatrix}, \tag{2.29}$$

so that they satisfy the transversality conditions of Maxwell's equations.

From the vanishing of the tangential component of the electric field and of the normal component of the magnetic field at the x and y boundaries of the cavity, one obtains the spatial profiles of the mode functions of the electromagnetic field [137]

$$\mathbf{f}_{\mathbf{k}}^{\hat{\lambda}_{\mathbf{k}},=}(\mathbf{r}) = C^{=} \begin{pmatrix} \cos(k_x x)\sin(k_y y)(\hat{x}\cdot\hat{\lambda}_{\mathbf{k}}) \\ \sin(k_x x)\cos(k_y y)(\hat{y}\cdot\hat{\lambda}_{\mathbf{k}}) \\ \sin(k_x x)\sin(k_y y)(\hat{z}\cdot\hat{\lambda}_{\mathbf{k}}) \end{pmatrix} \mathrm{e}^{\mathrm{i}k_z z}, \tag{2.30}$$

with the normalization constant $C^{=} = \sqrt{2/\mathcal{V}}$ if k_x, k_y, or $k_z = 0$, and $C^{=} = 2/\sqrt{\mathcal{V}}$ otherwise, $\mathcal{V} = L_x L_y L_z$ being the volume of the cavity. Here, the parallel bars superscript $=$ denotes the consideration of an infinite waveguide cavity.

Diagonalizing the Hamiltonian (2.25) while considering the full electromagnetic mode functions (2.30), with all the (n_x, n_y) bands, is a very challenging task. However, under some assumptions, high energy photons can be neglected, simplifying considerably the description.

2.3.1 Single cavity band approximation

Our goal is to simplify the Hamiltonian (2.25), while still allowing the system to enter in the strong light-matter coupling regime. For this purpose, we follow Ref. [136] and place ourselves in a regime where only the lowest frequency band, $(n_x, n_y) = (0, 1)$, resonates with the dipolar modes, which have an average frequency ω_0.

Then, from the geometrical constraint $L_y \gg L_x$, all the band with $n_x \neq 0$ are highly off-resonant with the dipole excitations. Indeed, even the lowest mode with $n_x \neq 0$ is associated with the irrelevant frequency $\omega^{\mathrm{ph}}_{100} = (L_y/L_x)\omega^{\mathrm{ph}}_{010} \gg \omega^{\mathrm{ph}}_{010}$. Therefore, we restrict ourselves to cavity modes with transverse wavenumber $k_x = 0$. This yields from Eq. (2.28) that $\nu_{\mathbf{k}} = \pi/2$ or $3\pi/2$, leading the mode functions (2.30) to simplify as

$$\mathbf{f}^{=}_{\mathbf{0n_yk_z}}(\mathbf{r}) = \sqrt{\frac{2}{\mathcal{V}}} \begin{pmatrix} \sin(\frac{\pi n_y}{L_y} y) \\ 0 \\ 0 \end{pmatrix} \mathrm{e}^{\mathrm{i}k_z z}, \tag{2.31}$$

where we drop the photon polarization index, since only $\hat{\lambda}_{\mathbf{k}} = \hat{2}_{\mathbf{k}}$ is relevant.

Now, for convenience, we consider that all the dipolar emitters are exactly centered inside the cavity, so that the position of the ith dipole reads $\mathbf{r}_i = (L_x/2, L_y/2, z_i)$. It implies from Eq. (2.31) that only the cavity modes with odd $n_y = 1, 3, 5\ldots$ can couple to the dipolar excitations. From Eq. (2.27), we have $\omega^{\mathrm{ph}}_{03k_z} \geq 3\omega^{\mathrm{ph}}_{010}$, so that we can ignore all the cavity modes $n_y > 1$, considering them off-resonant with the dipolar modes. For this being consistent with the above truncation of the cavity modes $n_x \neq 0$ we fix the aspect ratio of the cavity as $L_y/L_x = 3$.

Importantly, this approximation limits the allowed regime of parameters. It amounts to consider an ultraviolet cutoff frequency

$$\begin{aligned} \omega^{\mathrm{ph}}_{\mathrm{cutoff}} &= 3\omega^{\mathrm{ph}}_{010} = \omega^{\mathrm{ph}}_{030} = \omega^{\mathrm{ph}}_{100} = c\frac{\pi}{L_x} \\ &= \frac{\pi}{k_0 a}\frac{a}{L_x}\omega_0, \end{aligned} \tag{2.32}$$

which depends on the dimensionless dipole strength $k_0 a$ as well as on the cavity height L_x. For our approximation to be reasonable, we need $\omega^{\mathrm{ph}}_{\mathrm{cutoff}} \gg \omega_0$, and we recall that the point dipole approximation requires $k_0 a \ll 1$.

We discuss the validity of such single band approximation in Fig. 2.3, where we show the behavior of the cutoff frequency (2.32) as a function of the cavity height L_x, as well as the one of the lowest cavity mode considered, $\omega^{\mathrm{ph}}_{010} \equiv \omega^{\mathrm{ph}}_{0}$. Two different values of the dimensionless dipole strength $k_0 a = 0.05$ and $k_0 a = 0.10$ are shown in panels (a) and (b), respectively.

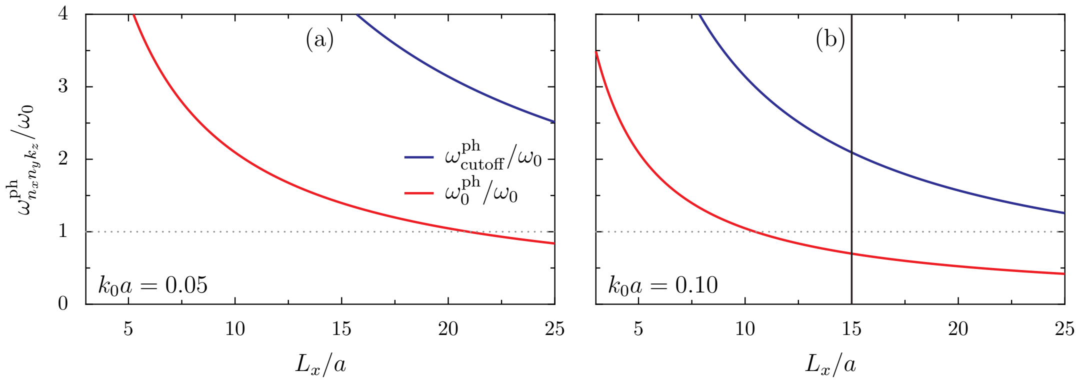

Figure 2.3: Cutoff frequency. Behavior of the cutoff frequency (2.32), and of the lowest cavity frequency considered in our single band approximation, $\omega^{\mathrm{ph}}_{010} \equiv \omega^{\mathrm{ph}}_0$, plotted in units of the average dipole frequency ω_0, as a function of the cavity height L_x, and for dimensionless dipole strength fixed to (a) $k_0 a = 0.05$ and (b) $k_0 a = 0.10$. The horizontal grey dotted line corresponds to the average dipole frequency ω_0, while the vertical black solid line in panel (b) points out our chosen upper bound for the cavity height. As in the remaining of the manuscript, the aspect ratio $L_y/L_x = 3$.

Fig. 2.3 reveals that the single band approximation becomes poorer as the cavity height L_x increases, the cutoff frequency becoming increasingly close to the average dipole frequency ω_0, represented as a grey dotted line. Larger values of $k_0 a$ reduce the acceptable range of cavity height, while smaller ones shift to larger L_x the regime where the considered band $(n_x, n_y) = (0, 1)$ resonates with the dipolar modes. In the remainder of the manuscript, we choose to fix $k_0 a = 0.1$, which limits the acceptable values of the cavity height L_x to $L_x/a \in [3, 15]$, the upper bound of this approximation being represented as a vertical black solid line in Fig. 2.3(b). We note that by limiting ourselves to such cavity heights, with fixed $k_0 a = 0.1$, we set a parameter-independent lower bound on the cutoff frequency, which is of about $\min[\omega^{\mathrm{ph}}_{\mathrm{cutoff}}] \sim 2\omega_0$. Having fixed $L_y = 3L_x$, the cavity height L_x is the only parameter left that handle the photonic degrees of freedom.

A comparison between the considered lowest band $(n_x n_y) = (0, 1)$ and the higher frequency bands, at the upper bound of our approximation, with $L_x/a = 15$, is proposed in Fig. 2.4. All the modes are represented in the first Brillouin zone, characterized by the lattice constant d of the emitter array. We recall that we take $k_z \in [-\pi/d, +\pi/d]$ in order to match the case of the emitters thermodynamic limit, in which k_z is conserved with the quasi-momentum of the dipolar excitation along the periodic array. By increasing the lattice constant d from $d = 4a$ in Fig. 2.4(a) to $d = 8a$ in Fig. 2.4(b), we observe that, as expected, the shrink of the first Brillouin zone flattens the dispersions, shifting downwards higher cavity modes. In both panels, however, we verify that higher cavity bands are highly off-resonant, even at the upper bound of our considered regime of cavity heights $L_x/a \in [3, 15]$. An

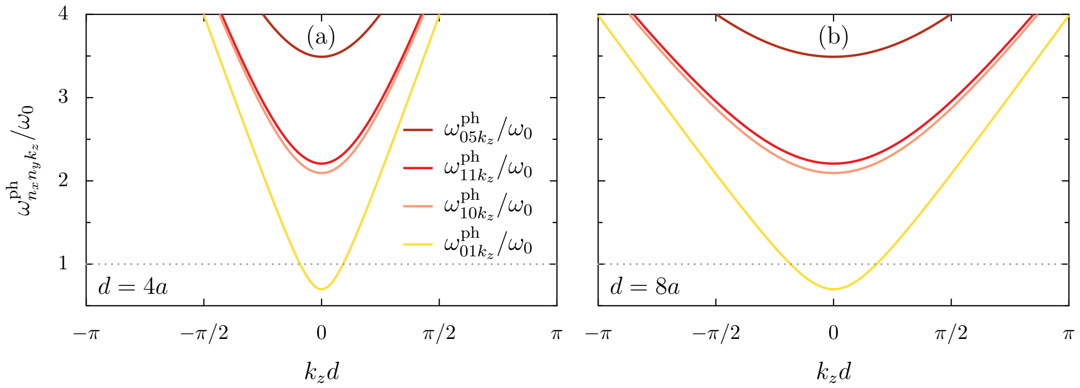

Figure 2.4: Lowest cavity bands. Comparison between the lowest frequency band $(n_x n_y) = (0, 1)$ (yellow line), and higher cavity bands $(n_x n_y) = (1, 0)$ (pink line), $(1, 1)$ (red line), and $(0, 5)$ (dark red line), when considering the upper bound of our single band approximation, where the cavity height $L_x/a = 15$. The cavity bands are plotted in the first Brillouin zone characterized by the lattice constant d of the emitter array, fixed to (a) $d = 4a$ and (b) $d = 8a$. The grey dotted line depicts the average bare dipole frequency ω_0, and, as in the remainder of the manuscript, the dimensionless dipole strength $k_0 a = 0.1$.

explicit analysis of the impact of higher cavity bands onto the system will be proposed in Chap. 4, confirming their irrelevance.

Therefore, in the following we restrict ourselves to the above regime, so that we can consider solely the coupling between dipolar emitters and the lowest-frequency cavity band $\omega^{\mathrm{ph}}_{01k_z} \equiv \omega^{\mathrm{ph}}_{k_z}$. Such single cavity band approximation results in the consideration of the photonic Hamiltonian

$$H_{\mathrm{ph}} = \sum_{k_z=-\pi/d}^{\pi/d} \hbar\omega^{\mathrm{ph}}_{k_z} c^{\dagger}_{k_z} c_{k_z}, \tag{2.33}$$

where the cavity dispersion (2.27) simplifies as

$$\omega^{\mathrm{ph}}_{k_z} = c\sqrt{\left(\frac{\pi}{L_y}\right)^2 + {k_z}^2}. \tag{2.34}$$

To better exemplify the regime of parameter under consideration, we present in Fig. 2.5 the behavior of the above photonic dispersion in units of ω_0 when increasing the cavity height L_x. As in Fig. 2.4, we represent the cavity modes in the first Brillouin zone, characterized by the lattice constant d of the emitter array. While for small values of L_x/a, the dispersion (2.34) stays high in frequency, increasing the cavity height allows it to approach and enter in resonance with the average dipole frequency ω_0, first for the lowest frequency mode ω^{ph}_0, and then for higher frequency modes $\omega^{\mathrm{ph}}_{k_z} \geq \omega^{\mathrm{ph}}_0$. Comparing Figs. 2.5(a) and 2.5(b), one observes that the shrinking of the first Brillouin

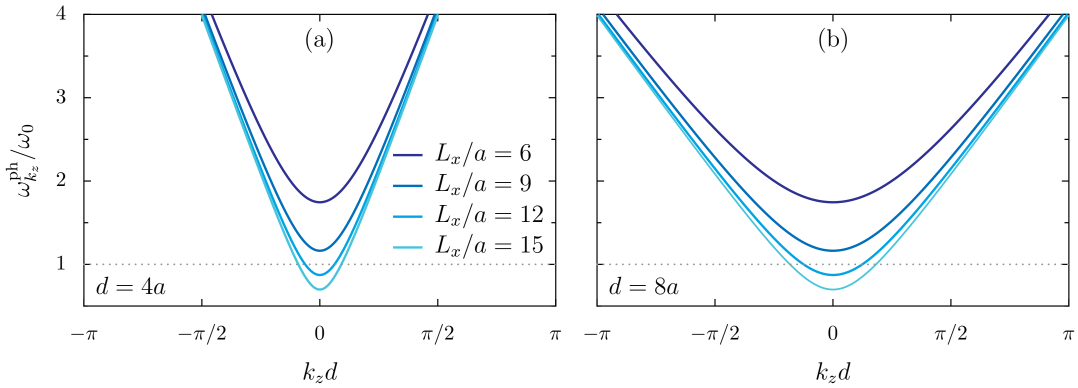

Figure 2.5: Influence of the cavity height. Considered photonic dispersion (2.34) in the single band approximation, in units of the average bare dipole frequency ω_0, and plotted in the first Brillouin zone characterized by the lattice constant d of the emitter array, fixed to (a) $d = 4a$ and (b) $d = 8a$. Increasing values of the cavity height L_x/a are shown, from dark to light blue lines, and the grey dotted line shows the average bare dipole frequency ω_0.

zone allows a larger number of photonic modes to approach the average bare dipolar frequency ω_0 when d/a is large.

With our single band approximation now being detailed, we can simplify the Hamiltonian (2.25). The vector potential (2.2) in an infinite waveguide cavity, once restricted to the $(n_x, n_y) = (0, 1)$ cavity band and $\hat{\lambda}_{\mathbf{k}} = \hat{2}_{\mathbf{k}}$ polarization, reads

$$\mathbf{A}^{=}(z) = \sum_{k_z=-\pi/d}^{\pi/d} \sqrt{\frac{4\pi\hbar c^2}{\mathcal{V}\omega^{\mathrm{ph}}_{k_z}}} \left(c_{k_z} \mathrm{e}^{\mathrm{i}k_z z} + c^{\dagger}_{k_z} \mathrm{e}^{-\mathrm{i}k_z z} \right) \hat{x}, \tag{2.35}$$

so that the paramagnetic $\mathbf{\Pi} \cdot \mathbf{A}$ Hamiltonian (2.15) reduces to

$$H^{=}_{\mathbf{\Pi}\cdot\mathbf{A}} = \mathrm{i}\hbar \sqrt{\frac{d}{L_z}} \sum_{i=1}^{\mathcal{M}} \sum_{k_z=-\pi/d}^{\pi/d} \sqrt{\frac{\omega_i}{\omega_0}} \xi_{k_z} \left(b_i^{\dagger} - b_i \right) \left(c_{k_z} \mathrm{e}^{\mathrm{i}k_z z_i} + c^{\dagger}_{k_z} \mathrm{e}^{-\mathrm{i}k_z z_i} \right), \tag{2.36}$$

and, the diamagnetic, $\mathbf{A}^2$ Hamiltonian (2.16) simplifies as

$$H^{=}_{\mathbf{A}^2} = \frac{\hbar d}{L_z} \sum_{i=1}^{\mathcal{M}} \sum_{k_z, k'_z} \frac{\xi_{k_z} \xi_{k'_z}}{\omega_0} \left[c_{k_z} \mathrm{e}^{\mathrm{i}k_z z_i} + c^{\dagger}_{k_z} \mathrm{e}^{-\mathrm{i}k_z z_i} \right] \left[c_{k'_z} \mathrm{e}^{\mathrm{i}k'_z z_i} + c^{\dagger}_{k'_z} \mathrm{e}^{-\mathrm{i}k'_z z_i} \right]. \tag{2.37}$$

In the above Hamiltonians, we introduced the light-matter coupling strength

$$\xi_{k_z} = \omega_0 \sqrt{\frac{2\pi a^3 \omega_0}{L_x L_y d \omega^{\mathrm{ph}}_{k_z}}}. \tag{2.38}$$

We show in Fig. 2.6 the behavior of its largest value, ξ_0, as a function of the

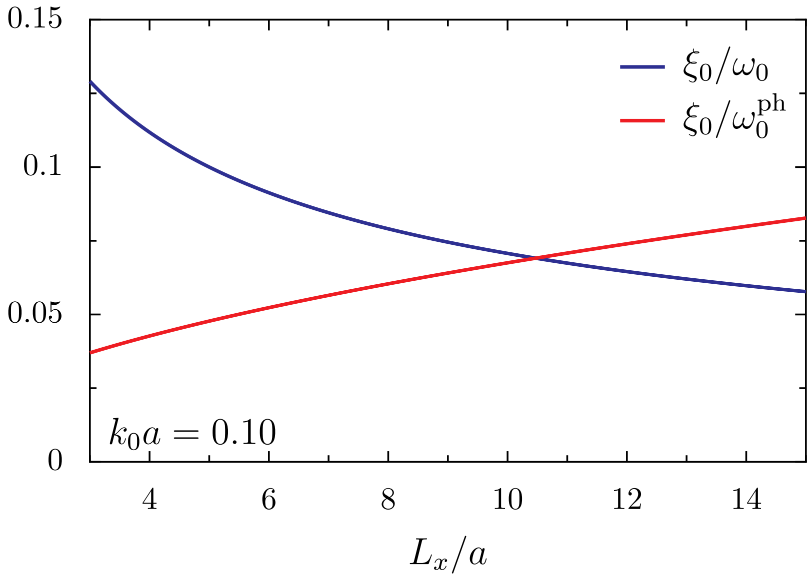

Figure 2.6: Light-matter coupling strength. Largest value of the light-matter coupling strength (2.38) as a function of the cavity height L_x, and in units of the average bare dipole frequency ω_0 (blue line) and of the lowest photon mode ω_0^{ph} (red line). The lattice constant of the emitter array $d = 4a$. We note that increasing such lattice constant just shifts downwards the two curves.

cavity height L_x, and in units of the average bare dipole frequency ω_0 (blue line), as well as in units of the lowest photonic mode ω_0^{ph} (red line).

Increasing the cavity height L_x reduces the light-matter coupling strength in units of ω_0. However, such behavior must be carefully considered. Indeed, as observed in Figs. 2.3 [cf. panel (b) for the case with $k_0 a = 0.1$] and 2.5, increasing L_x also allows resonance between cavity and dipole excitations. Therefore, counter-intuitively, while it reduces the light-matter coupling strength (2.38) in units of ω_0, increasing the cavity height allows for more proximity in frequency between the dipolar and photonic subspaces, and hence enhances the effects of the cavity photons onto the dipole excitations. This behavior will be reversed in the limit of large cavity size $L_x \gg a$, where our low-frequency, single cavity band approximation breaks down, and where one recovers the regime of a dipolar chain coupled to vacuum electromagnetic modes only, studied, e.g., in Refs. [19, 138].

In contrast, the light-matter coupling strength in units of the lowest photonic mode (red line in Fig. 2.6) increases with the cavity height L_x. Importantly, such light-matter coupling strength remains small in front of the bare dipolar and photonic frequencies, so that $\xi_0 \ll \omega_0$ and $\xi_0 \ll \omega_{k_z}^{\mathrm{ph}}$.

2.3.2 The emitter thermodynamic limit and photon Umklapp processes

As explained at the beginning of Sec. 2.3, in Chaps. 3 and 4 we will encounter the case of the emitter thermodynamic limit, dealing with an (infinitely) long periodic chain of dipoles with lattice constant d. In that case, the longitudinal photonic wavenumber k_z is conserved with the crystal wavenumber q associated with the dipolar excitation, so that both quantities can be represented in the first Brillouin zone. The periodicity of the system implies a $2\pi/d$ periodicity in the dispersion relations. When folding the photonic bands into the first Brillouin zone $k_z = q \in [-\pi/d, +\pi/d]$, the requirement of such periodicity leads to higher frequency bands, which are known as photon Umklapp processes, or diffraction orders.

Taking into account these high frequency modes results in the emitter thermodynamic limit to modify the vector potential (2.2) as

$$\mathbf{A}(\mathbf{r}_m^s) = \sum_{\mathbf{k},l,\hat{\lambda}_{\mathbf{k},l}} \sqrt{\frac{2\pi\hbar c^2}{\omega^{\mathrm{ph}}_{\mathbf{k},l}}} \left[\mathbf{f}^{\hat{\lambda}_{\mathbf{k},l}}_{\mathbf{k},l}(\mathbf{r}_m^s) c^{\hat{\lambda}_{\mathbf{k},l}}_{\mathbf{k},l} + \mathrm{H.c.} \right], \tag{2.39}$$

and the photonic Hamiltonian (2.6) as

$$H_{\mathrm{ph}} = \sum_{\mathbf{k},l,\hat{\lambda}_{\mathbf{k},l}} \hbar\omega^{\mathrm{ph}}_{\mathbf{k},l} c^{\hat{\lambda}_{\mathbf{k},l}\,\dagger}_{\mathbf{k},l} c^{\hat{\lambda}_{\mathbf{k},l}}_{\mathbf{k},l}. \tag{2.40}$$

Here, the photonic dispersion relation reads

$$\omega^{\mathrm{ph}}_{\mathbf{k},l} = c|\mathbf{k} - \mathbf{G}_l|, \tag{2.41}$$

where $\mathbf{G}_l = 2\pi l\hat{z}/d$ ($l \in \mathbb{Z}$) represents the set of reciprocal lattice vectors, so that the dispersion (2.41) is $2\pi/d$ periodic in the k_z direction.[5] In the above equations, the bosonic ladder operators $c^{\hat{\lambda}_{\mathbf{k},l}}_{\mathbf{k},l}$ and $c^{\hat{\lambda}_{\mathbf{k},l}\dagger}_{\mathbf{k},l}$ respectively annihilate and create a cavity photon with wavevector $\mathbf{k}$, Umklapp band index l, and transverse polarization $\hat{\lambda}_{\mathbf{k},l}$.

In the single cavity band approximation, which we introduced in the previous subsection, the photonic Hamiltonian (2.40) transforms into

$$H_{\mathrm{ph}} = \sum_{k_z,l} \omega^{\mathrm{ph}}_{k_z,l} c^\dagger_{k_z,l} c_{k_z,l}. \tag{2.42}$$

The photonic dispersion in the single cavity band approximation (2.34) now reads as

$$\omega^{\mathrm{ph}}_{k_z,l} = c\sqrt{\left(\frac{\pi}{L_y}\right)^2 + k_{zl}^2}, \tag{2.43}$$

---

[5] Equivalently, for a finite emitter array, taking into account Umklapp processes results in the consideration of wavenumbers $|k_z| > \pi/d$.

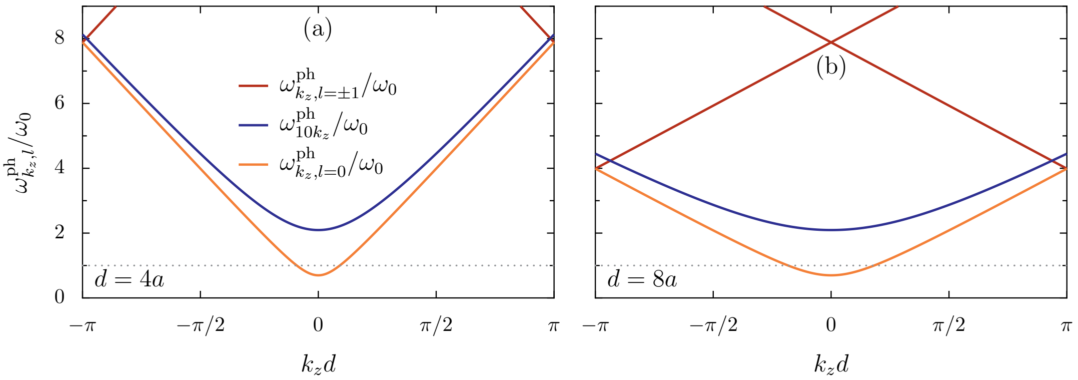

Figure 2.7: Photon Umklapp processes. Photonic dispersion (2.43) without photon Umklapp processes ($l = 0$, orange lines) and for the first Umklapp bands ($l \pm 1$, dark red lines), in units of the average bare dipolar frequency ω_0, and in the first Brillouin zone. The first neglected band $(n_x, n_y) = (1, 0)$ is shown in blue for comparison. The cavity height $L_x/a = 15$, and the lattice constant d of the emitter array characterizing the Brillouin zone is fixed to (a) $d = 4a$ and (b) $d = 8a$. The grey dotted line shows the average bare dipole frequency ω_0.

with the short form notation $k_{zl} = k_z - 2\pi l/d$.

In our modelling of the light-matter interaction of the present section, we restricted ourselves to $l = 0$, and did not consider photon Umklapp processes, characterized by $l \neq 0$. We show in Fig. 2.7 the full cavity dispersion (2.43) in the first Brillouin zone, without photon Umklapp processes ($l = 0$, orange lines) and with the first Umklapp bands ($l = \pm 1$, dark red lines). We compare it to the first neglected band ($\omega^{\mathrm{ph}}_{10k_z}$, blue lines) at the limit of validity of our single band approximation, with a cavity height $L_x/a = 15$. Two different lattice constants $d = 4a$ and $d = 8a$ are considered in Fig. 2.7(a) and Fig. 2.7(b), respectively. In both cases, Umklapp bands remain higher in frequency than the first neglected band for the most part of the Brillouin zone, so that we can in principle safely neglect them in our study. This is consistent with the fact that the latter are mostly irrelevant in the near-field regime, when the lattice constant $d \ll \lambda_0 = 2\pi/k_0$ [19], a regime in which we remain throughout this manuscript.

Importantly, however, at the edges of the Brillouin zone, around $k_z = \pm\pi/d$, the first Umklapp bands $l = \pm 1$ are lower in frequency than the first neglected band, especially in Fig. 2.7(b) when $d = 8a$. It is mainly in this wavenumber region that photon Umklapp processes may lead to quantitative effects on the system. This will lead us to reconsider such additional bands in Chap. 4, in which both the edges of the Brillouin zone and the $2\pi/d$-periodicity of the dispersion relation play an important role on some of the system properties.

2.3.3 The diamagnetic $\mathbf{A}^2$ term

As demonstrated in Sec. 2.2, the diamagnetic, $\mathbf{A}^2$ Hamiltonian originates directly from the minimal coupling substitution. Neglecting the diamagnetic term can thus lead to conceptual problems such as the loss of gauge invariance but also unphysical ground states [139]. It is, however, frequently discarded due to its quadratic nature in the light-matter coupling and several well-known quantum optics models such as the Rabi or Dicke model do not consider it. Interestingly, the notorious superradiant phase transition [140] of the latter Dicke model arises precisely because the diamagnetic term is neglected [141].[6]

For these and other reasons, the term has received a lot of interest in the recent literature. Being comprised of photonic degrees of freedom only, it acts as a photon self-energy term and dresses the photonic dispersion by inducing what is usually referred to as a diamagnetic shift. Such frequency shift being quadratic in the light-matter coupling strength, it is negligible in our model, as can be deduced from Fig. 2.6. In fact, perceptible differences due to the diamagnetic term such as gauge ambiguities were found in the context of the ultra strong coupling (USC) or deep strong coupling (DSC) regime only [147], in which we do not enter in this study.

Therefore, unless stated otherwise, we ignore the $\mathbf{A}^2$ Hamiltonian (2.37) in the remainder of the manuscript.

2.3.4 The rotating-wave approximation

To further simplify the Hamiltonian (2.13), we use in the remainder, unless stated otherwise, the rotating-wave approximation (RWA) [148]. It amounts to neglect coupling terms in the Hamiltonian that do not conserve the number of excitation, i.e., terms as $b_i^\dagger b_j^\dagger$, $b_i b_j$, $b_i^\dagger c_{k_z}^\dagger$, or $b_i c_{k_z}$. The name of such approximation stems from the interaction picture, in which the latter terms, known as counter-rotating, oscillate quickly as compared to terms conserving the number of excitations, which are almost stationary, so that they are said to be corotating with the uncoupled Hamiltonian. As long as the coupling strength associated with these terms is much smaller than the uncoupled, bare frequencies, their contribution to the dynamics as well as to the eigenspectrum and eigenvectors is weak. Indeed, the effects of the counter-rotating terms become sizable once the coupling strength is large enough. This is the sign of the entrance into the USC regime [149], which we do not consider in this study.

In the case of the dipolar RWA, this translates into the conditions $\omega_i + \omega_j \gg \Omega_{ij}$ and $\omega_i + \omega_j \gg |\omega_i - \omega_j|$, satisfied thanks to the inverse distance cube decreases of the dipole coupling strength (2.23). This approximation leads

---

[6] We note that there is still a debate about whether or not it can be a no-go theorem [142–145] for the phase transition to occur, and extensions of the model have been proposed to observe the phenomenon [146].

the dipolar Hamiltonian (2.22) to simplify as

$$H_{\mathrm{dp}}^{\mathrm{RWA}} = \sum_{i=1}^{\mathcal{M}} \hbar\omega_i {b_i}^{\dagger} b_i \;+ \sum_{\substack{i,j=1\\(i\neq j)}}^{\mathcal{M}} \frac{\hbar\Omega_{ij}}{2}\left({b_i}^{\dagger} b_j \;+ b_i\; {b_j}^{\dagger}\right). \tag{2.44}$$

On the other hand, the light-matter RWA requires $\omega_i + \omega_{k_z}^{\mathrm{ph}} \gg \xi_{k_z}$ and $\omega_i + \omega_{k_z}^{\mathrm{ph}} \gg |\omega_i - \omega_{k_z}^{\mathrm{ph}}|$, conditions that are fulfilled as observed in Figs. 2.3–2.6. It leads the paramagnetic light-matter coupling Hamiltonian in the single band approximation (2.36) to read

$$H_{\mathbf{\Pi}\cdot\mathbf{A}}^{=} = \mathrm{i}\hbar\sqrt{\frac{d}{L_z}} \sum_{i=1}^{\mathcal{M}} \sum_{k_z=-\pi/d}^{\pi/d} \sqrt{\frac{\omega_i}{\omega_0}}\xi_{k_z} \left({b_i}^{\dagger} c_{k_z} \mathrm{e}^{\mathrm{i}k_z z_i} - b_i\; c_{k_z}^{\dagger} \mathrm{e}^{-\mathrm{i}k_z z_i}\right). \tag{2.45}$$

Together with the neglection of the $\mathbf{A}^2$ Hamiltonian discussed in the previous subsection, the RWA leads us to the approximated total polaritonic Hamiltonian of the coupled cavity-emitters system in a waveguide geometry

$$H_{\mathrm{pol}}^{=} = H_{\mathrm{dp}}^{\mathrm{RWA}} + H_{\mathrm{ph}} + H_{\mathbf{\Pi}\cdot\mathbf{A}}^{=}, \tag{2.46}$$

with the photonic Hamiltonian given in Eq. (2.33), and the dipolar Hamiltonian in the RWA given in Eq. (2.44). We will study in detail such polaritonic Hamiltonian in the remainder of this manuscript, in particular in Chap. 4.

Finally, we note that other approximations not discussed here have also been made in order to obtain the Hamiltonian (2.46), such as multipolar corrections to the dipole-dipole coupling [150], as well as the effect of image charges arising from the perfectly conducting mirrors [129]. The influence of such image dipoles will be discussed in Appendix 4.C.

2.4 Dealing with a finite cuboidal cavity

While the infinite cavity considered in Sec. 2.3 models an open, *waveguide* cavity, a set-up which is experimentally attractive, the open boundaries and the continuous nature of the longitudinal photonic wavenumber k_z complicate the theoretical description when dealing with a finite number of emitters. Therefore, it can be useful to consider, for convenience, a finite *cuboidal* cavity, with closed walls in all the x, y and z directions, and a longitudinal size $L_z = L_{\mathrm{chain}} + 2d_{\mathrm{cav}} \not\to \infty$. Such a box cavity is sketched in Fig. 2.8, where the walls in the z direction are highlighted as hatched areas. While, as expected, it can have major effects on the physics around the edges of the cavity, it impacts only weakly the bulk physics. In the emitters thermodynamic limit $L_z \to \infty$ and $L_{\mathrm{chain}} \to \infty$, however, any boundary conditions in the z direction are equivalent.

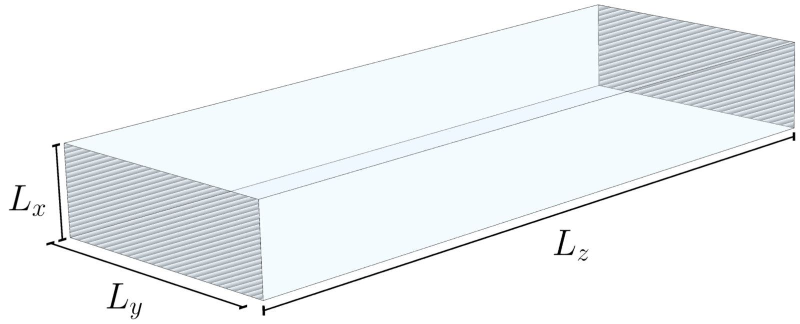

Figure 2.8: Cuboidal cavity. Sketch of the finite cuboidal cavity under consideration in this section. While as in Fig. 2.2, the cross section is such that $L_y \gg L_x$, here the longitudinal size L_z is large but finite, and all the walls in the x, y and z direction are considered as perfectly conducting mirrors.

The consideration of perfectly conducting mirrors on all cavity sides leads to the photonic wavevector

$$\mathbf{k} = \begin{pmatrix} k_x \\ k_y \\ k_z \end{pmatrix} = \begin{pmatrix} \frac{\pi n_x}{L_x} \\ \frac{\pi n_y}{L_y} \\ \frac{\pi n_z}{L_z} \end{pmatrix}, \tag{2.47}$$

with n_x , n_y, and $n_z \in \mathbb{N}$, so that, importantly, the longitudinal photonic wavenumber $k_z = \pi n_z / L_z$ is here not continuous. Hence, the photonic dispersion in the single cavity band approximation (2.34) reads here

$$\omega_{n_z}^{\text{ph}} = c\sqrt{\left(\frac{\pi}{L_y}\right)^2 + \left(\frac{\pi n_z}{L_z}\right)^2}, \tag{2.48}$$

where we made explicit the mode number index n_z. We consider $n_z \in [1, N_z]$, with $N_z = L_z/d$, so that $\max(k_z) = \pi N_z / L_z = \pi/d$, and the photonic modes (2.48) that couple to the emitters match the ones obtained previously considering the waveguide cavity as well as the emitters thermodynamic limit (see the discussion in the beginning of Sec. 2.3).

The vanishing of the tangential component of the electric field and of the normal component of the magnetic field at all the cavity boundaries leads the modes functions of the electromagnetic field to read [137]

$$\mathbf{f}_{\mathbf{k}}^{\hat{\lambda}_{\mathbf{k}},\square}(\mathbf{r}_i) = C^{\square} \begin{pmatrix} \cos(k_x x)\sin(k_y y)\sin(k_z z_i)(\hat{x}\cdot\hat{\lambda}_{\mathbf{k}}) \\ \sin(k_x x)\cos(k_y y)\sin(k_z z_i)(\hat{y}\cdot\hat{\lambda}_{\mathbf{k}}) \\ \sin(k_x x)\sin(k_y y)\cos(k_z z_i)(\hat{z}\cdot\hat{\lambda}_{\mathbf{k}}) \end{pmatrix}, \tag{2.49}$$

with the normalization constant $C^{\square} = 2/\sqrt{\mathcal{V}}$ if k_x, k_y, or $k_z = 0$, and $C^{\square} = 2\sqrt{2/\mathcal{V}}$ otherwise. Here, the box superscript $\square$ denotes the consideration of a cuboidal (box) cavity. Such spatial profiles of the vector potential lead the paramagnetic Hamiltonian (2.15) to read,

$$H^{\square}_{\mathbf{\Pi}\cdot\mathbf{A}} = \mathrm{i}\hbar\sqrt{\frac{d}{L_z}}\sum_{i=1}^{\mathcal{M}}\sum_{n_z=1}^{N_z}\sqrt{\frac{2\omega_i}{\omega_0}}\xi_{\pi n_z/L_z}\sin\left(\frac{\pi n_z}{L_z}z_i\right)\left(b_i^\dagger c_{n_z} - b_i\, c_{n_z}^\dagger\right), \tag{2.50}$$

with $\xi_{\pi n_z/L_z}$ the light-matter coupling strength (2.38), and where both the single cavity band approximation and the RWA have been used. Importantly, we note that as compared to the case of an infinite waveguide cavity [see Eq. (2.36)], here a sine function, highlighting the closed boundary conditions in the z direction, has replaced complex exponentials.

For clarity, we rewrite such light-matter coupling Hamiltonian as

$$H^{\square}_{\mathbf{\Pi}\cdot\mathbf{A}} = \mathrm{i}\hbar\sum_{i=1}^{\mathcal{M}}\sum_{n_z=1}^{N_z}\xi^{\square}_{in_z}\left(b_i^\dagger c_{n_z} - b_i\, c_{n_z}^\dagger\right), \tag{2.51}$$

where we defined the real-space light-matter coupling function as

$$\xi^{\square}_{in_z} = \omega_0\sqrt{\frac{4\pi a^3\omega_i}{\mathcal{V}\omega^{\mathrm{ph}}_{n_z}}}\sin\left(\frac{\pi n_z}{L_z}z_i\right). \tag{2.52}$$

Therefore, the total polaritonic Hamiltonian in a cuboidal geometry reads

$$H^{\square}_{\mathrm{pol}} = H^{\mathrm{RWA}}_{\mathrm{dp}} + H_{\mathrm{ph}} + H^{\square}_{\mathbf{\Pi}\cdot\mathbf{A}} \tag{2.53}$$

with the dipolar Hamiltonian in the RWA (2.44) and the photonic Hamiltonian (2.33) derived, respectively, in Sec. 2.3.1 and Sec. 2.3.4. Such polaritonic Hamiltonian will be at the heart of Chap. 3, as it allows for an exact numerical diagonalization of the full finite system, and as only the bulk of the chain is of relevance in the latter chapter.

In Chap. 4, however, we will be in particular interested in edge physics, so that in order to avoid any boundary effect, we will consider the infinite waveguide cavity presented in Sec. 2.3. In the latter chapter, we discuss in Sec. 4.8 how results from an infinite waveguide cavity can be recovered in the case of a finite cuboid cavity, with cavity walls in the z direction far enough from the ends of the emitter array.

2.5 Single mode approximation

While in our model, built similarly as what is sometimes coined the Hopfield model of light-matter interaction [71], we consider dipolar emitters coupled formally to an infinite number of cavity modes, most of the paradigmatic models of quantum optics use the single mode approximation, where the emitters are exactly at resonance with a single cavity mode.

	RWA	# emitters	# photonic modes
Quantum Rabi model [152]	×	1	1
Jaynes-Cummings model [153]	✓	1	1
Dicke model [140]	×	many	1
Tavis-Cummings model [154]	✓	many	1
Our model	× / ✓	many	many

Table 2.1: Some paradigmatic models of light-matter interaction using the single mode approximation (first four rows), as well as our model introduced in this chapter (fifth row), classified according to whether they consider the rotating wave approximation (RWA) or not, and to the number of emitters and photonic modes took into account. We note that our model may take into account counter-rotating terms (see, e.g., Appendix 3.B), although we use the RWA throughout most of this manuscript.

We list in the first four rows of Tab. 2.1 some of these renowned models of light-matter interaction [151], while the fifth row lists our model developed in this chapter. Importantly, the matter degrees of freedom in such quantum optic models are two-level quantum system, i.e., spin$-1/2$ degrees of freedom. Therefore, in contrast to our model of dipolar emitters, they may present quantum effects. However, we note that the single-mode models listed in Tab. 2.1 are commonly studied in the so-called single excitation manifold, where only a single excitation, either in the emitters or in the cavity, is considered. Interestingly, in this regime, although often presented as quantum emitters, the two-level systems behave as classical dipolar emitters [134], just as the ones we consider in our model. Notably, the Dicke and Tavis-Cummings models, considering many matter degrees of freedom, are, in the single excitation manifold, the closest models to the one we developed in this chapter.

2.6 Conclusions to Chapter 2

In this chapter, we introduced from the ground up a microscopic quantum model of the light-matter interaction between a generic one-dimensional assembly of dipolar emitters and the confined electromagnetic modes of an optical cavity. In particular, our Hamiltonian model has the specific feature of taking into account the coupling of matter to multiple cavity modes, through a spatially-dependent and dispersive light-matter coupling.

With the help of various approximations which we discussed in detail, such as the neglections of high frequency cavity modes, of the diamagnetic $\mathbf{A}^2$ Hamiltonian, and of counter-rotating terms, we derived a concise Hamiltonian that captures the main physics at play, and that is suitable both for fast numerical implementation and analytical investigation.

Two different cases of boundary conditions for the cavity were considered: an infinite cavity, equivalent to an open waveguide and resulting in the Hamiltonian (2.46), and a finite cuboidal cavity, resulting in the Hamiltonian (2.53).

Both models have advantages and drawbacks and will be used in the following chapters. First, we will make use of the finite cuboidal cavity (2.53) in Chap. 3 to study the interplay between disorder and strong light-matter coupling. It has the benefits of allowing an exact diagonalization of the full polaritonic system. Second, we employ the waveguide cavity (2.46) in Chap. 4 to study the fate of topological phases in the strong light-matter coupling regime. For such topological physics, the boundary conditions are of particular importance, justifying our use of the waveguide cavity which prevents boundary effects.

CHAPTER 3

DISORDER AND POLARITONS

In this chapter, we study the interplay between disorder and light-matter coupling by considering a disordered one-dimensional chain of dipolar emitters strongly coupled to a multimode optical cavity.

In the absence of light-matter coupling, a disordered one-dimensional chain of dipolar emitters is subject solely to the Anderson localization of the eigenstates. After reviewing this effect, in this chapter we embed the disordered chain in a multimode optical cavity so that it can enter in the strong light-matter coupling regime. To study the interplay between disorder and light-matter coupling, we analyze both the eigenspectrum and the driven dissipative transport properties of our polaritonic system. In the strong-coupling regime, we find that increasing disorder leads almost uncoupled dark states to acquire a photonic part, allowing them to inherit polaritonic long-range transport characteristics. Crucially, we show that this disorder-enhanced transport mechanism is increasingly noticeable when the considered dipoles are lossier, but that no enhancement is observed over very long distances.

The results presented in this chapter are mostly part of the published article T.F. Allard, G. Weick, *Disorder-enhanced transport in a chain of lossy dipoles strongly coupled to cavity photons*, Physical Review B **106**, 245424 (2022) [17].

In the previous chapter, we presented how we model the coupling of generic dipolar emitters to confined electromagnetic modes in an optical cavity, using a microscopically derived minimal coupling Hamiltonian. The aim of the present chapter is to use such formalism to study the interplay between disorder and strong light-matter coupling.

As introduced in Chap. 1, strongly-coupled systems give rise to polaritonic hybrid light-matter eigenstates, which, from their partly photonic nature, present efficient long-range transport characteristics [83–115], an effect that has been dubbed cavity-enhanced transport. Interestingly, a significant portion of the experiments on polariton propagation has been conducted using excitons in molecular amorphous semiconductors, materials which are highly disordered by nature. The behavior of such disordered polaritons has been the subject of early studies, with pioneering theoretical works [155–157] revealing unexpected phenomena, such as a cavity-protection effect, wherein polaritonic states exhibit greater robustness against disorder compared to other excitations.

Such a behavior goes beyond the well-known theory of Anderson localization which states (see Chap. 1) that in 1d and 2d systems, disorder makes all the eigenstates exponentially localized, threfore suppressing transport [22, 25]. However, it is important to note that the 1d and 2d Anderson localization is verified only for systems with short-range interactions, and the situation becomes in fact highly nontrivial when dealing with long-range interactions, as 1d systems can then exhibit extended states [27, 158–161]. Due to the fact that polaritons are partly mediated by cavity photons, they effectively experience a longer range coupling than usual matter excitations, and as a result, polaritonic excitations can be less affected by the suppression of transport arising from Anderson localization.

In order to investigate the field of disordered polaritons, we will consider in this chapter a finite disordered 1d chain of $\mathcal{N}$ dipolar emitters placed inside the finite cuboidal mirror cavity we introduced in Sec. 2.4. The system we study is sketched in Fig. 3.1, and, as depicted in the figure, we take into account disorder both in the individual resonance frequencies ω_i of each dipole, modeling possible inhomogeneities, and in the interdipole spacings d_i, accounting for positional uncertainties.

As we discussed in Chap. 2, our versatile model of dipolar emitters allows the description of a wide range of physical systems. In addition to, among others, plasmonic, dielectric or SiC chains of nanoparticles, it describes in particular molecular and semiconductor excitons [130] for which most of the recent experimental approaches on disordered polaritonic systems were performed [98–110]. We show in Figs. 3.2(a)-(b) two recent implementations of molecular polaritonic systems of this kind. In panel (a), reproduced from Ref. [107], distributed Bragg reflector (DBR) dielectric mirrors are used to create Fabry-Pérot microcavities into which molecular aggregates, typically dyes and in this case BODIPY molecules, are placed. Such dye molecules are naturally disordered and host Frenkel excitons. The latter excitations act as dipolar

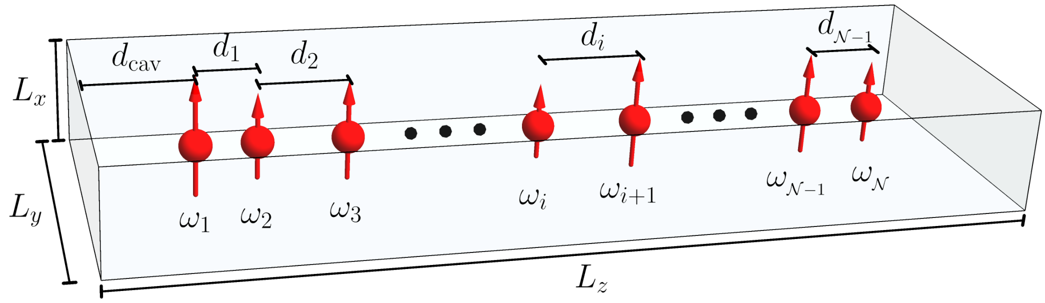

Figure 3.1: Disordered chain of dipoles in a cavity. Sketch of a disordered chain of $\mathcal{N}$ dipolar emitters polarized along the x axis, arranged along the z direction, and embedded in the middle of the cuboidal cavity described in Sec. 2.4. Each oscillating dipole on site $i \in [1, \mathcal{N}]$ with random frequency ω_i, is located at a random distance d_i from its neighbor to the right. The average individual resonance frequency is ω_0, while the average interdipole spacing is d. Unless stated otherwise, the distance between the first and last dipoles of the chain and the cavity wall in the z direction is fixed to $d_{\rm cav} = d$ is this chapter.

emitters, and can then strongly couple to the cavity. In panel (b), reproduced from Ref. [109], a dielectric DBR structure is coated with a dense film of molecular organic semiconductor dyes, in that case TDBC J-aggregates. The DBR hosts electromagnetic Bloch surface waves, which strongly couple to the Frenkel excitons of the molecular layer to give rise to extended Bloch surface wave polaritons (BSWP).

While from now on, much of the theoretical analysis of these experiments have been based on the single-mode Tavis-Cummings model [83–91, 93], the majority of materials used, such as Fabry-Pérot or plasmonic cavities, are intrinsically multimodal, so that it is of fundamental importance to go beyond single-mode models and take into account the cavity dispersion as well as a dispersive coupling, as pointed out in recent studies [92, 94, 95, 163–165].

Another interesting physical system our model could describe is a cold atomic cloud trapped in an optical resonator, operating in the regime where only a single excitation is present in the system, i.e., in the single excitation manifold [162, 166]. Fig. 3.2(c), reproduced from Ref. [162], presents a recent experimental realization of such a system, where, interestingly, controllable frequency disorder has been achieved. ^{6}Li atoms are confined at the antinodes of the cavity field, and a technique of crossed lasers illuminating the atoms allows an energy shift ϵ of their excited states, with a quasi-random intensity distribution ρ_a of tunable width W. We note that in such a particularly controllable cold atom experiment, a fine tuning of the system parameters allows its features to be described by single cavity mode models.

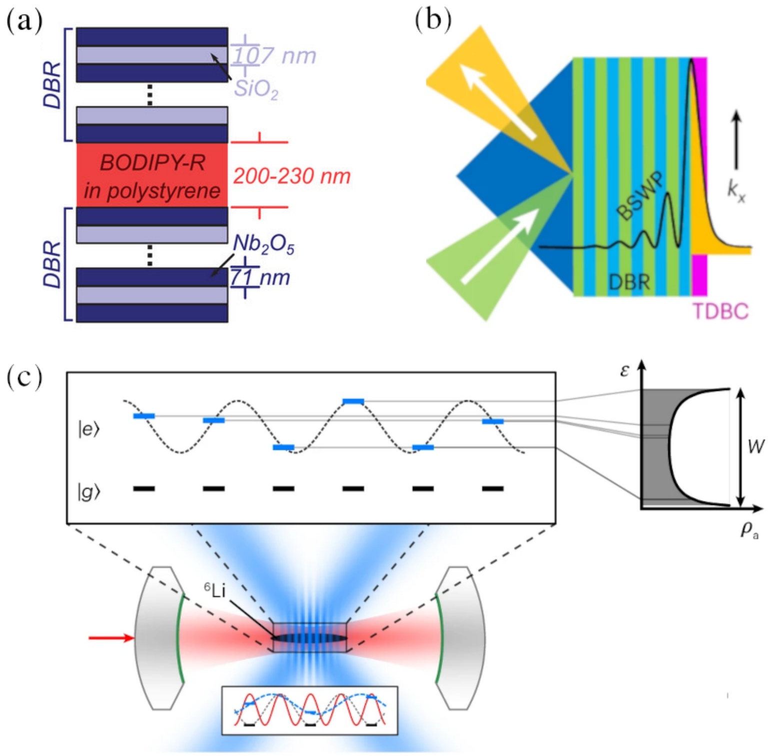

Figure 3.2: Experimental possibilities. Possible experimental realizations of our model of disordered polaritons. (a) Dye molecular aggregate, a naturally disordered organic semiconductor supporting Frenkel excitons, embedded in a dielectric mirror-based Fabry-Pérot cavity made of two distributed Bragg reflector (DBR) structures. (b) Dielectric DBR structure, hosting Bloch surface waves, strongly coupled to a coated dye molecular layer, giving rise to Bloch surface wave polaritons (BSWP). (c) Cloud of cold ^{6}Li atoms trapped in an optical resonator, subject to a random energy shift of their excited state induced by crossed light-shifting beams. Panels (a), (b), and (c) have been reproduced, respectively, from Refs. [107], [109], and [162].

Alongside the above-mentioned cavity-protection and cavity-enhanced transport effects, recent theoretical works [88, 90, 91] have shown that the photonic cavity can also lead to an improvement of the transport characteristics when increasing the disorder strength, instead of an expected suppression. This counterintuitive phenomenon was theoretically unveiled by considering a disordered single-mode Tavis-Cummings model, specifically a chain of emitters coupled to a single cavity mode through a spatially homogeneous coupling constant. Interestingly, in the past year, such enhanced transport induced by disorder has been observed in experiments, either using cold atoms as shown in Fig. 3.2(c) [162, 166], or in molecular systems in the context of vibrational strong coupling [167]. Therefore, the intricate interplay between disorder and strong light-matter coupling at the heart of disordered polaritons appears to be highly nontrivial, but its understanding is crucial, both to better understand the experiments we discussed above and for the fundamental questions it raises.

In this chapter, we employ our model sketched in Fig. 3.1 to investigate disordered polaritons beyond the commonly studied single-mode disordered Tavis-Cummings model, by incorporating an all-to-all quasistatic dipole-dipole coupling as well as the coupling to a multimode cavity. Through this framework, we demonstrate that disorder-enhanced transport can be readily understood as a consequence of an hybridization between dark and polaritonic states, which arises due to the increase in bandwidth caused by frequency disorder, the latter allowing new coupling between photons and dark states. This mechanism of disorder-induced hybridization enables dark states to inherit polaritonic properties, and thus to take advantage of cavity-enhanced transport.

Importantly, our study reveals distinct transport regimes for chains of large enough sizes, so that both cavity- and disorder-enhanced transport are only observed at intermediate distances. Specifically, the short-range propagation of dark states, resulting from nearest-neighbor quasistatic dipole-dipole coupling, cannot be enhanced through polaritonic hybridization. Only the long-range propagation benefits from cavity- and disorder-enhanced transport. Notably, no enhancement is observed over very long distances. Furthermore, we show that accounting for dipolar losses is crucial, as it leads the aforementioned effects of cavity- and disorder-enhanced transport to be increasingly noticeable.

The present chapter is organized as follows: Section 3.1 summarizes known results on a disordered chain of dipolar emitters, which, when considering nearest neighbor couplings only, is reduced to the 1d Anderson model of disordered systems. After reviewing Anderson localization in this celebrated model, we explore the effect of the all-to-all quasistatic dipolar coupling. Section 3.2 is then dedicated to the presentation of our Hamiltonian model for the coupling of the latter chain of emitters to a cuboidal multimode optical cavity. In Sec. 3.3, we study the particular case of the ordered chain in the emitter thermodynamic limit, in order to gain physical insights into the model.

The disordered case is studied in Sec. 3.4, where we discuss the localization properties of the system from an eigenspectrum analysis, and unveil the mixing between dipolar and photonic degrees of freedom induced by the interplay between strong light-matter coupling and disorder. Such a mixing leads to what is dubbed semilocalized eigenstates, and Sec. 3.5 is dedicated to the study of the precise nature of these states in our multimode model. Then, in Sec. 3.6, we study the transport along the chain in a driven-dissipative scenario, considering both lossy dipoles and lossy cavity mirrors. We first study the effects of strong coupling in an ordered chain, and then the interplay between disorder and cavity-enhanced transport in a disordered chain. Finally, we summarize our results and draw conclusions in Sec. 3.7, and we discuss some details of our model, such as the rotating wave approximation (RWA) and the effect of cavity losses, in the Appendices 3.A and 3.B.

3.1 Disordered chain of emitters

To model a bare disordered chain of dipolar emitters without any cavity, as sketched in Fig. 2.1, we rely on the dipolar Hamiltonian in the RWA (2.44) which we derived in the previous chapter.

To implement disorder, we consider the individual resonance frequencies ω_i in Eq. (2.44) as uncorrelated random variables distributed uniformly within an interval $[\omega_0 - W/2, \omega_0 + W/2]$, hence with an average resonance frequency ω_0, and a variance $W^2/12$. Moreover, we also consider the interdipole spacings d_i (see Fig. 3.1) as uncorrelated random variables distributed uniformly within an interval $[d(1-\Delta), d(1+\Delta)]$, the average spacing being d. This leads to randomness in the dipolar coupling strength Ω_{ij} between two dipoles on sites i and j, given in Eq. (2.23). Indeed, it depends on the separation distance between the dipoles, which reads

$$|\mathbf{r}_i - \mathbf{r}_j| = r_{ij} = \sum_{l=i}^{j-1} d_l. \tag{3.1}$$

The average dipolar coupling strength between two neighboring dipoles is then

$$\Omega = \overline{\Omega_{i,i+1}} = \frac{\omega_0}{2}\left(\frac{a}{d}\right)^3, \tag{3.2}$$

where the bar denotes averaging over the disorder realizations.

We note that our microscopically derived model imposes restrictions on these two disorder parameters. Indeed, on the one hand, the frequency disorder strength W/ω_0 is limited to values smaller than 2, to prevent the resonance frequencies ω_i to become negative. On the other hand, the dimensionless structural or positional disorder strength Δ is restricted to values smaller than $1 - 3a/d$, in order for the spacings d_i between dipoles to be greater than or equal to $3a$, allowing us to safely neglect multipolar effects and describe purely dipolar excitations [150].

In the remainder of this chapter, we choose an average spacing $d = 4a$, so that the dipoles are coupled in the near-field regime. We note that this regime is the most studied both experimentally [168–174] and theoretically [116, 117, 138, 175] for chains of plasmonic nanoparticles. Such a small interdipole spacing leads to $\Omega/\omega_0 = 1/128$.

3.1.1 The 1d Anderson model

In order to fully understand the effect of disorder on a chain of emitters, we begin our study by revisiting the 1d Anderson model [25]. This paradigmatic model can be derived from the dipolar Hamiltonian in the RWA (2.44)

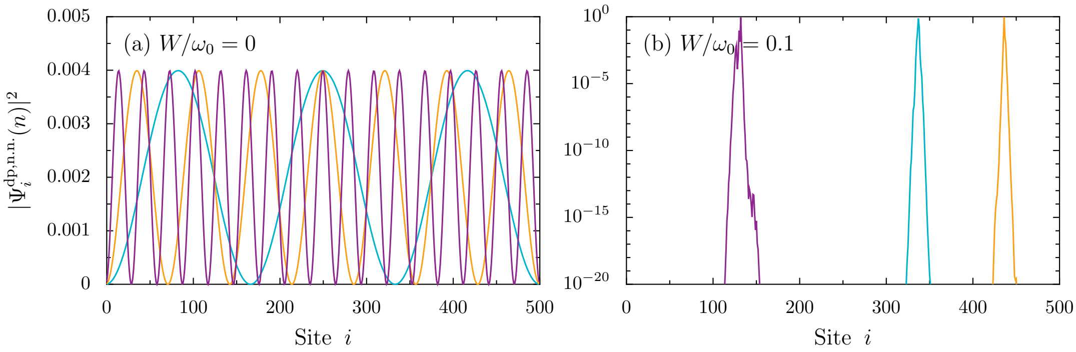

Figure 3.3: Anderson localization. Probability density $|\Psi_i^{\mathrm{dp,n.n}}(n)|^2$ associated with three randomly chosen eigenstates of the Hamiltonian (3.3), which describes a disordered chain of emitters with nearest neighbor coupling only, and which is equivalent to the 1d Anderson model of disordered systems. (a) In the absence of disorder, the eigenstates are extended plane waves. (b) For a nonzero disorder strength (here $W/\omega_0 = 0.1$), the eigenstates become exponentially localized. In the figure, the number of emitters $\mathcal{N} = 500$.

by considering nearest neighbor coupling only, and by setting the structural disorder Δ to zero. In that case, one obtains the Hamiltonian

$$H_{\mathrm{dp,n.n.}}^{\mathrm{RWA}} = \sum_{i=1}^{\mathcal{N}} \hbar\omega_i {b_i}^\dagger b_i \; + \sum_{i=1}^{\mathcal{N}-1} \hbar\Omega \left({b_i}^\dagger b_{i+1} + b_i {b_{i+1}}^\dagger \right), \tag{3.3}$$

which we numerically diagonalize to obtain, for each eigenstate $n \in [1, \mathcal{N}]$, the eigenvectors $\mathbf{\Psi}^{\mathrm{dp,n.n.}}(n) = (\Psi_1^{\mathrm{dp,n.n.}}(n), \ldots, \Psi_{\mathcal{N}}^{\mathrm{dp,n.n.}}(n))$, which are normalized as $\sum_{i=1}^{\mathcal{N}} |\Psi_i^{\mathrm{dp,n.n.}}(n)|^2 = 1$, as well as the eigenfrequencies $\omega_n^{\mathrm{dp,n.n.}}$.

We present in Fig. 3.3 the result of such a diagonalization by plotting the probability density $|\Psi_i^{\mathrm{dp,n.n}}(n)|^2$ of randomly chosen eigenstates, along the sites i of a chain comprising $\mathcal{N} = 500$ emitters. In Fig. 3.3(a), an ordered chain is considered by fixing the disorder strength $W/\omega_0 = 0$, so that all the bare individual frequencies $\omega_i = \omega_0$. In that case, the Hamiltonian (3.3) reduces to a tridiagonal Toeplitz matrix, allowing for an analytical diagonalization. The eigenvectors are just plane waves and read

$$\Psi_i^{\mathrm{dp,n.n}}(n) = \sqrt{\frac{2}{\mathcal{N}+1}} \sin\left(\frac{in\pi}{\mathcal{N}+1}\right), \tag{3.4}$$

where we used open boundary conditions $\Psi_0^{\mathrm{dp,n.n}}(n) = \Psi_{\mathcal{N}+1}^{\mathrm{dp,n.n}}(n) = 0$, as is implicit in the Hamiltonian (3.3).

Adding disorder with a strength $W/\omega_0 = 0.1$ in Fig. 3.3(b), in which one should note the logarithmic scale of the vertical axis, the plane waves become exponentially localized. This phenomenon is precisely the Anderson localization we briefly introduced in Chap. 1.

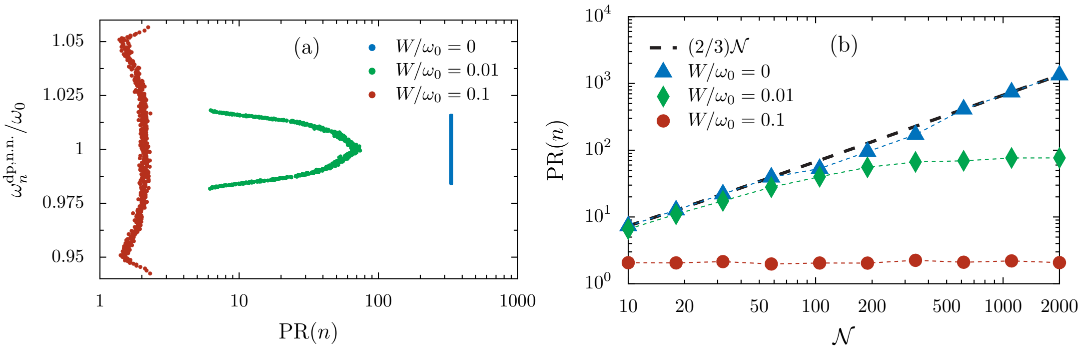

Figure 3.4: Participation ratio in the Anderson model. (a) Eigenfrequencies $\omega_n^{\text{dp,n.n.}}$, in units of the average bare frequency ω_0 and in ascending order, as a function of the participation ratio PR(n) [Eq. (3.5)], for increasing values of the disorder strength $W/\omega_0 = 0$, $W/\omega_0 = 0.01$ and $W/\omega_0 = 0.1$, and for a chain comprising $\mathcal{N} = 500$ emitters. (b) Scaling of the participation ratio with the system size $\mathcal{N}$, for the same increasing values of the disorder strength. In the figure, the data have been averaged over 100 disorder realizations.

To better characterize the localization of an eigenstate n, we use the participation ratio (PR) defined as [176, 177]

$$\text{PR}(n) = \frac{\left(\sum_{i=1}^{\mathcal{N}} |\Psi_i^{\text{dp,n.n.}}(n)|^2\right)^2}{\sum_{i=1}^{\mathcal{N}} |\Psi_i^{\text{dp,n.n.}}(n)|^4} = \frac{1}{\sum_{i=1}^{\mathcal{N}} |\Psi_i^{\text{dp,n.n.}}(n)|^4}. \tag{3.5}$$

The quantity (3.5) gives information about the typical number of sites i occupied by an eigenstate n. In 1d systems it is then related to the localization length. Extended states are characterized by a PR scaling with the total number of sites $\mathcal{N}$, while the PR of localized states is size-independent.

We show in Fig. 3.4 computations of the latter PR. To minimize fluctuations, all the data have been averaged over 100 disorder realizations.

In Fig. 3.4(a) the eigenfrequencies $\omega_n^{\text{dp,n.n.}}$ of the Anderson Hamiltonian (3.3) are plotted as a function of the PR, for increasing values of the disorder strength W. In the absence of disorder, the PR can be computed in the thermodynamic limit using the expression of the eigenvectors (3.4). One finds $\text{PR}(n) = 2(\mathcal{N}+1)/3$, just as the blue dots at a $\text{PR}(n) = 334$ for all n. Increasing the disorder strength to $W/\omega_0 = 0.01$ (green dots) and to $W/\omega_0 = 0.1$ (red dots) teaches us two effects of the disorder on the system. First, as the bare individual frequencies ω_i span a range that grows linearly with W, the bandwidth of the eigenspectrum similarly increases. Second, as the disorder strength increases, the eigenstates at the edges of the eigenspectrum become localized first. In contrast, eigenstates located at the center, where $\omega_n^{\text{dp,n.n.}} \sim \omega_0$, maintain a larger value of PR. Increasing further the disorder strength W while keeping a system of the same size would result in all eigenstates having a participation ratio PR ~ 1.

To accurately distinguish between extended and localized states, it is essential to examine the scaling of the PR with the system size $\mathcal{N}$. This is what we do in Fig. 3.4(b), where we focus on an eigenstate in the middle of the spectrum, while increasing values of the disorder strength W. In the case of zero disorder (blue triangles), we recover the result $\mathrm{PR}(n) \sim 2\mathcal{N}/3$. The eigenstates being plane waves, their length scale grows with the system size, confirming their extended character. For a disorder strength $W/\omega_0 = 0.01$ (green diamonds), two regimes of scaling are observed: The PR scales with the system size for small systems, and then converges to a constant value when $\mathcal{N}$ is large enough. This is explained by the fact that although disorder localizes the eigenstate, as demonstrated by the convergence of the PR to a given value, the localization length is larger than the size of the system for small values of $\mathcal{N}$, here until $\mathcal{N} \sim 100$. For a larger disorder strength $W/\omega_0 = 0.1$ (red dots), however, the PR remains constant. This indicates that the localization length of the eigenstate is smaller than the system size for all the values of $\mathcal{N}$ considered here.

In the case of the 1d system with nearest neighbor coupling only in consideration here, we note that it has been demonstrated that the localization length scales with the square of the disorder strength W [177]. Moreover, in the thermodynamic limit $\mathcal{N} \to \infty$, any infinitesimal value of W leads to the localization of all the eigenstates, i.e., the PR always converges to a constant value as the system size increases [30, 178].

3.1.2 Effect of the all-to-all quasistatic dipolar coupling

As we want to investigate the fate of Anderson localization in a chain of dipolar emitters strongly-coupled to a cavity, we need to go beyond the 1d Anderson model of Eq. (3.3). The first step to this aim is to incorporate the quasistatic all-to-all dipolar coupling, arising from the nonretarded part of the Coulomb interaction (2.10), which decays with the cube of the intersite distance. This is achieved by considering the dipolar Hamiltonian (2.44). To focus on the predominant frequency disorder strength W, we continue here to fix the positional disorder strength Δ to zero.

Through a similar numerical diagonalization as done in the previous subsection, one can directly obtain from the Hamiltonian (2.44) its eigenfrequencies ω_n^{dp} and eigenvectors $\mathbf{\Psi}^{\mathrm{dp}}(n)$.

We show in Fig. 3.5(a) the probability density $|\Psi_i^{\mathrm{dp}}(n)|^2$ of three randomly chosen eigenstates along the sites i of a chain of $\mathcal{N} = 500$ emitters, when considering a disorder strength $W/\omega_0 = 0.1$. We observe, similarly as for the Anderson model in Fig. 3.3(b), an exponential localization of the eigenstates (note the logarithmic scale of the vertical axis). However, and importantly, instead of a full exponential decay, the eigenstates present in addition a clear algebraic tail, characterized by a power-law exponent of 3. Such an

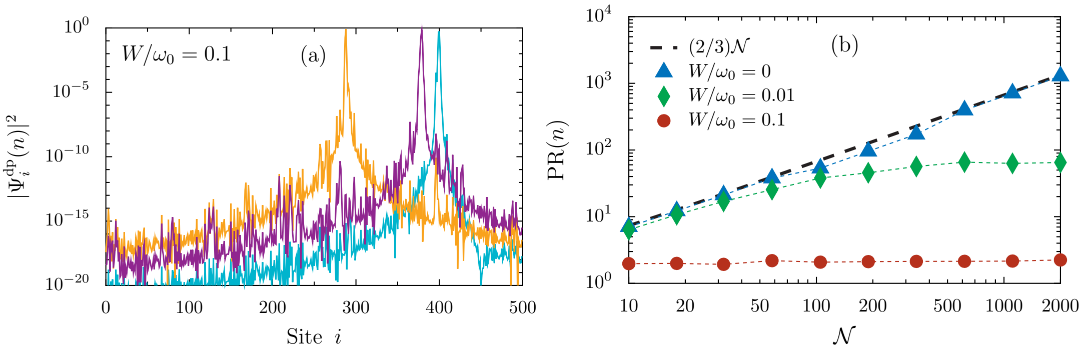

Figure 3.5: Anderson model with all-to-all quasistatic dipolar coupling. (a) Probability density $|\Psi_i^{\rm dp}(n)|^2$ associated with three randomly chosen eigenstates of the dipolar Hamiltonian (2.44), which describes a disordered chain of emitters with all-to-all quasistatic dipolar coupling. The disorder strength is set to $W/\omega_0 = 0.1$. (b) Scaling of the participation ratio with the system size $\mathcal{N}$, for increasing values of the disorder strength W, and after averaging the data over 100 disorder realizations. In the figure, we recall that no off-diagonal disorder is considered, i.e., $\Delta = 0$.

additional tail of the eigenstates arises directly from the all-to-all quasistatic dipolar coupling, as it decays with the same rate.

To characterize the localized or extended nature of the eigenstates, we analyse in Fig. 3.5(b) the scaling of the PR with the system size $\mathcal{N}$, focusing again on an eigenstate in the middle of the spectrum. Interestingly, the figure is almost identical to the one obtained for the Anderson model, Fig. 3.4(b), the PR converging through a constant value once some disorder is present in the system. Therefore, although presenting a power-law tail, the eigenstates of the dipolar Hamiltonian with all-to-all quasistatic coupling are still localized. This is explained by the fact that the dipolar all-to-all coupling is formally short-range, since it decays with the inter-site distance r as a power-law $1/r^p$, with $p = 3 > D$, where the dimension $D = 1$. Indeed, a formally long-range interaction, which can modify the localized or extended character of disordered eigenstates in 1d [27, 158–161], is defined as decaying with a power-law exponent $p < D$.

3.2 Coupling to a multimode optical cavity

Having examined Anderson localization in a disordered chain of bare dipolar emitters, we now explore the influence of the light-matter coupling by placing this chain inside a finite cuboidal cavity with hard-wall boundary conditions, as described in Sec. 2.4. Thus, the coupled cavity-emitters system is modeled by the polaritonic Hamiltonian (2.53), which expands as

$$\begin{aligned} H^{\square}_{\mathrm{pol}} = \sum_{i=1}^{\mathcal{N}} \hbar\omega_i {b_i}^{\dagger} b_i \; + \sum_{\substack{i,j=1 \\ (i\neq j)}}^{\mathcal{N}} \frac{\hbar\Omega_{ij}}{2} \left({b_i}^{\dagger} b_j \; + b_i \; {b_j}^{\dagger} \right) \\ + \sum_{n_z=1}^{N_z} \omega^{\mathrm{ph}}_{n_z} c^{\dagger}_{n_z} c_{n_z} + \mathrm{i}\hbar \sum_{i=1}^{\mathcal{N}} \sum_{n_z=1}^{N_z} \xi^{\square}_{i n_z} \left(b^{\dagger}_i c_{n_z} - b_i \, c^{\dagger}_{n_z} \right), \end{aligned} \tag{3.6}$$

with the dipole coupling strength Ω_{ij}, the photonic dispersion $\omega^{\mathrm{ph}}_{n_z}$, and the real-space light-matter coupling function $\xi^{\square}_{i n_z}$, given in Eqs. (2.23), (2.52), and (2.48), respectively.

The z coordinate of the ith dipole, entering in the latter light-matter coupling function, reads here $z_i = d_{\mathrm{cav}} + \sum_{l=1}^{i-1} d_l$. Since we are at first not interested in any edge effects, we fix for simplicity, unless stated otherwise, the distance to the cavity walls to $d_{\mathrm{cav}} = d$.

We note that in our microscopically derived model, the frequency disorder W is present both in the on- and off-diagonal elements of the Hamiltonian, as it enters in the dipole coupling strength (2.23) as well as in the light-matter coupling function (2.52), through the emitter resonance frequencies ω_i. This differs from toy models of disordered systems, in which frequency and coupling constants are independent parameters [25]. In such a particular case, frequency disorder can be called “on-diagonal disorder”.

In the following, we will first study the properties of the spectrum and eigenstates of the Hamiltonian (3.6), and then study the propagation along the chain in a driven-dissipative transport scenario, considering losses both in the dipoles and in the cavity mirrors.

3.3 Ordered chain in the thermodynamic limit

To gain insight on the model and for clarity, we begin by summarizing and further discussing results recently obtained in Ref. [179] for the simple case of an ordered chain in the thermodynamic limit, which can be solved analytically. Within the framework developed in Chap. 2 and Sec. 3.2, this implies to consider the disorder parameters $W = 0$ and $\Delta = 0$, such that $\omega_i = \omega_0$ and $d_i = d$.

By then going to the emitter thermodynamic limit $\mathcal{N} \to \infty$, both the longitudinal size of the cavity $L_z = (\mathcal{N} + 1)d \to \infty$ and of the dipole chain $L_{\mathrm{chain}} = (\mathcal{N} - 1)d \to \infty$, so that the system is translationally invariant, and one can use periodic boundary conditions for both the dipole chain and the cavity in the z direction. In that case, $L_z \sim L_{\mathrm{chain}} \sim \mathcal{N}d$, and the longitudinal photon momentum $k_z = 2\pi n_z / L_z$, with $n_z \in \mathbb{Z}$, is conserved with the quasimomentum associated to the dipolar excitation, $q = 2\pi p / \mathcal{N}d$, with

$p \in [-\mathcal{N}/2, +\mathcal{N}/2]$. Therefore, $k_z = q$ belongs to the first Brillouin zone $[-\pi/d, +\pi/d]$ characterized by the lattice constant d of the emitter array.

In this periodic situation, we label by $m \in [1, \mathcal{N}]$ the unit cell in which a single emitter i is enclosed. Since we consider in this chapter a unipartite lattice, the labels i and m are equivalent. This leads the z coordinate of the ith dipole inside the mth unit cell to simplify as $z_i = z_m = md$.

In this limit, translation invariance leads the boundaries of the cavity to be irrelevant, so that both the waveguide and box cavities are equivalent. Hence, in this section, we place ourselves in the case of an infinite waveguide cavity with periodic boundary conditions, as detailed in Sec. 2.3, and consider the polaritonic Hamiltonian (2.46). Within the emitter thermodynamic limit, it writes

$$\begin{aligned} H_{\mathrm{pol}}^{\infty} = & \sum_{m=1}^{\infty} \hbar\omega_0 b_m{}^{\dagger} b_m + \sum_{\substack{m,m'=1 \\ (m \neq m')}}^{\infty} \frac{\hbar\Omega}{2} \left(b_m{}^{\dagger} b_{m'} + b_m \, b_{m'}{}^{\dagger} \right) \\ & + \sum_{q=-\pi/d}^{\pi/d} \hbar\omega_q^{\mathrm{ph}} c_q^{\dagger} c_q \\ & + \frac{\mathrm{i}\hbar}{\sqrt{\mathcal{N}}} \sum_{m=1}^{\infty} \sum_{q=-\pi/d}^{\pi/d} \xi_q \left(b_m{}^{\dagger} c_q \mathrm{e}^{\mathrm{i}qmd} - b_m \, c_q^{\dagger} \mathrm{e}^{-\mathrm{i}qmd} \right). \end{aligned} \tag{3.7}$$

To diagonalize the Hamiltonian (3.7), we move into the wavevector space through the Fourier transform

$$b_m = \frac{1}{\sqrt{\mathcal{N}}} \sum_q \mathrm{e}^{\mathrm{i}mqd} b_q \qquad (m = 1, \ldots, \mathcal{N}). \tag{3.8}$$

Using then the relation

$$\sum_{m=1}^{\mathcal{N}} \mathrm{e}^{\mathrm{i}m2\pi(p-p')/\mathcal{N}} = \mathcal{N} \delta_{p,p'}, \tag{3.9}$$

the polaritonic Hamiltonian (3.7) becomes

$$H_{\mathrm{pol}}^{\infty} = \sum_q \boldsymbol{\phi}_q^{\dagger} \mathcal{H}_q \boldsymbol{\phi}_q, \qquad \mathcal{H}_q = \hbar \begin{pmatrix} \omega_q^{\mathrm{dp}} & \mathrm{i}\xi_q \\ -\mathrm{i}\xi_q & \omega_q^{\mathrm{ph}} \end{pmatrix}, \tag{3.10}$$

where $\mathcal{H}_q$ is the Bloch Hamiltonian, while $\boldsymbol{\phi}_q^{\dagger} = (b_q^{\dagger}, c_q^{\dagger})$ are the Bloch eigenvectors.

In the above expression, the photonic dispersion and the light-matter coupling strength are given, respectively, in Eqs. (2.34) and (2.38), whereas ω_q^{dp}

is the quasistatic dispersion of the collective dipolar excitation, i.e., the eigenspectrum of the dipolar Hamiltonian in the RWA (2.44) in the thermodynamic limit. It reads

$$\omega_q^{\mathrm{dp}} = \omega_0 + \Omega f_q, \tag{3.11}$$

with the lattice sum

$$f_q = 2 \sum_{m=1}^{\infty} \frac{\cos(mqd)}{m^3}, \tag{3.12}$$

that can be expressed in closed form in terms of the polylogarithm function $\mathrm{Li}_s(z) = \sum_{m=1}^{\infty} z^m / m^s$ as $f_q = \mathrm{Li}_3(\mathrm{e}^{\mathrm{i}qd}) + \mathrm{Li}_3(\mathrm{e}^{-\mathrm{i}qd})$.

Using a bosonic Bogoliubov transformation, one can readily diagonalize the Hamiltonian (3.10) as

$$H_{\mathrm{pol}}^{\infty} = \sum_{q,\tau} \omega_{q\tau}^{\mathrm{pol}} \beta_{q\tau}^{\dagger} \beta_{q\tau}, \tag{3.13}$$

where the two polaritonic bands are given by

$$\omega_{q\tau}^{\mathrm{pol}} = \frac{1}{2}\left(\omega_q^{\mathrm{ph}} + \omega_q^{\mathrm{dp}}\right) + \tau\sqrt{\xi_q^2 + \Delta_q^2}, \tag{3.14}$$

with $\Delta_q = (\omega_q^{\mathrm{ph}} - \omega_q^{\mathrm{dp}})/2$ being the light-matter detuning between the bare photonic and dipolar dispersions. We hereafter refer to the high (low) frequency band, labeled by the index $\tau = + (-)$, as the upper (lower) polariton UP (LP)

Finally, the Bogoliubov operators diagonalizing the Hamiltonian (3.10) are a linear combination of the dipolar and photonic ladder operators, $\beta_{q\tau} = u_{q\tau} b_q + v_{q\tau} c_q$. The modulus squared of the two coefficients $u_{q\tau}$ and $v_{q\tau}$, which are normalized as $|u_{q\tau}|^2 + |v_{q\tau}|^2 = 1$, thus represent, respectively, the dipolar part $\mathrm{D}_{q\tau}$ and the photonic part $\mathrm{Ph}_{q\tau}$ of the polaritonic eigenmodes. These latter quantities read

$$\mathrm{D}_{q\tau} = |u_{q\tau}|^2 = \frac{1}{2}\left(1 - \tau\frac{\Delta_q}{\sqrt{\xi_q^2 + \Delta_q^2}}\right) \tag{3.15a}$$

and

$$\mathrm{Ph}_{q\tau} = |v_{q\tau}|^2 = \frac{1}{2}\left(1 + \tau\frac{\Delta_q}{\sqrt{\xi_q^2 + \Delta_q^2}}\right). \tag{3.15b}$$

The result of the diagonalization procedure in the emitter thermodynamic limit with periodic boundary conditions is shown is Fig. 3.6, where we plot the polaritonic dispersion $\omega_{q\tau}^{\mathrm{pol}}$ [see Eq. (3.14)] in the first Brillouin zone (BZ), for cavity heights $L_x = 7a$ [Fig. 3.6(a)] and $L_x = 12a$ [Fig. 3.6(b)]. The colormap represents the photonic part $\mathrm{Ph}_{q\tau}$ of each eigenmodes, given in

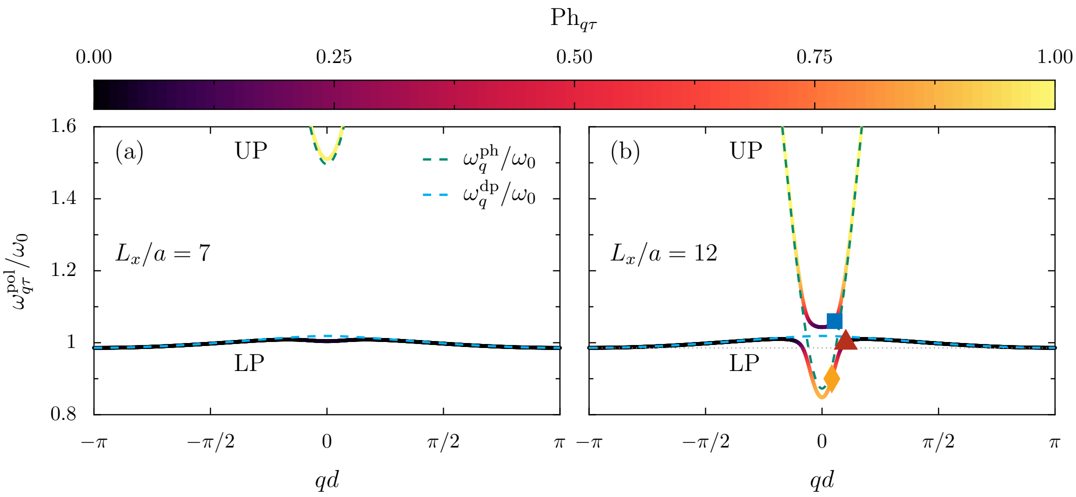

Figure 3.6: Polaritonic bandstructure. Dispersion relation $\omega_{q\tau}^{\mathrm{pol}}$ [see Eq. (3.14)] of an infinite, ordered dipole chain coupled to a cuboidal cavity with heights $L_x/a = 7$ (left panel) and $L_x/a = 12$ (right panel), in units of the bare dipole frequency ω_0 and as a function of the reduced wavenumber qd in the first Brillouin zone. The colormap represents the photonic weight $\mathrm{Ph}_{q\tau}$ of the mode [see Eq. (3.15b)], and the dotted grey line in panel (b) indicates the value of $\omega_{\pm\pi/d,-}^{\mathrm{pol}}$. The blue and green dashed lines represent the bare dipolar ω_q^{dp} [see Eq. (3.11)] and the bare photonic ω_q^{ph} [see Eq. (2.34)] dispersions, respectively. The orange, red, and blue symbols point out eigenstates that will be studied in detail in the sequel. We recall that, as in the remaining of this chapter, the interdipole spacing is $d = 4a$.

Eq. (3.15b). We also plot by blue and green dashed lines the dipolar ω_q^{dp} and photonic ω_q^{ph} bare dispersions, given respectively in Eqs. (3.11) and (2.34).

We first notice that, as discussed in Chap. 2, increasing the cavity height L_x (and hence L_y, since the aspect ratio is fixed to $L_y = 3L_x$) leads the bare dispersions ω_q^{dp} and ω_q^{ph} to enter in resonance. It induces an increasingly pronounced avoided crossing, typical of the strong-coupling regime.

When L_x becomes large enough, namely for $L_x \geqslant \omega_0\pi/3\omega_{q=0}^{\mathrm{dp}}k_0$ which corresponds to $L_x \simeq 10.3a$ with the parameters used in Fig. 3.6, the light-matter detuning $\Delta_q = (\omega_q^{\mathrm{ph}} - \omega_q^{\mathrm{dp}})/2$ can be smaller than 0, meaning that there is a crossing between the bare dipolar and photonic dispersions, i.e., a given wavenumber q_{res} where the two bare excitations are at resonance. From this point on, we can identify $\xi_{q_{\mathrm{res}}}$ [see Eq. (2.38)] with half of the Rabi splitting frequency. In the case of $L_x/a = 12$ shown in Fig. 3.6(b), the Rabi splitting frequency $\Omega_{\mathrm{RS}} \simeq 0.12\omega_0$.

From the colormap of Fig. 3.6, one observes that the hybridization between light and matter degrees of freedom is enhanced by increasing the cavity height L_x, in agreement with the entrance in the strong-coupling regime. The most hybridized states are the ones near the center of the BZ, for which the detuning Δ_q is around and below 0 [see expression (3.15b)]. In the following, we will refer to these highly hybridized states as *polaritons*. On the other hand, states that are apart from the center of the BZ, for which the detuning Δ_q is positive, remain almost unhybridized. The states in the LP branch that remain almost fully dipolar, namely with a photonic weight $\mathrm{Ph}_{q\tau} \lesssim 0.1$, will be referred to as *dark states*[1] (visible in black in Fig. 3.6). Unlike polaritons, these dark states all have an eigenfrequency very close to that of the isolated dipole frequency ω_0.

Finally, we indicate by a grey dotted line in Fig. 3.6(b) the eigenfrequency $\omega^{\mathrm{pol}}_{\pm\pi/d,-}$ of the darkest, least coupled eigenmode of the LP branch, sitting at the edge of the BZ. This highlights the fact that due to the dipolar coupling between the emitters, which leads to the collective dispersion relation given in Eq. (3.11), there are both LP eigenstates with a higher and lower eigenfrequency than that of the least coupled one, i.e., the bare dipolar band is not flat.

In the next section, by studying the localization properties of the disordered chain we will show that this at first sight trivial information becomes important, since the latter eigenstates presenting an eigenfrequency lower than $\omega^{\mathrm{pol}}_{\pm\pi/d,-}$ will be found to be particularly robust against disorder, while the ones above the dotted line constitute what will later be called the dark state band.

3.4 Localization properties of the finite disordered chain

We now move to a numerical study of the eigenstates of the finite disordered chain, considering the finite real space Hamiltonian (3.6). With the longitudinal size of the cavity $L_z \sim \mathcal{N}d$, we consider the number of photonic modes $N_z = \mathcal{N}$, so that $\max(k_z) = \pi/d$. This allows one to rewrite the Hamiltonian (3.6) in a $2\mathcal{N} \times 2\mathcal{N}$ matrix form using the basis vector $\boldsymbol{\varphi}^\dagger = (b_1^\dagger, \ldots, b_{\mathcal{N}}^\dagger, c_1^\dagger, \ldots, c_{\mathcal{N}}^\dagger)$.[2] In this context, the dipolar and photonic parts of a given eigenstate $n \in [1, 2\mathcal{N}]$, that is, the real space counterparts of $\mathrm{D}_{q\tau}$ and $\mathrm{Ph}_{q\tau}$ given in Eqs. (3.15), read

$$\mathrm{D}(n) = \sum_{i=1}^{\mathcal{N}} |\Psi_i(n)|^2 \tag{3.16a}$$

and

$$\mathrm{Ph}(n) = 1 - \mathrm{D}(n), \tag{3.16b}$$

---

[1] In contrast to single cavity mode models such as the Tavis-Cummings one, in a realistic multimode model there is no unambiguous definition of dark and polaritonic states [92], all the eigenstates being hybridized.

[2] We note that we do not consider the situation of decoupling cavity modes [180–182], which requires a block-diagonal Hamiltonian approach.

with the $2\mathcal{N}$-component normalized eigenvector of the Hamiltonian (3.6) $\mathbf{\Psi}(n) = (\Psi_1(n), \ldots, \Psi_{2\mathcal{N}}(n))$, the first $\mathcal{N}$ entries corresponding to the dipolar subspace.

As in Sec. 3.1, we characterize the localization of an eigenstate n with the participation ratio. Here, however, we sum over the dipolar subspace only, so that the PR reads

$$\mathrm{PR}(n) = \frac{\left(\sum_{i=1}^{\mathcal{N}} |\Psi_i(n)|^2\right)^2}{\sum_{i=1}^{\mathcal{N}} |\Psi_i(n)|^4}. \tag{3.17}$$

We insist on the fact that in this chapter, when we refer to an extended or delocalized state, we mean *delocalized at the scale of the system size*, namely, that the localization length is larger that the system. Indeed, no genuine finite size scaling argument has been performed to confirm that such states are still extended at the thermodynamic limit, as states that can be found, e.g., in three-dimensional disordered systems featuring an Anderson transition. A discussion about this possible ambiguity, including the scaling of the PR with the system size for $\mathcal{N} \in [100, 5000]$, is proposed in the next Sec. 3.5.

Here and hereafter, we fix the interdipole spacing disorder Δ to 0 and focus only on the effects of the frequency disorder W. Due to the fact that the individual frequencies ω_i appear both on- and off-diagonal in the dipolar Hamiltonian [see Eq. (3.6)], the frequency disorder affects the spectrum more than the interdipole spacing one Δ, which is purely off-diagonal. All the results shown here are then qualitatively the same with a spacing disorder $\Delta \neq 0$. The particular case of considering only off-diagonal disorder would however not lead to important disorder-induced effects as we observe here.[3]

3.4.1 Disorder-induced mixing of dipolar and photonic weights

To begin our study of a disordered chain of dipoles in a photonic cavity, we place ourselves in the strong-coupling regime, namely with a cavity height $L_x/a = 12$ [see Fig. 3.6(b) for the ordered counterpart], and we consider a chain of $\mathcal{N} = 1000$ dipolar emitters. We compute the average of the photonic part $\mathrm{Ph}(n)$ and of the participation ratio $\mathrm{PR}(n)$ of the eigenmodes n of the system over 100 disorder realizations, for increasing frequency disorder strength W. The result is shown in Figs. 3.7(a) and 3.7(b), as a function of both the eigenfrequencies ω_n^{pol} which are ordered in ascending order, and the disorder strength W.

---

[3] Nevertheless, considering only off-diagonal disorder leads to what is known as the Dyson singularity in the density of states [183]. In the presence of coupling beyond nearest neighbor, such singularity, located in the middle of the energy band, transforms into a finite peak comprising eigenstates that are slightly more localized than the surrounding ones [184, 185]. We found (not shown) that in the presence of strong light-matter coupling, similar conclusions may be drawn. A Dyson peak in the density of state is still present in the strong coupling regime, and it comprises eigenstates that are slightly more localized and more dipolar than the surrounding ones.

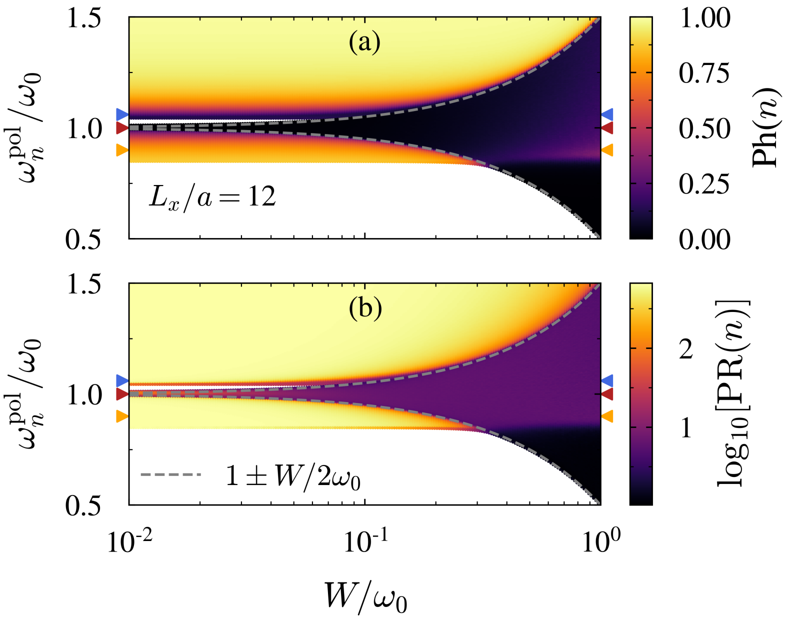

Figure 3.7: Effect of disorder on the polaritonic system. Colormaps of (a) the photonic weight Ph(n) and (b) the participation ratio PR(n) as a function of both the eigenfrequencies ω_n^{pol} and disorder strength W in units of the average dipole frequency ω_0. The cavity height is $L_x/a = 12$, the number of dipole is $\mathcal{N} = 1000$, and the data have been averaged over 100 disorder realizations.

We first discuss the spectrum for weak disorder strengths $W/\omega_0 \simeq 10^{-2}$, which could correspond typically to experimental uncertainties obtained in the fabrication of plasmonic nanoparticles, namely inhomogeneities in their sizes [171, 173, 186], resulting in different resonance frequencies ω_i [187–189]. In Fig. 3.7(a), we recognize the same behavior as with an ordered chain (see Fig. 3.6), namely that the bottom of the LP branch is mainly photonic, visible in orange, whereas the top is almost purely dipolar, visible in black around $\omega_n^{\mathrm{pol}}/\omega_0 = 1.0$. Furthermore, the bottom of the UP branch is mainly dipolar, while the rest of the band goes from predominantly photonic to almost purely photonic states. By comparing these results to the PR in Fig. 3.7(b), we observe that mainly photonic states have a very high PR, i.e., they are delocalized along the chain, while the almost purely dipolar dark states show a lower PR, hence being localized on a small number of sites. This expected behavior shows the cavity-protection effect, namely that polaritonic states are more robust against disorder than purely dipolar states [155]. We note that mainly dipolar states with a photonic weight Ph(n) $\simeq 0.25$, visible in purple in Fig. 3.7(a), already benefit from this effect.

By now increasing disorder, we observe in Figs. 3.7(a) and 3.7(b), as expected, an increase of the bandwidth of the polariton bands. This amounts to the closing of the bandgap such that we cannot unambiguously distinguish between LP and UP branches anymore, so that the system is no longer strictly in the strong-coupling regime. Interestingly, the growing portion of the spectrum is the one containing the dark states, namely the top of the LP branch, which in this sense behaves as an effective band. This observation agrees with Ref. [89], where similar behavior has been encountered. All the states outside this effective dark state band profit from the cavity-protection effect. We note that the dark state band is bounded from below by the least coupled, darkest mode, which, in the ordered chain picture, was marked as the dotted grey line in Fig. 3.6. As shown by the grey dashed lines in Figs. 3.7(a) and 3.7(b), the rate of expansion of the dark state band around ω_0 is $W/2$, that is, half the width of the rectangular distribution in which the individual dipole frequencies ω_i are randomly chosen. This is due to the fact that dark states have eigenfrequencies which are almost unchanged by cavity photons, so that they remain of the order of ω_i.

When this broadening of the eigenfrequencies approximately reaches the bottom of the LP branch, that is, when the disorder strength $W \gtrsim 0.3$, fully dipolar eigenstates which are totally localized with a $\mathrm{PR}(n) \simeq 1$ appear in the spectrum [see the black region at the bottom right of Figs. 3.7(a) and 3.7(b)]. In that respect and as detailed in the next subsection, for a given large enough disorder strength $W \gtrsim 0.3$ the model hosts three distinct phases as can be seen from Figs. 3.7(a) and 3.7(b): an exponentially localized, dark state phase composed of the eigenfrequencies $\omega_n^{\mathrm{pol}} \lesssim \omega_{q=0}^{\mathrm{ph}}$ (black region), a phase of mostly photonic states, not yet affected by disorder due to their eigenfrequencies $\omega_n^{\mathrm{pol}} \gtrsim \omega_0 + W/2$ (yellow-orange region), and a phase of mainly dipolar polaritons with an intermediate PR, made of states in the dark state band with eigenfrequencies $\omega_{q=0}^{\mathrm{ph}} \lesssim \omega_n^{\mathrm{pol}} \lesssim \omega_0 + W/2$ (purple region).

The latter intermediate phase presents the most interesting properties. We highlight them in Figs. 3.8(a) and 3.8(b), by showing horizontal cuts of Figs. 3.7(a) and 3.7(b), for the eigenmodes corresponding to the eigenfrequencies $\omega_n^{\mathrm{pol}}/\omega_0 = 0.9$, 1.0, and 1.06, plotted as orange, red, and blue solid lines, respectively. These eigenstates are also indicated, respectively, by an orange diamond, a red triangle, and a blue square in the ordered bandstructure of Fig. 3.6(b). At weak disorder strength, they correspond, respectively, to a mainly photonic polariton, a dark state, and a mainly dipolar polariton.

Crucially, we observe in Fig. 3.8(a) that by increasing the disorder strength, the dark state at $\omega_n^{\mathrm{pol}}/\omega_0 = 1.0$ (red line) has a photonic weight which increases linearly with the frequency disorder, at a rate around $0.25W/\omega_0$, as exemplified by the black dashed line. This disorder-induced gain of photonic weight leads to the fact that no more dark states are present at the frequency where they were present without disorder, i.e., around ω_0, since disorder hybridizes all of them to polaritons. Furthermore, the mainly photonic polariton at $\omega_n^{\mathrm{pol}}/\omega_0 = 0.9$ (orange line) changes drastically in nature when the disorder strength is increased, becoming a mainly dipolar polariton when its frequency enters the dark state band, that is when $W \gtrsim 2|\omega_n^{\mathrm{pol}} - \omega_0| = 0.2\omega_0$. Once in the dark state band, its photonic weight also follows a linear increase

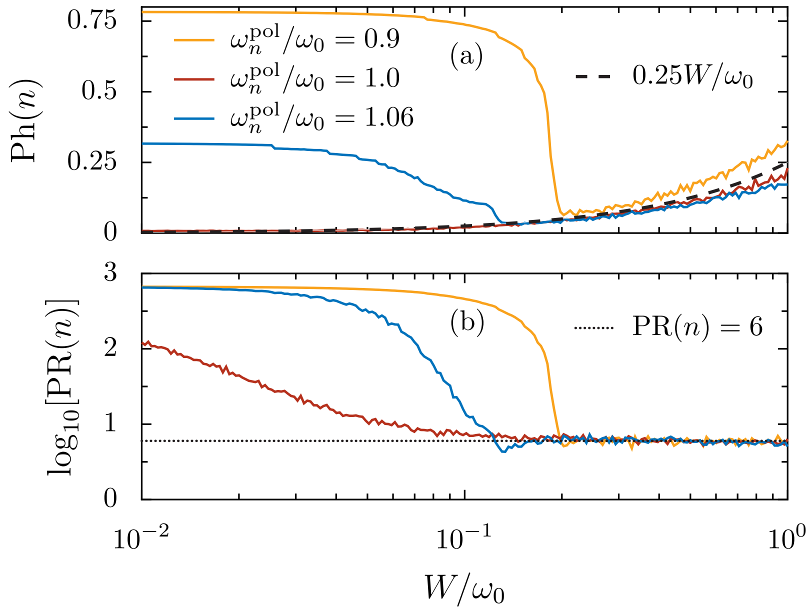

Figure 3.8: Effect of disorder: Emphasis on specific eigenstates. Horizontal cuts of the panels (a)-(b) of Fig. 3.7 at the eigenfrequencies $\omega_n^{\mathrm{pol}}/\omega_0 = 0.9$, 1.0, and 1.06, pointed out in Fig. 3.7 by orange, red, and blue triangles, respectively.

with disorder strength. Finally, the same mechanism occurs for the mainly dipolar polariton at $\omega_n^{\mathrm{pol}}/\omega_0 = 1.06$ (blue line). The corresponding PR values in Fig. 3.8(b) reveal that once in the dark state band, the states show an intermediate value of the PR, here $\mathrm{PR}(n) \simeq 6$, which, as opposed to the photonic weight, remains constant when the disorder strength increases. Importantly, this means that the PR of these states does not fall to 1 with strong disorder strength, in contrast to what is usually the case in 1d disordered systems. This can be understood from the fact that the disorder-induced hybridization of the dark states into polaritons allows them to inherit the polariton robustness against localization, that is, the cavity-protection effect.

In order to better understand the mixing of dipolar and photonic weights induced by disorder, we display in Fig. 3.9 the probability density $|\Psi_i(n)|^2$ along the sites i of the chain for the same three eigenstates, for which the same color code is used. It should be noted, however, that the results of Fig. 3.9 correspond to a given disorder realization. Increasing values of the disorder strength $W/\omega_0 = 0.01, 0.1$, and 1 are considered from left to right panels.

In Figs. 3.9(a)-3.9(c), we present our results for the mainly photonic polariton with eigenfrequency $\omega_n^{\mathrm{pol}}/\omega_0 = 0.9$. By increasing the disorder strength, the state goes from delocalized and mostly photonic in panels (a) and (b), to localized on multiple nonadjacent sites with a very small PR in panel (c). In the following we term these states "semilocalized", as recently proposed by Botzung *et al.* in Ref. [87], where they unveiled similar phenomena in a disordered Tavis-Cummings (TC) model. As studied in Refs. [87, 88,

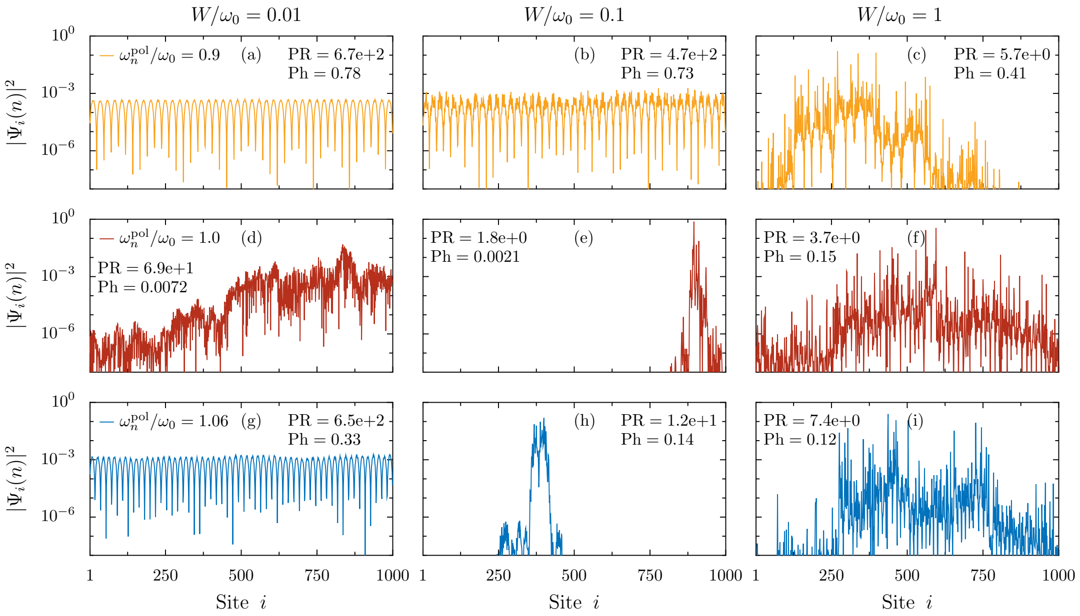

Figure 3.9: Effect of disorder: Shape of specific eigenstates. Probability density $|\Psi_i(n)|^2$ along the sites i of a chain of $\mathcal{N} = 1000$ dipoles, for different eigenfrequencies $\omega_n^{\mathrm{pol}}/\omega_0 = 0.9, 1.0$, and 1.06 (rows), and different disorder strength $W/\omega_0 = 0.01$, 0.1, and 1 (columns). In the figure, data are not averaged over disorder realizations and the cavity height $L_x/a = 12$.

90], semilocalized states can be seen as localized states, that is, an exponential peak with a size-independent PR, with long tails that have increased so that they are of the same order of magnitude as the original peak. In the next Sec. 3.5, we discuss the nature of the semilocalized states present in our model, and notably the differences with the ones found in Refs. [87, 88, 90]. In our model, these semilocalized states correspond to the purple region in Figs. 3.7(a) and 3.7(b), i.e., they belong to the dark state band with eigenfrequencies $\omega_{q=0}^{\mathrm{ph}} \lesssim \omega_n^{\mathrm{pol}} \lesssim \omega_0 + W/2$. They present a constant value of PR of the order of 10, as well as a photonic weight increasing linearly with the disorder strength.

In the second row of Fig. 3.9, we show the same quantities for a dark state with eigenfrequency $\omega_n^{\mathrm{pol}}/\omega_0 = 1.0$. As one can see from panel (d), this fully dipolar state already becomes affected by a weak disorder strength $W/\omega_0 = 0.01$, but the exponential localization occurs only at a stronger disorder strength $W/\omega_0 = 0.1$, visible in panel (e). We note that in addition to the exponential peak, exponentially localized states also include algebraic tails with very small amplitude. By increasing further the disorder strength to $W/\omega_0 = 1$ in panel (f), the state acquires a photonic weight and becomes semilocalized. The same mechanism is visible in the third row of Fig. 3.9 [panels (e)-(g)] for a mainly dipolar polariton with eigenfrequency $\omega_n^{\mathrm{pol}}/\omega_0 = 1.06$, which, due to its polaritonic nature, remains unaffected at weak disorder strength [see Fig. 3.9(g)].

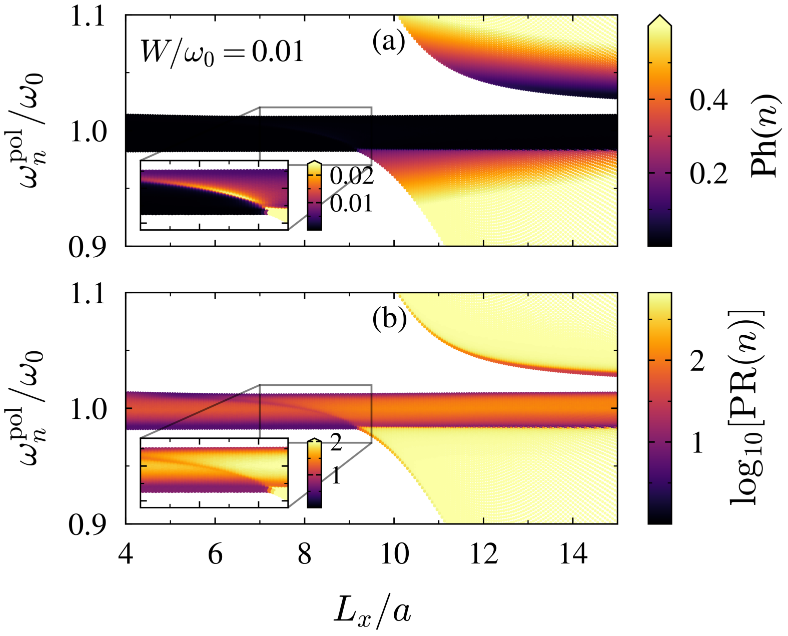

Figure 3.10: Effect of light-matter coupling for weak disorder strength. (a) Photonic weight Ph(n) and (b) participation ratio PR(n) as a function of both the reduced eigenfrequencies $\omega_n^{\mathrm{pol}}/\omega_0$ and cavity height L_x/a, for disorder strength $W/\omega_0 = 0.01$. The data have been averaged over 100 disorder realizations.

3.4.2 Influence of the light-matter coupling

Here we conclude the eigenspectrum analysis by studying the influence of the light-matter coupling on the eigenstate properties discussed previously. For that purpose, we compute the photonic weight [Eq. (3.16b)] and the PR [Eq. (3.5)] of the eigenmodes as a function of both the eigenfrequencies ordered in ascending order, and the cavity height L_x that controls the light-matter coupling.

We display in Fig. 3.10 the case of a weak disorder strength $W/\omega_0 = 0.01$. As can be seen from panel (a), in the weak-coupling regime ($L_x/a \lesssim 9$) the eigenstates are almost not hybridized and the LP branch corresponds only to dark states. The corresponding PR in panel (b) shows that these dark states are already localized, especially the modes near the band edges, whereas the ones around the middle of the band present a higher PR. This behavior of sharply localized band edges is usual in all 1d Anderson-like disordered systems [22]. In the insets of Fig. 3.10, we show a zoom around the modes which interact the most with cavity photons, namely the ones at the center of the BZ in the ordered chain picture (around $q = 0$ in Fig. 3.6). The inset of panel (a) shows that theses modes have a higher photonic weight than the surrounding ones, being the most hybridized states. However, the inset of panel (b) demonstrates that these states have a smaller PR than the surrounding ones,

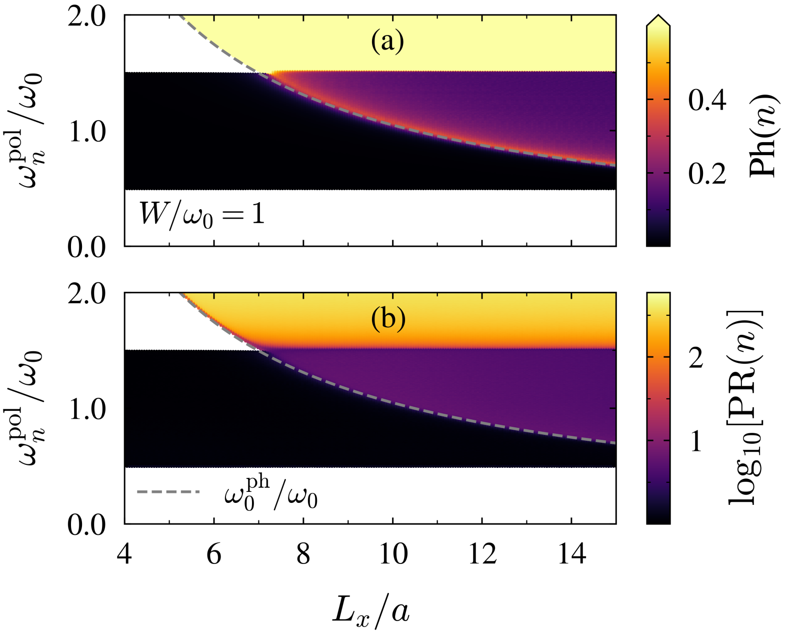

Figure 3.11: Effect of light-matter coupling for strong disorder strength. Same quantities as in Fig. 3.10, but for disorder strength $W/\omega_0 = 1$. The data have been averaged over 100 disorder realizations.

hence being more localized, despite their larger photonic weight. This counterintuitive behavior highlights the particularly nontrivial interplay between localization and light-matter hybridization.

At larger cavity heights ($L_x/a \gtrsim 9$), we see in Fig. 3.10 the emergence of polaritons at the bottom of the LP branch, with a high PR value. The existence of these eigenstates is permitted by the strong enough band modification due to the avoided-crossing, which allows eigenfrequencies smaller than the one of the darkest mode [which was marked as the grey dotted line in Fig. 3.6(b)].[4] In contrast, the top of the LP branch, that we previously coined the dark state band, remains composed of almost fully dipolar states [see panel (a)]. Looking at the corresponding PR in panel (b), one sees that the modes near the band edges of this dark state band are more localized than the ones in the middle, confirming the behavior of an effective band.

Then, in Fig. 3.11, we consider a larger disorder strength $W/\omega_0 = 1$. As we increase the cavity height L_x/a, we observe an increase of the share of semilocalized states, visible in purple both in Figs. 3.7 and 3.11. The frequency range occupied by these semilocalized states matches the part of the dark state

---

[4] This unusual transition, occurring here at a cavity height $L_x/a \simeq 9.1$, originates solely from the $1/r^3$ quasistatic dipole-dipole coupling that leads to a dipolar band which is not flat. Indeed, a flat dipolar dispersion, as considered in usual strong-coupling toy models, would lead to eigenfrequencies that are smaller than the most uncoupled one for any nonzero value of the light-matter coupling.

band overlapping with the bare photonic band, thus being bounded from below by the lowest bare photonic state $\omega^{\mathrm{ph}}_{q=0}$, which we represent as a function of L_x/a as a grey dashed line. This demonstrates that in our model, semilocalization can be understood as eigenstates being mixed to photonic states by the increase of the bandwidth induced by the frequency disorder. This permits new coupling between dipolar and photonic degrees of freedom. States with an eigenfrequency $\omega^{\mathrm{pol}}_n \lesssim \omega^{\mathrm{ph}}_{q=0}$, visible in black in Fig. 3.11, are the fully dipolar exponentially localized states, namely, dark states subject to Anderson localization. Due to their eigenfrequencies being lower than the ones of the photonic band, they cannot benefit from the disorder-induced mixing between dipolar and photonic degrees of freedom. On the other hand, states not already reached by the dark state band, with $\omega^{\mathrm{pol}}_n \gtrsim \omega_0 + W/2$, remain mainly photonic and delocalized [see the orange/yellow regions in Fig. 3.11], confirming the previous analysis of Fig. 3.7. Finally, we note that with such a large value of the disorder strength ($W/\omega_0 = 1$), we are able to see semilocalized states already for a small cavity height $L_x/a \simeq 7$, a value from which we considered the system being in the weak-coupling regime without disorder. The transition from dark to semilocalized states when increasing the disorder strength is smooth, but with the above explanation, we understand that for a given value of W, semilocalized states would be present only if $2|\omega^{\mathrm{ph}}_{q=0} - \omega_0| \lesssim W$, the light-matter coupling competing with disorder [87].

To conclude this section, by studying the eigenspectrum of our system, we have shown that the bandwidth increase led by frequency disorder tends to incorporate photonic states to the dark state band, leading to states that increase their photonic weight and become semilocalized. Almost fully dipolar dark states, such as the ones shown in panels (d)-(f) of Fig. 3.9, can thus undergo first a transition from being delocalized along the chain to being exponentially localized on a few sites, and then another transition to being semilocalized and turning into hybridized polaritonic states. As we will show in Sec. 3.6 by performing transport simulations in a driven-dissipative scenario, the latter hybridized states inherit long-range polaritonic transport properties. This remarkable phenomenon thus leads to a disorder-enhanced propagation along the chain, that is, to the decrease and then the re-increase of the long-range transport properties for increasing disorder.

3.5 On the nature of the semilocalized eigenstates

In the previous section, we unveiled that at large disorder strength the eigenstates of the Hamiltonian (3.6) can be of three very different types (cf. Fig. 3.7): (i) dipolar with a PR of order 1, (ii) hybridized with a PR of order 10, (iii) photonic with a PR of order $\mathcal{N}$. By inspection of the probability density $|\Psi_i|^2$ of these states along the sites $i \in [1, \mathcal{N}]$ of the chain, we found that the dipolar ones are exponentially localized in the chain, with very small power-law tails, so that we coin them as *localized*. The photonic states are homogeneously extended along the chain, and we term them *delocalized* at the scale of the system size, since their localization length is larger than the size of the chain.

The hybridized states, however, are localized on multiple, noncontiguous sites [see panels (c), (f), and (i) of Fig. 3.9, where $\mathcal{N} = 1000$], so that we coin them *semilocalized*, following Ref. [87] were similar features were observed in a disordered TC model. In the context of disordered systems, such neither localized nor delocalized states have been associated to multifractal, nonergodic extended states, which are notably a feature of the critical point of Anderson transitions [22]. Multifractal states have also been observed in disordered Floquet systems [190] as well as in long-ranged disordered systems [191, 192]. Recently, Dubail *et al.* [90] unveiled the multifractal nature of the semilocalized states present in a disordered TC model without any short-range hopping, and where the light-matter coupling acts as an effective long-range hopping term.

In this section, we study the nature of the semilocalized states present in our multimode light-matter coupling model, to ascertain whether they have the same properties as in simplified single-mode models, or if their particular localization profile comes from finite-size effects. To this end, we first conduct a scaling analysis of the participation ratio with the system size $\mathcal{N}$, then we perform a level statistics analysis, before we carry out a multifractal analysis through the scaling of the generalized participation ratio with the system size.

3.5.1 Scaling of the participation ratio

We show in Fig. 3.12 the scaling of the participation ratio $\mathrm{PR}(n)$ [defined in Eq. (3.5)] with the number of dipoles $\mathcal{N} \in [100, 5000]$, for increasing values of the disorder strength $W/\omega_0 = 0.01, 0.1$, and 1 from the left to the right panel. We note that to minimize fluctuations, all the results have been averaged over 100 disorder realizations. Such a scaling is of crucial importance to correctly conclude on the localization nature of the eigenstates. Indeed, the PR of a localized state must remain independent of the system size, while the one of an extended state should scale with the system size.

In Figs. 3.12(a) and 3.12(b), we display the results for the eigenstates corresponding to the eigenfrequencies $\omega_n^{\mathrm{pol}}/\omega_0 = 0.9$, 1, and 1.06, i.e., the same as the ones studied in Figs. 3.8 and 3.9. On the one hand, at small disorder strength in panel (a), two polaritonic states (plotted by orange diamonds and blue squares) show a PR increasing linearly with the number of dipoles $\mathcal{N}$, precisely following the growth rate $2(\mathcal{N}+1)/3$ plotted as a black dashed line, which corresponds to maximally extended eigenstates in an ordered ($W = 0$) system. On the other hand, the PR of the dark state, plotted by red triangles, increases at small system sizes before it converges to a constant value for large enough number of dipoles $\mathcal{N}$, demonstrating its localized nature despite its quite large localization length. At larger disorder strength in panel (b), the PR of both the mainly dipolar polariton (blue squares) and

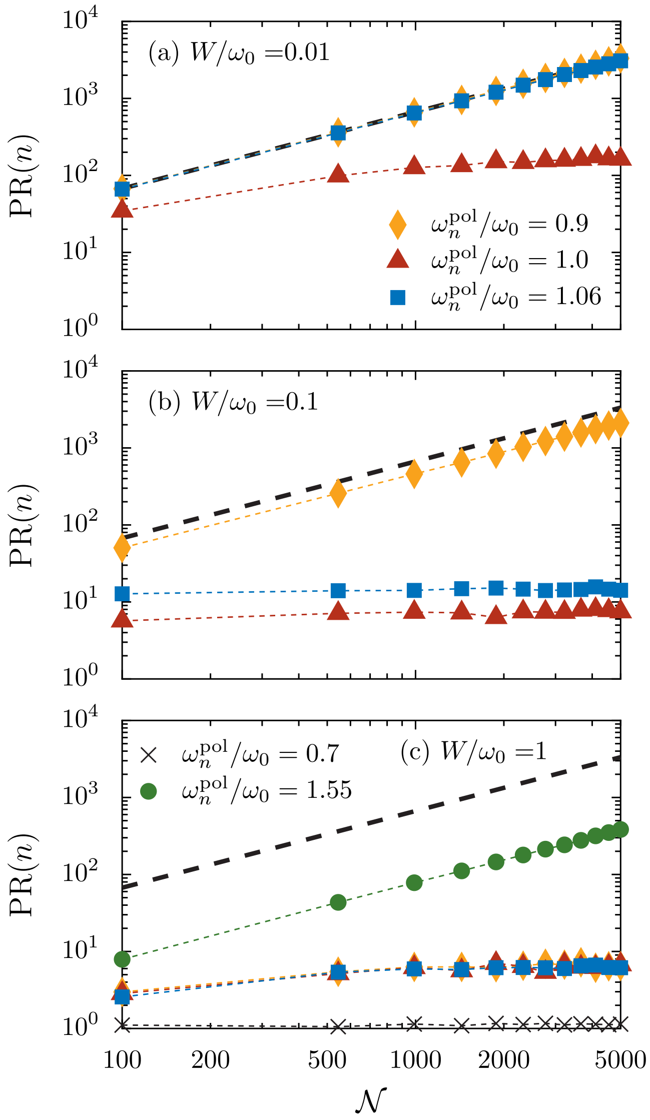

Figure 3.12: Scaling of the participation ratio. Participation ratio PR(n) [defined in Eq. (3.5)] as a function of the size of the chain $\mathcal{N}$, for the eigenmodes associated to the eigenfrequencies $\omega_n^{\rm pol}/\omega_0 = 0.9$, 1.0, and 1.06, with increasing disorder strength from the top to the bottom panel. Panel (c) shows in addition the result for the eigenmodes associated to the eigenfrequencies $\omega_n^{\rm pol}/\omega_0 = 0.7$ and 1.55. Extended states show a participation ratio growing linearly with $\mathcal{N}$, while localized states present a constant participation ratio. The black dashed line represents the maximum growth rate $2(\mathcal{N}+1)/3$. The cavity height $L_x/a = 12$, and the data have been averaged over 100 disorder realizations.

the dark state (red triangles) are drastically reduced and remain constant, indicating localized states, as already seen in Figs. 3.9(e) and 3.9(h). The mainly photonic polariton (orange diamonds) remains delocalized, although presenting a slightly reduced PR.

Finally, in Fig. 3.12(c), a larger disorder strength $W/\omega_0 = 1$ is considered and in addition to the three eigenstates discussed above which are now semilocalized, we also show the scaling of the PR of a mainly photonic polariton with eigenfrequency $\omega_n^{\text{pol}}/\omega_0 = 1.55$ (green circles) and of a fully dipolar dark state with eigenfrequency $\omega_n^{\text{pol}}/\omega_0 = 0.7$ (black crosses). In that context, one can see that all of the three previously discussed eigenstates present a PR that, after increasing at small sizes, converges to a constant value at larger sizes, confirming the fact that such semilocalized states are not extended. Moreover, the mainly photonic polariton (green circles) still has a growing PR, showing that such a state having an eigenfrequency $\omega_n^{\text{pol}} > \omega_0 + W/2$ remains extended. The eigenstates with frequencies $\omega_n^{\text{pol}} < \omega_{q=0}^{\text{ph}}$ newly allowed by the large value of the disorder strength are totally localized with a constant value of the PR around 1, as can be seen from the black crosses in Fig. 3.12(c). We note that we have also checked (not shown) that the photonic weight $\text{Ph}(n)$ of the eigenstates is not affected when increasing the system size, and is independent of the number of dipoles $\mathcal{N}$.

3.5.2 Level statistics analysis

We propose here an analysis of the nature of the semilocalized states observed in our model by means of level spacing statistics. To this end, we follow Ref. [193] and compute the distribution of level spacing ratios

$$\tilde{r}_n = \min\left(r_n, \frac{1}{r_n}\right), \tag{3.18}$$

with

$$r_n = \frac{s_n}{s_{n-1}}, \tag{3.19}$$

where $s_n = \omega_{n+1}^{\text{pol}} - \omega_n^{\text{pol}} \geqslant 0$ is the level spacing, the eigenfrequencies ω_n^{pol} being sorted in ascending order. The average $\langle \tilde{r}_n \rangle$ of such a level spacing ratio over a given window of eigenstates n has been shown to display a universal value according to the level statistics [194]. Moreover, the average level spacing ratio is scale invariant at the critical point of an Anderson transition. This allows one to monitor such transition between an extended phase, with statistics related to the random matrix ensembles, and a localized phase, with eigenfunctions exponentially localized on random sites, not overlapping so that the eigenvalues follow Poisson statistics [193, 195–197]. In contrast to the standard level spacing distribution, the quantity (3.18) has the advantage of not requiring any unfolding of the spectrum, since it is independent of the local density of states [193, 194].

In Fig. 3.13, we show such one-parameter scaling for increasing number of dipoles $\mathcal{N}$, using the same parameters as in the previous subsection. The averaging of the ratio (3.18) has been performed with 1/10 of the eigenstates of the spectrum centered around the middle of the dark state band in the case of an ordered chain, namely around the eigenfrequency $\omega_n^{\text{pol}}/\omega_0 = 0.9981$. The

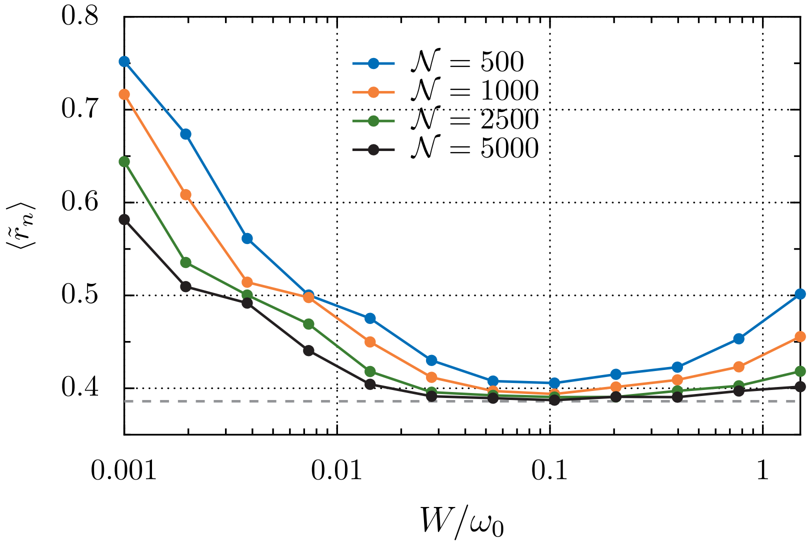

Figure 3.13: Level statistics. Average of the level spacing ratio $\langle\tilde{r}_n\rangle$ (see Eq. (3.18)) for eigenstates within the dark state band as a function of the disorder strength, for increasing sizes of the chain $\mathcal{N}$. The grey dashed line shows the exact value for Poisson statistics $\langle\tilde{r}_n\rangle^{\mathrm{PE}} = 2\ln 2 - 1 \simeq 0.39$. The cavity height $L_x/a = 12$, and the data have been averaged over 100 disorder realizations.

results were further averaged over 100 disorder realizations. As expected, there is no common intersection point between all the curves, demonstrating that there is no Anderson transition, as in usual 1d disordered systems. Instead, the average level spacing ratio converges to the exact value computed for the localized phase with Poisson statistics, $\langle\tilde{r}_n\rangle^{\mathrm{PE}} = 2\ln 2 - 1 \simeq 0.39$ [194], with diminishing disorder strength when the size of the system increases, as in the original 1d Anderson model [196]. At small disorder strength, the average ratio goes to 1, i.e., the value corresponding to an ordered system. Therefore, as expected in 1d [196], there is no extended phase with statistics related to random matrix ensembles.

Interestingly, when increasing further the disorder strength, we observe in Fig. 3.13 a rise of the average level spacing ratio, which corresponds to the semilocalization and hybridization of the dark states, as discussed in Sec. 3.4. The ratio $\langle\tilde{r}_n\rangle$ thus takes values between $\langle\tilde{r}_n\rangle^{\mathrm{PE}}$ and $\langle\tilde{r}_n\rangle = 1/2$, which corresponds to semi-Poissonian statistics [198, 199]. Such behavior is in line with the results obtained in a disordered TC model where multifractal semilocalized states were found to follow statistics that range from Poissonian to very close to semi-Poissonian, even at the thermodynamic limit [90].

Remarkably, however, in our multimode model we observe that increasing the size of the system leads to the rise of the average level spacing ratio at large disorder to be flattened, so that the ratio converges to the Poisson value even at large disorder strength, as visible for the case of $\mathcal{N} = 5000$ displayed by a black solid line in Fig. 3.13. Hence, for larger systems, a larger disorder strength is required to push the semilocalized states away from a Poisson statistics. This suggests that for a fixed, finite disorder strength W/ω_0 with the parameters chosen here, namely $d/a = 4$ and $L_x/a = 12$, the semilocalized states in our model would just follow a Poisson statistics at the thermodynamic limit $\mathcal{N} \to \infty$, as usual localized states.

3.5.3 Generalized participation ratio and multifractal analysis

To ascertain whether or not the semilocalized states of our multimode model follow a multifractal structure as in single-mode models [90], here we conduct a multifractal analysis by analyzing the scaling with the system size $\mathcal{N}$ of the generalized participation ratio, which is defined as [22]

$$\mathrm{PR}_{\mathfrak{q}}(n) = \frac{\left(\sum_{i=1}^{\mathcal{N}} |\Psi_i(n)|^2\right)^{\mathfrak{q}}}{\sum_{i=1}^{\mathcal{N}} |\Psi_i(n)|^{2\mathfrak{q}}} \underset{\mathcal{N}\to\infty}{\sim} \mathcal{N}^{\tau_{\mathfrak{q}}(n)}. \tag{3.20}$$

While localized and delocalized eigenstates are characterized, respectively, by a multifractal exponent $\tau_{\mathfrak{q}} = 0$ (with $\mathfrak{q} > 0$) and $\tau_{\mathfrak{q}} = \mathfrak{q} - 1$, any other behavior of $\tau_{\mathfrak{q}}$ as a function of $\mathfrak{q}$ implies multifractality [22]. We extract the multifractal exponent $\tau_{\mathfrak{q}}$ from a logarithmic linear regression of the generalized participation ratio (3.20) as a function of the system size $\mathcal{N}$, that we average over a frequency window $\omega_n^{\mathrm{pol}}/\omega_0 \in [0.9\,;1.4]$ corresponding to hybridized, semilocalized states. To minimize fluctuations, data obtained with system sizes $\mathcal{N} \in [10^2\,;10^3]$ and $\mathcal{N} \in \,]10^3\,;3\times10^3]$ have been further averaged over, respectively, 100 and 10 disorder realizations.

Figure 3.14 shows the resulting multifractal exponents extracted from different scaling procedures, considering only system sizes $\mathcal{N} \in [10^2\,;10^3]$ in blue, $\mathcal{N} \in [10^3\,;3\times10^3]$ in orange, and $\mathcal{N} \in [3\times10^3\,;10^4]$ in green. In the inset we exemplify such scaling behavior for the value $\mathfrak{q} = 0.12$, with numerical data represented as grey circles, and the linear regressions with solid lines. We observe that when increasing the system size $\mathcal{N}$, the multifractal exponents $\tau_{\mathfrak{q}}$ are getting closer and closer to their value for localized states, namely $\tau_{\mathfrak{q}} = 0$.

This drastically differs from the multifractal behavior found analytically at the thermodynamic limit in a simplified disordered TC model (see Eq. (8) of Ref. [90]) which we show as a black dashed line in Fig. 3.14. This suggests that the semilocalized states of our multimode model are not related to multifractal, nonergodic extended states at the thermodynamic limit. We note that in a single-mode version of our model, namely considering the Hamiltonian (3.6) with only the photonic mode $n_z = 1$, the exponent $\tau_{\mathfrak{q}}$ shows the same multifractal behavior as in the simplified disordered TC model considered in Ref. [90].

To conclude, the analysis conducted in this section suggests that the hybridized, semilocalized states present in our model through states localized in multiple, noncontiguous sites of the chain [see panels (c), (f), and (i) of

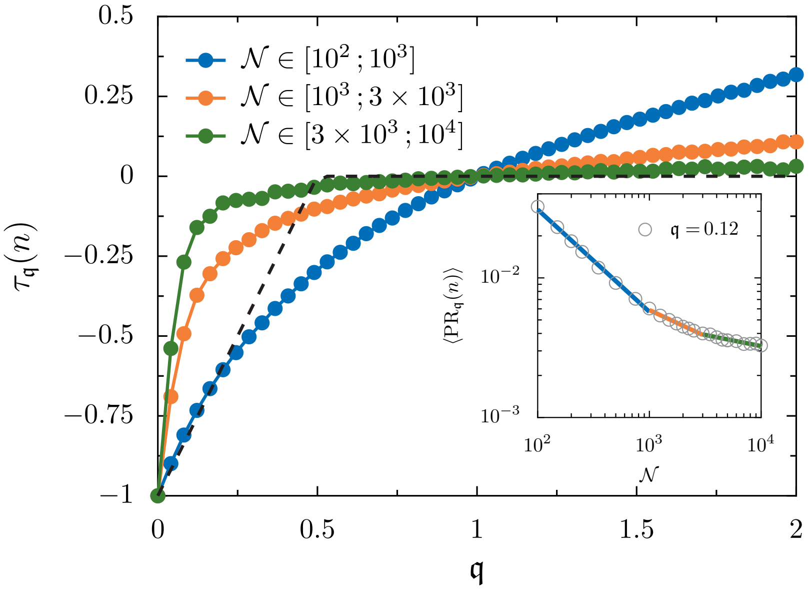

Figure 3.14: Multifractal analysis. Multifractal exponent of the semilocalized states $\tau_{\mathfrak{q}}(n)$ [as defined in Eq. (3.20)] as a function of $\mathfrak{q}$. The exponents have been extracted according to the procedure explained in the text (see colored dots). The black dashed line represents the analytical result found for a simplified disordered Tavis-Cummings model [90]. The inset exemplifies the scaling procedure for the value $\mathfrak{q} = 0.12$, with the circles showing numerical data. The cavity height $L_x/a = 12$ and the disorder strength $W/\omega_0 = 1$.

Fig. 3.9 where $\mathcal{N} = 1000$], behave in the thermodynamic limit as usual localized states following Poissonian statistics. Therefore, in our multimode model, the semilocalization properties of the dark states that are hybridized through disorder fade out as the system size increases.

3.6 Driven-dissipative transport scenario

We now move to transport simulations in order to elucidate the fate of the cavity-protection effect, as well as the disorder-induced mixing between dipolar and photonic degrees of freedom and semilocalization in the propagation characteristics along the chain. Crucially, unlike the recent studies of Refs. [88, 90, 91], we study transport through an out-of-equilibrium driven-dissipative scenario, which permits us to analyze the propagation of polaritonic excitations along the chain as a function of the driving frequency, and to study the effect of dissipation, taking into account inevitable losses both in the dipoles and in the mirror cavity.

For that purpose, we consider a driven-dissipative transport scenario by adding to the polaritonic Hamiltonian given in Eq. (3.6) a driving term

$$H_{\text{drive}}(t) = \hbar\Omega_{\text{R}} f(t) \left(b_1^\dagger + b_1\right), \tag{3.21}$$

which corresponds to a transversely polarized electric field with amplitude E_0 acting on the first dipole, with the Rabi frequency $\Omega_{\mathrm{R}} = E_0\sqrt{Q^2/2M\hbar\omega_0}$, and where $f(t)$ is a time-dependent function that depends on the driving frequency ω_{d}. In the following, we consider a drive $f(t) = \sin(\omega_{\mathrm{d}}t)$, corresponding to the first site of the chain being continuously illuminated by a monochromatic electric field.

We assume that the propagation dynamics can be approximated by the Lindblad master equation for the density matrix

$$\begin{aligned}\dot{\rho} = \frac{\mathrm{i}}{\hbar}\left[\rho, H_{\mathrm{pol}}^{\square} + H_{\mathrm{drive}}(t)\right] - \sum_i \frac{\gamma_i}{2}\left(\left\{b_i^\dagger b_i, \rho\right\} - 2b_i\rho b_i^\dagger\right) \\ - \sum_{n_z}\frac{\kappa_{n_z}}{2}\left(\left\{c_{n_z}^\dagger c_{n_z}, \rho\right\} - 2c_{n_z}\rho c_{n_z}^\dagger\right),\end{aligned} \tag{3.22}$$

where we consider two different phenomenological Markovian baths in order to take into account both the damping rates γ_i of the dipole excitations, typically coming from radiative and Ohmic losses, and the damping rates κ_{n_z} of the photons, arising from the imperfect cavity mirrors. In the remainder of this manuscript, we assume that the dipolar losses are independent of the dipole site, such that $\gamma_i = \gamma$, and that the cavity losses are independent of the photon mode, i.e., $\kappa_{n_z} = \kappa$.

In the following, we fix the cavity loss to $\kappa/\omega_0 = 0.001$. This is motivated by the fact that all the qualitative propagation features found here are independent of the value of κ, as long as it remains small enough, as is discussed in Appendix 3.A. The value of the dipolar damping rate γ, however, is of crucial importance and in order to illustrate its impact, we consider two different cases. The first one, $\gamma/\omega_0 = 0.001$, can be achieved experimentally in platforms with small or highly controllable losses such as, e.g., microwave resonators or dielectric and SiC nanoparticles. The second one, $\gamma/\omega_0 = 0.02$ represents the case of more lossy dipoles, which is naturally achieved in, e.g., nanoplasmonic setups where Ohmic losses are significant.

To study the transport properties along the chain of dipoles, we introduce the dimensionless dipole moment $p_i = \langle b_i + b_i^\dagger\rangle$ bared by the dipole i. The latter quantity is directly proportional to the dipole moment at site i, $\mathfrak{p}_i = -Q\sqrt{\hbar/2M\omega_0}\,p_i$. The associated power radiated in the far field by a dipole at site i is then given by the classical Larmor formula [119]

$$\mathcal{P}_i = \frac{2\omega_0^4}{3c^2}(\mathfrak{p}_i)^2 = \frac{4\pi a^2}{3}(k_0 a)^4 I_0\left(\frac{p_i}{\Omega_{\mathrm{R}}/\omega_0}\right)^2, \tag{3.23}$$

where $I_0 = cE_0{}^2/8\pi$ is the driving field intensity.

3.6.1 Steady-state solution of the Lindblad master equation

To obtain from the master equation (3.22) the steady-state solution for the amplitudes of the dimensionless dipole moments $|p_i|$ along the sites i of the chain, we introduce a corresponding momentum $\pi_i = \mathrm{i}\langle b_i - b_i^\dagger\rangle$, as well as the equivalent quantities for the photonic degrees of freedom, $p_{n_z}^{\mathrm{ph}} = \langle c_{n_z} + c_{n_z}^\dagger\rangle$ and $\pi_{n_z}^{\mathrm{ph}} = \mathrm{i}\langle c_{n_z} - c_{n_z}^\dagger\rangle$. Then, using the identity $\langle\dot{O}\rangle = \mathrm{Tr}\left\{\dot{\rho}O\right\}$, valid for any operator O, we obtain from the master equation (3.22) the system of coupled first order ordinary differential equations

$$\dot{p}_i = -\omega_i\pi_i - \frac{\gamma_i}{2}p_i + \sum_{n_z=1}^{\mathcal{N}}\xi_{in_z}p_{n_z}^{\mathrm{ph}} - \sum_{j\neq i}\Omega_{ij}\pi_j \tag{3.24a}$$

$$\dot{p}_{n_z}^{\mathrm{ph}} = -\omega_{n_z}^{\mathrm{ph}}\pi_{n_z}^{\mathrm{ph}} - \frac{\kappa_{n_z}}{2}p_{n_z}^{\mathrm{ph}} - \sum_{i=1}^{\mathcal{N}}\xi_{in_z}p_i \tag{3.24b}$$

$$\begin{aligned}\dot{\pi}_i = \omega_i p_i - \frac{\gamma_i}{2}\pi_i + \sum_{n_z=1}^{\mathcal{N}}\xi_{in_z}\pi_{n_z}^{\mathrm{ph}} + \sum_{j\neq i}\Omega_{ij}p_j \\ + 2\Omega_{\mathrm{R}}f\left(t\right)\delta_{1,n}\end{aligned} \tag{3.24c}$$

$$\dot{\pi}_{n_z}^{\mathrm{ph}} = \omega_{n_z}^{\mathrm{ph}}p_{n_z}^{\mathrm{ph}} - \frac{\kappa_{n_z}}{2}\pi_{n_z}^{\mathrm{ph}} - \sum_{i=1}^{\mathcal{N}}\xi_{in_z}\pi_i. \tag{3.24d}$$

Being interested in the stationary transport regime, we solve the above system for the steady-state solution using the complex representation $p_i = A_i\mathrm{e}^{\mathrm{i}\omega_{\mathrm{d}}t}$, and $f\left(t\right) = \mathrm{e}^{\mathrm{i}\omega_{\mathrm{d}}t}$. We note that the considered continuous periodic drive leads to a vanishing time-averaged dipole moment $\langle p_i\rangle_t$. However, its time-averaged amplitude $\langle|p_i|\rangle_t$ is nonzero. This procedure yields to steady-state solutions $\mathbf{P} = (|p_1|, |p_2|, \ldots, |p_{\mathcal{N}}|)$ as

$$\mathbf{P} = \mathcal{M}_{\mathrm{pol}}^{-1}\mathbf{D}, \tag{3.25}$$

where the $\mathcal{N}-$dimensional driving vector is given by $\mathbf{D} = (2\Omega_{\mathrm{R}}, 0, \ldots, 0)$, and the $\mathcal{N}\times\mathcal{N}$ matrix $\mathcal{M}_{\mathrm{pol}}$ reads

$$\begin{aligned}\mathcal{M}_{\mathrm{pol}} = \Big[\left(\omega_{\mathrm{d}} - \mathrm{i}\frac{\gamma}{2}\right)\left(\omega_{\mathrm{d}} - \mathrm{i}\frac{\kappa}{2}\right)\mathbb{1}_{\mathcal{N}} - \mathcal{M}_{\xi}\left(\mathbb{1}_{\mathcal{N}} - \mathcal{D}_2\right)\mathcal{M}_{\xi}^{\mathrm{t}}\Big] \\ \times\widetilde{\mathcal{M}}_{\mathrm{dp}}^{-1}\left[\frac{\omega_{\mathrm{d}} - \mathrm{i}\frac{\gamma}{2}}{\omega_{\mathrm{d}} - \mathrm{i}\frac{\kappa}{2}}\mathbb{1}_{\mathcal{N}} + \mathcal{M}_{\xi}\mathcal{D}_0\mathcal{M}_{\xi}^{\mathrm{t}}\right] - \widetilde{\mathcal{M}}_{\mathrm{dp}}.\end{aligned} \tag{3.26}$$

In the above matrix equation, $\mathbb{1}_{\mathcal{N}}$ is the $\mathcal{N}\times\mathcal{N}$ identity matrix, the matrix $\mathcal{M}_{\xi}$ is defined by its elements as $\left[\mathcal{M}_{\xi}\right]_{ij} = \xi_{ij}$, where $i, j = 1, \ldots, \mathcal{N}$, the diagonal matrices $\mathcal{D}_{\beta} = \mathrm{Diag}\left(\Omega_1^{\beta}, \Omega_2^{\beta}, \ldots, \Omega_{\mathcal{N}}^{\beta}\right)$, with the β-dependent function

$$\Omega_{n_z}^{\beta} = \frac{\left(\omega_{n_z}^{\mathrm{ph}}\right)^{\beta}}{(\omega_{n_z}^{\mathrm{ph}})^2 - \left(\omega_{\mathrm{d}} - \mathrm{i}\frac{\kappa}{2}\right)^2}, \tag{3.27}$$

and finally the matrix $\widetilde{\mathcal{M}}_{\mathrm{dp}}$ is given by

$$\widetilde{\mathcal{M}}_{\mathrm{dp}} = \mathcal{M}_{\mathrm{dp}} - \mathcal{M}_{\xi}\mathcal{D}_1\mathcal{M}_{\xi}^{\mathrm{t}}, \tag{3.28}$$

where $\mathcal{M}_{\mathrm{dp}}$ is defined by its elements as

$$\left[\mathcal{M}_{\mathrm{dp}}\right]_{ij} = \omega_i\delta_{ij} + \Omega_{ij}\left(1 - \delta_{ij}\right). \tag{3.29}$$

We have checked (not shown) that such steady-state solutions $|p_i|$ are well recovered after a finite time when one directly solves the system (3.24) using a numerical ordinary differential equation (ODE) solver.

3.6.2 Cavity-enhanced transport in an ordered chain

In order to understand the underlying transport mechanisms of the system, we begin our study by considering the ordered case ($W/\omega_0 = 0$), which, due to the presence of polaritonic excitations, already features interesting transport properties.

Indeed, cavity photon excitations having an intrinsically collective and delocalized character, they are naturally propagating at longer distances. Moreover, the light-matter coupling Hamiltonian (2.45) acts as an effective long-range coupling between the dipoles. Being in the Coulomb gauge, it can be seen as containing the retardation effects of the dipole-dipole interaction. In the limit of an infinite cavity, i.e., in vacuum, it thus amounts to consider the usual $1/r$ long-range dipole-dipole coupling term. Such a $1/r$ transport has been studied in the past in ordered [138, 175, 200] and disordered [117] systems, showing the above-mentioned effect of long-range transport enhancement by the light-matter coupling. In a finite cavity allowing for the strong-coupling regime, it has been shown in the particular case of a single mode Tavis-Cummings model [87, 88, 90] that under some approximations, the light-matter coupling can be expressed as a distance-independent hopping term. For the multimode cavity considered here, it consists in a longer but finite range effective coupling, for which we will unveil analytical expressions in the next Chap. 4.

Here, we demonstrate that such an effective coupling induced by the strong-coupling regime is directly visible through transport simulations. We begin our analysis by comparing transport properties in systems with different cavity heights.[5] To this end, in Fig. 3.15 we show on a log-log scale the steady-state amplitude of the dipole moment $|p_i|$ along the sites i of a chain of $\mathcal{N} = 2500$ dipoles, for cavity heights $L_x/a = 7$ (red lines) and $L_x/a = 12$ (blue lines). The amplitudes are given in units of $\Omega_{\mathrm{R}}/\omega_0$, since $|p_i| \propto \Omega_{\mathrm{R}}/\omega_0$. Two different dipole losses are considered, $\gamma/\omega_0 = 0.001$ (solid lines) and $\gamma/\omega_0 = 0.02$ (dotted lines), and the result corresponds to the driving of a

---

[5] Nevertheless, due to cavity confinement, the small heights $L_x/a \lesssim 9$ that lead here to the weak-coupling regime are not comparable to the weak coupling of a dipole chain to vacuum electromagnetic modes, recovered here for an infinite cavity.

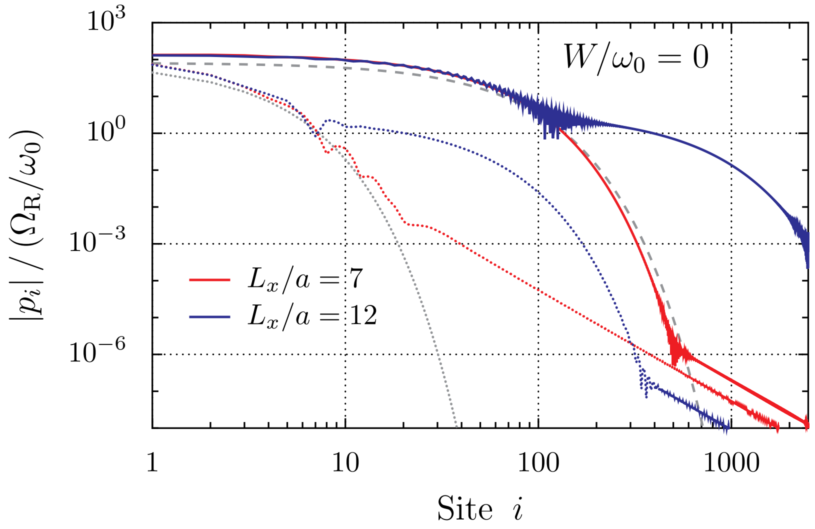

Figure 3.15: Energy transport in the weak- and strong-coupling regimes. Steady-state amplitude of the dipole moment $|p_i|$ on site i in units of the reduced Rabi frequency Ω_R/ω_0 in an ordered ($W/\omega_0 = 0$) chain of $\mathcal{N} = 2500$ dipoles, resulting from a monochromatic drive on the first dipole at a frequency $\omega_d/\omega_0 = 1.0$, corresponding to a dark state. Results are shown for different cavity heights $L_x/a = 7$ (red lines, weak coupling) and $L_x/a = 12$ (blue lines, strong coupling), and different dipole losses $\gamma/\omega_0 = 0.001$ (solid lines) and $\gamma/\omega_0 = 0.02$ (dotted lines). The dashed (dotted) grey line represents the analytical estimate (3.30) with $\gamma/\omega_0 = 0.001$ ($\gamma/\omega_0 = 0.02$).

dark state at frequency $\omega_d/\omega_0 = 1.0$. In the figure, the dashed and dotted grey lines show the result in the case of a quasistatic dipole chain, without any light-matter coupling, and only with nearest-neighbor quasistatic dipole interaction. Such a decay has been computed analytically in Ref. [175] for the root-mean-square of the dipole moment. Here, for the amplitude of the dipole moment it translates into

$$|p_i| = \frac{2}{\pi}\frac{\Omega_R}{\Omega}\left[\sqrt{1+\left(\frac{\gamma}{4\Omega}\right)^2} - \frac{\gamma}{4\Omega}\right]^i, \tag{3.30}$$

such that it follows an exponential decay $|p_i| \propto e^{-id/\zeta}$, with i being the dipole site and $\zeta = d/\text{arcsinh}\,(\gamma/4\Omega)$ the propagation length.

Remarkably, we observe from Fig. 3.15 that such an exponential decay is in very good agreement with the propagation of both the weak (red lines) and strong (blue lines) coupling regimes at short distances ($i \lesssim 100$) for small losses (solid lines), and at very short distances ($i \lesssim 10$) for larger losses (dotted lines). Therefore, strong coupling does not modify the short-range propagation properties of the dark states, which are entirely attributable to the nearest-neighbor quasistatic dipole-dipole coupling. The effect of the strong light-matter coupling becomes visible only at larger distances and takes the form of a second, less steep exponential decay, occurring after sharp oscillations that signal a change of regime.

After the exponential laws, the propagation follows an algebraic decay with slope $\sim 1/i^3$, visible as straight lines on the log-log scale of Fig. 3.15. Such a power-law results from the $1/r^3$ quasistatic dipole-dipole coupling of the dipolar Hamiltonian (2.44). It is hence also visible in the quasistatic case, without light-matter interaction, when going beyond the nearest-neighbor approximation performed in Eq. (3.30). Moreover, this behavior has also been noticed in dipole chains coupled to vacuum electromagnetic modes [117, 175, 200]. Importantly, such an algebraic decay leads the cavity-enhanced transport induced by strong coupling, that is, the second exponential regime, to be effective only for specific system sizes. At too large distances, namely here with dipole losses $\gamma/\omega_0 = 0.02$ for $i \gtrsim 300$ (see the crossing between the blue and red dotted lines), the algebraic decay becomes dominant and the propagation is again similar for systems in the weak- and strong- coupling regimes.

Now that we have studied the transport properties of a dark state in Fig. 3.15, we move to the propagation of polaritons. To that purpose, in Fig. 3.16 we fix the cavity height to $L_x/a = 12$ and we compare the propagation along the chain between driving frequencies $\omega_\mathrm{d}/\omega_0 = 0.9$, 1.0, and 1.06, which correspond, respectively, to a mainly photonic polariton, a dark state, and a mainly dipolar polariton. Note that states with the same eigenfrequencies were already studied in the previous section, see Figs. 3.8 and 3.9, where the same color code was used.

By looking at Fig. 3.16(a), where small dipole losses $\gamma/\omega_0 = 0.001$ are considered, it is clear that the amplitude of the dipole moment on the first site, $|p_1|$, is much smaller for polaritons (orange and blue lines) than for the dark state (red line). This can be understood from the fact that the drive (3.21), as well as the amplitude that we evaluate, are dipole-related quantities. The dark eigenmodes can thus be more easily excited by the drive than the polaritons, and the maximum amplitude resulting from a drive at a given frequency is then related to the dipolar part of the associated eigenstate.

The first exponential is very steep for the polaritons, especially for the one which is mainly photonic, in orange, leading to an inefficient short-range transport. Indeed, the first exponential regime arising solely from the quasistatic dipole-dipole interaction, it is less efficient for a state whose photonic part is important, and for the polaritons it occurs on the first three sites only. It is quickly supplanted by the second, photon-induced exponential which is less and less steep when the photonic part of the driven state increases (from red to blue to orange lines). Such second exponential decay allows for the cavity-enhanced transport, and the long-range propagation of the polaritons becomes better than the one of the dark state from $i \gtrsim 1000$. We note that the slight increase between the two exponentials arises from the change of regime.

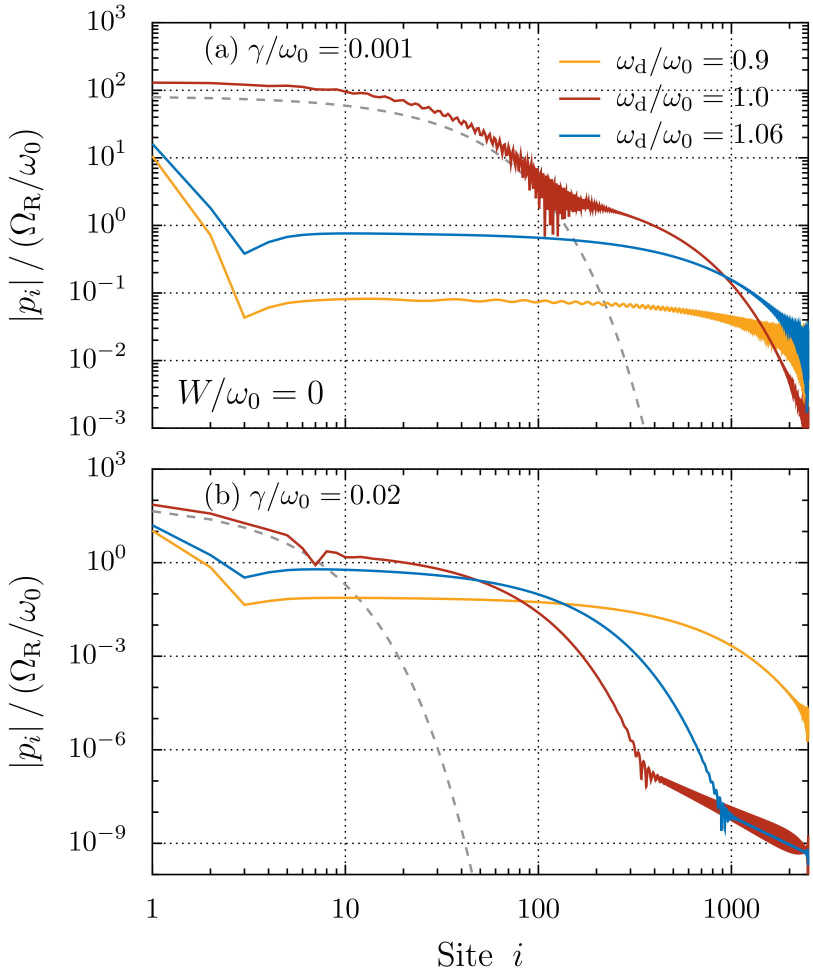

Figure 3.16: Dark state versus polariton energy transport. Same quantity as in Fig. 3.15, with dipole losses (a) $\gamma/\omega_0 = 0.001$ and (b) $\gamma/\omega_0 = 0.02$, but for a fixed cavity height $L_x/a = 12$ and different driving frequencies $\omega_\mathrm{d}/\omega_0 = 0.9$, 1.0, and 1.06, exciting respectively a mainly photonic polariton, a dark state, and a mainly dipolar polariton. The grey dashed lines show the analytical formula for $\omega_\mathrm{d}/\omega_0 = 1.0$ given in Eq. (3.30).

By increasing the dipole losses to $\gamma/\omega_0 = 0.02$ in Fig. 3.16(b), we observe that, crucially, it is mainly the first, dipole-induced exponential and thus the dark state propagation that suffers from larger losses. Thereby, it leads to a strong dominance of the polaritons at long distances, thanks to the second, photon-induced exponential regime. The mainly photonic polariton driven at $\omega_\mathrm{d}/\omega_0 = 0.9$, in orange, here leads to a dipole moment amplitude at the end of the chain, $|p_\mathcal{N}|$, which is 10^4 times larger than the one of the dark state in red. Due to the algebraic decay, however, the propagation of the dark state catches up the ones of the polaritons at a long enough distance, leading, importantly, to a size-dependency of the cavity-enhanced transport. For example, the mainly dipolar polariton (blue curve) shows a cavity-enhanced transport only from sites $i \sim 50$ to $i \sim 1000$.

To conclude this subsection, we have seen that the short-range transport is dominated by the nearest-neighbor quasistatic dipole-dipole coupling, that leads to a first exponential decay which provides efficient dark state propagation, but very poor polaritonic one. The medium and long-range transport are, on the other hand, highly influenced by the strong light-matter coupling, which leads to the appearance of a second exponential decay regime showing the effect of cavity-enhanced transport. The steepness of this photon-induced decay is flattened when the photonic part of the driven eigenstate increases, leading polaritons to propagate efficiently at long distances. At larger distances, however, an algebraic decay independent of the nature of the eigenstate cancels this transport enhancement. Crucially, the increase of dipole losses lowers essentially the short-range propagation, and has less impact on the photon-induced second exponential decay regime. This allows polaritons to better dominate medium and long-range transport when highly lossy dipoles are considered.

In the next subsection, we study the propagation along the chain in the presence of disorder. We show that the same transport mechanisms are present, with however, the crucial addition of the disorder-induced mixing between dipolar and photonic weights, which we unveiled in Sec. 3.4. Indeed, the dark states, that have been turned into semilocalized polaritonic states by disorder, will inherit the polaritonic propagation properties, that is, cavity-enhanced transport, that we discussed in this subsection.

3.6.3 Disorder-enhanced transport

The propagation along a disordered chain is presented in Fig. 3.17, where the cavity height $L_x/a = 12$. We show on a log-log scale the steady-state amplitude of the dipole moment $|p_i|$ along the sites i of the chain in units of the reduced Rabi frequency, resulting from a drive at frequency $\omega_\mathrm{d}/\omega_0 = 1.0$, for increasing disorder strength W. In Fig. 3.17(a), small dipole losses $\gamma/\omega_0 = 0.001$ are considered.

In such a case, we observe that increasing the disorder strength from $W/\omega_0 = 0$ (blue line) to $W/\omega_0 = 0.01$ (orange line) and $W/\omega_0 = 0.1$ (green line) suppresses more and more the transport, especially affecting the first exponential decay and the amplitude on the first site. Increasing further the disorder to $W/\omega_0 = 1$ (black line), we observe an even weaker short-range transport, but a stronger long-range one. Crucially, this long-range propagation arises from a flatter second exponential decay. The steepness of the latter decay being related to the photonic weight of the driven eigenstate, this corroborates the disorder-induced gain of photonic weight of the dark states around ω_0 that we unveiled in Fig. 3.8(a).

This demonstrates the link between the observed disorder-enhanced transport and the disorder-induced mixing between dark and photonic states, such that at strong disorder strength (black line), the state driven at $\omega_\mathrm{d}/\omega_0 = 1.0$ is not anymore an almost uncoupled dark state but an hybridized polariton. It thus propagates very similarly to polaritons in the absence of disorder (cf. the orange and blue lines in Fig. 3.16). We note that it also supports

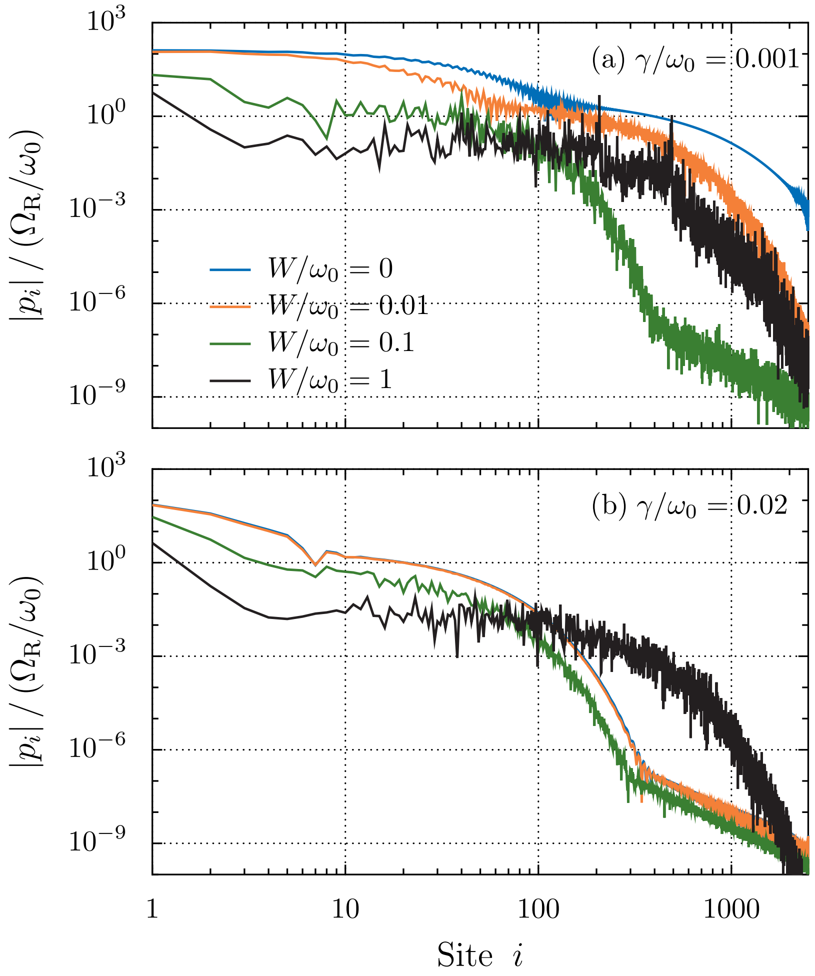

Figure 3.17: Disordered energy transport. Same quantity as in Fig. 3.15, with driving frequency $\omega_d/\omega_0 = 1.0$ corresponding to a dark state and dipole losses (a) $\gamma/\omega_0 = 0.001$ and (b) $\gamma/\omega_0 = 0.02$, but for a fixed cavity height $L_x/a = 12$ and increasing disorder strength W. The data have been averaged over 100 disorder realizations.

the observations made when looking at the localization of the eigenstates for increasing value of W in Fig. 3.9, where panels (d), (e), and (f) correspond, respectively, to the orange, green, and black curves of Fig. 3.17.

When increasing the dipoles losses to $\gamma/\omega_0 = 0.02$ in Fig. 3.17(b), the dark state transport is strongly reduced while the polaritonic one remains almost unaffected. This enables an increasingly effective disorder-enhanced transport when the considered dipoles are lossy. Here, it leads to a long-range propagation that is stronger with disorder than without, up to four orders of magnitudes of the steady state amplitude of the dipoles moment, around the sites $i \sim$ 300-400.

To highlight the effect of disorder on long-range transport, we show in Fig. 3.18 the evolution of the steady-state amplitude of the last dipole, $|p_\mathcal{N}|$, of a chain of $\mathcal{N} = 500$ dipoles when the frequency disorder is increased. We

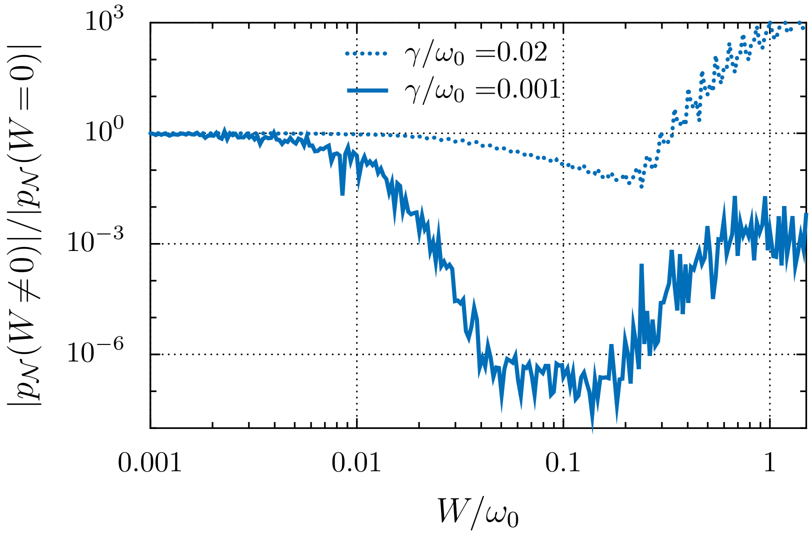

Figure 3.18: Advantage of loss in disordered long-range transport. Steady-state amplitude of the last dipole moment of the chain, $|p_{\mathcal{N}}|$, normalized by the one obtained without disorder, and as a function of the disorder strength W in units of ω_0. A chain of $\mathcal{N} = 500$ dipoles is considered, the driving frequency $\omega_{\mathrm{d}}/\omega_0 = 1.0$, the cavity height $L_x/a = 12$, and the data have been averaged over 100 disorder realizations.

normalize the value of the amplitude $|p_{\mathcal{N}}|$ by the one at the end of an ordered chain, $|p_{\mathcal{N}}(W=0)|$. Small dipole losses $\gamma/\omega_0 = 0.001$ (solid line) as well as larger ones $\gamma/\omega_0 = 0.02$ (dotted line) are considered, and the driving frequency is $\omega_{\mathrm{d}}/\omega_0 = 1.0$, just as in Fig. 3.17.

While the long-range transport is only slightly affected at small disorder strength, it becomes suppressed when W increases, in agreement with the eigenspectrum analysis of Sec. 3.4, where exponentially localized states were observed (see Fig. 3.9). Then, increasing further the disorder strength leads to the rise of the amplitude on the last dipole site, that is, to the disorder-enhanced transport regime. With small dipole losses (solid line), this increase does not exceed the value without disorder, remaining about 10^3 times smaller. But crucially, by considering more lossy dipoles (dotted line), an amplitude of the last dipole moment about 10^3 times larger than without disorder can be observed with a disorder strength $W/\omega_0 = 1.5$. We note that from $W/\omega_0 = 1$, the curves become essentially flat, indicating a regime where the amplitude is no longer affected by disorder.

This is in line with what has been termed disorder-independent transport in Ref. [88], where a study comparable to ours was carried out for a disordered Tavis-Cummings model in a two-terminal, lossless transmission setup. In our model, we explain this regime from the fact that once a state gained enough photonic weight to inherit an almost flat, efficient polaritonic transport up to the end of the chain, increasing further the disorder has no effect.

However, as well as the cavity-enhanced transport unveiled in Fig. 3.16, in our model, the size of the chain $\mathcal{N}$ is critical to observe the disorder-enhanced and disorder-independent transport regimes. This is due to the complexity of the propagation which is made of different regimes of decay, and especially due to the algebraic tail appearing at very large distances. For example, in Fig. 3.17(b), the highly disordered case with $W/\omega_0 = 1$ (black line) shows an enhanced propagation only between the sites $i \simeq 100$ and $i \simeq 2000$. To improve the transport at longer distances, a larger disorder strength should be considered, such that the photonic weight of the driven eigenstate further increases, leading to a flatter second exponential decay which can still dominate the algebraic decay at the end of the chain. Remarkably, however, since the disorder parameter W/ω_0 cannot be arbitrarily increased [see the discussion in Sec. 3.1], this points to the fact that the disorder-enhancement cannot be reached for too long chains by tuning only the frequency disorder.

We note that the fact that disorder-enhanced transport, which is a consequence of the presence of hybridized, semilocalized states, vanishes for very large system sizes and is relevant at intermediate distances only (see Fig. 3.17) is in line with our analysis of the nature of the semilocalized states discussed in Sec. 3.5, the latter fading out when the size of the system increases.

We illustrate this effect of size-dependence in Fig. 3.19, by computing the steady-state amplitude of the dipole moment normalized by the one without disorder, as a function of both the site i along the chain and the disorder strength W. The dipole losses $\gamma/\omega_0 = 0.02$ and the driving frequency $\omega_{\mathrm{d}}/\omega_0 = 1.0$, as in Fig. 3.17(b) and in Fig. 3.18 (dotted line).

In such a density plot, one can distinguish between the different regimes of transport induced by disorder, according to the size of the chain, i.e., to the site i. The white phase at the bottom of the plot shows that small disorder has no effect even on large chains, while the blue phase shows the Anderson localization regime, with a reduced transport. The red phase, at the top right of the plot, indicates the disorder-enhanced transport, especially where the amplitude of the dipole moment is larger with disorder than without. At short distances, such a red phase is absent, showing that no disorder-enhanced transport is achievable for small chains with the parameters considered here. For larger distances, one remarks that the disorder required to enter in the red phase goes linearly with the distance i, implying that a larger chain needs a larger disorder strength.

Furthermore, it is interesting to note that decreasing the dipolar coupling Ω can enhance the disorder-induced effects (not shown), allowing for a disorder-enhanced transport for smaller disorder strength W, and operating at shorter distances. In view of our model, we understand this by the fact that it would lead to a suppression of the first exponential decay, but would have less impact on the second one, the latter being mediated by cavity photons. The relative dominance of the polaritonic long-range transport over the dark state one would thus be larger, in a similar fashion as with

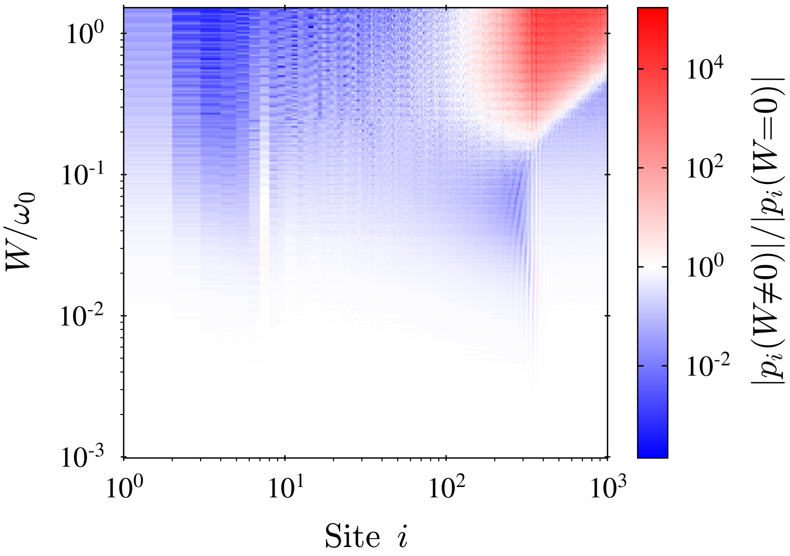

Figure 3.19: Size dependence of disorder-enhanced transport. Steady-state amplitude of the dipole moment $|p_i|$, normalized by the one obtained without disorder, as a function of both the site i along the chain and the disorder strength W in units of ω_0. The dipole losses $\gamma/\omega_0 = 0.02$, the driving frequency $\omega_\mathrm{d}/\omega_0 = 1.0$, the cavity height $L_x/a = 12$, and the data have been averaged over 100 disorder realizations.

the increase of dipole losses. At specific distances, a very small dipolar coupling can also lead to a revival of Anderson localization appearing after the disorder-enhanced and disorder-independent regimes, similarly to what was observed in Ref. [88]. However, decreasing the dipolar coupling, i.e., increasing the spacing d/a between the dipoles, would also go along with an overall reduction of the propagation [175].

Finally, to study the effect of driving frequencies $\omega_\mathrm{d}/\omega_0 \neq 1.0$, we show on Fig. 3.20 the steady-state amplitudes of the dipole moments in a density plot, as a function of both the driving frequency and the site i along a chain of $\mathcal{N} = 1000$ dipoles. On panels (a), (b), and (c), we compare the propagation in a chain with disorder strengths $W/\omega_0 = 0$, $W/\omega_0 = 0.1$, and $W/\omega_0 = 1$, respectively. We consider lossy dipoles, with $\gamma/\omega_0 = 0.02$, for the purpose of maximizing the dominance of the long-range polaritonic transport over the dark state one.

In Fig. 3.20(a), without disorder, a bright yellow spot around $\omega_\mathrm{d}/\omega_0 = 1.0$ demonstrates that the maximal amplitude is generated at short range by driving a dark state, supporting the fact that these states are more easily driven than polaritons. They present however inefficient long-range propagation (see the purple and black spots). At the bottom of the spectrum, a clear threshold can be seen around $\omega_\mathrm{d}/\omega_0 = 0.85$, corresponding to the minimum of the LP branch. The driven states below this threshold are not anymore eigenmodes of the system and hence present poor transport properties. Finally, the orange strips above and below the bright spot around $\omega_\mathrm{d}/\omega_0 = 1.0$

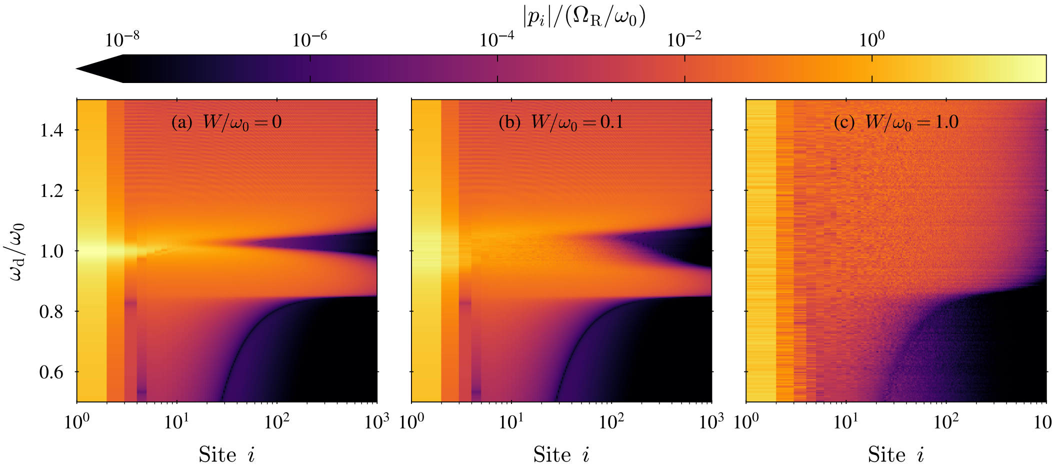

Figure 3.20: Influence of the driving frequency. Density plots of the steady-state amplitude of the dipole moment $|p_i|$ in units of the reduced Rabi frequency Ω_R/ω_0, as a function of both the site i and the driving frequency ω_d/ω_0. Three cases are presented: (a) Without disorder, (b) $W/\omega_0 = 0.1$, and (c) $W/\omega_0 = 1$. The dipole losses $\gamma/\omega_0 = 0.02$, the cavity height $L_x/a = 12$, and the data have been averaged over 100 disorder realizations.

correspond to hybridized polaritons, with poor short-range propagation but very good long-range one, as already observed in Fig. 3.16.

By adding disorder, in Fig. 3.20(b), we clearly see the expansion of the effective dark state band around $\omega_d/\omega_0 = 1.0$. This expansion goes along with a decrease of the transport efficiency, with the disappearance of the bright yellow spot at short range and the enlargement of the black spot at longer range. Polaritons outside the dark state band (orange strips), on the other hand, remain not affected by disorder, displaying the effect of cavity protection of their transport against disorder. When further increasing the disorder strength, in Fig. 3.20(c), all the frequencies up to $\omega_d/\omega_0 = 1.5$ belong to the dark state band. All these now hybridized and semilocalized states have approximately the same propagation characteristics. This, crucially, leads to an improved long-range transport of the dark states around $\omega_d/\omega_0 = 1.0$, which can be readily seen from the complete disappearance of the black spot.

We note that it also leads to a slightly enhanced short-range transport of the mainly photonic polaritons, the latter gaining a dipolar weight from the disorder-induced hybridization, allowing them to be more easily driven. Their long-range transport is however reduced by disorder. In agreement with what was observed in Sec. 3.4 through the fully dipolar and exponentially localized states visible as the black regions in Figs. 3.7(a) and 3.7(b), the eigenstates driven with a frequency essentially smaller than the lowest bare photonic state $\omega^{\mathrm{ph}}_{q=0}/\omega_0 \simeq 0.85$ do not inherit polaritonic propagation features, the light-matter coupling being not strong enough to let them be coupled to photons by the disorder.

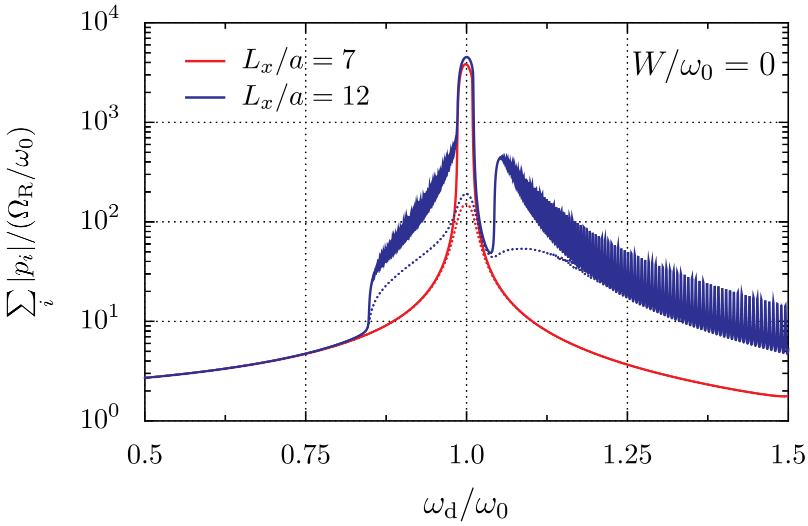

Figure 3.21: Absorption spectra in the weak- and strong-coupling regimes. Absorption spectrum as the sum of $\mathcal{N} = 1000$ dipole moment amplitudes $|p_i|$ in units of the reduced Rabi frequency $\Omega_\mathrm{R}/\omega_0$, as a function of the reduced driving frequency $\omega_\mathrm{d}/\omega_0$. Results are shown without disorder for two different cavity heights $L_x/a = 7$ (red lines, weak coupling) and $L_x/a = 12$ (blue lines, strong coupling), and two different dipole losses $\gamma/\omega_0 = 0.001$ (solid lines) and $\gamma/\omega_0 = 0.02$ (dotted lines).

3.6.4 Absorption spectra from transport computations

Another observable that can be obtained from our driven-dissipative computations are absorption spectra-like quantities. To access such quantities, we consider that the sum of all the steady-state dipole moment amplitudes, $\sum_{i=1}^{\mathcal{N}} |p_i|$, is at first order proportional to the electric field absorbed by the dipoles [201], so that its variation as a function of the driving frequency ω_d yields an absorption spectrum-like graph. Although they do not formally represent absorption spectra, such graphs still allow us to extract meaningful informations from our transport simulations, as discussed in the remainder of this subsection.

We begin with the case of an ordered chain, and show in Fig. 3.21 the absorption spectrum for cavity heights $L_x/a = 7$ (blue lines) and $L_x/a = 12$ (red lines). Two different dipole losses $\gamma/\omega_0 = 0.001$ (solid lines) and $\gamma/\omega_0 = 0.02$ (dotted lines) are considered.

While in the weak coupling regime, $L_x/a = 7$, the absorption spectrum is bell-shaped and centered around the dark state eigenfrequencies at $\omega_\mathrm{d}/\omega_0 = 1.0$, in the strong-coupling regime, $L_x/a = 12$, a rich structure appears. In addition to the central peak, which is slightly higher, we observe high absorption for driving frequencies associated to hybridized polaritons (see the dispersion in Fig. 3.6). These hybridized excitations are visible at the bottom of the LP branch, starting around $\omega_\mathrm{d}/\omega_0 = 0.85$, and in the UP branch, which is visible as a second peak starting around $\omega_\mathrm{d}/\omega_0 = 1.05$ and separated from

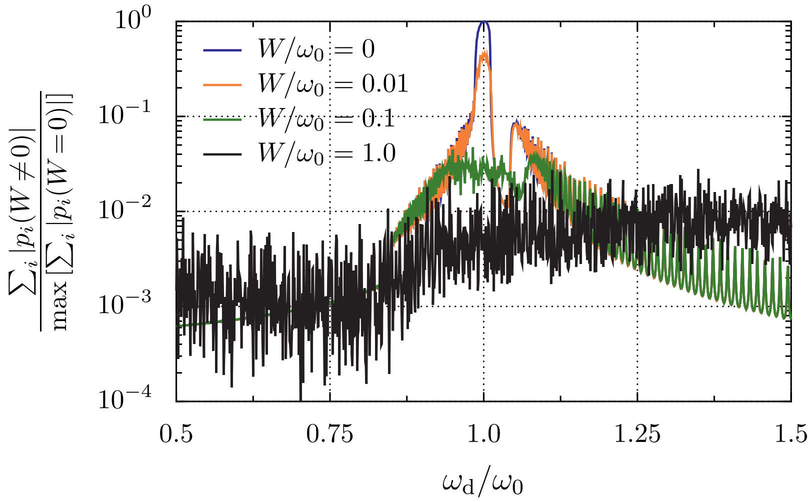

Figure 3.22: Disordered absorption spectra in the strong-coupling regime. Absorption spectrum for different disorder strengths W, normalized by the maximum of the one obtained without disorder. The results are shown for a chain of $\mathcal{N} = 500$ dipoles, with a cavity height $L_x/a = 12$, dipole losses $\gamma/\omega_0 = 0.001$, and have been averaged over 100 disorder realizations.

the LP branch by a gap. The fast oscillations are peaks corresponding to the different eigenfrequencies of the system, visible one by one due to the steep slope in the dispersion in these frequency regions. We can hence precisely recover the eigenmodes from this driven-dissipative scenario. However, the absorption spectrum of Fig. 3.21 does not reflect the transport properties along the whole chain, the sum over the amplitudes $|p_i|$ being obviously dominated by the first few terms. It then provides information mostly about the short-range propagation. This explains why the absorption is maximal for the dark eigenstates, and decreases when the driving frequency rises to more photonic eigenstates. Indeed, as discussed in the previous subsections, the dark states present the most efficient transport at short distances.

By increasing the dipole losses, from the solid to the dotted lines, the central peak is drastically reduced and the full width at half maximum is increased, as expected. The polaritons at the bottom of the LP and UP branches are less distinct from the dark states of the central peak, the latter being the most affected by dipole losses. Crucially, however, the two bands are still distinguishable and separated by a gap despite the larger dipole losses, indicating that the system is still in the strong-coupling regime.

The case of a disordered chain is shown in Fig. 3.22, where the sum of the amplitudes of the dipole moments along the chain for a given disorder strength, $\sum_{i=1}^{\mathcal{N}} |p_i(W \neq 0)|$, has been normalized by the maximum of the one found without disorder, $\max[\sum_{i=1}^{\mathcal{N}} |p_i(W = 0)|]$. We choose a cavity height $L_x/a = 12$ and we consider small dipole losses $\gamma/\omega_0 = 0.001$. By increasing the disorder strength from $W/\omega_0 = 0$ (blue line) to $W/\omega_0 = 0.01$ (orange line), and to $W/\omega_0 = 0.1$ (green line), the absorption is more and more suppressed for the driving frequencies corresponding to dark states, in a growing frequency window around $\omega_\mathrm{d}/\omega_0 = 1.0$. This is in agreement with what we observe in Sec. 3.4, namely that the effective dark state band grows with the disorder strength W around ω_0, while the polaritons outside the dark state band, with $\omega_n^\mathrm{pol} \gtrsim \omega_0 + W/2$, are not affected by disorder. The polaritons hence profit from this cavity-protection effect due to their eigenfrequencies being far from ω_0.

With a disorder strength $W/\omega_0 = 1$ (black line in Fig. 3.22), the dark state band includes now frequencies up to $1.5\,\omega_0$. Due to the disorder-induced hybridization mechanism, eigenstates at frequencies around $1.5\,\omega_0$ have gone from almost purely photonic polaritons to semilocalized polaritonic states with a significant dipolar part. This leads their absorption to become larger than the one without disorder, the dipolar part allowing them to be more easily excited and to acquire a better short-range propagation mediated by the quasistatic dipole-dipole coupling. Interestingly, we thus observe here a disorder-enhanced short-range transport, from almost fully photonic modes acquiring a dipolar part from the increased disorder strength, and inheriting efficient short-range dipolar transport.

3.7 Conclusions to Chapter 3

In this chapter, we took advantage of the model developed in Chap. 2 of dipolar emitters coupled to an optical cavity through a multimode light-matter coupling Hamiltonian to study a system of disordered polaritons. Importantly, this model goes beyond the typical single-mode coupling widely used in quantum optics, and also takes into account the all-to-all $1/r^3$ quasistatic dipole-dipole coupling.

In particular, we provided a study of the interplay between light-matter coupling, dipolar coupling, and disorder, through the analysis of both the localization properties and the transport along a chain of disordered dipoles strongly coupled to cavity photons. Crucially, losses in both the dipoles and the mirrors are taken into account. The disorder was considered on the individual resonance frequencies ω_i of the dipoles.

In our multimode model, all the eigenstates are hybridized by the strong light-matter coupling. However, we can distinguish the *dark states*, with eigenfrequencies around the average bare dipole resonance frequency ω_0 and almost zero photonic weight, and the *polaritons*, which have an eigenfrequency highly renormalized by the coupling and a significant photonic weight. We showed that at weak and medium disorder strengths, dark states suffer from Anderson localization, becoming exponentially localized on a few sites of the chain. On the other hand, the polaritons are more robust against frequency disorder, and show a cavity-protection effect [155, 157]. Notably, the only states impacted by disorder are the ones located in the same frequency window as the possible disordered individual dipole frequencies

ω_i, namely around $\omega_0 \pm W/2$. Increasing the disorder strength leads this frequency window to act as an effective dark state band, whose bandwidth increases at a rate $W/2$.

At large disorder strength, we have shown that the states located both in this dark state band and with an eigenfrequency larger than the lowest bare photonic mode $\omega^{\mathrm{ph}}_{q=0}$ are subject to a disorder-induced hybridization with photons, allowing new coupling between matter and photonic degrees of freedom. Indeed, the photonic part of these states increases linearly with the disorder strength and such states become semilocalized [87], i.e., localized in multiple nonadjacent sites. The eigenfrequencies smaller than $\omega^{\mathrm{ph}}_{q=0}$, on the other hand, cannot be hybridized through disorder, and suffer from the usual Anderson exponential localization.

By studying the transport of an excitation along the chain in a driven-dissipative scenario, we have shown that the strong light-matter coupling regime leads to a second exponential decay in the propagation, following a first one which is solely due to nearest-neighbor quasistatic dipole-dipole interactions. The larger the photonic part of the driven state is, the poorer the short-range propagation is, but the more flat this second exponential regime is. At large frequency disorder, the dark states, which have become polaritons through the above-mentioned mechanism of disorder-induced hybridization, inherit polaritonic transport properties, namely a poor short-range transport but an efficient long-range one. Moreover, we have found that this disorder-enhanced transport is not efficient over too long distances, or at least requires very large disorder strength. Indeed, the amount of disorder required to enter into such a regime increases linearly with the system size.

Crucially, we have shown that increasing the dipole losses impacts essentially the short-range transport, mediated by the quasistatic dipole-dipole coupling, which consequently increases the dominance of the polaritons at longer range. In this way, we have found that by considering highly lossy dipoles, a large frequency disorder can increase the long-range transport up to a factor 10^4 as compared to the case without disorder, see, e.g., around the site $i = 400$ in Fig. 3.17(b).

In terms of the power radiated by the dipoles, this phenomenon results in a remarkable increase of up to 8 orders of magnitude [see Eq. (3.23)]. Such a considerable enhancement of long-range transport could be useful particularly in the context of plasmonic nanoparticle chains, where experiments have witnessed limited transport distances [168–174], notably due to large Ohmic losses. Indeed, when considering plasmonic nanoparticles, the dimensionless dipole strength $k_0a = 0.1$ used throughout this work corresponds to nanoparticles with, e.g., radius $a = 7.6\,\mathrm{nm}$ and average resonance frequencies $\omega_0 = 2.6\,\mathrm{eV}/\hbar$. Considering a driving field intensity $I_0 = 1\,\mathrm{MW/cm^2}$, corresponding to, e.g., a laser of power $\mathcal{P}_0 = 7.1\,\mathrm{mW}$ focused on a spot of size $\pi\lambda_0^2 \simeq 0.71\,\mu\mathrm{m}^2$, the power radiated in the far field by a plasmonic nanoparticle with decay rate $\gamma/\omega_0 = 0.02$ around the site $i = 400$

[see Fig. 3.17(b)] can then be increased from $\mathcal{P}_{400}(W/\omega_0 = 0) \simeq 10^{-24}\,\mathrm{W}$ to $\mathcal{P}_{400}(W/\omega_0 = 1) \simeq 10^{-16}\,\mathrm{W}$. While the ordered case leads to a very small power which is clearly experimentally unreachable, a setup with sub-femtowatt sensitivity should detect the radiated power at the end of a highly disordered plasmonic chain.

Since the publication of our study [17], several experimental groups have witnessed some of the phenomena we discussed in our model. In particular, in Ref. [162], briefly introduced at the beginning of this chapter, the authors clearly witnessed disorder-enhanced transport in an ensemble of cold atoms strongly-coupled to an optical resonator. This observation is depicted in their Fig. 2(g)-(j), which shows similar results as our Fig. 3.20. Moreover, Fig. 2(l) of the same Ref. [162], which demonstrates the disorder-induced hybridization of dark states by showing the increase of photonic weight of semilocalized states as a function of disorder, presents a striking resemblance to our Fig. 3.8(a), in which we show the same quantity. A similar phenomenon of disorder-induced hybridization of dark states into polaritons has also been unveiled in the context of vibrational strong coupling within a disordered molecular ensemble [167].

Our model, which allowed to study the highly nontrivial interplay between disorder and light-matter coupling, opens the way to explore more complex systems which could be of larger dimensionality, operate in a stronger coupling regime, or feature topological properties. In particular, this last option is of great interest given its relevance to the growing field of topological photonics [14]. Indeed, combining disorder-robust topological edge states with photon-mediated couplings is a key challenge in this domain. In this regard, in the upcoming Chap. 4 we move into the realm of such topological physics and employ our model to study the fate of a topological system once strongly-coupled to a multimode cavity.

APPENDICES TO CHAPTER 3

3.A Effects of cavity losses

In the main text of this chapter, we fixed the cavity loss rate to $\kappa/\omega_0 = 10^{-3}$. In this appendix, we motivate this choice by comparing in Fig. 3.23 the propagation characteristics of an ordered chain for different values of cavity loss, from $\kappa/\omega_0 = 10^{-6}$ to $\kappa/\omega_0 = 10^{-1}$. The amplitude of the steady-state dipole moment $|p_i|$ in units of the reduced Rabi frequency $\Omega_{\mathrm{R}}/\omega_0$ is shown as a function of the dipole sites i along the chain. Two driving frequencies $\omega_{\mathrm{d}}/\omega_0 = 1.0$ and $\omega_{\mathrm{d}}/\omega_0 = 0.9$ are shown in Figs. 3.23(a) and 3.23(b), respectively. The dipole losses are fixed to $\gamma/\omega_0 = 0.001$, while the cavity height is chosen as $L_x/a = 12$.

In both panels, the qualitative behavior is substantially the same for cavity losses $\kappa/\omega_0 = 10^{-6}$ (purple lines) and $\kappa/\omega_0 = 10^{-3}$ (pink lines), justifying the choice made in the previous analysis. We observe that considering larger cavity losses $\kappa/\omega_0 = 10^{-2}$ (red lines) does not qualitatively change the results when driving a dark state in panel (a), showing the robustness of dark state propagation against cavity losses. As expected, however, the propagation of the mainly photonic polariton shown in Fig. 3.23(b) is more affected by the increase of cavity losses. Crucially, by increasing further the cavity loss rate to $\kappa/\omega_0 = 10^{-1}$ (yellow lines), the second exponential regime, that is, the cavity-enhanced transport, completely disappears in Fig. 3.23(a), showing that the system is not anymore in the strong-coupling regime. The dark state propagation is then very well described by the exponential regime mediated solely by the nearest-neighbor quasistatic dipole-dipole coupling, given by the analytical result of Eq. (3.30) and shown as a dashed grey line.

In the case of the mainly photonic polariton in Fig. 3.23(b), we observe similar results, namely that the long-range transport starts to become suppressed for cavity losses $\kappa/\omega_0 = 10^{-1}$. This transition from the strong- to the weak-coupling regime is expected, since the latter large cavity loss rate is of the order of the Rabi splitting frequency, $\Omega_{\mathrm{RS}} \simeq 0.12$. We note that similar conclusions can be drawn when the dipole losses are fixed to a larger value.

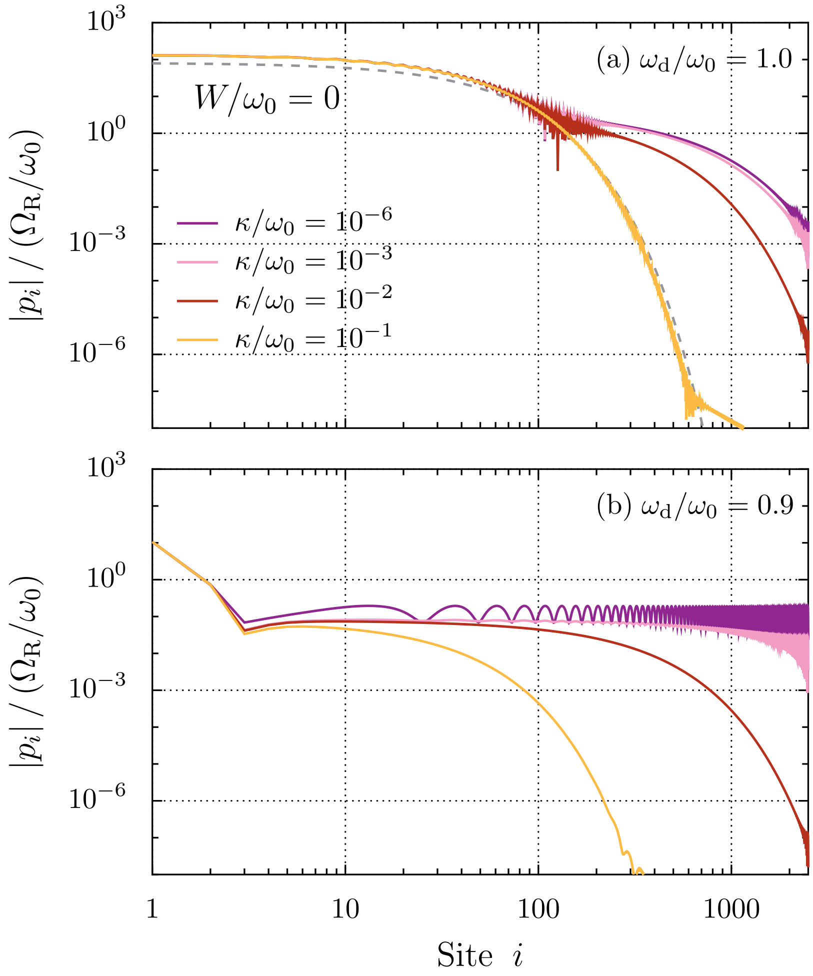

Figure 3.23: Effect of cavity losses. Steady-state amplitude of the dipole moment $|p_i|$ as a function of the dipole sites i for different values of the cavity loss parameter κ, in the case of an ordered chain. Panels (a) and (b) correspond to the driving, respectively, of a dark state with $\omega_d/\omega_0 = 1.0$ and of a mainly photonic polariton with $\omega_d/\omega_0 = 0.9$. The grey dashed line in panel (a) represents the exponential decay of Eq. (3.30). The dipole losses $\gamma/\omega_0 = 0.001$, and the cavity height $L_x/a = 12$.

Finally, we recall that the cavity quality factor $\mathcal{Q}$ is typically of the order of the inverse of the cavity loss rate in units of the average dipole frequency, ω_0/κ. This implies that the effects discussed in this work should be observed with cavity quality factors as low as $\mathcal{Q} \sim 10^2$.

3.B Beyond the rotating wave approximation

While in all our analysis we used the RWA, presented in Sec. 2.3.4, in this appendix we provide justifications for such an approximation. To this end, we consider the effects of counter-rotating terms in both the eigenvalues and transport properties of an ordered chain.

Considering the counter-rotating terms, the polaritonic Hamiltonian (3.6) that we employed until now in this chapter transforms into

$$\begin{aligned} H_{\text{pol}}^{\square,\text{CR}} &= H_{\text{dp}} + \sum_{n_z=1}^{\mathcal{N}} \hbar\omega_{n_z}^{\text{ph}} c_{n_z}^{\dagger} c_{n_z} \\ &\quad + \mathrm{i}\hbar \sum_{i=1}^{\mathcal{N}} \sum_{n_z=1}^{\mathcal{N}} \tilde{\xi}_{in_z} \left(b_i^{\dagger} - b_i\right) \left(c_{n_z}^{\dagger} + c_{n_z}\right), \end{aligned} \tag{3.31}$$

where the dipolar Hamiltonian with counter-rotating terms is given in Eq. (2.22).

In the limit of an ordered chain, similarly to what has been done in Sec. 3.3, one can rewrite the Hamiltonian (3.31) in Fourier space using periodic boundary conditions and diagonalize it using a Hopfield-Bogoliubov transformation. The diagonalization leads to the polaritonic dispersion

$$w_{q\tau}^{\text{pol}} = \sqrt{\Gamma_q^2 + \tau\sqrt{\Gamma_q^4 - (w_q^{\text{dp}})^2 \left[(\omega_q^{\text{ph}})^2 - 4\frac{\tilde{\xi}_q^2}{\omega_0}\omega_q^{\text{ph}}\right]}}, \tag{3.32}$$

where we have introduced the quantity

$$\Gamma_q^2 = \frac{1}{2}\left[\left(\omega_q^{\text{ph}}\right)^2 + \left(w_q^{\text{dp}}\right)^2\right], \tag{3.33}$$

with the bare photonic dispersion given in Eq. (2.34), and where

$$w_q^{\text{dp}} = \omega_0\sqrt{1 + 2f_q\frac{\Omega}{\omega_0}} \tag{3.34}$$

is the dispersion of the dipolar Hamiltonian with counter-rotating terms (2.22). Details on this diagonalization procedure can be found in the supplementary material of Ref. [179], with the only difference that here we neglect the diamagnetic A^2-term (2.16) in the light-matter Hamiltonian.

In Fig. 3.24, we show a comparison between the polaritonic dispersions obtained with (orange line) and without (green line) the RWA, given respectively by Eqs. (3.14) and (3.32). We observe that the two band structures overlap almost perfectly, with very slight differences noticeable only around the center of the Brillouin zone, where the light-matter coupling is maximal. This is in agreement with the fact that our model does not allow the ultra-strong coupling (USC) regime to be reached, since one enters into the latter regime once the effects of the counter-rotating terms become sizable [149], which is clearly not the case here. Fig. 3.24 also justifies a posteriori the neglection of the diamagnetic A^2-term (2.16) in the light-matter coupling Hamiltonian. Indeed, as a matter of fact, perceptible differences in the eigenspectrum caused by the absence of such a diamagnetic term were found in the context of the

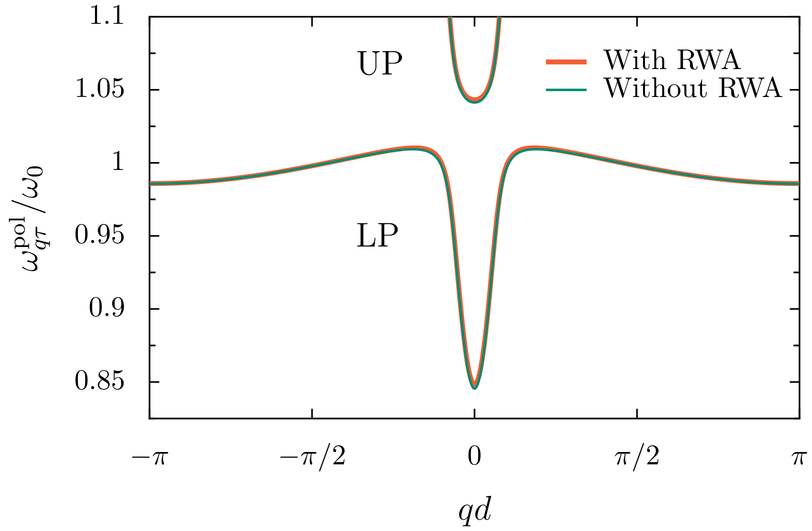

Figure 3.24: Polaritonic dispersion beyond the RWA. Polaritonic band structure of an ordered chain in the thermodynamic limit, in units of the bare frequency ω_0, and as a function of the reduced wavenumber qd in the first Brillouin zone. In orange, we show the dispersion used in Sec. 3.3, which is obtained using the RWA and given by Eq. (3.14), and we compare it to the one obtained without using the approximation, given by Eq. (3.32) and shown in green. The considered cavity height is $L_x/a = 12$.

ultra-strong or deep-strong coupling regime only [151].

However, in the case of driven-dissipative transport computations, special attention has to be taken when using the RWA. Indeed, it has been shown [202–206] that using the RWA along with a Lindblad master equation may lead to inaccurate dynamics, especially when dropping the counter-rotating terms directly in the Hamiltonian, as we have done in Sec. 3.6. In Fig. 3.25, we thus compare our transport results obtained with (orange lines) and without (green lines) neglecting the counter-rotating terms in the Hamiltonian entering in the Lindblad master equation (3.22). We show on a log-log scale the amplitude of the steady-state dipole moment $|p_i|$ in units of the reduced Rabi frequency $\Omega_{\mathrm{R}}/\omega_0$, as a function of the dipole site i along the chain, when driving a dark state with $\omega_{\mathrm{d}}/\omega_0 = 1.0$ (solid lines), and a mainly photonic polariton with $\omega_{\mathrm{d}}/\omega_0 = 0.9$ (dotted lines). As can be seen from Fig. 3.25, the propagation is qualitatively the same with and without the RWA. The small differences arise essentially from the very slight frequency shift visible in Fig. 3.24, implying the fact that using a given driving frequency ω_{d} does not drive an eigenstate with exactly the same photonic weight in the case of employing or not the RWA in the computation.

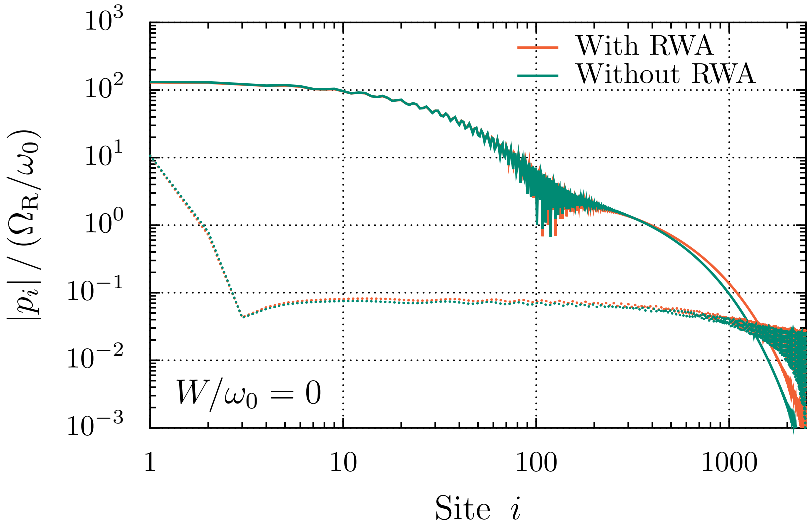

Figure 3.25: Transport simulation beyond the RWA. Steady-state amplitude of the dipole moment $|p_i|$ in units of the reduced Rabi frequency $\Omega_\mathrm{R}/\omega_0$ along the sites i of an ordered chain. The results are shown with (orange) and without (green) the RWA. Two different driving frequencies are considered: $\omega_\mathrm{d}/\omega_0 = 1.0$, which drives a dark state is shown as solid lines, and $\omega_\mathrm{d}/\omega_0 = 0.9$, which drives a polariton with a large photonic part is shown as dotted lines. The cavity height $L_x/a = 12$, and the dipole and mirror losses are respectively fixed to $\gamma/\omega_0 = 0.001$ and $\kappa/\omega_0 = 0.001$.

CHAPTER 4

TOPOLOGY AND POLARITONS

In this chapter, a dimerized chain of dipolar emitters strongly coupled to a multimode optical waveguide is studied.

Such a system mimicks a variation with an effective photon-mediated coupling of the paradigmatic Su-Schrieffer-Heeger (SSH) model, which features a nontrivial topological phase and hosts topological edge states. After summarizing some of the main properties of the SSH model, we discuss the effects of the light-matter coupling, both on the topological phases and on the edge states. In the strong-coupling regime, we observe the hybridization of the dipolar topological edge states with cavity photons, leading to what we coin polaritonic edge states. Although these states are not fully localized on the edges, they present unusual properties, such as efficient edge-to-edge transport characteristics, the occupancy of a large portion of the frequency spectrum, and a strong tolerance to structural disorder.

The results in the present chapter are mostly part of the published article T.F. Allard, G. Weick, *Multiple polaritonic edge states in a Su-Schrieffer-Heeger chain strongly coupled to a multimode cavity*, Physical Review B **108**, 245417 (2023) [18]

In addition to their fundamental interest, topological phases of matter have aroused in recent years a lot of attention for their ability to host edge states that are robust against perturbations [36, 37]. The appeal for these robust edge states, together with the progress in engineering light-matter interaction in many experimental platforms, have led to a growing interest in topological phenomena in photonic systems [13–15]. A newly developing field is now the combination of topological photonics with the physics of strong light-matter coupling, in which polaritonic excitations have shown attractive properties [16].

The underlying effect of the strong light-matter interaction is an effective long-distance coupling mediated by cavity photons. Recent experimental findings have highlighted its significance in topological phenomena, particularly in the behavior of topological edge states [207]. Moreover, an active literature has recently been devoted to extensions of one-dimensional topological models, such as the renowned Su-Schrieffer-Heeger (SSH) model [61], by incorporating additional couplings [124, 128, 136, 208–225].

In this chapter, we go one step further by addressing the influence of strong coupling between a multimode optical waveguide to a bipartite chain of emitters. As in Chap. 3, we treat the emitters as ideal, classical dipoles, and the coupling, derived in Chap. 2, is multimodal, dispersive and spatially-dependent. Notably, we recall that the consideration of multiple photonic modes has proven to be essential to correctly model cavity-induced effects [17, 92, 94, 163–165], and it is here a key ingredient of our model. While a preliminary investigation of the polaritonic SSH model has been carried out in Ref. [136], highlighting the impact of the optical cavity on the topological phases of the system, here, we focus on the fate of the edge states exhibited by the system. To do so, we refine the model derived in Ref. [136] in order to avoid any boundary effects that could influence the edge states. From the hybridization of the dipolar and cavity photon excitations into polaritons, we observe in the strong light-matter coupling regime the formal loss of the in-gap edge states that are present in the topological phase of the original SSH model, with their merging into the polaritonic bulk. Although this may at first appear detrimental to the topological properties of the system, here we demonstrate that, interestingly, bulk polaritons in resonance with the formally lost edge states inherit a large edge localization, so that we coin these new, cavity-induced states "polaritonic edge states".

Originating from the diffusion of edge localization onto numerous bulk polaritons, we demonstrate that these exotic edge states present properties that are of particular interest. Specifically, dissipative transport simulations allow us to unveil exceptional polaritonic edge state transport, as well as a wide frequency range at which the latter states can be driven. Additionally, the consideration of a disordered bipartite chain allows us to uncover the remarkable tolerance of the polaritonic edge states to off-diagonal disorder.

The chapter is organized as follows. We start in Sec. 4.1 by introducing our model to describe a dimerized chain of emitters, which, when considering nearest neighbor dipolar coupling only, mimicks a dipolar counterpart to the SSH model of polyacetylene [61]. We summarize the properties of such a paradigmatic model and then discuss the addition of all-to-all quasistatic couplings between the emitters. We describe in Sec. 4.2 the strong coupling of such a chain to a multimode waveguide cavity, and derive what we call the polaritonic SSH Hamiltonian. From such a model, we then derive an effective bipartite Hamiltonian taking into account the photon-mediated effective coupling between the emitters.

Our study of the polaritonic SSH model begins with the investigation of its bulk spectrum in Sec. 4.3, first using the full Hamiltonian, and then the previously derived effective bipartite Hamiltonian. We take advantage of the latter effective Hamiltonian to explore the topological phases of the polaritonic SSH model in Sec. 4.4, and to study the unusual multiple polaritonic edge states that are present in its finite spectrum in Sec. 4.5. Then, in Secs. 4.6 and 4.7 we study, respectively, the transport properties and the robustness to disorder of such polaritonic edge states. Finally, in Sec. 4.8 we discuss the influence of the boundary conditions of the cavity, and we summarize our results and discuss further perspectives of our work in Sec. 4.9. Appendices 4.A, 4.B, and 4.C complement the discussion by veryfing the validity of, respectively, the single cavity band approximation, the use of the effective Hamiltonian, and the neglection of image dipoles.

4.1 Dimerized chain of dipoles and the SSH model

We begin our study by generalizing the model of $\mathcal{M}$ generic coupled dipolar emitters presented in Sec. 2.2 to a bipartite array with 2 dipoles per unit cell. Except in Sec. 4.7 where we will introduce disorder, we consider in this chapter identical dipoles, all with the same bare resonance frequency ω_0, and arranged in an ordered bipartite array, with a lattice constant d. As in the previous chapters, the chain is arranged in the z direction, and the dipoles polarized transversely along the x direction.

A sketch of such a dimerized chain of emitters is provided in Fig. 4.1. $\mathcal{N}$ unit cells, each containing 2 dipole sites which we label as A and B, are considered, so that the lattice is comprised of $\mathcal{M} = 2\mathcal{N}$ dipoles.[1] We denote the intra-cell distance between dipoles as d_1, and the inter-cell one as d_2.

4.1.1 A bosonic counterpart to the SSH model

To model the chain of dipoles sketched in Fig. 4.1, we repeat the procedure detailed in Sec. 2.2, but now differentiate between dipoles belonging to the sublattices A and B.

---

[1] We consider a lattice with an even number of sites.

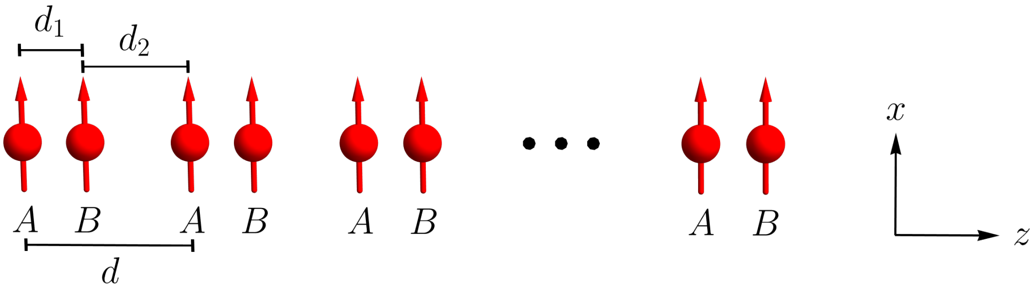

Figure 4.1: Dimerized chain of emitters. Sketch of a dimerized chain of $\mathcal{M} = 2\mathcal{N}$ dipolar emitters, all polarized along the same x direction, and arranged along the z direction. The dipoles, each with bare resonance frequency ω_0, belong either to the A or B sublattice and are separated by the alternating distances d_1 and d_2, so that the lattice constant $d = d_1 + d_2$.

We first consider nearest neighbor coupling only, so that there is no coupling between dipoles belonging to the same sublattice. The corresponding nearest neighbor dipolar Hamiltonian reads

$$\begin{aligned} \mathrm{H}^{\mathrm{RWA}}_{\mathrm{dp,n.n.}} = &\hbar\omega_0 \sum_{m=1}^{\mathcal{N}} \left(a^\dagger_m a_m + b^\dagger_m b_m \right) + \hbar\Omega_1 \sum_{m=1}^{\mathcal{N}} \left(a^\dagger_m b_m + a_m b^\dagger_m \right) \\ &+ \hbar\Omega_2 \sum_{m=1}^{\mathcal{N}-1} \left(a^\dagger_{m+1} b_m + a_{m+1} b^\dagger_m \right), \end{aligned} \tag{4.1}$$

where we have neglected counter-rotating terms, as justified in Sec. 2.3.4. In the expression above, the bosonic operators $a^\dagger_m$ ($b^\dagger_m$) and a_m (b_m) create and annihilate, respectively, a dipolar excitation in the cell $m \in [1, \mathcal{N}]$ and sublattice A (B), polarized along the x axis and with resonance frequency ω_0. Due to the dimerized nature of the chain, two distinct nearest neighbor dipolar coupling strengths are present and read

$$\Omega_{1,2} = \frac{\omega_0}{2} \left(\frac{a}{d_{1,2}} \right)^3, \tag{4.2}$$

with the intra- and inter-cell dipole-dipole distances d_1 and d_2 defined in Fig. 4.1. The difference between the latter distances encodes the dimerization of the chain, and is quantified by the dimerization parameter

$$\epsilon = \frac{d_1 - d_2}{d}. \tag{4.3}$$

The Hamiltonian (4.1), which was first introduced in Ref. [226], represents a bosonic counterpart to the SSH model of polyacetylene [61]. The latter tight-binding model, devised in 1979 to describe the electrical conductivity of polyacetylene polymers,[2] is known as an emblematic model featuring topological physics in one dimension, and behaves similarly to a topological insulator.[3] It describes a single spinless electron hopping in a 1D staggered lattice.

Tuning the nearest neighbor couplings (4.2), which are equivalent to the hopping energies of a spinless electron between neighboring sites in the SSH model, allows us to tune the dimerization (4.3). A dimerization $\epsilon > 0$ ($\epsilon < 0$) then corresponds to nearest neighbor couplings $\Omega_1 < \Omega_2$ ($\Omega_1 > \Omega_2$), which are associated with a nontrivial (trivial) topological invariant. The only difference of the Hamiltonian (4.1) with the original SSH model, except the bosonic nature of its excitations,[4] is the addition of an on-site energy term through the bare frequency ω_0 of the dipoles, which just implies an overall shift of the eigenfrequencies.

To diagonalize the Hamiltonian (4.1), we consider the thermodynamic limit $\mathcal{N} \gg 1$, so that translation invariance allows one to use periodic boundary conditions and move into wavevector space through the Fourier transforms

$$a_m = \frac{1}{\sqrt{\mathcal{N}}} \sum_q \mathrm{e}^{\mathrm{i}mqd} a_q \tag{4.4a}$$

and

$$b_m = \frac{1}{\sqrt{\mathcal{N}}} \sum_q \mathrm{e}^{\mathrm{i}mqd} b_q. \tag{4.4b}$$

In the above expression, the bosonic ladder operators $a_q^\dagger$ ($b_q^\dagger$) and a_q (b_q) create and annihilate, respectively, a dipolar excitation with resonance frequency ω_0 polarized along the x axis on the A (B) sublattice. Their associated longitudinal quasimomentum is $q = 2\pi p/\mathcal{N}d \in [-\pi/d, +\pi/d]$, in the Brillouin zone, with $p \in [-\mathcal{N}/2, +\mathcal{N}/2]$, exactly as for the unipartite chain in Chap. 3.

We note that the above Fourier transforms act on the cell index only, and do not take into account the difference in real space position of the A and B sites. This will allow the momentum-space Hamiltonian and its associated eigenstates to be periodic in the Brillouin zone, however, both of them depend on the choice of unit cell. Other conventions, which involve the precise positions of the A and B sites within the unit cell, have no such ambiguity but lose their periodicity in the Brillouin zone [35, 227].

---

[2] We note that a somewhat similar, but different by its symmetries [227], one dimensional toy model featuring topological properties was already explored in 1939 by Shockley [228].

[3] Strictly-speaking, the SSH model is not a typical topological insulator, as its topological properties may be ill-defined at the thermodynamic limit [227]. However, it does model a simple one dimensional system featuring symmetry-protected edge states.

[4] However, for the single-particle, spinless systems in study here, the quantum statistics of the excitations are inconsequential.

One can then rewrite the Hamiltonian (4.1) in its two band Bloch form,

$$\mathrm{H}^{\mathrm{RWA}}_{\mathrm{dp,n.n.}} = \sum_q \psi_q^{\mathrm{n.n.}\dagger} \mathcal{H}_q^{\mathrm{dp,n.n.}} \ \psi_q^{\mathrm{n.n.}} \ , \tag{4.5}$$

where the index $\tau = +\ (-)$ corresponds to the upper (lower) dipolar band, with the eigenspinors $\psi_q^{\mathrm{n.n.}} = (a_q, b_q)$, and where the $2\pi/d$ periodic Bloch Hamiltonian

$$\mathcal{H}_q^{\mathrm{dp,n.n.}} = \hbar \begin{pmatrix} \omega_0 & \Omega_1 + \mathrm{e}^{-\mathrm{i}qd}\Omega_2 \\ \Omega_1 + \mathrm{e}^{\mathrm{i}qd}\Omega_2 & \omega_0 \end{pmatrix}. \tag{4.6}$$

Using a bosonic Bogoliubov transformation, one can diagonalize the above Bloch Hamiltonian, and finds the dispersion relation

$$\omega_{q\tau}^{\mathrm{dp,n.n.}} = \omega_0 + \tau|\Omega_1 + \mathrm{e}^{-\mathrm{i}qd}\Omega_2|, \tag{4.7}$$

and the Bloch eigenspinor

$$|\psi_{q\tau}^{\mathrm{n.n.}}\rangle = \frac{1}{\sqrt{2}} \begin{pmatrix} 1 \\ \tau\, \mathrm{e}^{\mathrm{i}\phi_q^{\mathrm{n.n.}}} \end{pmatrix}, \tag{4.8}$$

where the phase

$$\phi_q^{\mathrm{n.n.}} = \arg(\Omega_1 + \mathrm{e}^{-\mathrm{i}qd}\Omega_2). \tag{4.9}$$

Such a q-dependent phase factor that discriminates between the upper and lower components of the eigenspinors is typical of topologically nontrivial systems [34].

Exactly as the original SSH Hamiltonian, the Hamiltonian (4.6) presents the following symmetries.

- The (spinless) commuting anti-unitary time-reversal symmetry,

$$\mathcal{T}\mathcal{H}_q^{\mathrm{dp,n.n.}}\mathcal{T} = \mathcal{H}_{-q}^{\mathrm{dp,n.n.}*}, \qquad [\mathcal{T}, \mathcal{H}_q^{\mathrm{dp,n.n.}}] = 0, \qquad \mathcal{T}^2 = +1, \tag{4.10}$$

  which is fulfilled since the coupling constants $\Omega_{1,2}$ are real.

- The anti-commuting unitary chiral (or sublattice) symmetry

$$\mathcal{S} = \sigma_z, \qquad \{\mathcal{S}, \mathcal{H}_q^{\mathrm{dp,n.n.}}\} = 0, \qquad \mathcal{S}^2 = +1. \tag{4.11}$$

- The anti-commuting anti-unitary charge (or particle-hole) symmetry

$$\mathcal{C} = \mathcal{S}\mathcal{T}, \qquad \{\mathcal{C}, \mathcal{H}_q^{\mathrm{dp,n.n.}}\} = 0, \qquad \mathcal{C}^2 = +1. \tag{4.12}$$

- As well as the unitary inversion symmetry,

$$\sigma_x \mathcal{H}_{-q}^{\mathrm{dp,n.n.}} \sigma_x = \mathcal{H}_q^{\mathrm{dp,n.n.}}, \qquad {\sigma_x}^2 = +1, \tag{4.13}$$

with the inversion center being in the middle of a unit cell, and which is fulfilled since the emitters belonging to the A and B sublattices have the same onsite frequency ω_0.

In all of the above equations, we used the three Pauli matrices, that read

$$\sigma_x = \begin{pmatrix} 0 & 1 \\ 1 & 0 \end{pmatrix}, \qquad \sigma_y = \begin{pmatrix} 0 & -i \\ i & 0 \end{pmatrix} \quad \text{and} \quad \sigma_z = \begin{pmatrix} 1 & 0 \\ 0 & -1 \end{pmatrix}. \tag{4.14}$$

In regards with the Altland-Zirnbauer table of topological insulators [46], which we briefly introduced in Chap. 1 (see Tab. 1.1), the SSH model can thus be either in the AIII or BDI Altland-Zirnbauer class with a nontrivial topological invariant in 1d, depending on which symmetry of the model we enforce (the D class in 1d, on the other hand, represents the Kitaev chain). In particular, from the particle-hole symmetry, or, similarly, from the inversion symmetry, the SSH model presents a $\mathbb{Z}_2$ topological invariant,[5] the Zak phase, which can be readily computed as [226]

$$\begin{aligned} \vartheta^{\text{Zak}} &= \mathrm{i} \int_{-\pi/d}^{+\pi/d} \mathrm{d}q \, \langle \psi_{q\tau}^{\text{n.n}} | \partial_q \psi_{q\tau}^{\text{n.n}} \rangle \\ &= \begin{cases} 0, & \Omega_1 > \Omega_2 \quad (\epsilon < 0) \\ \pi, & \Omega_1 < \Omega_2 \quad (\epsilon > 0) \end{cases}, \end{aligned} \tag{4.15}$$

and which is defined modulo 2π. Note that we do not display in Eq. 4.15 the band index τ of the Zak phase as the result is band independent. To be more specific, we note that, in contrast to the terminology used in most of the literature, Eq. (4.63) does not formally represent a Zak phase but rather π times a winding number defined with respect to a specific choice of unit cell, as discussed in detail in Ref. [227]. For simplicity, here we stay consistent with most of the literature, and use such a strictly speaking wrong denomination.

Therefore, as expected, the dipolar SSH model (4.1) presents the same bulk properties as the ones of the original SSH model, and features a topological phase transition (TPT) at $\epsilon = 0$ ($\Omega_1 = \Omega_2$), with a gap closing at the edges of the Brillouin zone $q = \pm\pi/d$ [see the bandstructure (4.7)]. From the bulk-edge-correspondence, a mathematically proven theorem for Hamiltonians belonging to Altland-Zirnbauer classes of the tenfold way [229], one then expects from the nontrivial invariants (4.15) associated with both upper and lower bands the presence of two degenerate topological edge states in the spectrum of a finite chain, which are pinned at the gap closing frequency ω_0. These edge states will be there as long as one remains in the symmetry class allowing the presence of the nontrivial topological invariant. Hence, they are protected against any perturbation, such as disorder, that does not modify

---

[5] Note that from the $\mathcal{S}$ symmetry, one can also define a $\mathbb{Z}$ topological invariant, the winding number ν, which we will encounter in Sec. 4.4.2. In the SSH model, both are equivalent, as values of the winding number larger than 1 require chiral-preserving coupling beyond nearest neighbor.

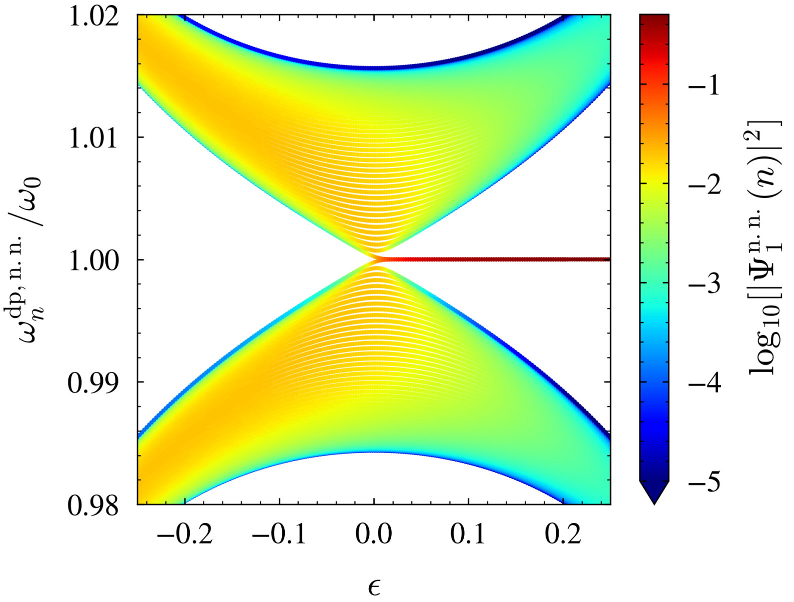

Figure 4.2: Finite eigenspectrum of the SSH model. Eigenfrequencies $\omega_n^{\mathrm{dp,n.n.}}$ of the dipolar SSH Hamiltonian with nearest neighbor coupling only [see Eq. (4.1)], in units of ω_0 and in ascending order, as a function of the dimerization parameter ϵ. As a color code, we show the logarithm of the probability density on the first site $i = 1$ of the chain associated with each eigenstate n, so that eigenstates highly localized on the edges appear as red. The chain is comprised of $\mathcal{N} = 50$ dimers, i.e., 100 dipoles, and, as in the remaining of this chapter, the lattice constant is fixed to $d = 8a$.

the Hamiltonian symmetry class. For instance, off-diagonal positional disorder on the interdipoles distances, which respects the chiral symmetry, does not destroy the topological edge states of the SSH model.

To verify such statements, we compute the finite eigenspectrum of the real-space Hamiltonian (4.1) using an exact numerical diagonalization procedure. The result is shown in Fig. 4.2 as a function of the dimerization parameter ϵ, and for a dimerized chain comprising $\mathcal{N} = 50$ dimers. In the figure, and as in the remaining of this chapter, we fix the lattice constant value to $d = 8a$. To highlight the presence or absence of edge states, we show in addition as a color code the logarithm of the probability density on the first site on the chain associated with each eigenstate n. We readily observe from Fig. 4.2 the mirror symmetry of the spectrum around the frequency ω_0. Such a symmetric eigenspectrum is implied by the chiral symmetry as well as by the particle-hole one. Moreover, we observe the closing of the bandgap when the dimerization $\epsilon = 0$, and the presence of two degenerate midgap edge states with eigenfrequency ω_0 as long as $\epsilon > 0$, corroborating the above discussion on the bulk-edge correspondence.

We also present in Fig. 4.3(a)-(b) the shape of these two topological edge

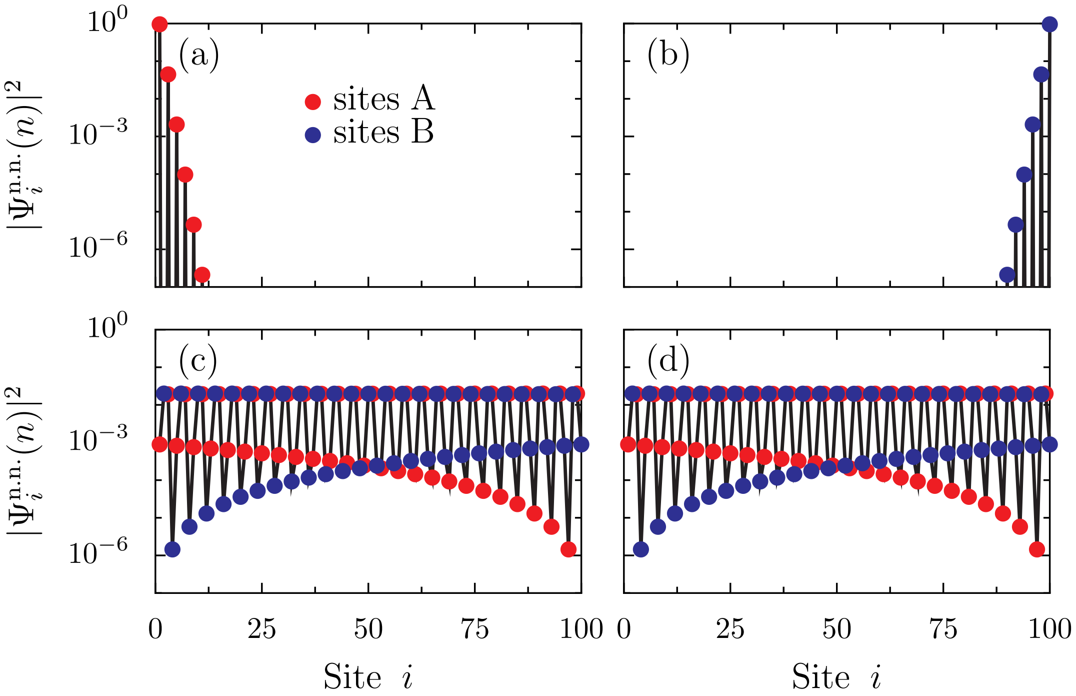

Figure 4.3: Eigenstates of the SSH model. Probability density $|\Psi_i^{\text{n.n.}}(n)|^2$ along the sites i of a chain with dimerization $\epsilon = 0.25$ and comprising $\mathcal{N} = 50$ dimers, for (a)-(b) the two degenerate topological midgap edge states, and (c)-(d) two standard delocalized bulk states. The red and blue dots represent, respectively, sites belonging to the A and B sublattices.

states, in the case of a dimerization $\epsilon = 0.25$, by plotting on a logarithmic scale their probability density $|\Psi_i^{\text{n.n.}}(n)|^2$ as a function of the dipole sites i along the chain. The red (blue) points correspond to sites belonging to the A (B) sublattice.

The two topological edge states are exponentially localized, with a localization length $\zeta = \ln(\Omega_1/\Omega_2)$. From the $\mathcal{S}$ symmetry of the model, they are located either on the A or B sublattice exclusively.[6] For comparison, we also present in Fig. 4.3(c)-(d) the shape of two standard bulk eigenstates, that are delocalized along the chain as plane waves.

4.1.2 All-to-all quasistatic coupling

While the dipolar Hamiltonian with nearest neighbor coupling only (4.1) is an interesting toy model allowing to recover all of the usual topological properties of the SSH model, it does not take into account the all-to-all quasistatic Coulomb interaction (2.10), which is essential for our modelling of coupled dipolar emitters.

---

[6] We note that for large enough $\mathcal{N}$ the edge states are (numerically) degenerated, so that one can choose to represent them either on one edge each, or as a superposition and therefore both sharing the two edges of the chain.

Such an additional coupling modifies both the spectrum and the symmetries of the model. By considering it, the SSH Hamiltonian (4.1) becomes [210]

$$\begin{aligned}
\mathrm{H}_{\mathrm{dp}}^{\mathrm{RWA}} = \hbar\omega_0 &\sum_{m=1}^{\mathcal{N}} \left(a_m^\dagger a_m + b_m^\dagger b_m\right) \\
&+ \sum_{m=1}^{\mathcal{N}} \sum_{m'=m}^{\mathcal{N}} \frac{\hbar\Omega}{(m'-m+d_1/d)^3} \left(a_m^\dagger\, b_{m'} + a_m\, b_{m'}^\dagger\right) \\
&+ \sum_{m=1}^{\mathcal{N}-1} \sum_{m'=m+1}^{\mathcal{N}} \frac{\hbar\Omega}{(m'-m-d_1/d)^3} \left(b_m^\dagger\, a_{m'} + b_m\, a_{m'}^\dagger\right) \\
&+ \sum_{m=1}^{\mathcal{N}-1} \sum_{m'=m+1}^{\mathcal{N}} \frac{\hbar\Omega}{(m'-m)^3} \left(a_m^\dagger\, a_{m'} + b_m^\dagger\, b_{m'} + a_m\, a_{m'}^\dagger + b_m\, b_{m'}^\dagger\right),
\end{aligned} \tag{4.16}$$

with the dipolar coupling strength Ω being the same as already defined in Chap. 3 in Eq. (3.2), with the dipolar coupling strength Ω being the same as already defined in Chap. 3 in Eq. (3.2). The second and third lines of Eq. (4.16) account for the all-to-all coupling between different sublattices, while the fourth line couples emitters in the same sublattice. The above dipolar Hamiltonian can be reorganized in the more compact form

$$\begin{aligned}
\mathrm{H}_{\mathrm{dp}}^{\mathrm{RWA}} = \hbar\omega_0 &\sum_{m=1}^{\mathcal{N}} \left(a_m^\dagger a_m + b_m^\dagger b_m\right) + \hbar\Omega \sum_{m,m'=1}^{\mathcal{N}} g_{m-m'} \left(a_m^\dagger\, b_{m'} + a_m\, b_{m'}^\dagger\right) \\
&+ \frac{\hbar\Omega}{2} \sum_{\substack{m,m'=1 \\ (m\neq m')}}^{\mathcal{N}} f_{m-m'} \left(a_m^\dagger\, a_{m'} + b_m^\dagger\, b_{m'} + a_m\, a_{m'}^\dagger + b_m\, b_{m'}^\dagger\right),
\end{aligned} \tag{4.17}$$

where we defined the all-to-all intra- and inter-sublattice sums as, respectively,

$$f_{m-m'} = \frac{1}{|m-m'|^3} \tag{4.18a}$$

and

$$g_{m-m'} = \frac{1}{|m-m'-d_1/d|^3}. \tag{4.18b}$$

Using the same thermodynamic limit $\mathcal{N} \gg 1$ and Fourier transform (4.4) as in the previous subsection, one obtains the Bloch Hamiltonian

$$\mathcal{H}_q^{\mathrm{dp}} = \hbar \begin{pmatrix} \omega_0 + \Omega f_q & \Omega g_q \\ \Omega g_q^* & \omega_0 + \Omega f_q \end{pmatrix}, \tag{4.19}$$

where the reciprocal counterparts of the dipolar intra- and inter-sublattice sums (4.18) read

$$f_q = 2 \sum_{m=1}^{\infty} \frac{\cos(mqd)}{m^3} \tag{4.20a}$$

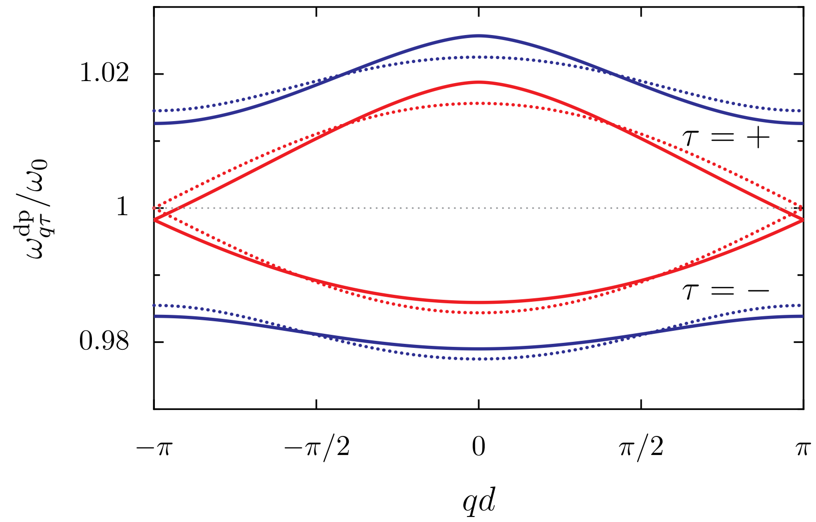

Figure 4.4: Bandstructure of the dipolar SSH model. Dipolar dispersion of the dimerized chain of dipoles, with (solid lines) and without (dotted lines) dipolar coupling beyond nearest neighbor. Both the cases of an open gap, with a dimerization $\epsilon = 0.25$ (blue lines) and of a closed gap, with a dimerization $\epsilon = 0$ (red lines) are shown.

and

$$g_q = \sum_{m=0}^{\infty}\left[\frac{\mathrm{e}^{\mathrm{i}mqd}}{(m+d_1/d)^3}+\frac{\mathrm{e}^{-\mathrm{i}(m+1)qd}}{(m+d_2/d)^3}\right], \tag{4.20b}$$

respectively. A bosonic Bogoliubov transformation then leads to the eigenfrequencies

$$\omega^{\mathrm{dp}}_{q\tau} = \omega_0 + \Omega f_q + \tau\,\Omega|g_q|, \tag{4.21}$$

and Bloch eigenspinors

$$|\psi_{q\tau}\rangle = \frac{1}{\sqrt{2}}\begin{pmatrix}1\\ \tau\,\mathrm{e}^{\mathrm{i}\phi_q}\end{pmatrix}, \tag{4.22}$$

where the phase

$$\phi_q = \arg(g_q). \tag{4.23}$$

We note that without the inter-sublattice sum g_q, we find the exact same relation as found in the case of an ordered unipartite chain as studied in Sec. 3.3 [cf. Eq. (3.11)]. This is consistent with the fact that without the $A-B$ and $B-A$ inter-sublattices interactions the dimerized chain corresponds only to a superposition of two isolated simple chains.

We display the two-band dispersion relation (4.21) in Fig. 4.4, in the first Brillouin zone and for dimerizations $\epsilon = 0$ (red solid lines) and $\epsilon = 0.25$ (blue solid lines). For comparison, we also show the bandstructure obtained in the nearest neighbor case [see Eq. (4.7), and Fig. 4.2 for the real-space counterpart] as dotted lines.

One first deduces from Fig. 4.4 that the addition of all-to-all dipole-dipole couplings yields only a slight renormalization of the eigenfrequencies, the solid and dotted lines being close in energy to each other. In both cases, using the language of condensed matter electronic systems, we observe the "metallic" phase when $\epsilon = 0$, as red lines, with a gap closing at the edges of the Brillouin zone, and the "insulating" phase, when $\epsilon \neq 0$, as blue lines, with an open gap between the upper and lower dipolar bands $\tau = \pm$. In Ref. [210], the authors analyzed the bulk properties of the Bloch Hamiltonian (4.19), and showed that the all-to-all quasistatic coupling does not interfere with the bulk topological features. Notably, around the edges of the Brillouin zone, one observes in the figure (half of) a massless Dirac cone when $\epsilon = 0$ (red lines), and (half of) a massive Dirac cone when $\epsilon \neq 0$ (blue lines). This stems from the fact that both the nearest neighbor and all-to-all dispersions Eqs. (4.7) and (4.21) are governed around $q = \pm\pi/d$ by a pseudorelativistic 1D Dirac-like spectrum [210, 226].

However, importantly, one notes from Fig. 4.4 the absence of mirror symmetry around the frequency ω_0 between the upper and lower dipolar bands when considering all-to-all coupling (solid lines), in contrast with the nearest neighbor case (dotted lines). Such an asymmetry between the two bands reveals the absence of particle-hole ($\mathcal{C}$) and chiral ($\mathcal{S}$) symmetries, these latter being broken by the intra-sublattice sum (4.20a), which results in q-dependent diagonal terms in the Bloch Hamiltonian (4.19). In regard to the Altland-Zirnbauer classification Tab. 1.1, the dipolar Hamiltonian with all-to-all quasistatic coupling (4.17) can therefore only belong to the classes A or AI, which are topologically trivial in 1D.

One can wonder how, then, could the authors of Ref. [210] compute a quantized topological invariant and observe a TPT at $\epsilon = 0$, in all respects similar to that of the original SSH model ?

First, the on-diagonal, chiral breaking term is small. Indeed, for a lattice constant $d = 8a$, the first next-to-nearest neighbor coupling is associated to a coupling strength $\Omega = 1/1024$, while the smallest nearest neighbor coupling strength is $\Omega_1 = 1/250$, when $\epsilon = 0.25$. The dispersion is then only slightly renormalized, as observed in Fig. 4.4, and in-gap edge states are still visible in the finite spectrum.

Moreover, the interesting twist arises from the inversion symmetry (4.13), which is still satisfied by the Hamiltonian (4.17). Indeed, one can show that in 1D, inversion symmetry can solely leads to a quantized $\mathbb{Z}_2$ topological invariant [230], in agreement with what was observed in Ref. [210]. However, such a topological invariant not being protected by chiral or particle-hole symmetry, it does not lead to *protected* topological edge states. The breaking of chiral symmetry leads the edge states of the Hamiltonian (4.17) to not being pinned exactly in the middle of the gap, to not being located on a single sublattice only, and to not being formally robust to perturbation such as positional disorder, in clear contrast with the topological edge states of the original SSH model.

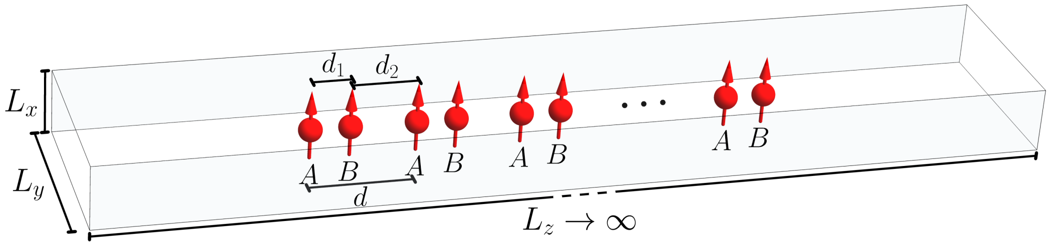

Figure 4.5: SSH dipole chain in a waveguide cavity. Sketch of the dimerized chain of oscillating dipoles depicted in Fig. 4.1, but now placed in the middle of an optical waveguide cavity with open ends, perfectly conducting mirrors in the x and y planes, and lengths L_x, L_y, and $L_z \to \infty$.

4.2 Coupling to a multimode optical cavity

Now that we understand the basic properties of the quasistatic dipolar SSH chain (4.17), we investigate the effects of the light-matter coupling. Indeed, from their dipolar nature, the emitters we consider always couple to a photonic environment, either with the photonic vacuum or with confined electromagnetic modes in an optical structure. Here we consider their coupling to a multimode waveguide cavity, using the formalism proposed in Chap. 2. The model under study in the following is then represented in Fig. 4.5. A similar SSH chain embedded in a multimode cavity has been first studied in Ref. [136], where the authors investigated in particular the topological phases of the system. However, and importantly, while Ref. [136] considered hard wall boundaries for the cavity in the three space directions, here we opt for periodic boundary conditions in the z direction, so that we consider a finite dipole chain embedded into an infinite cavity with a longitudinal size $L_z = L_{\text{chain}} + 2d_{\text{cav}} \to \infty$, as we described in Sec. 2.3.

We recall that this limit is equivalent to an open waveguide cavity, with open boundary conditions in the z direction. Our motivation to consider such a waveguide cavity is twofold. First, it may be experimentally more accessible than a closed cuboidal cavity. Second, as we are in particular interested in the properties of the edge states forming around the first and last dipole of the chain, we wish to avoid any boundary effects due to the cavity walls at the two ends of the chain. While this choice of boundary condition could be viewed, at first sight, as a minor change, it in fact drastically affects the localization of the eigenstates of the system at the two ends of the chain. Indeed, the finite spectrum of the polaritonic SSH Hamiltonian in a waveguide cavity, which we derive in the present section and study in Sec. 4.5, considerably differs from what was found in Ref. [136]. A discussion on these boundary effects is proposed in Sec. 4.8.

Moreover, in this chapter, unless otherwise specified, we take into account in our model photon Umklapp processes, also known as diffraction orders, which we introduced in Sec. 2.3.2. The consideration of such additional photonic bands that are folded within the first Brillouin zone is here justified by our wish to compute bulk topological quantities in Sec. 4.4, which formally require periodicity in the first Brillouin zone. Additionnally, while Umklapp processes do not qualitatively influence any of the results of our study, such additional terms allow analytical simplifications of our model, as we shall see in Sec. 4.2.3.

4.2.1 Polaritonic Hamiltonian

We extend the model of a 1D chain of generic dipolar emitters coupled to a multimode waveguide cavity developed in Chap. 2 to the case of the bipartite array sketched in Fig. 4.5, where we recall that all the emitters have the same resonance frequency ω_0 and are located at regular positions in an array with lattice constant d. The only difference with Chap. 2 is that one has now to distinguish between emitters in sublattices A and B, so that the $\mathbf{\Pi}\cdot\mathbf{A}$ light-matter coupling Hamiltonian (2.15) reads here

$$\mathrm{H}_{\mathbf{\Pi}\cdot\mathbf{A}} = \frac{Q}{Mc}\sum_{s=A,B}\sum_{m=1}^{\mathcal{N}} \mathbf{\Pi}_m^s \cdot \mathbf{A}(\mathbf{r}_m^s). \tag{4.24}$$

It couples the quantized conjugate momenta of emitters in the unit cell m and sublattices $s = A$ and $s = B$,

$$\mathbf{\Pi}_m^A = \mathrm{i}\sqrt{\frac{M\hbar\omega_0}{2}}\left({a_m}^\dagger - a_m\right)\hat{x} \tag{4.25a}$$

and

$$\mathbf{\Pi}_m^B = \mathrm{i}\sqrt{\frac{M\hbar\omega_0}{2}}\left({b_m}^\dagger - b_m\right)\hat{x}, \tag{4.25b}$$

to the quantized vector potential $\mathbf{A}$ [see Eq. 2.39 in which we included Umklapp processes] evaluated at the position of each dipole within the cavity

$$\mathbf{r}_m^s = \left(\frac{L_x}{2}, \frac{L_y}{2}, z_m^s\right). \tag{4.26}$$

Here, the z coordinate of a dipole in the unit cell m belonging to the A or B sublattice reads

$$z_m^A = (m-1)d + d_{\mathrm{cav}} = md - d_1/2 + \vartheta \tag{4.27a}$$

or

$$z_m^B = (m-1)d + d_{\mathrm{cav}} + d_1 = md + d_1/2 + \vartheta, \tag{4.27b}$$

respectively, where we defined the constant distance

$$\vartheta = d_{\mathrm{cav}} + d_1/2 - d. \tag{4.28}$$

Considering the single band approximation (see Sec. 2.3.1), the rotating-wave approximation (see Sec. 2.3.4) and a infinitely long waveguide cavity with periodic boundary conditions in the z direction (see Sec. 2.3), the light-matter coupling Hamiltonian (4.24) simplifies as

$$\mathrm{H}^{=}_{\mathbf{\Pi}\cdot\mathbf{A}} = \mathrm{i}\hbar \sum_{m=1}^{\mathcal{N}} \sqrt{\frac{d}{L_z}} \sum_{q,l} \xi_{q,l} \left[\left(a_m^\dagger \, \mathrm{e}^{\mathrm{i}q_l z_m^A} + b_m^\dagger \, \mathrm{e}^{\mathrm{i}q_l z_m^B} \right) c_{q,l} - \mathrm{H.c.} \right], \tag{4.29}$$

with $q_l = q - 2\pi l/d$, q being the longitudinal wavenumber of the cavity photons, belonging to the first Brillouin zone, and $l \in \mathbb{Z}$ being the Umklapp band index, or diffraction order. The light-matter coupling strength writes

$$\xi_{q,l} = \omega_0 \sqrt{\frac{2\pi a^3 \omega_0}{d L_x L_y \omega_{q,l}^{\mathrm{ph}}}}, \tag{4.30}$$

where the photonic dispersion $\omega_{q,l}^{\mathrm{ph}}$ is given in Eq. (2.43). To get rid of the constant phase $q_l\vartheta$ in the exponential functions of the Hamiltonian (4.29), we redefine in the remainder the photon ladder operators as $c_{q,l} \to c_{q,l}\mathrm{e}^{-\mathrm{i}q_l\vartheta}$.

This leads the full polaritonic Hamiltonian we consider in this chapter to write

$$\begin{aligned}
\mathrm{H}^{=}_{\mathrm{pol}} = {} & \hbar\omega_0 \sum_{m=1}^{\mathcal{N}} \left(a_m^\dagger a_m + b_m^\dagger b_m \right) + \hbar\Omega \sum_{m,m'=1}^{\mathcal{N}} g_{m-m'} \left(a_m^\dagger \, b_{m'} + a_m \, b_{m'}^\dagger \right) \\
& + \frac{\hbar\Omega}{2} \sum_{\substack{m,m'=1 \\ (m\neq m')}}^{\mathcal{N}} f_{m-m'} \left(a_m^\dagger \, a_{m'} + b_m^\dagger \, b_{m'} + a_m \, a_{m'}^\dagger + b_m \, b_{m'}^\dagger \right) \\
& + \mathrm{i}\hbar \sum_{m=1}^{\mathcal{N}} \sqrt{\frac{d}{L_z}} \sum_{q,l} \xi_{q,l} \left[\mathrm{e}^{\mathrm{i}mq_l d} \left(a_m^\dagger \, \mathrm{e}^{-\mathrm{i}\chi_{q,l}} + b_m^\dagger \, \mathrm{e}^{\mathrm{i}\chi_{q,l}} \right) c_{q,l} - \mathrm{H.c.} \right] \\
& + \sum_{q,l} \hbar\omega_{q,l}^{\mathrm{ph}} c_{q,l}^\dagger c_{q,l},
\end{aligned} \tag{4.31}$$

where the first two lines represent the dipolar Hamiltonian (4.17) presented in the previous subsection, the third line the light-matter coupling Hamiltonian (4.29), and the last line corresponds to the cavity photon Hamiltonian (2.33). We note that the phase $\chi_{q,l} = q_l d_1/2$ in Eq. (4.31) encodes the different location in the unit cell of the dipolar excitations belonging to the A or B sublattice. In the following, we refer to the Hamiltonian (4.31) as the full polaritonic SSH Hamiltonian. Despite this appellation, we recall that several approximations have been made, such as the neglection of multipolar corrections to our point-dipole modelling, of counter-rotating terms, as well as the effect of image dipoles originating from the perfectly metallic cavity walls. Notably, a comprehensive study of the effect of the latter image dipoles is conducted in Appendix 4.C, in which we show that they do not qualitatively change any of the results of our study.

4.2.2 Schrieffer-Wolff transformation and effective Hamiltonian

Since we are mainly concerned by how the strong light-matter interaction renormalizes the dipolar subsystem, it can be advantageous to build an effective Hamiltonian out of the full polaritonic Hamiltonian (4.31). To this end, we integrate out the photonic degrees of freedom of the Hamiltonian (4.31) by performing the Schrieffer-Wolff unitary transformation [231]

$$\tilde{\mathrm{H}}^{=}_{\mathrm{pol}} = \mathrm{e}^{S^{=}}\mathrm{H}^{=}_{\mathrm{pol}}\mathrm{e}^{-S^{=}} \simeq \mathrm{H}^{=}_{\mathrm{pol}} + [S^{=}, \mathrm{H}^{=}_{\mathrm{pol}}] + \frac{1}{2}[S^{=}, [S^{=}, \mathrm{H}^{=}_{\mathrm{pol}}]]. \tag{4.32}$$

Here, using the fact that the quasistatic dipole-dipole coupling strength $\Omega/\omega_0 \ll 1$, the anti-Hermitian operator $S^{=}$ (i.e., $S^{=\dagger} = -S^{=}$) can be determined such that

$$[S^{=}, \mathrm{H}^{\mathrm{RWA}}_{\mathrm{dp}}(\Omega = 0) + H_{\mathrm{ph}}] = -\mathrm{H}^{=}_{\mathbf{\Pi}\cdot\mathbf{A}}, \tag{4.33}$$

so as to eliminate coupling terms of the order of $\Omega\xi^2_{q,l}/{\omega_0}^3$ in the effective Hamiltonian. Here, $\mathrm{H}^{\mathrm{RWA}}_{\mathrm{dp}}(\Omega = 0)$ corresponds to the dipolar Hamiltonian (4.17) in the limit of zero dipolar coupling strength Ω. From the condition (4.33), we find

$$S^{=} = -\mathrm{i}\sum_{m=1}^{\mathcal{N}}\sqrt{\frac{d}{L_z}}\sum_{q,l}\frac{\xi_{q,l}}{\omega^{\mathrm{ph}}_{q,l} - \omega_0}\left[\mathrm{e}^{\mathrm{i}mq_l d}c_{q,l}\left(a^{\dagger}_{m}\mathrm{e}^{-\mathrm{i}\chi_{q,l}} + b^{\dagger}_{m}\mathrm{e}^{\mathrm{i}\chi_{q,l}}\right) + \mathrm{H.c.}\right]. \tag{4.34}$$

The dipolar and photonic subspaces are then perturbatively decoupled to second order in the light-matter coupling strength,

$$\tilde{\mathrm{H}}^{=}_{\mathrm{pol}} \simeq \mathrm{H}^{\mathrm{RWA}}_{\mathrm{dp}} + H_{\mathrm{ph}} + \frac{1}{2}[S^{=}, \mathrm{H}^{=}_{\mathbf{\Pi}\cdot\mathbf{A}}] \equiv \tilde{\mathrm{H}}^{\mathrm{RWA},=}_{\mathrm{dp}} + \tilde{\mathrm{H}}^{=}_{\mathrm{ph}}. \tag{4.35}$$

Computing the commutator in Eq. (4.35) and focusing on the dipolar subspace, we obtain the effective bipartite Hamiltonian

$$\begin{aligned}
\tilde{\mathrm{H}}^{\mathrm{RWA},=}_{\mathrm{dp}} = \hbar\tilde{\omega}^{=}_{0}\sum_{m=1}^{\mathcal{N}}\left(a^{\dagger}_{m}a_{m} + b^{\dagger}_{m}b_{m}\right)& \\
+ \frac{\hbar\Omega}{2}\sum_{\substack{m,m'=1\\(m\neq m')}}^{\mathcal{N}}\tilde{f}^{=}_{m-m'}\left(a^{\dagger}_{m}\,a_{m'} + b^{\dagger}_{m}\,b_{m'} + \mathrm{H.c.}\right)& \\
+ \hbar\Omega\sum_{m,m'=1}^{\mathcal{N}}\tilde{g}^{=}_{m-m'}\left(a^{\dagger}_{m}\,b_{m'} + \mathrm{H.c.}\right).&
\end{aligned} \tag{4.36}$$

Here, the onsite frequency ω_0 and the intra- and intersublattice sums $f_{m-m'}$ and $g_{m-m'}$ are renormalized by the cavity photons [compare with Eq. (4.17)] as

$$\tilde{\omega}_0^{=} = \omega_0 - \frac{d}{2\pi} \sum_{l=-\infty}^{+\infty} \int_{-\pi/d}^{+\pi/d} \mathrm{d}q \, \frac{\xi_{q,l}^2}{\omega_{q,l}^{\mathrm{ph}} - \omega_0}, \tag{4.37a}$$

$$\tilde{f}_{m-m'}^{=} = f_{m-m'} - \frac{1}{\Omega} \frac{d}{2\pi} \sum_{l=-\infty}^{+\infty} \int_{-\pi/d}^{+\pi/d} \mathrm{d}q \, \frac{\xi_{q,l}^2 \, \mathrm{e}^{\mathrm{i}(m-m')q_l d}}{\omega_{q,l}^{\mathrm{ph}} - \omega_0}, \tag{4.37b}$$

and

$$\tilde{g}_{m-m'}^{=} = g_{m-m'} - \frac{1}{\Omega} \frac{d}{2\pi} \sum_{l=-\infty}^{+\infty} \int_{-\pi/d}^{+\pi/d} \mathrm{d}q \, \frac{\xi_{q,l}^2 \, \mathrm{e}^{\mathrm{i}(m-m'-d_1/d)q_l d}}{\omega_{q,l}^{\mathrm{ph}} - \omega_0}, \tag{4.37c}$$

where we used the fact that we consider an infinitely long cavity with $d_{\mathrm{cav}} \to \infty$, so that $L_z \to \infty$, and we can take the continuous limit for the quasimomentum q

$$\frac{2\pi}{L_z} \sum_{q=-\pi/d}^{+\pi/d} \to \int_{-\pi/d}^{+\pi/d} \mathrm{d}q. \tag{4.38}$$

We note that our perturbation theory provides a convenient way to take into account the effect of all the Umklapp bands. Moreover, it allows a transparent interpretation of the effects of the strong light-matter coupling, as the above renormalized quantities account for an effective coupling between the dipoles which is mediated by the cavity photons. However, as any perturbative scheme, it limits the allowed regime of parameters of the model. Indeed, as can be deduced from Eq. (4.34), such a perturbation theory breaks down once the photonic and dipolar subspaces overlap, namely when $\omega_{q,l}^{\mathrm{ph}} \geq \omega_0$. This happens as soon as the cavity height $L_x/a \geq \pi/3k_0 a \equiv L_x^{\mathrm{SW}}/a \simeq 10.5$. In Appendix 4.B, we will check that our Schrieffer-Wolff approach qualitatively reproduces the results obtained from a diagonalization of the full polaritonic Hamiltonian (4.31), as long as the cavity height $L_x \lesssim 10a$.

Tuning the cavity transverse dimensions so that the photon dispersion (2.34) approaches the two dipolar bands then allows one to enter in the strong light-matter coupling regime. Hence, the Hamiltonian (4.36) can be viewed as another variation of a dipolar SSH model, with hoppings being highly modified by the strong coupling to a multimode optical cavity. In the sequel of this chapter, we therefore refer to such a model as the effective polaritonic SSH model.

Although strong coupling does not fundamentally modify the symmetries of the effective Hamiltonian [compare Eqs. (4.17) and (4.36)], it can significantly increase the chiral-breaking, intrasublattice interaction (4.37b), which can become dominant over the chiral-preserving, intersublattice one (4.37c). As we will discuss in Sec. 4.3, this increased asymmetry between the two sublattices strongly modifies the bulk spectrum. We will show in Sec. 4.4 that the topological phases of the effective Hamiltonian (4.36) are also affected by the light-matter coupling.

4.2.3 Cavity-induced effective dipole-dipole couplings

Before investigating the bulk properties of the polaritonic SSH model, we gain physical insight into the effect of the light-matter coupling on dipolar excitations, by analytically evaluating the cavity-induced renormalized quantities (4.37).

The renormalization terms appear as

$$\frac{d}{2\pi}\sum_{l=-\infty}^{+\infty}\int_{-\pi/d}^{+\pi/d}\mathrm{d}q\frac{\xi_{q,l}^2}{\omega_{q,l}^{\mathrm{ph}}-\omega_0}\,\mathrm{e}^{\mathrm{i}vq_ld}=\frac{2\omega_0a^3}{L_xL_y}\mathcal{I}(v), \tag{4.39}$$

with integrals of the form

$$\begin{aligned}\mathcal{I}(v)&=\sum_{l=-\infty}^{+\infty}\int_{-\pi/d}^{+\pi/d}\mathrm{d}q\,\frac{\omega_0^2\,\mathrm{e}^{\mathrm{i}vq_ld}}{\omega_{q,l}^{\mathrm{ph}}(\omega_{q,l}^{\mathrm{ph}}-\omega_0)}\\&=\int_{-\infty}^{+\infty}\mathrm{d}q\,\frac{\omega_0^2\,\mathrm{e}^{\mathrm{i}vqd}}{\omega_{q,0}^{\mathrm{ph}}(\omega_{q,0}^{\mathrm{ph}}-\omega_0)},\end{aligned} \tag{4.40}$$

where $v=0$, $v=m-m'$, or $v=m-m'-d_1/d$. Surprisingly, we note the simplification of the integral arising from the inclusion of all the Umklapp bands $l\neq 0$. Neglecting such bands yields actually to an additional term in Eq. (4.40), which takes the form of a very small oscillating algebraic tail in the intra- and intersublattice coupling renormalizations.

The particular case of $\mathcal{I}(v=0)$ can be readily evaluated. It appears in the cavity-renormalized onsite frequency [cf. Eq. (4.37a)], which therefore reads

$$\tilde{\omega}_0=\omega_0-\frac{2\omega_0a^2k_0a}{L_xL_y}\frac{\omega_0}{\sqrt{(\omega_{0,0}^{\mathrm{ph}})^2-\omega_0{}^2}}\left[\arctan\left(\frac{\omega_0}{\sqrt{(\omega_{0,0}^{\mathrm{ph}})^2-\omega_0{}^2}}\right)+\frac{\pi}{2}\right]. \tag{4.41}$$

Such renormalized frequency is slightly redshifted as compared with the bare frequency ω_0 (less than about 0.3 %). The difference increases with the cavity height L_x as the photon frequency $\omega_{0,0}^{\mathrm{ph}}$ approaches the bare emitters frequency ω_0.

For the intra- and intersublattice coupling renormalizations, where v equals, respectively, $m-m'$ and $m-m'-d_1/d$, we use the fact that in our perturbation theory the photonic frequency remains larger than the bare emitter one, so that we can rewrite the effective coupling integrals $\mathcal{I}(v)$ as

$$\mathcal{I}(v) = \sum_{p=2}^{\infty} \int_{-\infty}^{+\infty} \mathrm{d}q \left(\frac{\omega_0}{\omega_{q,0}^{\mathrm{ph}}} \right)^{p} \mathrm{e}^{\mathrm{i}vqd} \equiv \sum_{p=2}^{\infty} \mathcal{J}_p(v), \tag{4.42}$$

which can be evaluated as an infinite sum of modified Bessel functions of the second kind $K_\nu(z)$,

$$\mathcal{J}_p(v) = \frac{\sqrt{\pi}(k_0 d)^p}{\Gamma(p/2)d} \left(\frac{|v|L_y}{2\pi d} \right)^{\frac{p-1}{2}} K_{\frac{p-1}{2}} \left(|v| \frac{\pi d}{L_y} \right), \tag{4.43}$$

where $\Gamma(z)$ represents the gamma function. We note that in all the results we present in this work involving the finite spectrum, namely, in Secs. 4.5, 4.6, and 4.7, we truncate such infinite sum to $p_{\max} = 100$, having checked the irrelevance of higher-order terms. Each term in the sum of Eq. (4.42) corresponds to an nearly-exponential decay, and the sum is dominated by the first, $p = 2$ term

$$\mathcal{J}_2(v) = \frac{(k_0 d)^2 L_y}{2d^2} \exp\left(-|v| \frac{\pi d}{L_y} \right), \tag{4.44}$$

a pure exponential decay with a clear dependence on the cavity width $L_y = 3L_x$.

To conclude this subsection, we demonstrated that the cavity renormalizes the quasistatic, power-law dipole-dipole couplings $f_{m-m'}$ and $g_{m-m'}$ of Eq. (4.18) through the addition of a quasi-exponential decay, whose decay length is governed by the cavity transverse dimensions L_x and L_y. Increasing the cavity width and height, i.e., entering in the strong-coupling regime, leads the latter exponential decay to fall on larger distances, so that the cavity-induced effective dipole-dipole coupling becomes stronger. Such an exponential decay induced by the strong-coupling regime allows for a large effective dipole-dipole coupling at intermediate distances, and was notably at the origin of the cavity-enhanced transport observed in Sec. 3.6. At very long distances, however, the cavity-induced exponential decay will be superseded by the quasistatic power-law couplings (4.18), as also seen in Sec. 3.6. In the next sections, we study how this additional dipole-dipole coupling influences the properties of the polaritonic SSH model.

4.3 Bulk polaritonic Hamiltonian

We begin our study of the SSH chain embedded in a multimode optical cavity by investigating its bulk properties, and in particular its bulk eigenspectrum. To this end, we consider in this section the emitters thermodynamic limit, assuming a chain composed of $\mathcal{N} \to \infty$ dimers, in a similar fashion as what is done for the unipartite chain in Sec. 3.3. We first examine the full polaritonic Hamiltonian (4.31), and then analyze the effective Hamiltonian (4.36).

4.3.1 Three-band polaritonic Hamiltonian

To gain physical insights into the polaritonic SSH model, we first study the full Hamiltonian (4.31) without perturbation theory. Notably, this allows us to unveil the genuine polaritonic properties of the model through an analysis of Hopfield's coefficients, investigating quantitatively the hybridization of light and matter excitations. To this end, however, we neglect in this subsection Umklapp processes by considering only the $l = 0$ band, as the inclusion of higher modes would results in the loss of analytical calculation, and does not change qualitatively any of our conclusions.

In the emitters thermodynamic limit $\mathcal{N} \to \infty$, any boundary conditions in the z direction of the cavity are equivalent, and the longitudinal size of the cavity $L_z \sim \mathcal{N} d \to \infty$. Moving into Fourier space through the Fourier transforms (4.4), the full polaritonic Hamiltonian in the emitters thermodynamic limit, and without Umklapp processes, can be written in its Bloch form as

$$\mathrm{H}^{\infty}_{\mathrm{pol}} = \sum_q \boldsymbol{\varphi}_q^{\dagger} \mathcal{H}_q^{\mathrm{pol}} \boldsymbol{\varphi}_q, \tag{4.45}$$

in the basis $\boldsymbol{\varphi}_q = (a_q, b_q, c_q)$, and where the three-band polaritonic Bloch Hamiltonian reads

$$\mathcal{H}_q = \hbar \begin{pmatrix} \omega_0 + \Omega f_q & \Omega g_q & \mathrm{i}\xi_q \mathrm{e}^{-\mathrm{i}\chi_q} \\ \Omega g_q^* & \omega_0 + \Omega f_q & \mathrm{i}\xi_q \mathrm{e}^{\mathrm{i}\chi_q} \\ -\mathrm{i}\xi_q \mathrm{e}^{\mathrm{i}\chi_q} & -\mathrm{i}\xi_q \mathrm{e}^{-\mathrm{i}\chi_q} & \omega_q^{\mathrm{ph}} \end{pmatrix}. \tag{4.46}$$

Such three-band polaritonic SSH model has been studied in Ref. [136]. As shown in the latter reference, a Hopfield-Bogoliubov transformation leads the diagonal form

$$\mathrm{H}^{\infty}_{\mathrm{pol}} = \sum_{qj} \omega_{qj}^{\mathrm{pol}} \gamma_{qj}^{\dagger} \gamma_{qj}, \tag{4.47}$$

where the three-band polaritonic dispersion is the solution of a cubic equation and reads

$$\omega_{qj}^{\mathrm{pol}} = \frac{2\left(\omega_0 + \Omega f_q\right) + \omega_q^{\mathrm{ph}}}{3} + \frac{2\Gamma_q}{3} \cos\left(\frac{\Phi_q + 2\pi s_j}{3}\right), \tag{4.48}$$

where the function

$$s_j = \lceil j/2 \rceil + (-1)^j \tag{4.49}$$

orders the frequency bands via the index $j \in \{1, 2, 3\}$, which labels, respectively, the mostly photonic upper polariton band (UP), and the mostly dipolar medium and lower polariton (MP and LP) bands.

In the above equations (4.48)–(4.49), $\lceil x \rceil$ is the ceiling function, and we introduced the frequency

$$\Gamma_q = \sqrt{3\Omega^2|g_q|^2 + 6\xi_q^2 + \left(\omega_q^{\mathrm{ph}} - \omega_0 - \Omega f_q\right)^2}, \tag{4.50}$$

and the angle

$$\begin{aligned}\Phi_q =& \arccos\left(\frac{1}{\Gamma_q^3}\left\{27\Omega|g_q|\xi_q^2\cos\left(\phi_q + 2\chi_q\right)\right.\right.\\ &\left.\left.+\left(\omega_q^{\mathrm{ph}} - \omega_0 - \Omega f_q\right)\left[9\left(\xi_q^2 - \Omega^2|g_q|^2\right) + \left(\omega_q^{\mathrm{ph}} - \omega_0 - \Omega f_q\right)^2\right]\right\}\right).\end{aligned} \tag{4.51}$$

The Hopfield-Bogoliubov operator diagonalizing the Hamiltonian (4.47),

$$\gamma_{qj} = \mathrm{A}_{qj}a_q + \mathrm{B}_{qj}b_q + \mathrm{C}_{qj}c_q, \tag{4.52}$$

is a linear combination of the dipolar and photonic degrees of freedom. The modulus squared of the Hopfield coefficients A_{qj}, B_{qj} and C_{qj}, normalized as $|\mathrm{A}_{qj}|^2 + |\mathrm{B}_{qj}|^2 + |\mathrm{C}_{qj}|^2 = 1$, represent respectively the part of the polaritonic eigenmode that arises from the dipolar excitation on the A sublattice, from the dipolar excitation on the B sublattice, and from the cavity photon excitation. Their expression, which can be extracted from the diagonalization procedure, write

$$\mathrm{A}_{qj} = \frac{1}{\sqrt{2 + \xi_q^2|\Xi_{qj}|^2}}, \tag{4.53a}$$

$$\mathrm{B}_{qj} = \frac{1}{\sqrt{2 + \xi_q^2|\Xi_{qj}|^2}}\,\frac{\xi_q^2 - \left(\omega_q^{\mathrm{ph}} - \omega_{qj}^{\mathrm{pol}}\right)\left(\omega_0 + \Omega f_q - \omega_{qj}^{\mathrm{pol}}\right)}{\Omega g_q^*\left(\omega_q^{\mathrm{ph}} - \omega_{qj}^{\mathrm{pol}}\right) - \xi_q^2\mathrm{e}^{2\mathrm{i}\chi_q}} \tag{4.53b}$$

and

$$\mathrm{C}_{qj} = \frac{-\mathrm{i}\xi_q\mathrm{e}^{-\mathrm{i}\chi_q}}{\sqrt{2 + \xi_q^2|\Xi_{qj}|^2}}\Xi_{qj}, \tag{4.53c}$$

with the frequency

$$\Xi_{qj} = \frac{\Omega g_q^* - \mathrm{e}^{2\mathrm{i}\chi_q}\left(\omega_0 + \Omega f_q - \omega_{qj}^{\mathrm{pol}}\right)}{\Omega g_q^*\left(\omega_q^{\mathrm{ph}} - \omega_{qj}^{\mathrm{pol}}\right) - \xi_q^2\mathrm{e}^{2\mathrm{i}\chi_q}}. \tag{4.54}$$

From their modulus square, we define the dipolar and photonic parts

$$\mathrm{D}_{qj} = |\mathrm{A}_{qj}|^2 + |\mathrm{B}_{qj}|^2 \tag{4.55a}$$

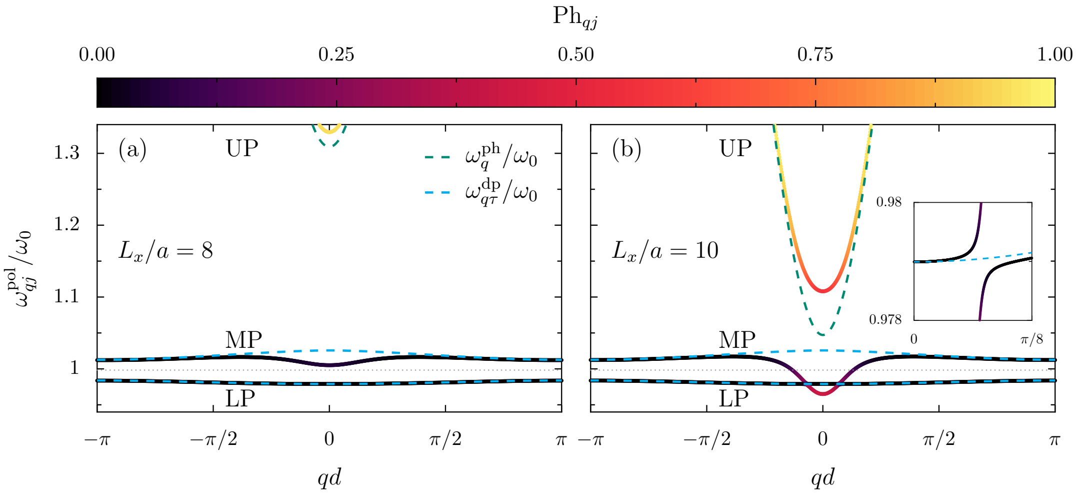

Figure 4.6: Three-band Hamiltonian dispersion. Bandstructure $\omega_{qj}^{\mathrm{pol}}$ of the full three-band polaritonic Hamiltonian (4.45), in units of ω_0 and in the first Brillouin zone. The colorcode represents the photonic weight Ph_{qj} of each eigenstate [see Eq. (4.55b)], from black (dipolar states) to reddish (hybridized polaritons) and yellow (photonic states). The green and blue dashed lines show the bare photonic and dipolar dispersions, given, respectively, in Eqs. (2.34) and (4.21). The cavity height is (a) $L_x/a = 8$ and (b) $L_x/a = 10$, while in both panels the dimerization $\epsilon = 0.25$ [cf. Eq. (4.3)].

and

$$\mathrm{Ph}_{qj} = |C_{qj}|^2 \tag{4.55b}$$

of a given polaritonic eigenmode, similarly to the quantities (3.15) defined in Chap. 3.

The full polaritonic bandstructure (4.48) is shown in the first Brillouin zone in Fig. 4.6, for a dimerization parameter $\epsilon = 0.25$ and increasing cavity dimensions [which, we recall, encode the light-matter coupling strength (2.38)]. We represent as a colorcode the photonic weight (4.55b) associated with each eigenstate, from black (fully dipolar dark state) to yellow (fully photonic state). In the figure, we further plot for comparison the bare dipolar dispersion ω_q^{dp} [Eq. (4.21)] and the bare photonic one ω_q^{ph} [Eq. (2.33)] by blue and green dashed lines, respectively.

At a cavity height $L_x = 8a$ [see Fig. 4.6(a)], the bare dipolar and photonic bands are only weakly renormalized into polaritonic bands, and the black color of the LP and MP bands indicate that they are only comprised of dipolar dark states. The effect of the light-matter coupling becomes stronger for $L_x = 10a$ [see Fig. 4.6(b)], once the bare photonic band approaches resonance with the bare dipolar ones. In the latter case, we observe an avoided crossing scheme between the UP and MP bands, a typical signature of the strong-coupling regime. The redshift of the MP band causes a second avoided crossing scheme, now between the MP and LP bands, which we highlight in the inset of panel (b). Importantly, we observe states in red and orange around the center of the Brillouin zone where $q = 0$, demonstrating the presence of hybridized polaritonic states, with mixed dipolar and photonic weights, not only in the UP band, but also in the MP and LP bands.

4.3.2 Effective two-band Hamiltonian

While the full polaritonic Hamiltonian (4.31) is exact within the single band approximation and neglection of Umklapp processes and allows for a good physical understanding of the model through the photonic weight (4.53c) [see Fig. 4.6], it has the drawbacks of hiding the direct effects of the cavity onto the dipolar subspace, and to modify the typical SU(2) bipartite SSH model into a more complicated SU(3) three-band Hamiltonian [136]. Therefore, we study here the bulk properties of the effective polaritonic SSH Hamiltonian (4.36) which we derived in Sec. 4.2.2.

By performing a Fourier transformation on the Hamiltonian (4.36), and considering a number of dimers $\mathcal{N} \to \infty$, we obtain an effective two-band Hamiltonian in reciprocal space $\tilde{\mathrm{H}}_{\mathrm{dp}}^{\mathrm{RWA},\infty} = \sum_q \psi_q^\dagger \tilde{\mathcal{H}}_q \psi_q$, with the Bloch Hamiltonian

$$\tilde{\mathcal{H}}_q = \hbar \begin{pmatrix} \omega_0 + \Omega \tilde{f}_q & \Omega \tilde{g}_q \\ \Omega \tilde{g}_q^* & \omega_0 + \Omega \tilde{f}_q \end{pmatrix}, \tag{4.56}$$

and the spinor creation operator $\psi_q^\dagger = (a_q^\dagger, b_q^\dagger)$. The Bloch Hamiltonian (4.56) has the exact same form as the one of the bare dipolar SSH Hamiltonian (4.19) we studied in Sec. 4.1. Here, however, the reciprocal counterparts of the bare dipolar inter- and intrasublattice sums f_q and g_q, given in Eq. (4.20) are renormalized by the cavity as, respectively,

$$\tilde{f}_q = f_q - \frac{1}{\Omega} \sum_{l=-\infty}^{+\infty} \frac{\xi_{q,l}^2}{\omega_{q,l}^{\mathrm{ph}} - \omega_0} \tag{4.57a}$$

and

$$\tilde{g}_q = g_q - \frac{1}{\Omega} \sum_{l=-\infty}^{+\infty} \frac{\xi_{q,l}^2 \, \mathrm{e}^{-2\mathrm{i}\chi_{q,l}}}{\omega_{q,l}^{\mathrm{ph}} - \omega_0}. \tag{4.57b}$$

A Bogoliuobov transformation of the effective Bloch Hamiltonian (4.56) leads to the eigenfrequencies

$$\tilde{\omega}_{q\tau}^{\mathrm{dp}} = \omega_0 + \Omega \tilde{f}_q + \tau \Omega |\tilde{g}_q|, \tag{4.58}$$

where $\tau = +\,(-)$ denotes the high- (low-)energy band, and to the eigenspinors

$$|\tilde{\psi}_{q\tau}\rangle = \frac{1}{\sqrt{2}} \begin{pmatrix} 1 \\ \tau \, \mathrm{e}^{\mathrm{i}\tilde{\phi}_q} \end{pmatrix}, \tag{4.59}$$

where the phase

$$\tilde{\phi}_q = \arg(\tilde{g}_q). \tag{4.60}$$

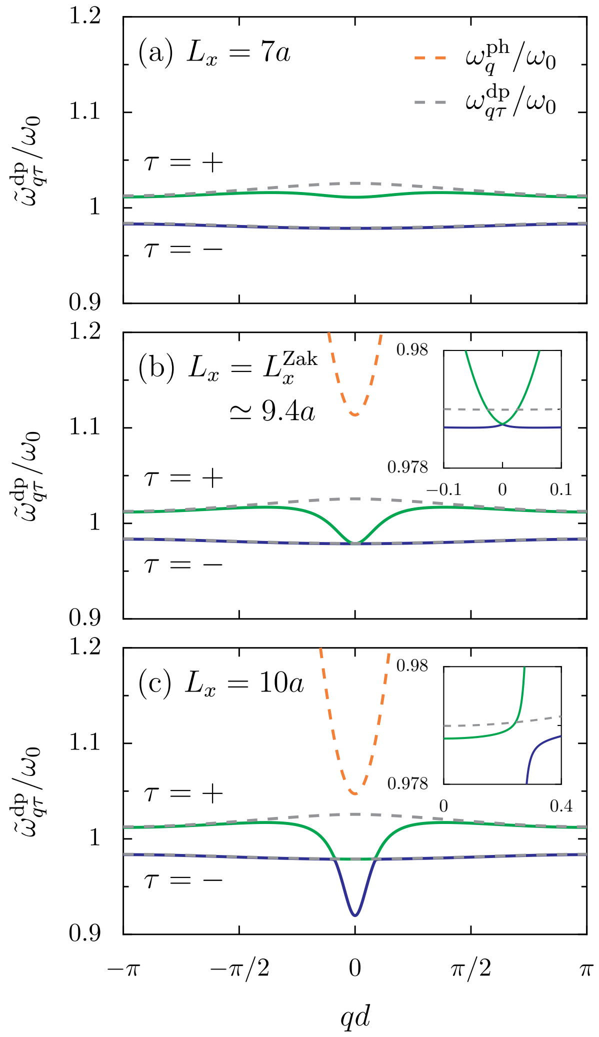

Figure 4.7: Effective two-band Hamiltonian dispersion. Green and blue solid lines: Effective polaritonic dispersions $\tilde{\omega}_{q,\tau=\pm}^{\rm dp}$ from Eq. (4.58), in units of the bare dipole frequency ω_0 and in the first Brillouin zone for cavity heights (a) $L_x = 7a$, (b) $L_x = L_x^{\rm Zak} \simeq 9.4a$, and (c) $L_x = 10a$. Gray and orange dashed lines: Bare dipolar dispersion $\omega_q^{\rm dp}$ [Eq. (4.21)] and photonic one $\omega_q^{\rm ph}$ [Eq. (2.34)], respectively. Inset of panel (b): Detail of the gap closing at $q = 0$ taking place when $L_x = L_x^{\rm Zak}$. Inset of panel (c): Detail of the avoided crossing between the two dipolar bands appearing from $L_x > L_x^{\rm Zak}$. Only the lowest, $l = 0$, photonic band is visible on the figure. In the figure, the dimerization parameter $\epsilon = 0.25$, the Umklapp index $l \in [-l_{\max}, +l_{\max}]$ with $l_{\max} = 100$, and we recall that the dimensionless dipole strength $k_0 a = 0.1$.

The renormalized dipolar dispersion (4.58) is shown in Fig. 4.7 in the first Brillouin zone, for increasing cavity dimensions and for a dimerization parameter $\epsilon = 0.25$ [cf. Eq. (4.3)]. The upper ($\tau = +$) and lower ($\tau = -$) bands are displayed by green and blue solid lines, respectively.

In Fig. 4.7(a), we consider a cavity height $L_x = 7a$. In such a case, similarly as what we observed for the full polaritonic model in Fig. 4.6, the photonic modes [not visible on the scale of Fig. 4.7(a)] are too high in energy to significantly renormalize the dipolar bands. Notably, only the upper polaritonic effective branch (green solid line) is redshifted around the center of the Brillouin zone, while the lower one (blue solid line) is essentially unaffected by the light-matter coupling. On the one hand, only the dispersion at the center of the Brillouin zone is renormalized due to the fact that all the modes with large wavenumber are out of resonance with the photons. On the other hand, the asymmetric behavior between the two dipolar bands can be understood physically from the fact that for the transverse dipole-dipole interaction at play here, the antiparallel alignment of the dipole moments within a dimer (↑↓) is energetically favored. It leads the low-energy band to behave as a dark band, which only weakly couples to light, while the high-energy band, which favors parallel alignment of the dipoles (↑↑), can significantly couple to light and is thus referred to as being a bright band.

As we already observed in Fig. 4.6 for the full model, when increasing the cavity height, the photonic modes become closer in energy from the bare dipolar ones, so that the bright band ($\tau = +$) is further renormalized in a standard avoided-crossing scheme, while the dark one ($\tau = -$) still remains unaffected by the light-matter coupling. Here, within our effective two-band Hamiltonian, such growing asymmetry between the bands makes clear the broken chiral symmetry of the model, boosted by the cavity-induced renormalization of the intrasublattice sum $\tilde{f}_q$ in Eq. (4.57a). This is what allows the bright modes around the center of the Brillouin zone to increasingly fill the gap between the two bands. At a cavity height L_x^{edge} (not shown), whose significance will become clearer in the next sections, approximately half of the gap is filled. Through our effective two-band model, we find the latter cavity height to be close to

$$\frac{L_x^{\mathrm{edge}}}{a} \simeq \frac{\pi}{3k_0a} - \frac{8k_0a}{f_0 + g_0 + 0.002\omega_0/\Omega}\left(\frac{d}{a}\right)^2, \tag{4.61}$$

where we approximated the middle of the gap to $0.998\omega_0$. In the above equation, $k_0a = \omega_0 a/c = 0.1$ (see Sec. 2.3.1), and, importantly, g_0 depends on the dimerization parameter [see Eq. (4.20b)]. With the parameters of Fig. 4.7, one has $L_x^{\mathrm{edge}} \simeq 8.7a$.

At an even larger cavity height, the bright band fills entirely the energy gap (for all q's), so that the system is not anymore in an "insulating" phase, but becomes "metallic" in the language of condensed matter electronic systems. In our effective model, such transition occurs when $\tilde{\omega}^{\mathrm{dp}}_{q=0,\tau=+} = \tilde{\omega}^{\mathrm{dp}}_{q=\pi/d,\tau=-}$, at a cavity height coined in Ref. [136] as L_x^{gap}. Using the same parameters as in Fig. 4.7, $L_x^{\mathrm{gap}} \simeq 9.3a > L_x^{\mathrm{edge}}$

Figure 4.7(b) displays our results for the cavity height $L_x = L_x^{\mathrm{Zak}} \simeq 9.4a$, where, importantly, the upper band (green line) touches the lower one (blue line) at $q = 0$, as highlighted in the inset where a zoom on the two curves around the center of the Brillouin zone is shown. Such critical cavity height L_x^{Zak} has been introduced in Ref. [136], and bears its name from the TPT that arises here, and which is associated with a modification of the Zak phase. Our effective two-band model allows us to easily interpret this result analytically. Indeed, from Eqs. (4.57)–(4.58), we have $\tilde{\omega}^{\text{dp}}_{q=0,\tau=+} = \tilde{\omega}^{\text{dp}}_{q=0,\tau=-}$ when the renormalization of the sublattice sum (4.57b) due to the light-matter coupling counteracts the original sublattice sum (4.20b), i.e., $|\tilde{g}_0| = 0$. Considering only the lowest Umklapp index $l = 0$ for simplification, this arises for the cavity height

$$\frac{L_x^{\text{Zak}}}{a} = \frac{\pi}{3k_0a} - \frac{4k_0a}{g_0}\left(\frac{d}{a}\right)^2. \tag{4.62}$$

A detailed discussion of the unusual topological phases of our system is presented in the next Sec. 4.4.

In Fig. 4.7(c), we further increase the cavity height to $L_x = 10a$, so that the proximity in energy of the photonic modes (orange line) redshifts the upper, bright band (green line) into the lower, dark one (blue line). This results, similarly as what we observed for the full model in Fig. 4.6(b), in another avoided-crossing scheme, now between the two effective upper ($\tau = +$) and lower ($\tau = -$) dipolar bands, as highlighted in the inset of Fig. 4.7(c), where a zoom on the two curves is provided. Hence, as long as $L_x > L_x^{\text{Zak}}$ the two effective bands anticross, so that the bandgap for a fixed wavenumber q is open again. However, we emphasize that, as was already the case in Fig. 4.7(b), the energy gap for all q's is closed, so that the system is here "metallic".

4.4 Topological phases of polaritons

To pursue the study of the bulk properties of the polaritonic SSH model, we now analyze its topological phases. These latter have been partly investigated in Ref. [136] for the full polaritonic Hamiltonian (4.46). Specifically, the fate of the bulk-boundary correspondence under the strong light-matter coupling regime was examined, that is, the accordance between bulk-related topological invariants and the number of edge states in the finite-size system. To deal with the particular three-band and SU(3) symmetry of the full model, the authors of Ref. [136] had to use fairly unconventional techniques, such as complicated numerical integrations and poor man's approaches to build an effective SU(2) two-band model.

Here, we use the Schrieffer-Wolff effective Hamiltonian (4.56) derived in the previous sections to further investigate the topological phases of the polaritonic SSH model and deepen the results of Ref. [136].

In particular, we take advantage of our simpler effective two-band model to analyze its topology through standard methods, which allows us to gain physical insights and to make direct comparisons with the dipolar SSH model with and without all-to-all quasistatic coupling [given, respectively,

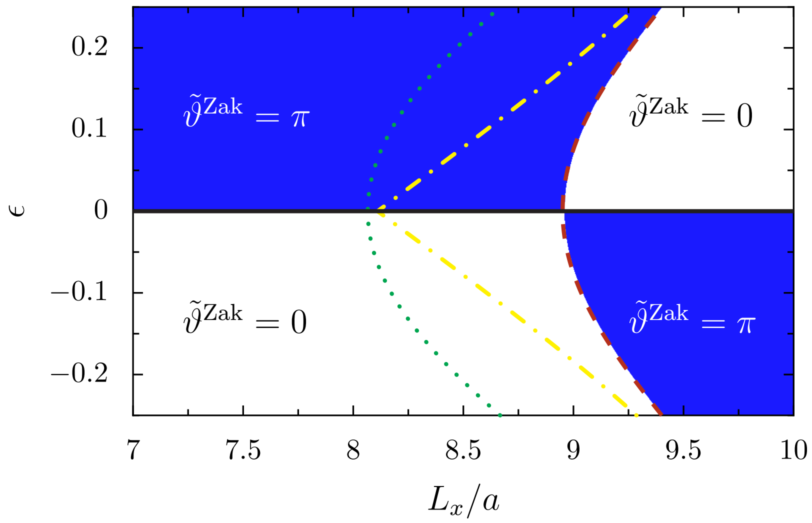

Figure 4.8: Zak phase diagram. Topological phase diagram from the computation of the Zak phase $\tilde{\vartheta}^{\mathrm{Zak}}$ [see Eq. (4.63)] in the (L_x, ϵ) parameter space. The green dotted, yellow dash-dotted, and red dashed lines correspond, respectively, to $L_x = L_x^{\mathrm{edge}}$ [see Eq. (4.61)], $L_x = L_x^{\mathrm{gap}}$, and $L_x = L_x^{\mathrm{Zak}}$ [see Eq. (4.62)]. In the figure, the Umklapp index $l \in [-l_{\mathrm{max}}, +l_{\mathrm{max}}]$ with $l_{\mathrm{max}} = 100$.

in Eqs. (4.19) and (4.6)]. Moreover, we disclose original findings by exploring both the $\epsilon < 0$ and $\epsilon > 0$ cases [see Eq. (4.3)], which, in the dipolar SSH model, correspond respectively to the trivial and topological phases.

4.4.1 Inversion symmetry and Zak phase diagram

Despite its broken chiral symmetry ($\{\tilde{\mathcal{H}}_q, \sigma_z\} \neq 0$), the effective two-band Hamiltonian (4.56) conserves inversion symmetry ($\sigma_x \tilde{\mathcal{H}}_{-q} \sigma_x = \tilde{\mathcal{H}}_q$), where σ_x and σ_z denote the first and third Pauli matrix, respectively [see Eq. (4.14)]. Importantly, this ensures that the Zak phase [232, 233]

$$\tilde{\vartheta}^{\mathrm{Zak}} = \mathrm{i} \int_{-\pi/d}^{+\pi/d} \mathrm{d}q \, \langle \tilde{\psi}_{q\tau} | \partial_q \tilde{\psi}_{q\tau} \rangle \mod 2\pi \tag{4.63}$$

is quantized, and defines a meaningful $\mathbb{Z}_2$ topological invariant of the model [52, 230]. In the above definition of the Zak phase, $|\tilde{\psi}_{q\tau}\rangle$ are the eigenspinors of the effective two-band Hamiltonian, given in Eq. (4.59). We evaluate Eq. (4.63) using the Wilson-loop approach [234], which is gauge invariant as well as suitable for numerical implementation.

Our results of such computation of the Zak phase (4.63) is shown in Fig. 4.8 as a phase diagram in the (L_x, ϵ) parameter space. Two TPTs between the trivial ($\tilde{\vartheta}^{\mathrm{Zak}} = 0$, white regions) and topological phases ($\tilde{\vartheta}^{\mathrm{Zak}} = \pi$, blue regions) are visible. A first one, induced by the variation of the dimerization of the chain, is present at $\epsilon = 0$ and indicated as a black solid line. Such a transition characterizes the two topological phases of the original SSH model, and results from a bandgap closing at $q = \pm\pi/d$. The second TPT, indicated by a red dashed line, arises at $L_x = L_x^{\mathrm{Zak}}$ [see Eq. (4.62)], and is solely induced by the strong light-matter coupling which leads to a bandgap closing at $q = 0$ [see Fig. 4.7(b)].

Due to this cavity-induced transition, the nontrivial and trivial phases of the model in the weak-coupling regime (lower and upper left regions in Fig. 4.8), which, notably, are similar to that of the original SSH model, are reversed in the strong-coupling regime (lower and upper right regions in Fig. 4.8).

Importantly, the cavity-induced TPT happens once the system is already metallic, since L_x^{Zak} (red dashed line in Fig. 4.8) is larger than L_x^{gap} (yellow dash-dotted line). Therefore, as will be discussed in the next section, while the dimerization-induced TPT (solid black line) is associated with the presence or absence of edge states as in the original SSH model, the cavity-induced TPT (red dashed line) does not influence the presence (or absence) of edge states. This led Ref. [136] to conclude on the breakdown of the bulk-edge correspondence for this system.[7] We note that as chiral symmetry is broken in the system, the bulk-edge correspondence from the tenfold way may not be relevant to consider. Rather, it may be more pertinent to examine the surface charge theorem, which is applicable to inversion-symmetric systems [235]. Such a study is however out of the scope of the present manuscript.

Analogous behaviors have been observed theoretically in similar bipartite systems, from driven ultracold fermions [208] to zigzag waveguide lattices [209], toy models with next-nearest-neighbor hopping [211], plasmonic nanoparticles in vacuum [212], or quantum antiferromagnets [214]. Using zigzag waveguide lattices, the presence of a nontrivial quantized Zak phase associated with the absence of edge states (that is, what we observe in our model in the lower right region in Fig. 4.8) has been recently experimentally detected [219]. The common feature of the systems studied in Refs. [208, 209, 211, 212, 214, 219] is that there is a coupling parameter breaking the chiral symmetry, which, once enhanced, leads one of the bulk band to increasingly fill the energy gap. In our polaritonic system, such parameter is the transverse dimension of the cavity, which allows one to tune the effective photon-mediated dipole-dipole coupling.

4.4.2 Winding number approach

To conclude our study of the topological phases of the polaritonic SSH model (4.31), we provide a graphical treatment of its bulk topological properties. To this aim, we take advantage of our two-band effective Hamiltonian (4.56) to compute the winding number ν of the system. While such winding number is formally well-defined as a topological invariant for chiral-symmetric

---

[7] Note that in an (unphysical) model which would conserve chiral symmetry, i.e., Hamiltonian (4.56) with $\tilde{f}_q = 0$, such cavity-induced TPT would *not* break the bulk-edge correspondence, since $L_x^{\mathrm{edge}} = L_x^{\mathrm{gap}} = L_x^{\mathrm{Zak}}$, so that the system remains in an “insulating" phase, except at the critical transition point.

Hamiltonians only, it can still give us valuable information on the topological phases of the system thanks to a graphical representation.

We rewrite the Bloch Hamiltonian (4.56) as

$$\tilde{\mathcal{H}}_q = \hbar \begin{pmatrix} \omega_0 + \Omega \tilde{f}_q & \Omega \tilde{g}_q \\ \Omega \tilde{g}_q^* & \omega_0 + \Omega \tilde{f}_q \end{pmatrix} = \hbar(\omega_0 + \Omega \tilde{f}_q)\mathbb{1}_2 + \boldsymbol{\sigma} \cdot \tilde{\mathbf{d}}_q, \tag{4.64}$$

with the 2×2 identity matrix $\mathbb{1}_2$, the Pauli vector $\boldsymbol{\sigma} = (\sigma_x, \sigma_y, \sigma_z)$, and the winding vector

$$\tilde{\mathbf{d}}_q = \hbar\Omega|\tilde{g}_q| \begin{pmatrix} \cos\tilde{\phi}_q \\ -\sin\tilde{\phi}_q \\ 0 \end{pmatrix}, \tag{4.65}$$

where the phase $\tilde{\phi}_q$ is given in Eq. (4.60).

The direction in which such winding vector points encodes the internal structure of the Bloch eigenstates (4.59) of the Hamiltonian (4.64), which, we recall, do not depend on the chiral-breaking couplings $\tilde{f}_q$. Due to the $2\pi/d$-periodicity of the Bloch Hamiltonian, the winding vector $\tilde{\mathbf{d}}_q$ traces out a closed curve in the plane (d_x, d_y) when the wavenumber q runs through the whole Brillouin zone $[-\pi/d, +\pi/d]$. The number of times such closed loop winds counterclockwisely around the origin $(0, 0)$ defines what is called the bulk winding number ν of the curve, an integer that characterizes, as the Zak phase (4.63), the topology of the Hamiltonian [34].

This graphical representation of the model topology is presented in Fig. 4.9, as parametric plots of the winding vector (4.65) in the (d_x, d_y) plane. Four different cases, corresponding to the four different frames observed in the Zak phase diagram of Fig. 4.8, are considered. First, in panels (a) and (b) of Fig. 4.9, the dimerization $\epsilon = 0.25$, so that we place ourselves at the top of the Zak phase diagram of Fig. 4.8. In panel (a), the weak-coupling regime is considered, with a cavity height $L_x = 7a$, and we observe a bulk winding number $\nu = 1$, indicating a topologically nontrivial phase. In contrast, in panel (b), the system is in the strong-coupling regime, with $L_x = 10a$, and a value of $\nu = 0$ is observed. As anticipated, such values of the bulk winding numbers are in exact agreement with the computation of the Zak phase (4.63).

Then, in panels (c) and (d) of Fig. 4.9, the dimerization $\epsilon = -0.25$, so that we place ourselves at the bottom of the Zak phase diagram Fig. 4.8. While panel (c) shows the winding vector for a cavity height $L_x = 7a$, panel (d) represents the case of $L_x = 10a$. Here, the weak-coupling regime case presents a value of $\nu = 0$, while the strong-coupling regime ones a value of $\nu = 1$. Again, this is in exact agreement with the results of the Zak phase computation discussed in Sec. 4.4.1.

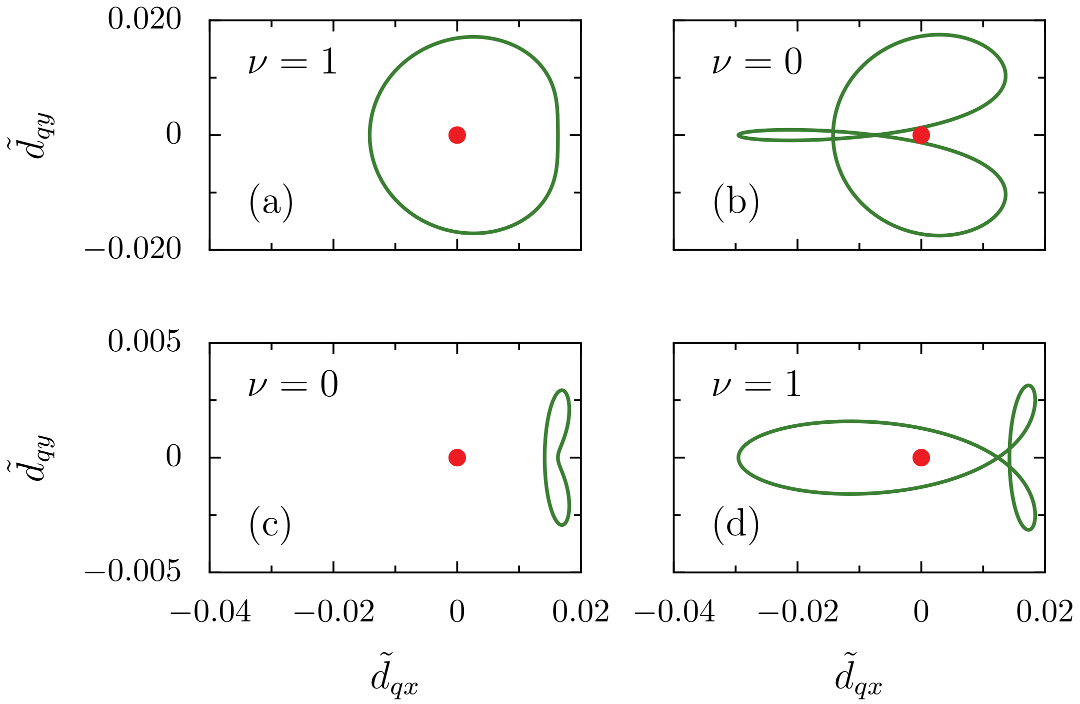

Figure 4.9: Winding number. Winding vector $\tilde{\mathbf{d}}_q$ in the first Brillouin zone [see Eq. (4.65)], and corresponding winding number ν, i.e., the number of time the winding vector encircles (counterclockwise) the origin $(0, 0)$ marked by a red dot. The four panels (a)-(d) show the four different topological phases visible in Fig. 4.8. The considered parameters are $\epsilon = 0.25$ in panels (a),(b) and $\epsilon = -0.25$ in panels (c),(d), while $L_x = 7a$ in panels (a),(c) and $L_x = 10a$ in panels (b),(d). In the figure, the Umklapp index $l \in [-l_{\max}, +l_{\max}]$ with $l_{\max} = 100$.

4.5 Multiple polaritonic edge states

We now move to a discussion of the properties of the finite polaritonic SSH chain. We recall that we here consider a finite chain of dipoles embedded in an infinitely-long waveguide cavity, in contrast to what was done in Ref. [136]. This has a drastic impact on the edge states which we study in this section, as we will show in Sec. 4.8.

To determine the spectral properties of the finite system, we write the real-space effective bipartite Hamiltonian $\tilde{\mathrm{H}}_{\mathrm{dp}}^{\mathrm{RWA},=}$, given in Eq. (4.36), in a $2\mathcal{N} \times 2\mathcal{N}$ matrix form using the basis vector $\boldsymbol{\varphi}^\dagger = (a_1^\dagger, \ldots, a_{\mathcal{N}}^\dagger, b_1^\dagger, \ldots, b_{\mathcal{N}}^\dagger)$, and we numerically diagonalize it to obtain its polaritonic eigenfrequencies $\tilde{\omega}_n^{\mathrm{dp}}$ and eigenvectors $\boldsymbol{\Psi}(n) = (\Psi_1(n), \ldots, \Psi_{2\mathcal{N}}(n))$, where n labels the eigenvalues in ascending order.

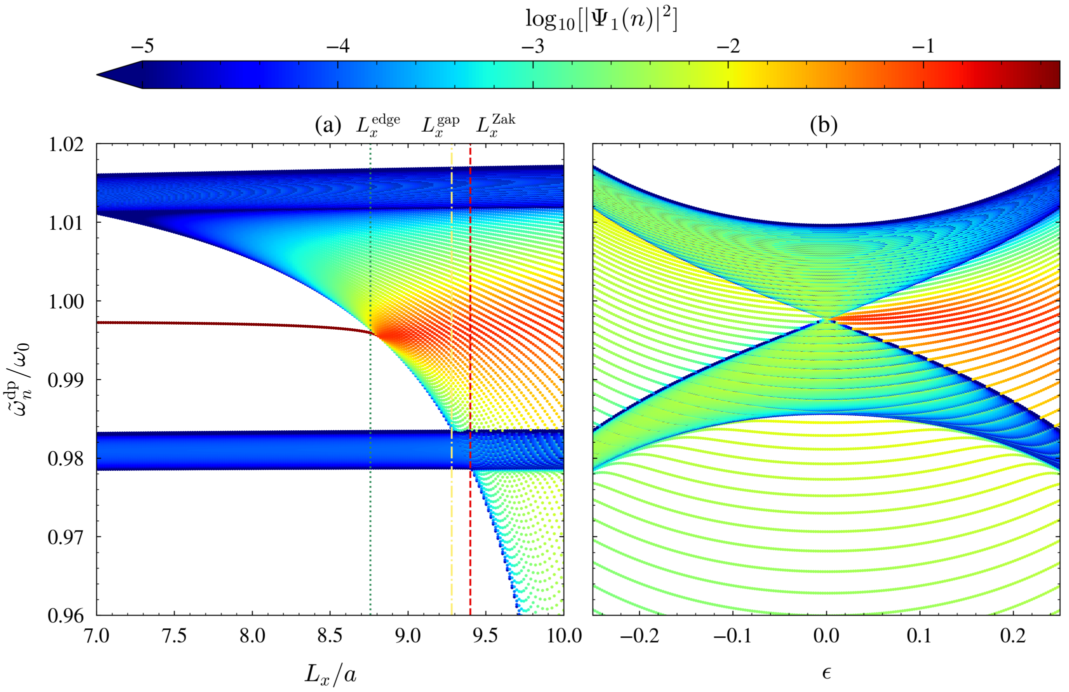

Figure 4.10: Finite polaritonic eigenspectrum. Real-space polaritonic eigenfrequencies $\tilde{\omega}_n^{\rm dp}$ (in units of the bare dipole frequency ω_0) as a function of (a) the cavity height L_x and (b) the dimerization parameter ϵ [Eq. (4.3)]. The color code associated with each eigenstate n represents its probability density on the first dipole site $i = 1$, so that it highlights the presence (red) or absence (green or blue) of edge states. We fix the dimerization parameter to $\epsilon = 0.25$ in panel (a), while the cavity height $L_x = 10a$ in panel (b), and we consider a finite chain of $\mathcal{N} = 250$ dimers, i.e., 500 dipoles.

4.5.1 Eigenspectrum

We show the result of the procedure discussed above in Fig. 4.10, where the eigenfrequencies are plotted as a function of the cavity height L_x in panel (a) and as a function of the dimerization parameter ϵ in panel (b). As in Fig. 4.2, we highlight the presence or absence of edge states through a color code associated to each eigenstate n, which represents its probability density $|\Psi_1(n)|^2$ on the first site of the chain, on a logarithmic scale.

In Fig. 4.10(a), we consider a dimerization $\epsilon = 0.25$, corresponding to the topological sector of the original as well as dipolar SSH model. On the left of the figure, the weak light-matter coupling regime is considered, where the two dipolar bands are only slightly renormalized by the cavity photons [cf. Fig. 4.7(a) for the Fourier-space equivalent]. The blue color associated with these two dipolar bands reveals no particular localization on the first site of the chain. However, two (nearly degenerate) in-gap edge states are visible in dark red, showing their pronounced localization on the first dipole site. By comparison with the preceding discussion on the bulk topological invariant in Sec. 4.4 such a situation corresponds to the upper left region of Fig. 4.8, where a nontrivial Zak phase is found. We have checked (not shown) that for $\epsilon < 0$, there are, as expected, no such edge states. In the weak-coupling regime, the bulk-edge correspondence is thus fulfilled, two edge states being present while the two dipolar bands each present a Zak phase of $\tilde{\vartheta}^{\mathrm{Zak}} = \pi$. Nevertheless, we emphasize that these two dipolar edge states are not symmetry-protected topological edge states as the ones found in the original, chiral-symmetric, SSH model. Indeed, we recall that due to the quasistatic dipole-dipole coupling from Eq. (4.18a), the system does not fulfill chiral symmetry, even in the absence of light-matter coupling.

By increasing the cavity height L_x in Fig. 4.10(a), the lower, dark band is not affected by the light-matter coupling and its edge localization remains constant. However, the upper band continuously fills the gap, as seen through the avoided crossing scheme with the photonic band in the bulk spectrum [cf. Figs. 4.7(b) and 4.7(c)]. As demonstrated using the full polaritonic model in Fig. 4.6, the states filling the gap are genuine polaritons, arising from the hybridization of the dipoles with cavity photons. The two dipolar edge states, however, are only slightly redshifted in energy when increasing the cavity height, mainly due to the renormalization of the bare frequency ω_0 into $\tilde{\omega}_0 \simeq 0.998\omega_0$, [see Eqs. (4.37a) and (4.41) for an analytical expression of the redshift]. Physically, we attribute this weak change to the fact that the edge states are mainly dark.

As can be seen from Fig. 4.10(a), the fact that the dipolar edge states and the upper bright band are not similarly shifted in energy as we increase the cavity height allows the polaritons that comprise the latter band to reach the edge state eigenfrequencies. Such merging of the dipolar edge states into the bright band arises at a cavity height L_x^{edge}, marked as a green dotted line. From this particular cavity height on, we observe the formal disappearance of the two dipolar edge states. Nevertheless, all of the polaritons belonging to the bright band with an eigenfrequency close to that of the edge states inherit their edge localization, as visible through the red spot on the right of Fig. 4.10(a), which grows as the cavity height is further increased. We coin these particular states “polaritonic edge states”. As we will see in the following, such peculiar states share some of their properties with the original edge states, but also of photonic states originating from the cavity.

From two very localized and nearly degenerated in-gap edge states in the weak-coupling regime, we thus get in the strong-coupling regime numerous polaritonic edge states that are present in a broad frequency range in the bulk of the spectrum. We insist, however, on the fact that this transition from two dipolar to multiple polaritonic edge states does not represent a TPT. Indeed, it is not associated with a change of bulk topological invariant, as visible in Fig. 4.8.

The above-discussed results contrast with what we observe while computing the bulk topological invariant in Sec. 4.4 Indeed, for cavity heights $L_x^{\mathrm{edge}} < L_x < L_x^{\mathrm{Zak}}$, a nontrivial Zak phase of π is found (see the upper left region in Fig. 4.8), while numerous polaritonic edge states are present. Thus, the bulk-edge correspondence in term of *number* of edge states is not anymore satisfied. Moreover, the TPT visible as a red dashed line for $L_x = L_x^{\text{Zak}}$ does not interfere with the polaritonic edge states which we observe in the finite spectrum of Fig. 4.10(a). We attribute the latter breakdown of the bulk-edge correspondence to the fact that the TPT takes place in a system which is already metallic, as $L_x^{\text{Zak}} > L_x^{\text{gap}}$, the gap having been closed by the complete chiral symmetry breaking induced by the light-matter coupling.

In Fig. 4.10(b), we investigate the effect of the dimerization parameter ϵ, and consider the strong light-matter coupling regime with a cavity height $L_x = 10a > L_x^{\text{Zak}}$. We observe here the absence of edge states when $\epsilon < 0$, as it is the case in the usual or dipolar SSH model. Looking at the two right frames of the Zak phase diagram in Fig. 4.8, the bulk invariant indicates however a topological phase for $\epsilon < 0$. Therefore, the bulk-edge correspondence is again not verified here. We note that such situation (nontrivial bulk topological invariant and absence of edge states) has been experimentally observed in an SSH system that preserves inversion but breaks chiral symmetry [219], similarly as here.

When $\epsilon > 0$, we find ourselves in the case studied previously on the right side of Fig. 4.10(a), and we observe that increasing the dimerization parameter ϵ enlarges the energy window in which polaritonic states inherit edge localization.

4.5.2 Participation ratio and scaling with the system size

To study in detail the polaritonic edge states and to maximize the frequency range where they appear, we consider in the following a dimerization $\epsilon = 0.25$ and a cavity height $L_x = 10a$. To better characterize their localization properties, we use the participation ratio (PR), already defined in Eq. 3.5, and which, in the system studied in this chapter, reads

$$\mathrm{PR}(n) = \frac{\left(\sum_{i=1}^{2\mathcal{N}} |\Psi_i(n)|^2\right)^2}{\sum_{i=1}^{2\mathcal{N}} |\Psi_i(n)|^4}. \tag{4.66}$$

We recall that such a quantity provides information on the typical number of dipole sites i occupied by an eigenstate n.

Our results are displayed in Fig. 4.11 for a chain of $\mathcal{N} = 250$ dimers, where the eigenfrequencies are plotted as a function of the PR on a logarithmic scale, with the color code representing again the probability density at the first site. Interestingly, the PR of the polaritonic edge states, visible as colored dots from light blue to dark red, follows a bell-shaped curve approximately centered around the eigenfrequency that corresponds to the edge states in the weak-coupling regime ($\tilde{\omega}_n^{\text{dp}} \simeq 0.998\omega_0$). Within the parameters used in the figure, we observe here 8 polaritonic edge states for which at least 5 % of the probability density is found on the first site of the chain only, distributed in a

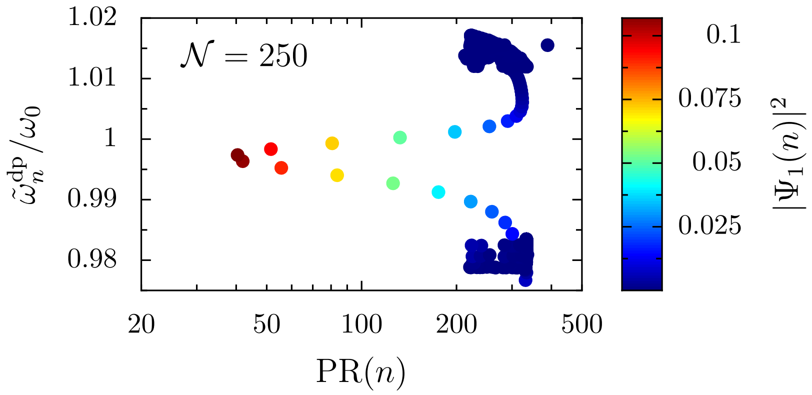

Figure 4.11: Polaritonic edge states participation ratio. Real-space polaritonic eigenfrequencies $\tilde{\omega}_n^{\mathrm{dp}}/\omega_0$ as a function of the participation ratio $\mathrm{PR}(n)$, as defined in Eq. (4.66). The colorscale represents the corresponding probability density on the first site, $i = 1$, of the chain. In the figure, the cavity height $L_x = 10a$, the dimerization parameter $\epsilon = 0.25$, and the chain is comprised of $\mathcal{N} = 250$ dimers.

frequency window of about $0.01\omega_0$. However, their PR contrasts with that of an edge state in the original SSH model or in the weak-coupling regime, here taking large values in between about 40 and 200, instead of approximately 2.

This difference is illustrated in Fig. 4.12(a), where we plot the scaling of the participation ratio $\mathrm{PR}(n)$ with the number of dimers $\mathcal{N}$, for the 6 polaritonic edge states with the lowest PR (colored dots), as well as for the two dipolar edge states present in the weak-coupling regime [visible on the left of Fig. 4.10(a)], for a cavity height $L_x = 7a$ (dark red triangles). Extended states, i.e., states with a localization length larger than the system, are characterized by a PR scaling linearly with the number of dimers $\mathcal{N}$, while the PR of states that are formally localized must be size-independent. Following such classification, one observes in Fig. 4.12(a) that the polaritonic edge states are not formally localized, their PR scaling with the system size, with a growth rate approaching the maximal one for a bipartite chain, $4(\mathcal{N}+1)/3$, shown as a black dashed line.

Such scaling with the PR is drastically different from the one we observe in the weak-coupling regime (dark red triangles), in which the edge states have a constant PR of about 2, as it is the case in the original SSH model [34]. This key difference between edge states in the weak- and strong-coupling regimes originates solely from the fact that in the latter case, polaritonic edge states feature a significant bulk part, induced by their hybridization with the cavity photons, and are therefore no longer only localized on the ends of the dipole chain, so that their localization length increases naturally with the size of the chain.

Moreover, while for small chain sizes a clear difference in PR is visible between each polaritonic edge states, such a dissimilarity fades out when the number of dimers $\mathcal{N}$ increases. We explain this behavior by the increasing

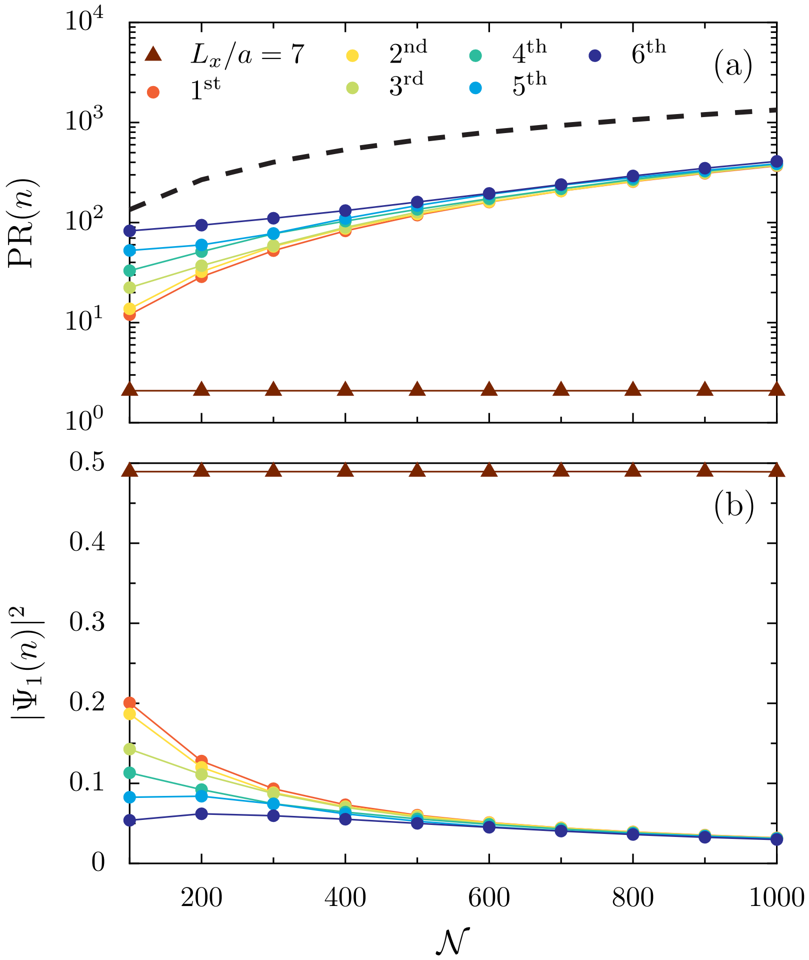

Figure 4.12: Impact of the system size. Scaling of (a) the participation ratio and (b) the probability density on the first site with the number of dimers $\mathcal{N}$. The dark red triangles correspond to the dipolar edge states present in the weak-coupling regime, with a cavity height $L_x = 7a$ [cf. Fig. 4.10(a)]. The colored dots correspond to the first six states with the lowest participation ratio in the strong-coupling regime, with a cavity height $L_x = 10a$. The black dashed line in panel (a) shows the maximum growth rate of the PR for a bipartite chain, $4(\mathcal{N}+1)/3$. In the figure, the dimerization parameter $\epsilon = 0.25$.

number of polaritonic edge states when the size of the chain increases. Indeed, as the density of states with an eigenfrequency around $\tilde{\omega}_0$ increases, the number of polaritonic states which resonate with the original edge states, and hence which inherit their edge localization, grows. The 6 states we show in Fig. 4.12(a) are therefore more and more similar as $\mathcal{N}$ increases.

In Fig. 4.12(b), we present our results for the scaling of the probability density on the first site of the chain $|\Psi_1(n)|^2$ with the number of dimers $\mathcal{N}$, for the same states as in Fig. 4.12(a). In the weak-coupling regime, as in the original SSH model, almost half of the probability density of the edge states is located

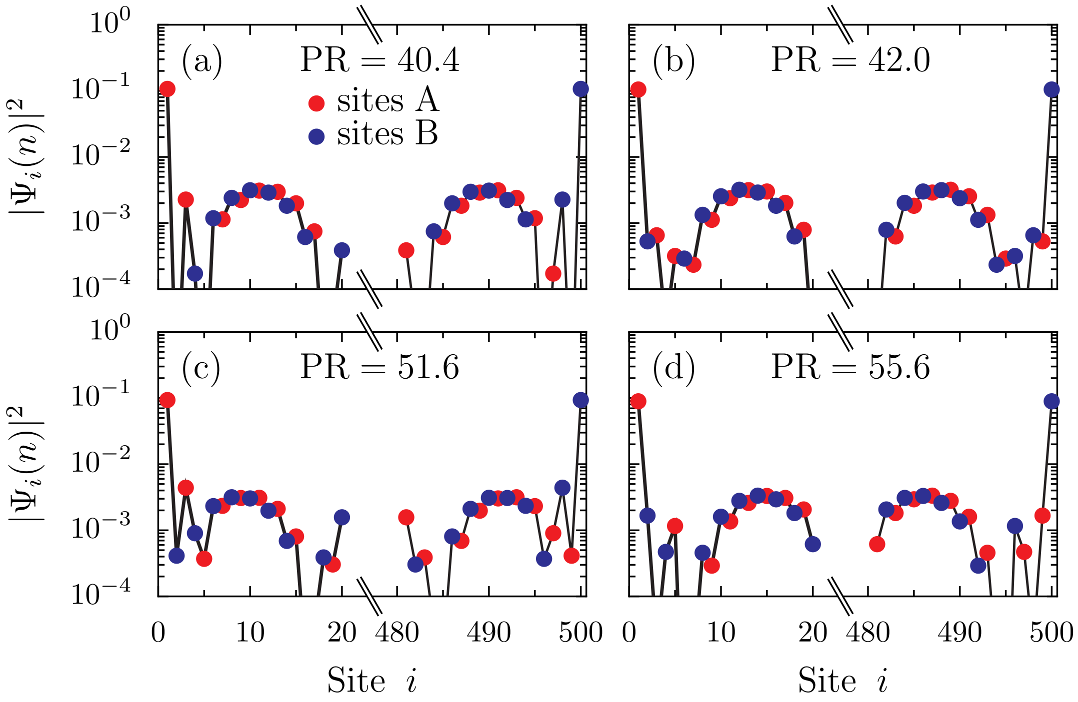

Figure 4.13: Shape of the polaritonic edge states. Probability density $|\Psi_i(n)|^2$ along the sites i of a chain comprised of $\mathcal{N} = 250$ dimers, for the states n with (a) the first, (b) second, (c) third, and (d) fourth lowest participation ratio. The red and blue dots represent, respectively, sites belonging to the A and B sublattices. The cavity height $L_x = 10a$ and the dimerization $\epsilon = 0.25$.

on the first site of the chain (the other half being localized on the last site), independently of the system size. In the strong-coupling regime, however, the situation is less usual. While for small system sizes, a fifth of the probability density of some polaritonic edge states can be located on the first site of the chain only, such fraction decreases and slowly tends towards a few percents, when the chain becomes longer.

Similarly to the scaling of the PR, such a behavior is explained by the growing number of polaritonic edge states when the system size increases. This leads the edge localization to be shared between more and more polaritonic edge states. Interestingly, we will demonstrate in Sec. 4.6 that despite this diffusion of the edge localization between numerous states, driven-dissipative transport simulations with lossy dipoles, taking into account the linewidth of the excitations, allow these polaritonic edge states to be probed.

4.5.3 Polaritonic edge states

To conclude this section, and before studying the transport properties of the polaritonic edge states, we here discuss their shape in real space. For this purpose, the probability density along a chain of $\mathcal{N} = 250$ dimers is shown in Fig. 4.13 in the strong-coupling regime ($L_x = 10a$) and for $\epsilon = 0.25$, for the

4 most localized states with the lowest PR. The probability density is represented on a logarithmic scale, while the horizontal axis has been truncated to focus on the edges of the chain. The red (blue) points correspond to sites belonging to the A (B) sublattice. One observes that these 4 polaritonic states display a clear localization on their edges, with more than an order of magnitude higher than their probability density in the bulk of the chain.

Two distinct regimes of spatial extensions are apparent on each of these states. First, on the first few and last few sites, the states are exponentially localized on the edges, with for some of the states an alternation between sites A and B, as is the case of the chirally-symmetric topological edge states of the original SSH model. Second, in the bulk of the chain we observe a non-negligible probability density, evenly distributed along the chain, similarly to extended plane waves. While the first regime is reminiscent of topological edge states of the original SSH model, the second demonstrates the polaritonic nature of these states, having inherited the delocalized, plane-wave nature of the cavity photons.

4.6 Edge state transport

To relate the results obtained in Sec. 4.5 with measurable quantities, here we investigate the transport of excitations in the polaritonic SSH model. Specifically, we focus on the potential contribution of edge states on energy transport throughout the chain, which has been recently unveiled experimentally [236] and theoretically investigated with the help of a simplified Tavis-Cummings model [223].

We use a similar approach to that used when studying transport of ordered and disordered polaritons in Chap. 3 (see Sec. 3.6), and consider a driven-dissipative scenario by adding the driving term

$$\mathrm{H}_{\mathrm{drive}}(t) = \hbar\Omega_{\mathrm{R}} \sin(\omega_{\mathrm{d}} t) \left(a_1 + a_1^\dagger\right) \tag{4.67}$$

to the effective Hamiltonian (4.36). The equation above models the continuous illumination of the first dipole site, which belongs to the A sublattice, by a transversely polarized monochromatic electric field with amplitude E_0 and driving frequency ω_{d}, with $\Omega_{\mathrm{R}} = E_0\sqrt{Q^2/2M\hbar\omega_0}$ the corresponding Rabi frequency. We assume that the dynamics can be described by the Lindblad master equation for the density matrix

$$\begin{aligned}\dot{\rho} = \frac{\mathrm{i}}{\hbar}&\left[\rho, \tilde{\mathrm{H}}_{\mathrm{dp}}^{\mathrm{RWA},=} + \mathrm{H}_{\mathrm{drive}}(t)\right] \\ &- \frac{\gamma}{2}\sum_{m=1}^{\mathcal{N}}\left(\left\{a_m^\dagger a_m + b_m^\dagger b_m, \rho\right\} - 2a_m\rho a_m^\dagger - 2b_m\rho b_m^\dagger\right).\end{aligned} \tag{4.68}$$

As in Sec. 3.6, the damping rate γ quantifies the influence of a phenomenological Markovian bath responsible for the dissipation of the dipolar emitters.

Dissipation typically originates from radiative and Ohmic losses, and in this chapter, we consider $\gamma = 0.002\omega_0$. Such a narrow linewidth can be achieved experimentally using emitters with weak losses, such as, e.g., microwave resonators or dielectric and SiC nanoparticles [124, 129].

To characterize the excitation of an emitter belonging to the A (B) sublattice, we introduce its dimensionless dipole moment $p_m^A = \langle a_m + a_m^\dagger \rangle$ ($p_m^B = \langle b_m + b_m^\dagger \rangle$). Solving the master equation (4.68), employing a similar method as the one we detailed in Sec. 3.6.1, we obtain the steady-state amplitudes $|p_i|$ bared by a dipole on the site i of the chain, which belongs either to the A or B sublattice. We recall that these dimensionless amplitudes are proportional to the square root of the power radiated in the far field by a dipole, through the classical Larmor formula [119], as shown in Eq. (3.23).

Figure 4.14 displays our findings for the steady-state amplitudes $|p_i|$ of the dipole moments, scaled by the Rabi frequency in units of the bare dipole frequency, $\Omega_\mathrm{R}/\omega_0$, and as a function of the sites i of a chain comprised of $\mathcal{N} = 100$ dimers. The first site is driven at a frequency $\omega_\mathrm{d} = 0.998\omega_0 \simeq \tilde{\omega}_0^=$, corresponding approximately to the edge state eigenfrequencies in the weak-coupling regime. The propagation signals are shown in a log-linear plot for both the weak- ($L_x/a = 7$) and strong-coupling ($L_x/a = 10$) regimes, by red and blue symbols, respectively.

In Fig. 4.14(a) we consider a dimerization parameter $\epsilon = +0.25$. Edge states are clearly visible in both coupling regimes, through a large rise of the excitation at the end of the chain, the dipole moment increasing there by one order of magnitude. In the first few sites of the chain, the propagation signal quickly decays for both coupling regimes, following an exponential decay which is reminiscent of the nearest-neighbor dipole-dipole coupling [175]. However, for longer distances, the transport characteristics are very distinct. On the one hand, for $L_x/a = 7$ (red dots), we observe a steep quasi-exponential decay, induced by the light-matter coupling, followed by an algebraic tail decaying with the inverse distance cubed, arising from the quasistatic dipole-dipole coupling. On the other hand, for $L_x/a = 10$ (blue dots), the propagation follows an exponential decay with a large decay length, rendering the decay profile nearly flat.

This second exponential decay originates solely from the cavity-induced effective dipole-dipole coupling (see Sec. 4.2). Such a decay is physically explained by the hybridization of the bright, upper dipolar band with cavity photons, and stands for the polaritonic cavity-enhanced transport unveiled in Chap. 3. It is the exact same phenomenon as we observed for ordered and disordered polaritonic transport in Sec. 3.6, which gives rise to cavity- and disorder-enhanced transport. The slope in a log-linear plot of such a cavity-induced exponential decay is dictated by both the damping rate γ and the cavity height L_x, becoming flatter as the latter increases. Therefore, the driving of the polaritonic edge states plotted as blue dots in Fig. 4.14(a) presents interesting transport characteristics, allowing for efficient end-to-end edge state transport, as opposed to what is observed in red for the dipolar edge

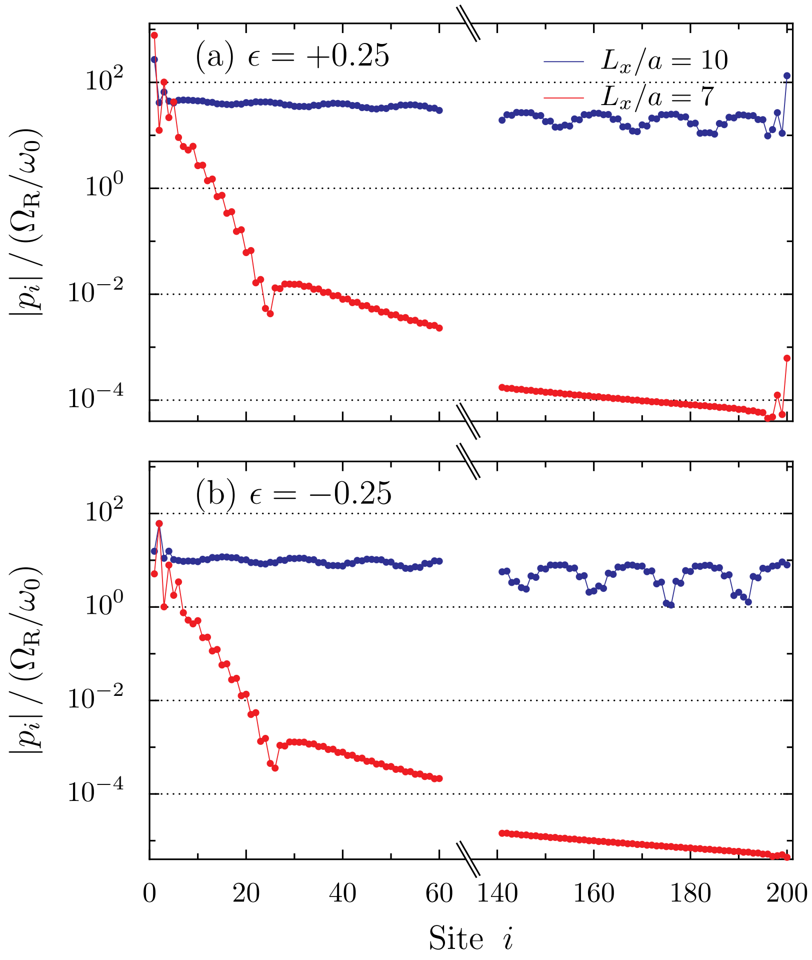

Figure 4.14: Edge state transport. Steady-state amplitude of the dipole moment $|p_i|$ (in units of $\Omega_\mathrm{R}/\omega_0$) as a function of the dipole site i, for a chain with dimerization (a) $\epsilon = +0.25$ and (b) $\epsilon = -0.25$. The red (blue) symbols correspond to the weak- (strong-)coupling regime, with a cavity height $L_x = 7a$ ($L_x = 10a$). The propagation results from a monochromatic drive on the first dipole site at a frequency $\omega_\mathrm{d} = 0.998\omega_0$. The chain is comprised of $\mathcal{N} = 100$ dimers with damping rates $\gamma = 0.002\omega_0$.

state. We note that for very long chains or more lossy dipoles, the algebraic tail is also present in the polaritonic transport, as discussed in Chap. 3.

In Fig. 4.14(b), we study the propagation along the chain when the first dipole is driven at the same frequency $\omega_\mathrm{d} = 0.998\omega_0$, now for $\epsilon = -0.25$. As discussed in the previous section, such negative value of the dimerization ϵ is associated with the absence of edge states. The same transport regimes as in Fig. 4.14(a) are observed, but no rise of the dipole moment is found at the end of the chain. Moreover, there is an overall decrease of the dipole moment amplitudes along the chain as compared to the $\epsilon = +0.25$ case. This is in agreement with the so-called dimerization-assisted transport that has been studied in detail in Ref. [223].

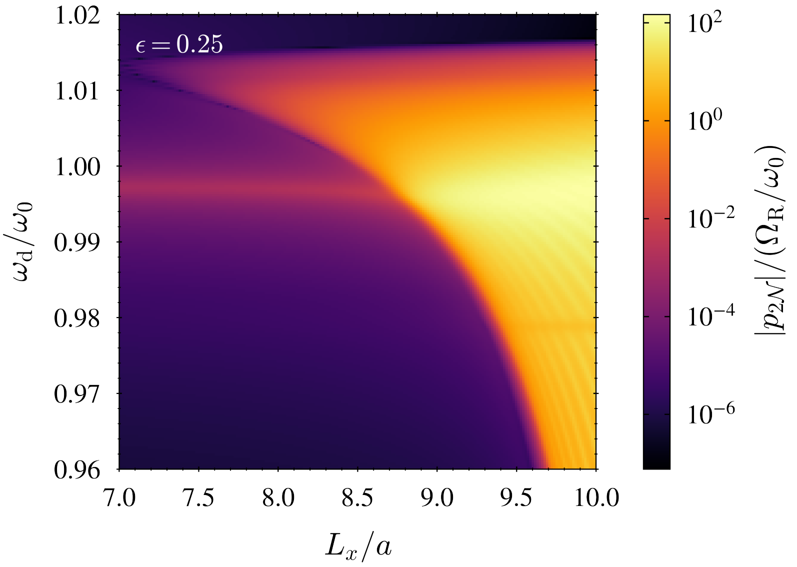

Figure 4.15: End-to-end transport. Steady-state amplitude of the last dipole moment of the chain $|p_{2\mathcal{N}}|$ (in units of $\Omega_\mathrm{R}/\omega_0$), for increasing cavity heights L_x/a and driving frequencies $\omega_\mathrm{d}/\omega_0$. In the figure, $\mathcal{N} = 100$, $\epsilon = 0.25$, and $\gamma = 0.002\omega_0$.

To highlight the effect of the cavity on end-to-end transport, we display in Fig. 4.15 a density plot of the normalized steady-state amplitude of the last dipole moment of the chain, $|p_{2\mathcal{N}}|/(\Omega_\mathrm{R}/\omega_0)$, using a logarithmic scale, as a function of both the cavity height L_x/a and the driving frequency $\omega_\mathrm{d}/\omega_0$. A chain of $\mathcal{N} = 100$ dimers with a dimerization $\epsilon = 0.25$ is considered. Interestingly, Fig. 4.15 has similarities with Fig. 4.10(a), which shows the probability density of the eigenstates at one end of the chain as a function of the cavity height, with a dimerization parameter also fixed to the same value as here. Hence, we recover the properties of the spectrum in our transport simulations.

The light orange layer on the right of Fig. 4.15 in the strong-coupling regime corresponds to the driving of the polaritons that originate from the bright, upper dipolar band which is continuously redshifted when the cavity height is increased [as seen in Fig. 4.10(a)]. Owing from their polaritonic nature, they feature enhanced transport characteristics, notably through the cavity-induced exponential decay discussed above in Fig. 4.14, explaining their large dipole moment amplitude at the end of the chain. In contrast, when driving at a frequency corresponding to the bare dipolar bands in the weak-coupling regime [around $\omega_\mathrm{d}/\omega_0 = 0.980$ and $\omega_\mathrm{d}/\omega_0 = 1.015$, cf. Fig. 4.10(a)], only a small dipole moment is found on the last site of the chain, demonstrating poor transport properties.

Examining driving frequencies around $\omega_\mathrm{d}/\omega_0 = 1$ in Fig. 4.15, we observe the presence of the edge states, which show a particularly large dipole moment at the end of the chain. Notably, in the weak-coupling regime, here for cavity heights $L_x \lesssim L_x^{\text{edge}} \simeq 8.7a$, the dipolar edge states appear as a dark orange beam in the center left of Fig. 4.15. In the strong-coupling regime, here for cavity heights $L_x \gtrsim L_x^{\text{edge}}$, the polaritonic edge states are visible through the bright yellow spot in the center right of Fig. 4.15. Crucially, we observe that the latter bright spot spreads over a broad range of driving frequencies.

Therefore, in addition to allowing very efficient edge state transport between the two ends of the chain, the cavity also largely broadens the edge state frequency band. These two cavity-induced properties could lead to easier edge state probing.

4.7 Robustness to disorder

To complement our study of the cavity-induced polaritonic edge states featured by the polaritonic SSH model (4.36), we now examine their robustness to disorder. To achieve this, we use the formalism developed in Chap. 3, where we included disorder, and apply it to the dimerized chain of emitters.

4.7.1 Off-diagonal positional disorder

We start by studying specifically the effect of disorder in the intra- and interdimer spacings d_1 and d_2 (see Fig. 4.5). This corresponds to off-diagonal disorder in our system. We assume these spacings to be uncorrelated random variables uniformly distributed within the interval $[d_{1,2}(1-\Delta), d_{1,2}(1+\Delta)]$, where the dimensionless parameter Δ is the amplitude of the spacing fluctuations and characterizes the disorder strength. At this stage, we do not consider any disorder in the frequencies of the emitters.

Interestingly, the introduction of off-diagonal disorder in the system does not break the chiral symmetry of the bipartite chain, so that it does not alter the topological edge states of the original (chirally-symmetric) SSH model [34]. However, as discussed in Secs. 4.1 and 4.2, due to the dipole-dipole couplings beyond nearest-neighbors the polaritonic SSH model does not fulfill chiral symmetry, both in the weak- and strong-coupling regimes. On the one hand, although being reminiscent of the chiral symmetry of the original SSH model, the polaritonic edge states should therefore not present any formal robustness against off-diagonal disorder. On the other hand, polaritons, through their photonic part, have been proven robust against disorder, presenting a cavity-protection effect [155, 157], which we discussed in detail in Chap. 3. The interplay between polaritonic edge states and disorder is thereby highly nontrivial.

We clarify this point by presenting in Fig. 4.16 the disorder-averaged real-space polaritonic eigenfrequencies $\tilde{\omega}_n^{\text{dp}}/\omega_0$ as a function of the dimensionless disorder strength Δ. These eigenfrequencies have been obtained through a numerical diagonalization of the disordered version of the effective Hamiltonian (4.36), which we do not show here. In the figure, we consider a chain

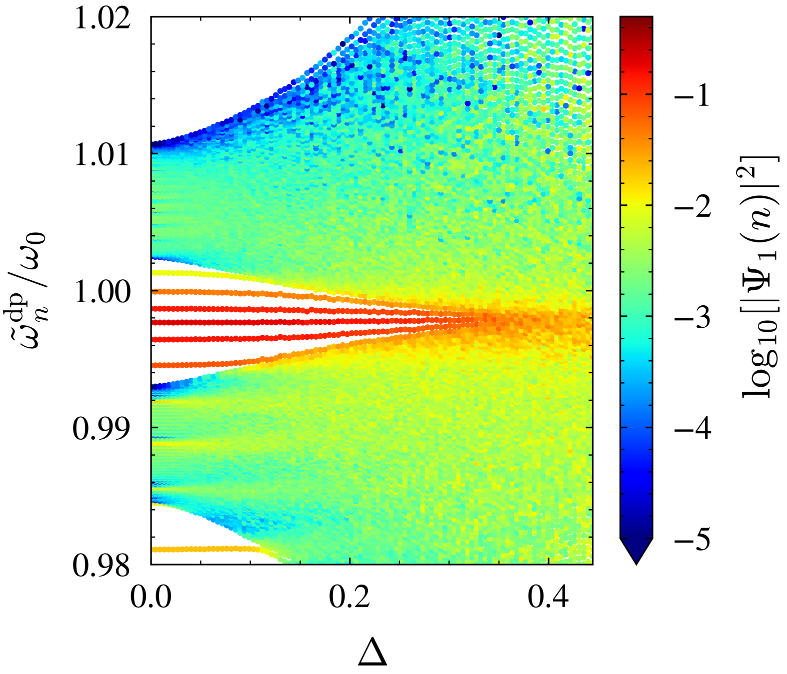

Figure 4.16: Effect of positional disorder. Real-space polaritonic eigenfrequencies $\tilde{\omega}_n^{\mathrm{dp}}$ (in units of the bare dipole frequency ω_0) as a function of the dimensionless disorder strength Δ. The color code associated with each eigenstate n represents its probability density on the first dipole site $i = 1$, so that it highlights the presence (red) or absence (green or blue) of edge states. A chain of $\mathcal{N} = 100$ dimers with an average value of the dimerization parameter $\epsilon = 0.1$ embedded in a waveguide cavity with height $L_x = 10a$ is considered, and the data have been averaged over 100 disorder realizations.

of $\mathcal{N} = 100$ dimers with an average dimerization parameter $\epsilon = 0.1$, embedded in a cavity with height $L_x = 10a$. As in Fig. 4.10, the color code displays, on a logarithmic scale, the probability density on the first dipole site $i = 1$ associated with each eigenstate n, so that it reveals the presence (red) or absence (green or blue) of states that are highly localized at the two ends of the chain.

We observe in Fig. 4.16 the characteristic bandwidth widening as the disorder strength increases. Importantly, only the dipolar eigenstates, corresponding to the eigenfrequencies of the bare dipolar bands, here around $\tilde{\omega}_n^{\mathrm{dp}}/\omega_0 = 0.990$ and $\tilde{\omega}_n^{\mathrm{dp}}/\omega_0 = 1.005$, undergo this effect. In contrast, the eigenfrequencies of the polaritonic states, that are highly renormalized by the cavity photons, remain constant on average at small disorder strength. The latter polaritons, showing the cavity-protection effect, are visible in Fig. 4.16 through the yellow stripes in the lower left region of the figure, as well as through the red stripes, showing the polaritonic edge states, around $\tilde{\omega}_n^{\mathrm{dp}}/\omega_0 = 1$. Such robustness of the polaritons against disorder fades out as they merge into the dipolar bands. As anticipated by the broken chiral symmetry, the polaritonic edge states (red stripes in Fig. 4.16) are therefore not formally robust against off-diagonal disorder, but can survive at high levels of disorder, with a large probability density of 0.1 on the first site up to $\Delta \simeq 0.25$ with the parameters considered in the figure. We attribute this tolerance to disorder both to their polaritonic nature and to their topological origin, being reminiscent of the topologically-protected edge states of the original, chiral-symmetric SSH model. Indeed, dipolar edge states present in the weak-coupling regime, although not being polaritonic, also show remarkable tolerance to off-diagonal disorder, up to the closing of the bandgap induced by the bandwidth increase led by disorder (not shown).

Interestingly, once the off-diagonal disorder is strong enough to let the polaritonic edge states merge into the dipolar bands, the dipolar states with eigenfrequencies close to that of the edge states inherit part of their edge localization, as apparent through the orange spot in the center right of Fig. 4.16. This mechanism bears resemblance to what gives rise to the polaritonic edge states, as we described in Sec. 4.5, i.e., the fact that edge and bulk states are not similarly affected by the increase of a given parameter (here the off-diagonal disorder strength Δ, in Sec. 4.5 the cavity height L_x).

4.7.2 Frequency disorder

We now investigate the impact of disorder in the bare individual frequencies of the emitters. As in Chap. 3, we treat these bare frequencies as uncorrelated random variables distributed uniformly within an interval $[\omega_0 - W/2, \omega_0 + W/2]$. The dimensionless parameter W/ω_0 therefore describes the frequency disorder strength.

In Fig. 4.17, we present the disorder-averaged real-space polaritonic eigenfrequencies $\tilde{\omega}_n^{\mathrm{dp}}/\omega_0$ as a function of the frequency disorder strength W/ω_0, obtained through a numerical diagonalization of a disordered version of the effective Hamiltonian (4.36), which we do not show here. The color code as well as the parameters used in the figure are the same as the ones used in the preceding subsection in Fig. 4.16. However, we exclude here any positional disorder by setting $\Delta = 0$.

We observe in Fig. 4.17 that already a small amount of disorder in the frequencies, namely $W/\omega_0 = 0.02$ which corresponds to a 1% deviation, closes the band gap. In contrast with what we observed for the positional disorder in Fig. 4.16, here the edge state localization is completely destroyed by the closing of the band gap, and when the edge states merge into the dipolar bands, no residual edge localization is found. This can be understood by the fact that, unlike positional disorder which preserved chiral symmetry, frequency disorder destroys all the symmetries of the Hamiltonian. Consequently, both the edge states and the bulk bands are affected in the same manner by the frequency disorder.

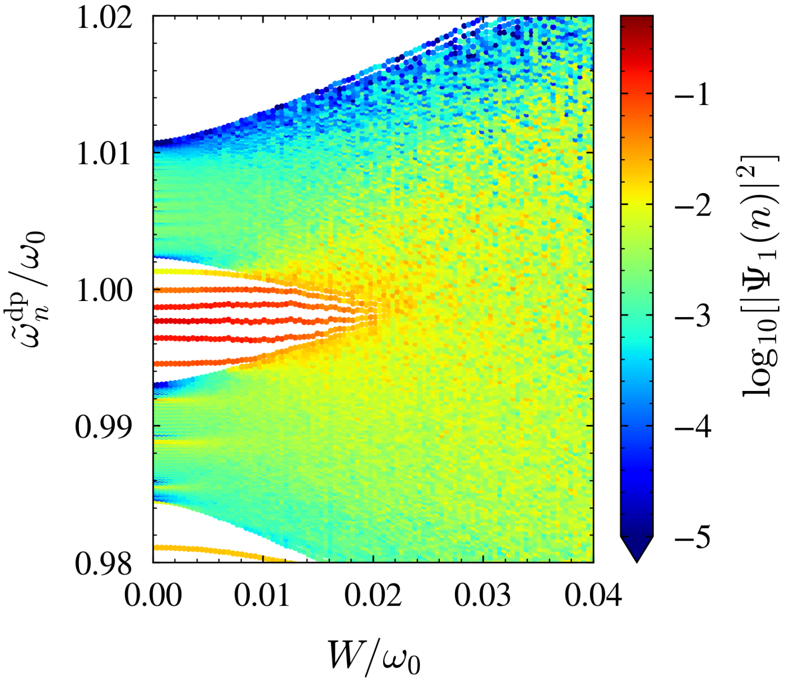

Figure 4.17: Effect of frequency disorder. Same quantities as in Fig. 4.16, but now as a function of the frequency disorder strength W/ω_0. In the figure, the dimensionless positional disorder strength $\Delta = 0$, the dimerization parameter $\epsilon = 0.1$, the cavity height $L_x = 10a$, a chain of $\mathcal{N} = 100$ dimers has been considered, and the data have been averaged over 100 disorder realizations.

4.8 Influence of the cavity walls

As presented in Sec. 4.2, we considered here a finite dipolar chain embedded in an infinite waveguide cavity. This amounted to consider a distance to the cavity walls $d_{\mathrm{cav}} \to \infty$, and is motivated by the fact that we are here interested in edge states, forming at the two ends of the dipolar chain, so that we want to avoid any possible boundary effect of the cavity walls in the z direction.

In a previous study of an SSH dipolar chain coupled to a multimode cavity [136], the authors considered a finite cuboidal cavity, with perfect mirrors in the z direction located at a distance $d_{\mathrm{cav}} = d - d_1/2$ of the two ends of the emitter array.

In this section, we demonstrate that such a distance to the cavity walls has a crucial impact on the formation of polaritonic edge states. Indeed, while the bulk spectra are the same, the polaritonic edge states we studied in this chapter are of a different nature from those observed in Ref. [136].

4.8.1 Schrieffer-Wolff transformation with a finite cuboidal cavity

To compare the finite spectrum and eigenstates of a dipolar SSH chain in an infinite waveguide cavity which we studied in Secs. 4.5, 4.6, and 4.7, to the ones of a dipolar SSH chain in a finite cuboidal box cavity, as studied in Ref. [136], we need to establish comparable models. To this aim, we start by deriving an effective Hamiltonian using a cuboidal cavity, akin to the effective Hamiltonian derived for the waveguide cavity in Sec. 4.2.2. Moreover, alongside this whole section, we neglect Umklapp processes, as they do not modify substantially the properties of the eigenspectrum and eigenstates, and were not considered in Ref. [136].

By adapting to the dipolar SSH chain (4.17) the formalism describing the light-matter coupling to a finite cuboidal cavity presented in Sec. 2.4, we obtain the Hamiltonian

$$\begin{aligned} \mathrm{H}_{\mathrm{pol}}^{\square} = {} & \hbar\omega_0 \sum_{m=1}^{\mathcal{N}} \left(a_m^\dagger a_m + b_m^\dagger b_m \right) + \hbar\Omega \sum_{m,m'=1}^{\mathcal{N}} g_{m-m'} \left(a_m^\dagger\, b_{m'} + a_m\, b_{m'}^\dagger \right) \\ & + \frac{\hbar\Omega}{2} \sum_{\substack{m,m'=1 \\ (m\neq m')}}^{\mathcal{N}} f_{m-m'} \left(a_m^\dagger\, a_{m'} + b_m^\dagger\, b_{m'} + a_m\, a_{m'}^\dagger + b_m\, b_{m'}^\dagger \right) \\ & + \mathrm{i}\hbar \sum_{m=1}^{\mathcal{N}} \sum_{n_z=1}^{N_z} \left[\xi_{mn_z}^{A,\square} \left(a_m^\dagger c_{n_z} - a_m c_{n_z}^\dagger \right) + \xi_{mn_z}^{B,\square} \left(b_m^\dagger c_{n_z} - b_m c_{n_z}^\dagger \right) \right] \\ & + \sum_{n_z=1}^{N_z} \hbar\omega_{n_z}^{\mathrm{ph}} c_{n_z}^\dagger c_{n_z}, \end{aligned} \tag{4.69}$$

with the dipolar coupling strength Ω [Eq. (2.23)], the bare dipolar intra- and inter-sublattice sums $f_{m-m'}$ and $g_{m-m'}$ [Eq. (4.18)], and the photonic dispersion $\omega_{n_z}^{\mathrm{ph}}$ [Eq. (2.48)]. In the above expression, the mode-dependent light-matter coupling functions acting on the A and B sublattices are

$$\xi_{mn_z}^{A,\square} = \omega_0 \sqrt{\frac{4\pi a^3 \omega_0}{L_x L_y L_z \omega_{n_z}^{\mathrm{ph}}}} \sin\left(\frac{\pi n_z}{L_z} z_m^A \right) \tag{4.70a}$$

and

$$\xi_{mn_z}^{B,\square} = \omega_0 \sqrt{\frac{4\pi a^3 \omega_0}{L_x L_y L_z \omega_{n_z}^{\mathrm{ph}}}} \sin\left(\frac{\pi n_z}{L_z} z_m^B \right), \tag{4.70b}$$

which depend, notably, on the coordinate z_m^A or z_m^B, given in Eq. (4.27), and on the cavity length $L_z = (\mathcal{N}-1)d + d_1 + 2d_{\mathrm{cav}}$. We recall that the number of photonic modes N_z is chosen such that the largest photonic wavenumber is $\max(k_z) = \pi N_z / L_z = \pi/d$. This amounts to neglect Umklapp processes. Here, for non-integer values of N_z, we truncate to $N_z = \lfloor L_z/d \rfloor$, with the help of the floor function $\lfloor x \rfloor$.

Performing next a Schrieffer-Wolff transformation, as done in Sec. 4.2.2, and focusing on the renormalized dipolar subspace, we obtain the effective Hamiltonian

$$\begin{aligned}\tilde{\mathrm{H}}_{\mathrm{dp}}^{\mathrm{RWA},\square} = &\sum_{m=1}^{\mathcal{N}} \left(\hbar\tilde{\omega}_m^{A,\square} a_m^{\dagger} a_m + \hbar\tilde{\omega}_m^{B,\square} b_m^{\dagger} b_m\right) \\ &+ \frac{\hbar\Omega}{2} \sum_{\substack{m,m'=1 \\ (m\neq m')}}^{\mathcal{N}} \left[\tilde{f}_{m-m'}^{A,\square}\left(a_m^{\dagger} a_{m'} + \mathrm{H.c.}\right) + \tilde{f}_{m-m'}^{B,\square}\left(b_m^{\dagger} b_{m'} + \mathrm{H.c.}\right)\right] \\ &+ \hbar\Omega \sum_{m,m'=1}^{\mathcal{N}} \tilde{g}_{m-m'}^{\square}\left(a_m^{\dagger} b_{m'} + \mathrm{H.c.}\right). \end{aligned} \tag{4.71}$$

Here, the onsite frequency ω_0 and the intra- and intersublattice sums $f_{m-m'}$ and $g_{m-m'}$ are renormalized by the cavity photons [compare with Eq. (4.17)] as

$$\tilde{\omega}_m^{A,\square} = \omega_0 - \sum_{n_z=1}^{N_z} \frac{\left(\xi_{mn_z}^{A,\square}\right)^2}{\omega_{n_z}^{\mathrm{ph}} - \omega_0}, \tag{4.72a}$$

$$\tilde{\omega}_m^{B,\square} = \omega_0 - \sum_{n_z=1}^{N_z} \frac{\left(\xi_{mn_z}^{B,\square}\right)^2}{\omega_{n_z}^{\mathrm{ph}} - \omega_0}, \tag{4.72b}$$

$$\tilde{f}_{m-m'}^{A,\square} = f_{m-m'} - \frac{1}{\Omega} \sum_{n_z=1}^{N_z} \frac{\xi_{mn_z}^{A,\square}\xi_{m'n_z}^{A,\square}}{\omega_{n_z}^{\mathrm{ph}} - \omega_0}, \tag{4.72c}$$

$$\tilde{f}_{m-m'}^{B,\square} = f_{m-m'} - \frac{1}{\Omega} \sum_{n_z=1}^{N_z} \frac{\xi_{mn_z}^{B,\square}\xi_{m'n_z}^{B,\square}}{\omega_{n_z}^{\mathrm{ph}} - \omega_0}, \tag{4.72d}$$

and

$$\tilde{g}_{m-m'}^{\square} = g_{m-m'} - \frac{1}{\Omega} \sum_{n_z=1}^{N_z} \frac{\xi_{mn_z}^{A,\square}\xi_{m'n_z}^{B,\square}}{\omega_{n_z}^{\mathrm{ph}} - \omega_0}. \tag{4.72e}$$

We note that, in contrast to the renormalization induced by a waveguide cavity [cf. Eq. (4.57)], here the A and B sites are modified unevenly, resulting in an asymmetry between the two sublattices and a formal lack of inversion symmetry within a single unit cell. This is in stark contrast to the effective Hamiltonian (4.36) of a finite chain in a waveguide cavity, which presents an inversion symmetry within each unit cell, in the sense that the same on-site frequency is associated to the A and B dipole sites of a given dimer, as it is the case when considering the thermodynamic limit for the bulk Hamiltonian [see the equal diagonal elements of the Bloch Hamiltonian Eq. (4.56)].

This observation highlights the fact that considering a cuboidal cavity to study the real-space finite polaritonic SSH model, as done in Ref. [136], may be misleading. Indeed, the real-space Hamiltonian with a cuboidal cavity

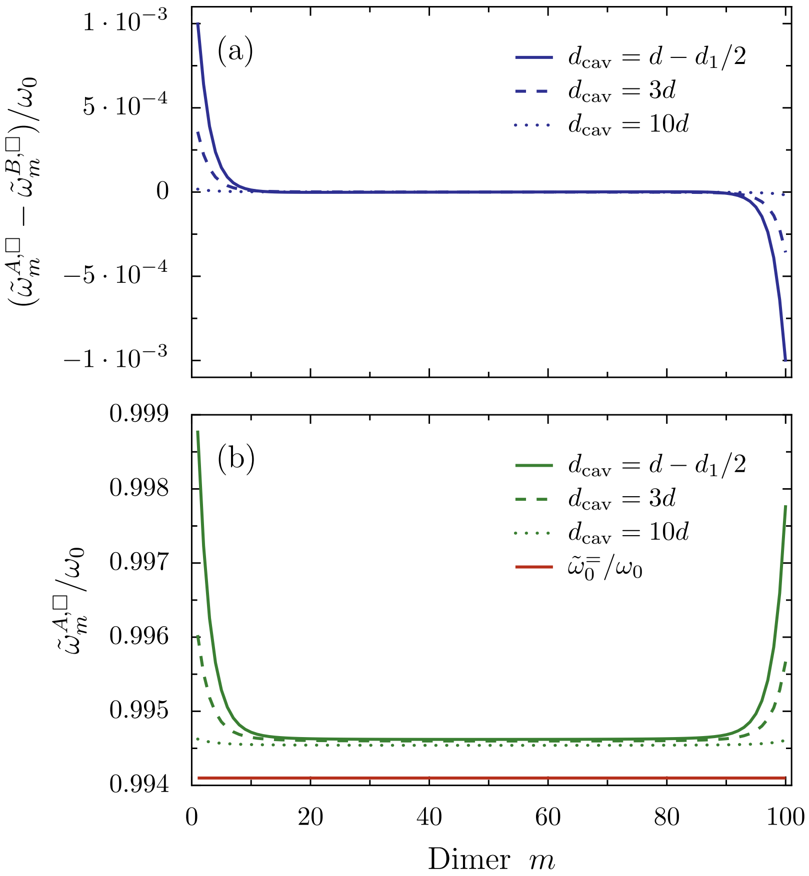

Figure 4.18: Onsite frequency renormalization. (a) Detuning $(\tilde{\omega}_m^{A,\square} - \tilde{\omega}_m^{B,\square})/\omega_0$ between the renormalized frequencies on the sites A and B [given, respectively, in Eqs. (4.72a) and (4.72b)] of a given dimer m along the chain, illustrating the effect of the cavity walls in the z direction. (b) Value of the renormalized frequency on the sites A, $\tilde{\omega}_m^{A,\square}$ in units of ω_0 and as a function of the dimer number m along the chain. In both panels, increasing values of the distance to the cavity walls d_{cav} are considered. The chain under consideration in the figure is comprised of $\mathcal{N} = 100$ dimers, has a dimerization $\epsilon = 0.25$, and is embedded in a cavity of height $L_x = 10a$.

lacks, at least perturbatively, the same symmetries as the equivalent Fourier-transformed polaritonic SSH model. Therefore, comparing the edge properties of the real space Hamiltonian (4.71), which presents a site-dependent offset between the A and B on-site frequencies, with the bulk properties of the Fourier space Hamiltonian (4.56), which has no such offset, may be ambiguous. This potential issue supports our choice of using an infinite waveguide cavity, which allows for an unambiguous comparison between Fourier-transformed and real-space Hamiltonians.

4.8.2 Effect of the distance to the cavity walls d_{cav}

To investigate the influence of the distance to the cavity walls d_{cav} on the effective Hamiltonian (4.71), we examine in detail the renormalized onsite frequencies $\tilde{\omega}_m^{A,\square}$ and $\tilde{\omega}_m^{B,\square}$.

In Fig. 4.18(a), we display the difference between the renormalized frequencies on the sites A and B of a given dimer m, $\tilde{\omega}_m^{A,\square} - \tilde{\omega}_m^{B,\square}$, in units of ω_0 and as a function of the dimer number m along the chain. Looking at the solid line, which represents the case $d_{\mathrm{cav}} = d - d_1/2$ considered in Ref. [136], we observe a negligible difference for the dimers in the bulk of the chain, but a sizeable one on the edges. Increasing the distance to the cavity walls to $d_{\mathrm{cav}} = 3d$ (dashed line) and $d_{\mathrm{cav}} = 10d$ (dotted line) results in the detuning between the A and B sites to fade out, so that the limit of a waveguide cavity is restored with walls in the z direction far enough from the ends of the chain. Furthermore, one observes a symmetry of Fig. 4.18(a) around the center of the chain, showing that inversion symmetry of the whole system, i.e., the symmetry between a site A of one end and a site B of the other end, is still present.

By studying the value of the renormalized onsite frequency $\tilde{\omega}_m^{A,\square}$ along the chain in Fig. 4.18(b), we similarly observe a drastic dissimilarity between the bulk and the edges of the chain. Considering a distance $d_{\mathrm{cav}} = d - d_1/2$ as in Ref. [136] almost does not alter the bare onsite frequencies at the edges, as visible through the green solid line which almost reaches the point where $\tilde{\omega}_m^{A,\square} = \omega_0$ in the first dimers of the chain. Increasing the distance d_{cav} to $3d$ (dashed line) and $10d$ (dotted line) increases the renormalization, and ultimately leads to recover the renormalized onsite frequency $\tilde{\omega}_0^{=}$ obtained using the infinite waveguide cavity in Sec. 4.2.3, and depicted as a red solid line in the figure.

The difference between the edge and bulk behavior of the renormalization on the onsite frequencies illustrates in a clear manner the influence of the cavity walls in the z direction. Indeed, the walls reduce the effect of the strong light-matter coupling on the edges of the chain.

Moreover, the dissimilarity between the cavity-induced renormalized onsite frequencies in the bulk and edges of the chain may be similar in consequences to a defect at the edges. Such kind of defect at the end of a one-dimensional system is known to lead to the presence of Tamm edge states. Interestingly, such Tamm edge states have been previously identified in Ref. [179] in a regular chain embedded in a closed cuboidal cavity using a similar model as the one employed here, but with walls in the z direction in close proximity with the ends of the chain. We verified that Tamm states are also present in the dimerized chain under study here, provided that we consider a closed box cavity. Indeed, using an infinite waveguide cavity as done in Secs. 4.5, 4.6, and 4.7 suppresses the impact of the walls in the z direction, and the system does not host any Tamm edge states. As they constitute a boundary effect only, we will not discuss Tamm states further in this manuscript.

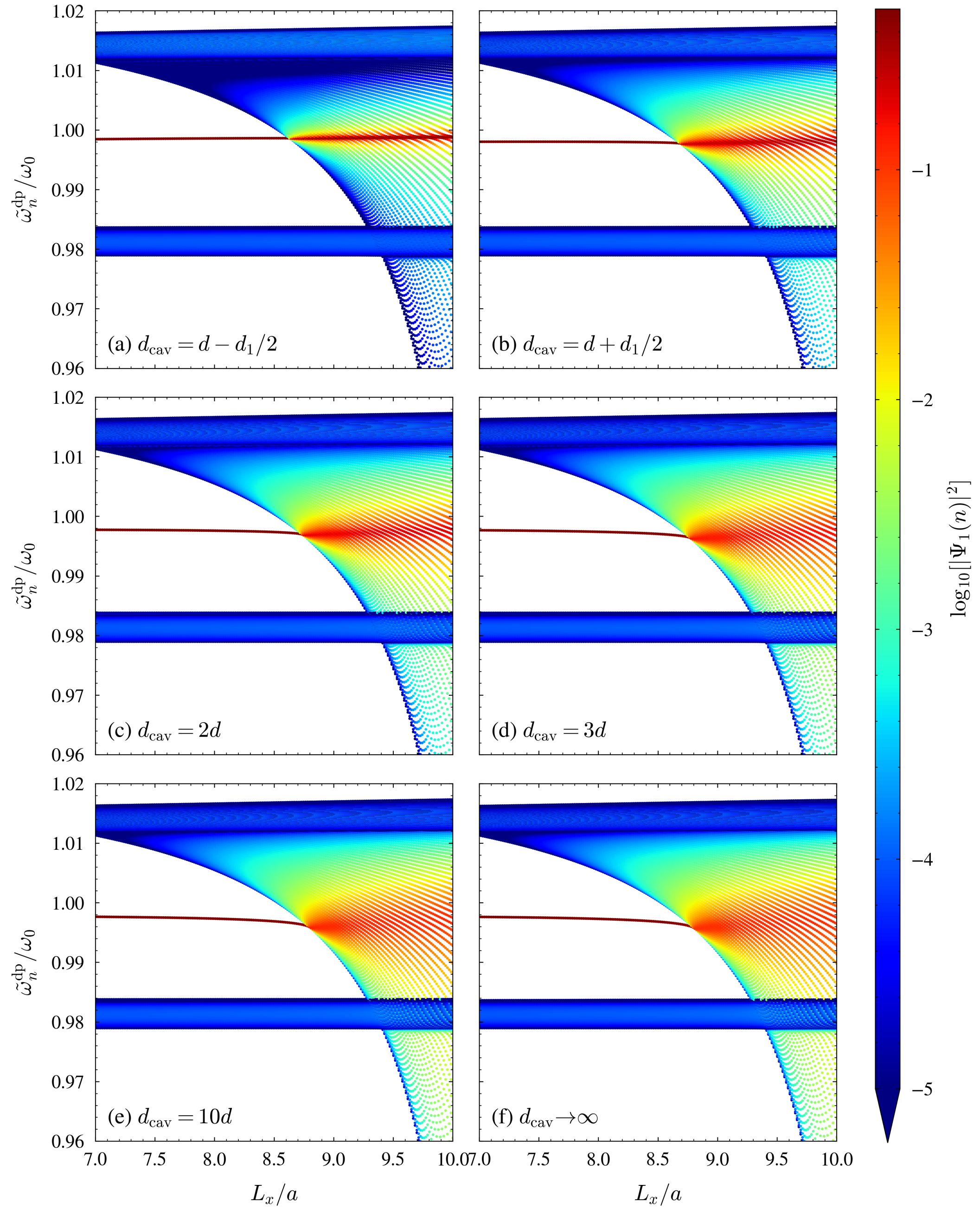

Figure 4.19: Influence of d_{cav}. Eigenspectrum as a function of the cavity height L_x/a, with a dimerization $\epsilon = 0.25$. The color associated to each eigenstate n indicates the logarithm of its probability density on the first site $|\Psi_1(n)|^2$. A reddish (bluish) color denotes a state highly (poorly) localized on the edges of the chain. Panels (a)-(e), computed from the effective Hamiltonian (4.71) that considers a finite cuboidal cavity, show increasing distances to the cavity walls d_{cav}, with panel (a) corresponding to the case considered in Ref. [136]. Panel (f) presents the case of an infinite waveguide cavity, and is computed from the effective Hamiltonian (4.36) with the $l = 0$ Umklapp index only.

To explore how the boundaries of the cavity affect the eigenstates and especially the polaritonic edge states of the Hamiltonian (4.71), we numerically diagonalize the latter considering a dimerization $\epsilon = 0.25$, and several values of the distance to the cavity walls d_{cav}. For each value, we compute the eigenfrequencies $\tilde{\omega}_n^{\mathrm{pol}}$ as a function of the cavity height L_x, as we have done in Fig. 4.10(a). The results are presented in Fig. 4.19. To identify edge localization, a colorcode indicates the logarithm of the probability density $|\Psi_1(n)|^2$ of an eigenstate n on the first site of the chain, from blue (not localized on the edges) to red (highly localized on the edges).

In panel (a) of Fig. 4.19, we consider a distance $d_{\mathrm{cav}} = d - d_1/2$, as done in Ref. [136]. With walls that close from the ends of the chain, edge states can localize not only on the dipoles, but also on the cavity walls, so that they are less affected by the strong light-matter coupling, and to diffuse much less in the bulk. This leads, in the strong-coupling regime, to a persistence of the edge states (see the straight red line) and to very few polaritons inheriting edge localization.

Finally, increasing such a distance from $d_{\mathrm{cav}} = d + d_1/2$ in Fig. 4.19(b) to $d_{\mathrm{cav}} = 10d$ in Fig. 4.19(e) makes visible an enhancement of the diffusion of edge states into bulk polaritons in the strong-coupling regime, through the spreading of a red spot in the eigenspectrum. Therefore, moving away the cavity walls in the z direction leads to the formation of a growing number of polaritonic edge states, and to all the exotic properties which we discussed in Sec. 4.5. In Fig. 4.19(f), we show for comparison the results we obtained using our waveguide cavity approach [as in Fig. 4.10(a)[8]]. The eigenspectrum is undistinguishable from Fig. 4.19(e), demonstrating that as long as $d_{\mathrm{cav}} \gtrsim 10d$ the boundary effects are insignificant, and the two approaches lead to the same eigenspectrum and localization properties.

4.9 Conclusions to Chapter 4

In summary, in this chapter we have analyzed in detail the effect of strong light-matter coupling on topological edge states, studying the eigenspectrum, the eigenstates, as well as the transport properties of a bipartite chain of emitters (modelled as point dipoles) strongly coupled to a multimode waveguide cavity. Such a system mimicks a variation of the celebrated two-band Su-Schrieffer-Heeger model, with the addition of an effective dipole-dipole coupling mediated by the cavity photons. We have found such cavity-mediated coupling to take the form of an exponential decay whose decay length increases as one enters in the strong-coupling regime.

We have shown that the effect of the strong light-matter coupling is to hybridize and redshift the bright dipolar band into a polaritonic one, which

---

[8] Incidentally, we note that in Fig. 4.10(a), in contrast to Fig. 4.19(f), Umklapp processes are took into account. By comparing the two figures, one observes the very weak effect of Umklapp processes on the eigenspectrum.

strongly breaks the chiral symmetry of the model, and which closes the energy gap and lead the system to become metallic. In this regime, a cavity-induced topological phase transition, i.e., a change in the bulk topological invariant of the system, is observed. We find that such a transition, which takes place in a gapless regime, is not associated with the appearance nor disappearance of edge states, leading the bulk-edge correspondence not to be fulfilled.

In the topological sector of the original SSH model, the strong-coupling regime leads the in-gap edge states to merge into the polaritonic bulk band. We have unveiled that even if the formal in-gap edge states are thus destroyed, all the polaritons entering in resonance with the edge states inherit part of their localization properties. Edge localization in then diffused into multiple polaritonic edge states that keep a delocalized bulk part and cover a wide frequency range. Our results highlight the peculiar properties of these polaritonic edge states, in particular, these latter taking advantage of their polaritonic nature to allow efficient energy transport between the two ends of the chain. Moreover, the broadening of the edge state frequency band makes them sensitive to a wide range of driving frequencies. These two unusual cavity-induced effects on topological edge states may facilitate their experimental detection.

Furthermore, by studying the impact of disorder on the interdipole spacings, we have demonstrated the tolerance of the polaritonic edge states to disorder. Thanks both to their polaritonic nature and topological origin, polaritonic edge states being reminiscent of the symmetry-protected edge states of the original SSH model, they can survive at high levels of off-diagonal disorder. Finally, we compared our model of a waveguide cavity to the one of a closed cuboid cavity considered in Ref. [136], and unveiled the major influence of cavity walls in the z direction, the latter significantly altering the nature of the edge states present in the system.

Our model, allowing a detailed numerical and partly analytical understanding of the strong light-matter coupling effects on topological edge states, could constitute a building block of a more general theory of topological polaritonics, essential to the successful implementation of topological photonic technologies. A direct and attractive extension of our present model is its generalization to ultra- and deep-strong light-matter couplings, these latter allowing surprising quantum effects [149, 151, 237].

APPENDICES TO CHAPTER 4

4.A Beyond the single cavity band approximation

To ascertain the validity of the single cavity band approximation, which we introduced in Sec. 2.3.1 and consider throughout the manuscript, we investigate in this appendix the eigenspectrum of the polaritonic SSH Hamiltonian when considering the coupling of two different cavity bands to dipolar excitations. Taking into account the $(n_x, n_y) = (0, 3)$ cavity photon band, the photonic Hamiltonian (2.33) becomes

$$\mathrm{H}_{\mathrm{ph}}^{n_y=\{1,3\}} = \sum_q \left(\omega_q^{\mathrm{ph}} c_q^\dagger c_q + \omega_q^{\mathrm{ph},n_y=3} c_{q,n_y=3}^\dagger c_{q,n_y=3} \right), \tag{4.73}$$

with the single cavity band photon dispersion ω_q^{ph} given in Eq. (2.34), and where the bosonic ladder operator $c_{q,n_y=3}^\dagger$ ($c_{q,n_y=3}$) creates (annihilates) a cavity photon excitation with longitudinal wavenumber q and frequency

$$\omega_q^{\mathrm{ph},n_y=3} = c\sqrt{\left(\frac{3\pi}{L_y}\right)^2 + q^2}. \tag{4.74}$$

The full polaritonic Hamiltonian (4.31) then becomes

$$\mathrm{H}_{\mathrm{pol,n_y=\{1,3\}}}^{\infty} = \sum_q \boldsymbol{\varphi}_q^{n_y=\{1,3\}\,\dagger} \mathcal{H}_q^{\mathrm{pol},n_y=\{1,3\}} \boldsymbol{\varphi}_q^{n_y=\{1,3\}}, \tag{4.75}$$

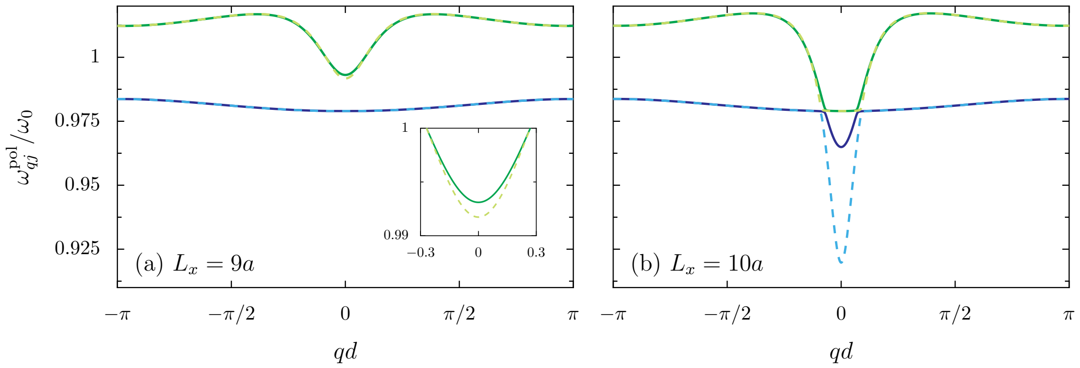

Figure 4.20: Validity of the Schrieffer-Wolff effective Hamiltonian. Solid lines: Lowest MP ($j = 2$) and LP ($j = 3$) bands of the full polaritonic dispersion $\omega^{\mathrm{pol}}_{qj}$ [see Eq. (4.48)]. Dashed lines: Lower ($\tau = -$) and upper ($\tau = +$) bands of the effective dispersion $\tilde{\omega}^{\mathrm{dp}}_{q\tau}$ [see Eq. (4.58)]. Two different cavity heights $L_x = 9a$ and $L_x = 10a$ are considered in panels (a) and (b), and in both panels the dimerization $\epsilon = 0.25$.

where we use here the basis $\boldsymbol{\varphi}_q^{n_y=\{1,3\}} = (a_q, b_q, c_q, c_{q,n_y=3})$, and where the 4-band Bloch Hamiltonian reads

$$\mathcal{H}_q^{\mathrm{pol},n_y=\{1,3\}} = \hbar \begin{pmatrix} \omega_q^{\mathrm{dp}} + \Omega f_q & \Omega g_q & \mathrm{i}\xi_q \mathrm{e}^{-\mathrm{i}\chi_q} & -\mathrm{i}\xi_q^{n_y=3}\mathrm{e}^{-\mathrm{i}\chi_q} \\ \Omega g_q^* & \omega_q^{\mathrm{dp}} + \Omega f_q & \mathrm{i}\xi_q \mathrm{e}^{\mathrm{i}\chi_q} & -\mathrm{i}\xi_q^{n_y=3}\mathrm{e}^{\mathrm{i}\chi_q} \\ -\mathrm{i}\xi_q \mathrm{e}^{\mathrm{i}\chi_q} & -\mathrm{i}\xi_q \mathrm{e}^{-\mathrm{i}\chi_q} & \omega_q^{\mathrm{ph}} & 0 \\ \mathrm{i}\xi_q^{n_y=3}\mathrm{e}^{\mathrm{i}\chi_q} & \mathrm{i}\xi_q^{n_y=3}\mathrm{e}^{-\mathrm{i}\chi_q} & 0 & \omega_q^{\mathrm{ph},n_y=3} \end{pmatrix}. \tag{4.76}$$

In the above Bloch Hamiltonian, the light-matter coupling strength associated to the $(n_x, n_y) = (0, 3)$ cavity mode reads

$$\xi_q^{n_y=3} = \omega_0 \sqrt{\frac{2\pi a^3 \omega_0}{L_x L_y d\, \omega_q^{\mathrm{ph},n_y=3}}}. \tag{4.77}$$

A numerical diagonalization procedure allows one to obtain the 4-band dispersion of the Hamiltonian (4.76). We verified that the three lowest bands of such a 4-band dispersion are almost indistinguishable from the 3-band dispersion Eq. (4.48). This supports our use of the single cavity band approximation all along the manuscript.

4.B Validity of the effective two-band Hamiltonian

In this appendix, we verify the validity of the effective bipartite Hamiltonian (4.36) derived in Sec. 4.3.2. To this end, we compare in Fig. 4.20 the full polaritonic bandstructure $\omega^{\mathrm{pol}}_{qj}$ [see Eq. (4.48)], represented as solid lines, to the effective two-band dispersion $\tilde{\omega}^{\mathrm{dp}}_{q\tau}$ [see Eq. (4.58)], represented as dashed lines and obtained by an integration of the cavity degrees of freedom. In the figure, the dimerization $\epsilon = 0.25$.

In Fig. 4.20(a), with a cavity height $L_x = 9a$, the two effective bands $\tilde{\omega}^{\mathrm{dp}}_{q,\tau=\pm}$ (dashed lines), and the two lowest polaritonic $\omega^{\mathrm{pol}}_{q,j=2}$ (MP) and $\omega^{\mathrm{pol}}_{q,j=3}$ (LP) bands are in almost perfect agreement. As highlighted in the inset, the effective dispersion slightly overestimates the band renormalization around the center of the Brillouin zone, induced by the strong-coupling regime and originating from the avoided crossing scheme with the photonic band. This overestimation gets worse in Fig. 4.20(b), in which the cavity height is increased to $L_x = 10a$, and thus approaches the value $L^{\mathrm{SW}}_x/a = \pi/3k_0a \simeq 10.5$ for which the bare photonic and dipolar dispersions are in resonance so that the Schrieffer-Wolff transformation breaks down. Indeed, the lowest eigenfrequency of the effective Hamiltonian, $\tilde{\omega}^{\mathrm{dp}}_{q=0,\tau=-} \simeq 0.92\omega_0$, while the one of the full polaritonic Hamiltonian $\omega^{\mathrm{pol}}_{q=0,j=3} \simeq 0.97\omega_0$. The Schrieffer-Wolff transformation therefore induces an exaggeration of the effects of the cavity, mimicking a larger value of the cavity height L_x/a.

While the effective Hamiltonian thus does not quantitatively reproduce the bandstructure for cavity heights L_x approaching L^{SW}_x, the qualitative behavior is well replicated, and considering $L_x = 10a$ in the effective model just amounts to consider $L_x \simeq 11a$ in the full polaritonic model. This validation of the Schrieffer-Wolff transformation justifies our use of the effective Hamiltonian (4.36) in this chapter, and the case $L_x = 10a$ is considered as the upper bound of the effective model.

4.C Effect of image dipoles

Throughout all this manuscript, we neglected the effect of image dipoles occuring from the cavity walls that are treated as perfectly reflecting mirrors. Indeed, in order for the electric potential to be vanishing on the cavity walls, which we consider as perfectly conducting metallic plates, effective, or "image" dipoles must be considered. The latter are located outside of the cavity and serve the only purpose of satisfying the proper boundary conditions of the Poisson problem under consideration [119].

These additional dipoles couple to the real ones inside the cavity, and therefore induce a renormalization of the quasistatic dipolar eigenfrequencies. While such a modification of the quasistatic dispersion is irrelevant in the case of the disordered polaritons studied in Chap. 3 – all the observed effects originating solely from the light-matter coupling – it could in principle be of importance in the context of the Su-Schrieffer-Heeger model studied in this Chapter, as the quasistatic dispersion hosts the topology of the model.

In this appendix, we thus consider the image dipoles originating from the waveguide cavity sketched in Fig. 4.5, and demonstrate that they are not important for the regime of parameters considered in this study.

In the presence of the cavity walls, the quasistatic dipolar Hamiltonian in the rotating wave approximation (4.17) transforms into

$$\mathrm{H}^{\mathrm{RWA}}_{\mathrm{dp,im}} = \mathrm{H}^{\mathrm{RWA}}_{\mathrm{dp}} + \mathrm{H}^{x}_{\mathrm{im}} + \mathrm{H}^{y}_{\mathrm{im}}, \tag{4.78}$$

where the contribution of image dipoles originating from walls in the $\sigma = \{x, y\}$ direction reads

$$\mathrm{H}^{\sigma}_{\mathrm{im}} = \sum_{m=1}^{\mathcal{N}} \sum_{m'=1}^{\mathcal{N}} \sum_{s} \sum_{s'} \sum_{k \in \mathbb{Z}^*} \frac{\mathbf{p}^{s}_{m} \cdot \tilde{\mathbf{p}}^{\sigma,s}_{m'k} - 3 \left(\mathbf{p}^{s}_{m} \cdot \hat{n}^{\sigma,ss'}_{mm'k}\right) \left(\tilde{\mathbf{p}}^{\sigma,s'}_{m'k} \cdot \hat{n}^{\sigma,ss'}_{mm'k}\right)}{2 \left|\mathbf{r}^{s}_{m} - \mathbf{R}^{\sigma,s'}_{m'k}\right|^{3}}. \tag{4.79}$$

Such a Hamiltonian is simply the sum of the Coulomb potential energy between all real and image dipoles, where one notes that the latter energy is half the one between real dipoles [238].

In the above Hamiltonian (4.79), the index m labels the unit cell comprising each pair of dipoles, and the index $s = \{A, B\}$ the corresponding sublattice. The position vector $\mathbf{r}^{s}_{m}$ gives the location of a real dipole, as given in Eq. (4.26), while image dipoles induced by the x and y cavity walls are located, respectively, at the positions

$$\mathbf{R}^{x,s}_{mk} = \left((2k+1)\frac{L_x}{2}, \frac{L_y}{2}, z^{s}_{m}\right), \tag{4.80a}$$

and

$$\mathbf{R}^{y,s}_{mk} = \left(\frac{L_x}{2}, (2k+1)\frac{L_y}{2}, z^{s}_{m}\right), \tag{4.80b}$$

with the index $k \in \mathbb{Z}^*$ labelling the image dipole σ coordinate, and where z^{s}_{m} being given in Eqs. (4.27). Furthermore, the unit vector $\hat{n}^{\sigma,ss'}_{mm'k} = (\mathbf{r}^{s}_{m} - \mathbf{R}^{\sigma,s'}_{m'k})/|\mathbf{r}^{s}_{m} - \mathbf{R}^{\sigma,s'}_{m'k}|$.

All the real dipoles inside the cavity are polarized along the x axis, so that their dipole moments $\mathbf{p}^{s}_{m} = -Qh^{s}_{m}\hat{x}$, where $-Q$ is their effective charge, and h^{s}_{m} their displacement field. The polarization of the image dipoles, however, depend on the cavity mirror location. Indeed, on the one hand, the reflection of x-polarized dipoles on the cavity walls in the x direction induce image dipoles which are also polarized along the x direction, so that their dipole moments are $\tilde{\mathbf{p}}^{x,s}_{mk} = -Qh^{s}_{m}\hat{x}$. On the other hand, the cavity walls in the y direction induce image dipoles with alternating opposite polarization signs, so that their moments read $\tilde{\mathbf{p}}^{y,s}_{mk} = -(-1)^{k}Qh^{s}_{m}\hat{x}$.

The contributions from the walls in the x and y directions therefore read

$$\mathrm{H}_{\mathrm{im}}^{x} = \frac{Q^2}{2} \sum_{m=1}^{\mathcal{N}} \sum_{m'=1}^{\mathcal{N}} \sum_{s} \sum_{s'} \sum_{k \in \mathbb{Z}^*} h_m^s \, h_{m'}^{s'} \frac{1 - 3\frac{(kL_x)^2}{(kL_x)^2 + (z_m^s - z_{m'}^{s'})^2}}{\left[(kL_x)^2 + (z_m^s - z_{m'}^{s'})^2\right]^{3/2}}, \tag{4.81a}$$

and

$$\mathrm{H}_{\mathrm{im}}^{y} = \frac{Q^2}{2} \sum_{m=1}^{\mathcal{N}} \sum_{m'=1}^{\mathcal{N}} \sum_{s} \sum_{s'} \sum_{k \in \mathbb{Z}^*} h_m^s \, h_{m'}^{s'} \frac{(-1)^k}{\left[(kL_y)^2 + (z_m^s - z_{m'}^{s'})^2\right]^{3/2}}, \tag{4.81b}$$

respectively. Using the quantization scheme for the displacement h_m^s given in Eq. (2.20), and discarding counter-rotating terms, one can then write the dipolar Hamiltonian renormalized by the cavity mirrors in the rotating wave approximation as

$$\begin{aligned} \mathrm{H}_{\mathrm{dp,im}}^{\mathrm{RWA}} = \hbar\omega_0^{\mathrm{im}} \sum_{m=1}^{\mathcal{N}} \left(a_m^\dagger a_m + b_m^\dagger b_m\right) + \hbar\Omega \sum_{m,m'=1}^{\mathcal{N}} g_{m-m'}^{\mathrm{im}} \left(a_m^\dagger \, b_{m'} + a_m \, b_{m'}^\dagger\right) \\ + \frac{\hbar\Omega}{2} \sum_{\substack{m,m'=1 \\ (m \neq m')}}^{\mathcal{N}} f_{m-m'}^{\mathrm{im}} \left(a_m^\dagger \, a_{m'} + b_m^\dagger \, b_{m'} + a_m \, a_{m'}^\dagger + b_m \, b_{m'}^\dagger\right). \end{aligned} \tag{4.82}$$

Such a renormalized Hamiltonian has the exact same form as the quasistatic Hamiltonian in the absence of the mirrors [compare with Eq. (4.17)]. However, the change of boundary conditions induced by the consideration of metallic cavity walls leads the bare frequency ω_0, as well as the intra- and inter-sublattice couplings $f_{m-m'}$ and $g_{m-m'}$ [given in Eqs. (4.18)] to be modified as

$$\omega_0^{\mathrm{im}} = \omega_0 \left[1 - 2\left(\frac{a}{L_x}\right)^3 \zeta(3) - \frac{3}{4}\left(\frac{a}{L_y}\right)^3 \zeta(3)\right], \tag{4.83a}$$

$$\begin{aligned} f_{m-m'}^{\mathrm{im}} = f_{m-m'} & \left[1 - 2\sum_{k=1}^{\infty} \frac{2\left(\frac{kL_x}{d(m-m')}\right)^2 - 1}{\left[1 + \left(\frac{kL_x}{d(m-m')}\right)^2\right]^{5/2}} \right. \\ & \left. + 2\sum_{k=1}^{\infty} \frac{(-1)^k}{\left[1 + \left(\frac{kL_y}{d(m-m')}\right)^2\right]^{3/2}}\right], \end{aligned} \tag{4.83b}$$

and

$$g^{\mathrm{im}}_{m-m'} = g_{m-m'} \left[1 - 2\sum_{k=1}^{\infty} \frac{2\left(\frac{kL_x}{d(m-m')-d_1}\right)^2 - 1}{\left[1 + \left(\frac{kL_x}{d(m-m')-d_1}\right)^2\right]^{5/2}} \right.$$
$$\left. + 2\sum_{k=1}^{\infty} \frac{(-1)^k}{\left[1 + \left(\frac{kL_y}{d(m-m')-d_1}\right)^2\right]^{3/2}} \right], \tag{4.83c}$$

respectively. Here, the typical dipole length scale a is defined in Eq. (2.7), while $\zeta(3) \simeq 1.202$ is Apéry's constant. From these expressions, one can already understand the effect of image dipoles on the system. We expect the influence of image dipoles to become increasingly noticeable as the size of the cavity is reduced. Indeed, the closer the mirrors are, the closer are image dipoles from real dipoles, and thus the stronger is the real-dipole-image-dipole coupling. In our model, we fixed the cavity width L_y to $L_y = 3L_x$. Therefore, the dominant contribution of image dipoles should originate from mirrors in the x direction.

This is what we observe in the expressions (4.83), as the second terms in the r.h.s. of Eqs. (4.83) account for the mirror in the x direction, while the third terms account for the mirror in the y direction. The renormalization of the bare frequency in Eq. (4.83a) increases as L_x/a and L_y/a decrease, while the renormalization of the dipole-dipole couplings Eqs. (4.83b) and (4.83c) increases as L_x/d and L_y/d decrease. While the bare frequency ω_0 is redshifted by image dipoles, the dipole-dipole couplings Eqs. (4.83b) and (4.83c) are reduced, the cavity mirrors screening the quasistatic Coulomb interaction. Therefore, the consideration of a small cavity leads to effectively increasing the distance between neighboring emitters, decreasing the quasistatic dipole-dipole coupling.

Considering now the light-matter coupling between the cavity photons and the dipolar excitations, as presented in Sec. 4.2.1, and performing a Schrieffer-Wolff transformation to isolate perturbatively the dipolar subspace, as detailed in Sec. 4.2.2, we obtain the effective bipartite Hamiltonian

$$\begin{aligned}\tilde{\mathrm{H}}^{\mathrm{RWA,im,=}}_{\mathrm{dp}} = {} & \hbar\tilde{\omega}^{\mathrm{im,=}}_0 \sum_{m=1}^{\mathcal{N}} \left(a^\dagger_m a_m + b^\dagger_m b_m\right) \\ & + \frac{\hbar\Omega}{2} \sum_{\substack{m,m'=1 \\ (m\neq m')}}^{\mathcal{N}} \tilde{f}^{\mathrm{im,=}}_{m-m'} \left(a^\dagger_m\, a_{m'} + b^\dagger_m\, b_{m'} + \mathrm{H.c.}\right) \\ & + \hbar\Omega \sum_{m,m'=1}^{\mathcal{N}} \tilde{g}^{\mathrm{im,=}}_{m-m'} \left(a^\dagger_m\, b_{m'} + \mathrm{H.c.}\right).\end{aligned} \tag{4.84}$$

Here, the onsite frequency ω_0 and the intra- and intersublattice sums $f_{m-m'}$ and $g_{m-m'}$ are renormalized both by the image dipoles and cavity photons [compare with Eq. (4.17)] as

$$\tilde{\omega}_0^{\mathrm{im},=} = \omega_0^{\mathrm{im}} - \frac{d}{2\pi} \sum_{l=-\infty}^{+\infty} \int_{-\pi/d}^{+\pi/d} \mathrm{d}q \, \frac{\xi_{q,l}^2}{\omega_{q,l}^{\mathrm{ph}} - \omega_0^{\mathrm{im}}}, \tag{4.85a}$$

$$\tilde{f}_{m-m'}^{\mathrm{im},=} = f_{m-m'}^{\mathrm{im}} - \frac{1}{\Omega} \frac{d}{2\pi} \sum_{l=-\infty}^{+\infty} \int_{-\pi/d}^{+\pi/d} \mathrm{d}q \, \frac{\xi_{q,l}^2 \, \mathrm{e}^{\mathrm{i}(m-m')q_l d}}{\omega_{q,l}^{\mathrm{ph}} - \omega_0^{\mathrm{im}}}, \tag{4.85b}$$

and

$$\tilde{g}_{m-m'}^{\mathrm{im},=} = g_{m-m'}^{\mathrm{im}} - \frac{1}{\Omega} \frac{d}{2\pi} \sum_{l=-\infty}^{+\infty} \int_{-\pi/d}^{+\pi/d} \mathrm{d}q \, \frac{\xi_{q,l}^2 \, \mathrm{e}^{\mathrm{i}(m-m'-d_1/d)q_l d}}{\omega_{q,l}^{\mathrm{ph}} - \omega_0^{\mathrm{im}}}. \tag{4.85c}$$

Using the thermodynamic limit $\mathcal{N} \gg 1$ and going into reciprocal space through the Fourier transforms (4.4), one then obtains the effective two-band Bloch Hamiltonian

$$\mathcal{H}_q^{\mathrm{dp,im}} = \hbar \begin{pmatrix} \omega_0^{\mathrm{im}} + \Omega \tilde{f}_q^{\mathrm{im}} & \Omega \tilde{g}_q^{\mathrm{im}} \\ \Omega \tilde{g}_q^{\mathrm{im}*} & \omega_0^{\mathrm{im}} + \Omega \tilde{f}_q^{\mathrm{im}} \end{pmatrix}. \tag{4.86}$$

The Bloch Hamiltonian (4.86) has the exact same form as the one derived in Sec. 4.3.2 [cf. Eq. (4.56)], except that the cavity-renormalized intra- and inter-sublattices $\tilde{f}_q^{\mathrm{im}}$ and $\tilde{g}_q^{\mathrm{im}}$ are here additionally renormalized by the image dipoles, and read, respectively,

$$\tilde{f}_q^{\mathrm{im}} = f_q^{\mathrm{im}} - \frac{1}{\Omega} \sum_{l=-\infty}^{+\infty} \frac{\xi_{q,l}^2}{\omega_{q,l}^{\mathrm{ph}} - \omega_0^{\mathrm{im}}}, \tag{4.87a}$$

and

$$\tilde{g}_q^{\mathrm{im}} = g_q^{\mathrm{im}} - \frac{1}{\Omega} \sum_{l=-\infty}^{+\infty} \frac{\xi_{q,l}^2 \, \mathrm{e}^{-2\mathrm{i}\chi_{q,l}}}{\omega_{q,l}^{\mathrm{ph}} - \omega_0^{\mathrm{im}}}, \tag{4.87b}$$

with the dipolar lattice sums only renormalized by image dipoles being given by

$$
\begin{aligned}
f_q^{\mathrm{im}} = \sum_{m=1}^{\infty} \frac{2\cos(mqd)}{m^3} & \left[1 - 2\sum_{k=1}^{\infty} \frac{2\left(\frac{kL_x}{d(m-m')}\right)^2 - 1}{\left[1+\left(\frac{kL_x}{d(m-m')}\right)^2\right]^{5/2}} \right. \\
& \left. + 2\sum_{k=1}^{\infty} \frac{(-1)^k}{\left[1+\left(\frac{kL_y}{d(m-m')}\right)^2\right]^{3/2}} \right],
\end{aligned}
\tag{4.88a}
$$

and

$$
\begin{aligned}
g_q^{\mathrm{im}} = {} & \left(\frac{d}{d_1}\right)^3 \left[1 - 2\sum_{k=1}^{\infty} \frac{2\left(\frac{kL_x}{d_1}\right)^2 - 1}{\left[1+\left(\frac{kL_x}{d_1}\right)^2\right]^{5/2}} + 2\sum_{k=1}^{\infty} \frac{(-1)^k}{\left[1+\left(\frac{kL_y}{d_1}\right)^2\right]^{3/2}} \right] \\
& + \sum_{m=1}^{\infty} d^3 \left\{ \frac{\mathrm{e}^{imqd}}{(dm+d_1)^3} \left[1 - 2\sum_{k=1}^{\infty} \frac{2\left(\frac{kL_x}{dm+d_1}\right)^2 - 1}{\left[1+\left(\frac{kL_x}{dm+d_1}\right)^2\right]^{5/2}} \right. \right. \\
& \left. + 2\sum_{k=1}^{\infty} \frac{(-1)^k}{\left[1+\left(\frac{kL_y}{dm+d_1}\right)^2\right]^{3/2}} \right] \\
& + \frac{\mathrm{e}^{-imqd}}{(dm-d_1)^3} \left[1 - 2\sum_{k=1}^{\infty} \frac{2\left(\frac{kL_x}{dm-d_1}\right)^2 - 1}{\left[1+\left(\frac{kL_x}{dm-d_1}\right)^2\right]^{5/2}} \right. \\
& \left. \left. + 2\sum_{k=1}^{\infty} \frac{(-1)^k}{\left[1+\left(\frac{kL_y}{dm-d_1}\right)^2\right]^{3/2}} \right] \right\}.
\end{aligned}
\tag{4.88b}
$$

We note that in the absence of the waveguide cavity, such dipolar lattice sums in Fourier space are given in Eqs. (4.20).

A Bogoliuobov transformation of the effective Bloch Hamiltonian (4.86) leads to the eigenfrequencies

$$
\tilde{\omega}_{q\tau}^{\mathrm{dp,im}} = \omega_0^{\mathrm{im}} + \Omega \tilde{f}_q^{\mathrm{im}} + \tau \Omega |\tilde{g}_q^{\mathrm{im}}|, \tag{4.89}
$$

where $\tau = +\,(-)$ denotes the high- (low-)energy band.

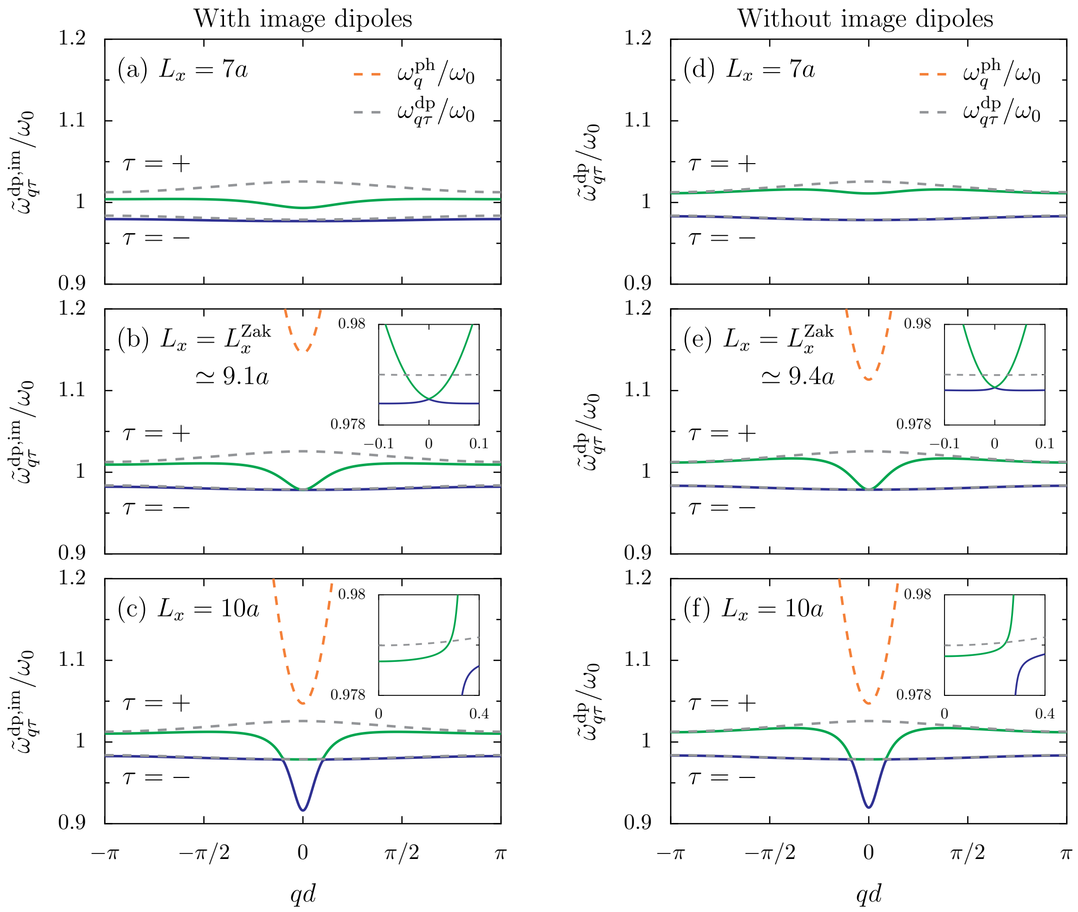

Figure 4.21: Effect of image dipoles on the polaritonic dispersion. Comparison between the effective polaritonic dispersion with image dipoles $\tilde{\omega}_{q\tau}^{\rm dp,im}$ [panels (a)-(c)] and without image dipoles $\tilde{\omega}_{q\tau}^{\rm dp}$ [panels (d)-(f), which reproduce Fig. 4.7]. In the figure, the dimerization parameter $\epsilon = 0.25$, the lattice constant $d = 8a$, and the Umklapp index $l \in [-l_{\rm max}, +l_{\rm max}]$ with $l_{\rm max} = 100$.

We plot the effective polaritonic dispersion (4.89) in Figs. 4.21(a)-(c), for increasing cavity heights $L_x = 7a$, $L_x = L_x^{\rm Zak}$, and $L_x = 10a$, where $L_x^{\rm Zak}$ is defined as the height corresponding to the closing of the gap at $q = 0$. We compare these bandstructures to the one obtained neglecting image dipoles, as done in Fig. 4.7, and here reproduced in Figs. 4.21(d)-(f). As anticipated, the effect of image dipoles on the eigenspectrum is almost unperceptible for cavity heights $L_x > d$ [compare Figs. (4.89)(b)-(c) and Figs. (4.89)(e)-(f)]. A slight redshifting is however visible for $L_x = 7a$ [compare Fig. (4.89)(a) and Fig. (4.89)(b)], along with a reduction of the bandwidth. Such a bandwidth narrowing reflects the decrease of the quasistatic dipole-dipole coupling. One also note the slight modification of the cavity height associated to $L_x^{\rm Zak}$.

Similar conclusions on the influence of image dipoles on the eigenspectrum can be made analyzing the finite polaritonic spectrum $\tilde{\omega}_n^{\rm dp,im}$, by numerically

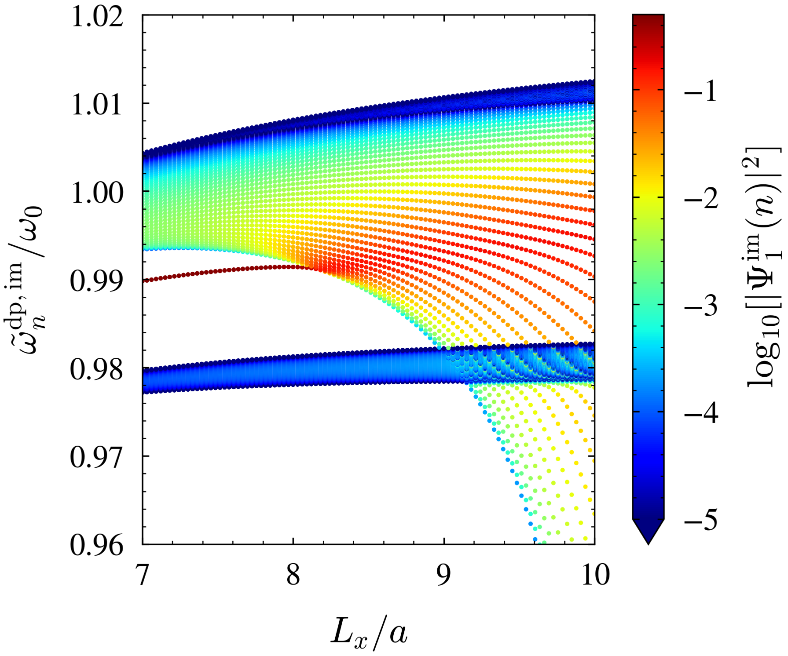

Figure 4.22: Effect of image dipoles on the finite polaritonic eigenspectrum. Same quantities as plotted in Fig. 4.10(a), but here including the effect of image dipoles. The dimerization parameter is fixed to $\epsilon = 0.25$, and a finite chain of $\mathcal{N} = 100$ dimers is considered.

diagonalizing the Hamiltonian Eq. (4.84). The results of such a diagonalization for a finite chain of $\mathcal{N} = 100$ dimers are shown in Fig. 4.22, in which the eigenfrequencies are plotted as a function of the cavity height L_x, with a colorcode indicating the logarithm of the probability density on the first site of the chain of each eigenstate. The same quantities have been shown neglecting image dipoles in Fig. 4.10. Comparing Figs. 4.22 and 4.10, one notices the increasing redshift and bandwidth narrowing of the spectrum as the cavity height is reduced.

From this eigenspectrum analysis in both Fourier and real space, we conclude on the validity of the neglection of image dipoles. Indeed, aside from a slight quantitative renormalization of the eigenfrequencies, no qualitative changes are found for the cavity heights under consideration in this work. We verified from a computation of the Zak phase (4.63) that the topological invariant is not modified either. We note, however, that for extremely small cavity heights $L_x \lesssim d_{1,2}$, which we do not consider in this work, perceptible modifications originating from image dipoles are found. Notably, the bandwidth narrowing induced by the consideration of image dipoles leads to an additional bandgap closing and re-opening at $q = 0$ for very small cavity heights L_x between $2a$ and $5a$. Such bandgap closing and re-opening is associated with a change of topological invariant, as well as with the appearance and disappearance of edge states. Indeed, such image-induced topological phase transition occurs in a system in an “insulating” phase, i.e., with a finite

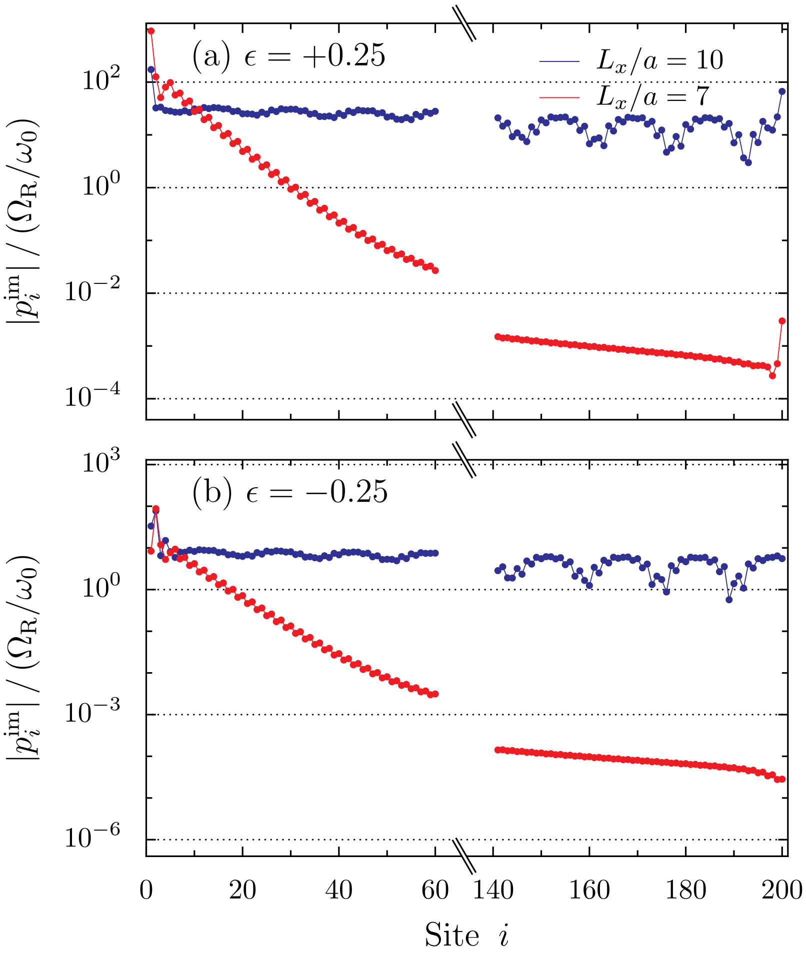

Figure 4.23: Effect of image dipoles on edge state transport. Same quantities as plotted in Fig. 4.14, but here including the effect of image dipoles. Panels (a) and (b) correspond to a dimerization parameters $\epsilon = +0.25$ and $\epsilon = -0.25$, respectively, while the red (blue) symbols correspond to transport in the weak- (strong-)coupling regime, with a cavity height $L_x = 7a$ ($L_x = 10a$). The propagation results from a monochromatic drive on the first dipole site at a frequency $\omega_{\mathrm{d}} = 0.990\omega_0$. The chain is comprised of $\mathcal{N} = 100$ dimers with damping rates $\gamma = 0.002\omega_0$.

energy gap, so that the bulk-edge correspondence is valid. This is in contrast to the light-matter coupling-induced topological phase transition studied in Sec. 4.4, which occurs in a “metallic” phase, and for which we observed a change of topological invariant which is not associated to the appearance nor disappearance of edge states.

Finally, to conclude our discussion on the validity of the neglection of image dipoles, we study the transport properties of the edge states through a driven-dissipative scenario, as we have done in Sec. 4.6.

Fig. 4.23 displays our results for the steady-state amplitude of the dipole moment p_i^{im} as a function of the dipole site i, when considering the full Hamiltonian (4.84). The parameters are the same as in Fig. 4.14, which shows the same quantities but without considering the effect of image dipoles. Comparing Figs. 4.23 and 4.14, we observe that all the qualitative transport features are the same. Indeed, the two regimes of transport – a cavity-induced exponential decay whose decay length depends on the cavity height, followed by an algebraic tail with a $1/r^3$ power-law – are still present.

On the one hand, one observes that the effect of image dipoles on the polaritonic transport (blue lines) are unperceptible. On the other hand, in the weak-coupling regime (red lines), image dipoles remove the unphysical oscillations between the exponential and algebraic regimes, smoothening the curves, and allow the exponential decay to be neater (a tidy, straight line in the log-lin plot of Fig. 4.23). We therefore conclude that the inclusion of image dipoles in our model only leads to quantitative changes in the edge state transport properties, so that their neglection is justified in order to simplify our model, as our goal is to provide a model which is as simple as possible, analytically tractable, and that allows for not resource-hungry numerical computations.

GENERAL CONCLUSIONS AND OUTLOOK

In this thesis work, we have endeavored to contribute to the understanding of the influence of the strong light-matter coupling regime on two major fields of condensed matter physics: disordered systems and topological phases of matter. To this end, we investigated the strong-coupling between a multimode optical cavity and, firstly, a one-dimensional disordered system in Chap. 3, and secondly, a one-dimensional topological system hosting topological edge states in Chap. 4.

In both cases, we unveiled a tremendous impact of the strong light-matter coupling on the system properties. In particular, we demonstrated the importance of considering a multimode and dispersive cavity, and disclosed that the specific effect of the strong-coupling of a chain of dipolar emitters to such a cavity is an effective, photon-mediated, dipole-dipole coupling which decays exponentially.

This photon-mediated coupling serves as the underlying mechanism for most of the cavity-induced physical effects reported in this thesis. Indeed, such an effective coupling is visible through the transport characteristics along the system as an additional exponential decay, which follows the first one induced by the nearest-neighbor quasistatic dipolar coupling. Most importantly, its steepness is directly related to the light-matter coupling and to the hybridization of the eigenstates between photonic and dipolar degrees of freedom. The larger the photonic part of the polaritonic eigenstate is, the poorer its short-range propagation, but the more flat this second exponential regime, so that energy transport over longer distances is made possible by the strong-coupling regime.

In Chap. 3, it is precisely this additional regime of exponential decay that enables the phenomenon of cavity-enhanced transport of polaritons. Moreover, along with the disorder-induced hybridization of dark states into polaritons, it gives rise to the emergence of disorder-enhanced transport. In Chap. 4, the pronounced breaking of the chiral symmetry in the system, which leads to a cavity-induced topological phase transition characterized by a change of the system's topological invariant, and to the hybridization of the edge states into polaritonic edge states is also achieved through such a long-range effective coupling. Besides that, the latter photon-mediated decay plays a crucial role in enhancing the transport properties of the polaritonic edge states, resulting in efficient end-to-end energy transport within the system.

To conclude this manuscript, the work carried out in the course of this thesis has also opened up some perspectives and raised new questions.[1]

In that respect, while our study has been focused on the individual interplay between disorder and strong coupling, and topology and strong coupling, it lacks a complete study of the full interplay between disorder and topology in a strongly-coupled light-matter system. Indeed, knowing the fascinating link between disorder and topology (see, for instance, the discussion in footnote 6 on p.11), a specific study of disordered topological polaritons is particularly exciting. Recent studies investigated in detail the properties of the disordered SSH model with nearest neighbor coupling only [239], revealing intriguing disorder-induced topological transitions [240]. The extension of these studies to the polaritonic SSH model we developed in Chap. 4, in which we already briefly investigated the effect of disorder in Sec. 4.7, may constitute an appealing and direct perspective of our work.

Furthermore, another attractive extension of our study would be to investigate the effect of dimensionality on all the phenomena we observed. Indeed, while our analysis focused on one-dimensional systems, it is well established that both Anderson localization and topological phases of matter significantly depend on the dimensionality of the system under consideration [22, 46]. Additionally, the impact of light-matter coupling on dipolar emitters can be more pronounced in higher dimensions, in particular in three-dimensional systems, where the realization of ultra- and deep-strong light-matter coupling regimes has been successfully achieved solely through the coupling to the vacuum electromagnetic field [186, 241].

These stronger regimes of light-matter coupling have been shown to give rise to a host of intriguing phenomena, notably in the context of topological phases of matter [207, 237, 242–244], and are now experimentally reachable [149, 151]. Importantly, in contrast with the strong-coupling one, the ultra- and deep-strong coupling regimes may lead to quantum effects. This highlights an important limitation of our study, namely that our model only permits investigations up to the strong-coupling regime, and this limitation was even more apparent in the context of the waveguide cavity examined in Chap. 4, where some perturbative methods had to be employed. The development of our theoretical framework in order to incorporate stronger regimes of light-matter coupling is therefore another appealing perspective, as it would in addition enable the quantum theory we employ to fully unleash its potential.

---

[1] In the words of John A. Wheeler: “We live on an island surrounded by a sea of ignorance. As our island of knowledge grows, so does the shore of our ignorance.”.

RÉSUMÉ EN FRANÇAIS

Introduction

La physique de la matière condensée, dont l'origine moderne peut être attribuée aux travaux pionniers d'Einstein sur l'effet photoélectrique [1] et sur la capacité thermique des solides [2], vise à examiner les propriétés microscopiques et macroscopiques de la matière à partir des effets collectifs d'un grand nombre de particules, et notamment à étudier les différentes *phases* de la matière au sens le plus large. Au cours du XXe siècle, elle est devenue l'un des domaines les plus prolifiques de la physique, et, pour preuve, la sous-section "cond-mat" de la plateforme de prépublication arXiv est aujourd'hui la catégorie de physique la plus active.

Dans le domaine de la matière condensée, deux branches ont particulièrement attiré l'attention au cours des cinquante dernières années. La première est le domaine des systèmes désordonnés, dans lequel l'effet de localisation d'Anderson a révélé qu'un morceau de matériau métallique peut être transformé en un isolant par du désordre microscopique, ce dernier conduisant à la localisation des fonctions d'onde des électrons. La deuxième est la physique des phases topologiques de la matière, qui englobe notamment l'emblématique effet Hall quantique entier. Cette branche permit en particulier de classer rigoureusement les isolants topologiques, des matériaux pouvant se comporter comme isolants dans leur volume, mais comme métalliques sur leurs surfaces ou bords, grâce à des états de surface ou de bord topologiques pouvant être protégés par les symétries du matériaux. L'étude des phases topologiques permit d'expliquer ces nouveaux états de la matière à travers des concepts empruntés à la topologie.

De façon intéressante, à la fois la localisation d'Anderson et les phases topologiques de la matière ont la particularité, bien qu'elles aient été développées à l'origine pour l'étude de systèmes électroniques quantiques, de provenir fondamentalement de phénomènes ondulatoires [3, 4].

L'émergence de ces effets en physique de la matière condensée est donc le résultat de la dualité quantique onde-particule des électrons. En effet, la localisation d'Anderson et la physique topologique ont été étudiées dans des domaines bien au-delà des systèmes électroniques, aussi variés que l'acoustique [3, 5], les ondes de surface en eau peu profonde [6–8], les atomes froids [9, 10] ou la photonique [11–15].

Un autre domaine qui s'est rapidement développé au cours des dernières décennies est la physique du couplage fort lumière-matière, qui étudie le comportement d'excitations hybrides collectives lumière-matière appelées polaritons. Alors que la matière se couple ordinairement faiblement au vide électromagnétique, l'utilisation de cavités optiques, c'est-à-dire du confinement des modes du champ électromagnétique, permet d'amplifier l'interaction lumière-matière. Une fois dans ce qui est appelé le régime de couplage fort, il a été démontré que l'hybridation des excitations de la matière avec les photons permet de modifier significativement les propriétés des matériaux, notamment par l'intermédiaire d'un couplage à longue portée entre les degrés de liberté de la matière qui est induit par les photons [16]. En tant qu'excitations collectives ondulatoires, les polaritons pourraient en principe être soumis aux phénomènes de localisation d'Anderson, ainsi qu'aux phénomènes topologiques mentionnés ci-dessus.

L'objectif de cette thèse est de combiner ces trois domaines d'étude actifs en examinant ce qu'il advient de la localisation d'Anderson ainsi que des phases topologiques de la matière et de leurs états topologiques de bord associés, dans le contexte de systèmes lumière-matière fortement couplés. Une caractéristique particulière de notre approche théorique est de se concentrer sur des structures unidimensionnelles, et de modéliser le couplage lumière-matière à l'aide d'un hamiltonien dérivé de manière microscopique qui décrit des cavités optiques multimodes réalistes.

Afin d'adresser cet objectif, ce manuscrit a été organisé de la façon suivante :

- Le Chapitre 1 a pour but de fournir une introduction préliminaire aux différents domaines d'étude considérés dans ce manuscrit, à savoir, la localisation d'Anderson dans les systèmes désordonnés, le concept des phases topologiques de la matière, et pour finir la physique du couplage fort lumière-matière.
- Le Chapitre 2 est dédié au cadre théorique que nous utilisons pour modéliser le couplage lumière-matière. À travers une approche hamiltonienne dans la jauge de Coulomb, nous dérivons un modèle d'un réseau unidimensionnel d'émetteurs dipolaires couplés aux modes électromagnétiques confinés d'une cavité optique multimode.
- Le Chapitre 3 contient nos investigations sur le devenir de la localisation d'Anderson en une dimension dans le régime de couplage fort lumière-matière. À l'aide du modèle développé dans le Chapitre 2, nous étudions à la fois le spectre et les propriétés de transport sous forçage et dissipation d'une chaîne désordonnée de dipôles fortement

couplés à une cavité multimode. L'un des principaux résultats de ce chapitre est l'émergence du transport amélioré par le désordre, un phénomène découlant de l'hybridation induite par le désordre des états sombres en polaritons.

- Le Chapitre 4 concerne notre étude de l'interaction entre les phénomènes topologiques et le couplage fort lumière-matière. En s'appuyant sur la théorie développée dans le Chapitre 2, nous analysons les propriétés d'une chaîne d'émetteurs dipolaires dimerisée fortement couplée aux photons de la cavité. Un tel système représente une variation du célèbre modèle de Su-Schrieffer-Heeger du polyacétylène, avec l'ajout d'un couplage dipôle-dipôle effectif médié par les photons. Nous étudions le spectre du modèle, ses propriétés de transport sous forçage et dissipation, et en particulier le devenir de ses caractéristiques topologiques. L'un des principaux résultats de ce chapitre est l'hybridation des états topologiques de bord originaux en ce que nous appelons des états de bord polaritoniques, ces derniers présentant des propriétés inhabituelles et n'émergeant que dans le régime de couplage fort.
- Enfin, nous tirons des conclusions sur les effets du désordre et de la topologie dans les systèmes lumière-matière fortement couplés, et nous plaçons notre travail en perspective, discutant ses limitations et proposant des études futures sur le sujet.

Dans ce résumé de thèse en français, nous présentons succinctement chacun des quatre chapitres ainsi que la conclusion décrites plus haut, en insistant en particulier sur les parties introductives, et en reproduisant certains des résultats les plus significatifs.

1 Préliminaires

1.1 Les systèmes désordonnés et la localisation d'Anderson

La présence inévitable d'impuretés, d'inhomogénéités ou d'irrégularités rend le désordre omniprésent dans la Nature. Cela fait de la structure cristalline parfaite l'exception plutôt que la règle, et dans la plupart des cas réalistes, on doit composer avec une certaine quantité de hasard et de désordre dans son expérience. Parmi de nombreux phénomènes fascinants induits par le désordre, la localisation d'Anderson, de part son universalité, a conduit à son propre domaine actif de recherche.

Dans son travail précurseur publié en 1958 [25], Anderson a considéré un modèle de liaisons fortes d'un électron se déplaçant dans un réseau désordonné. Sur chaque site du réseau, l'électron ressent une énergie potentielle aléatoire, choisie dans un intervalle de largeur W. Une fois piégé sur un site, l'électron peut sauter vers le site voisin le plus proche par effet tunnel.

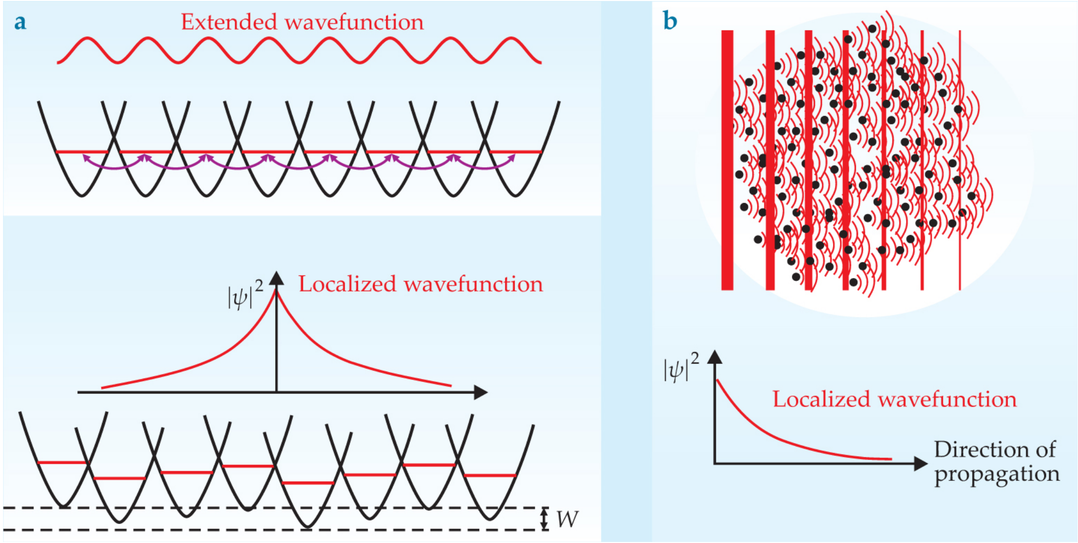

Figure 1: Localisation d'Anderson. Le panneau (a) montre un schéma du modèle d'Anderson, tandis que le panneau (b) illustre le phénomène d'interférence sous-jacent à la localisation d'Anderson. Figure reproduite de la Ref. [28].

Un tel système est esquissé dans la Fig. 1(a). Dans le panneau supérieur, le réseau a une structure cristalline, de sorte que la propagation de l'électron est régie par le théorème de Bloch, qui implique une fonction d'onde étendue. Dans le panneau inférieur, le paysage de potentiel ressenti par l'électron est désordonné. Lorsque la force du désordre W est suffisamment grande, la fonction d'onde se localise exponentiellement dans l'espace, conduisant à une absence de diffusion et à une suppression totale de la conduction, rendant ainsi le matériau isolant. La vision d'Anderson du comportement d'un électron dans un potentiel aléatoire contraste ainsi de manière drastique avec celle de petites particules classiques, pour lesquelles il est bien connu, par exemple à partir des expériences de Jean Perrin, que le désordre conduit à un mouvement diffusif [29].

Il a par la suite été réalisé que la localisation d'Anderson découle uniquement d'un mécanisme subtil d'interférence des ondes, de sorte qu'elle est applicable à toute onde se propageant dans un milieu désordonné. Dans le cas des électrons dans les solides, les interférences se produisent entre plusieurs chemins de diffusion des électrons. Lorsque ces chemins ont des positions initiales et finales largement séparées, des interférences destructrices se produisent, piégeant l'électron dans sa position initiale.

Une illustration qualitative de ce phénomène est faite dans la Fig.1(b). Les lignes rouges verticales représentent le front d'onde d'une onde plane se propageant dans un milieu avec de nombreuses impuretés, représentées par des points noirs. Une fois que l'onde plane est diffusée par les impuretés, les ondelettes sont rediffusées et interfèrent alors de manière cohérente les unes avec les autres. Pour une quantité suffisamment importante d'impuretés, l'interférence est destructive dans la direction de propagation, de sorte que l'amplitude de la fonction d'onde décroisse exponentiellement.

L'universalité de la localisation d'Anderson en physique des ondes a suscité un regain d'intérêt pour son exploration au cours des dernières décennies. Elle s'est révélée pertinente dans une grande variété de domaines de la physique classique, de l'acoustique [3] à l'océanographie [6], la photonique [11], ou même la géologie [33].

L'étude de la localisation d'Anderson dans ces domaines classiques peut nécessiter de nouvelles considérations théoriques. Alors que les électrons dans les solides peuvent être modélisés, sous certaines approximations, avec des couplages en proches voisins, les systèmes impliquant, par exemple, des excitations polaritoniques donnent lieu à un couplage à plus longue portée, ce qui pourrait rendre la théorie standard de la localisation d'Anderson inadéquate. C'est en partie ce à quoi nous nous attellerons dans le chapitre 3, où l'accent sera mis sur l'interaction entre le désordre et les polaritons.

1.2 Les phases topologiques de la matière

Le deuxième sujet que nous aborderons dans ce manuscrit concerne la physique des phases topologiques de la matière. En 1980, une découverte expérimentale par von Klitzing, Dorda et Pepper [42] d'un phénomène aujourd'hui connu sous le nom d'effet Hall quantique entier a révélé qu'un gaz d'électrons en deux dimensions, soumis à de basses températures et à un fort champ magnétique perpendiculaire, présentait une conductance de Hall caractérisée par des paliers quantifiés extrêmement précis, si précis que leur valeur était jusqu'à récemment utilisée dans un contexte de métrologie. Aux limites de ce gaz d'électrons bidimensionnel, des états de bord chiraux ont été prédits, permettant au matériau de manifester des propriétés métalliques à ses bords, bien qu'étant isolant dans son ensemble [43]. De manière remarquable, ces deux caractéristiques particulières, à savoir l'existence d'un invariant entier provenant des propriétés de volume du matériau, et la présence d'états de bord chiraux, ont montré une robustesse face aux imperfections et au désordre dans le matériau, et il se trouve qu'il existe en fait une connexion profonde entre ces propriétés, connue sous le nom de correspondance bord-volume [44].

L'étude de l'effet Hall quantique entier a marqué le début de ce qui sera plus tard appelé, au sens large du terme, les "isolants topologiques", un concept bien plus vaste qui a ouvert la voie à toute une nouvelle branche de la physique [36, 37]. Un isolant topologique se distingue par son comportement particulier en tant que matériau isolant dans son ensemble, mais qui présente des états de surface ou de bord conducteurs lorsqu'il est placé à l'interface d'un isolant conventionnel, typiquement le vide. Ici, le terme "topologique" provient de la discipline mathématique de la topologie, qui cherche notamment à classifier les objets restant inchangés lors d'une déformation continue. Par exemple, une sphère et un cube peuvent se déformer continûment l'un dans l'autre, les rendant topologiquement équivalents. Inversement, une sphère et un tore ne peuvent pas subir de telles déformations continues, ce qui les établit comme topologiquement distincts. Pour passer d'un de ces objets topologiquement distincts à un autre, une transition de phase topologique, telle que percer la sphère ou remplir le tore, doit avoir lieu. Dans ce contexte, une propriété globale caractérisant la topologie de ces objets est leur genre $\mathcal{G}$ – autrement dit leur nombre de trou – qui prend une valeur de 0 pour la sphère et le cube, mais de 1 pour le tore. La quantité $\mathcal{G}$ sert d'invariant topologique du système et manifeste donc, par définition, une robustesse face aux déformations continues. Dans le cas des isolants topologiques en physique, plutôt que des objets géométriques, ce sont les hamiltoniens que nous cherchons à classer, et leurs structures de bandes, qui proviennent typiquement des électrons se propageant dans des cristaux, qui subissent des déformations. De cette façon, l'effet Hall quantique entier découvert en 1980 peut être vue comme une phase de la matière topologiquement distincte de toutes les autres phases de la matières précédemment connues.

Pour étudier les isolants topologiques, nous nous concentrons sur les hamiltoniens dont le spectre contient une bande interdite, un *bandgap* (notons qu'il y a aussi des supraconducteurs topologiques, où la bande interdite réfère au gap supraconducteur). L'invariant topologique du système, calculé à partir des propriétés des fonctions d'ondes des électrons, restera alors robuste à toute déformation de la structure de bande qui ne ferme pas le bandgap. En d'autres termes, l'invariant topologique ne change pas aussi longtemps que le matériau reste isolant. En conséquence, les états de bord associés avec la phase topologique non triviale sont également robustes à toute déformation continue de la structure de bande de l'hamiltonien. En pratique, cette robustesse se manifeste par une résistance au désordre, parfois à condition que certaines symétries du système soient préservées. Cette robustesse des états de bord est une des raisons pour lesquelles la physique des phases topologiques attire une si grande attention. En effet, de nombreuses applications potentielles ont été imaginées pour ces matériaux, particulièrement pour les technologiques quantiques et photoniques, telles que les technologies laser, la spintronique, ou encore l'informatique quantique.

Une percée importante dans le domaine des phases topologiques de la matière fut la classification complète de toutes les phases, quelque soit la dimension du système, en 10 classes d'hamiltoniens satisfaisant ou non certaines symétries discrètes du système, le "tenfold way" [45, 46]. En effet, en 1996, Altland et Zirnbauer ont démontré que tous les hamiltoniens peuvent être classifiés sur la base de deux symétries fondamentales : la symétrie par renversement du temps ($\mathcal{T}$), et la symétrie de charge ($\mathcal{C}$), aussi connue sous le nom de symétrie particule-trou [55]. Ces deux symétries correspondent à des transformations anti-unitaires, ce qui signifie qu'elles peuvent être écrites comme le produit d'une matrice unitaire $\mathcal{U}$ et de l'opérateur de conjugaison complexe $\mathcal{K}$. Cela implique, de façon importante, que ces symétries peuvent possiblement prendre deux valeurs différentes une fois mises au carré: $+1$ ou -1. En distinguant entre le signe positif ou négatif de leur carré, et en considérant également le cas où aucune symétrie n'est satisfaite, on obtient

Symmetry				**Dimension**							
AZ class	$\mathcal{T}$	$\mathcal{C}$	$\mathcal{S}$	**1**	**2**	**3**	**4**	**5**	**6**	**7**	**8**
A	0	0	0	0	$\mathbb{Z}$	0	$\mathbb{Z}$	0	$\mathbb{Z}$	0	$\mathbb{Z}$
AIII	0	0	+1	$\mathbb{Z}$	0	$\mathbb{Z}$	0	$\mathbb{Z}$	0	$\mathbb{Z}$	0
AI	+1	0	0	0	0	0	$\mathbb{Z}$	0	$\mathbb{Z}_2$	$\mathbb{Z}_2$	$\mathbb{Z}$
BDI	+1	+1	+1	$\mathbb{Z}$	0	0	0	$\mathbb{Z}$	0	$\mathbb{Z}_2$	$\mathbb{Z}_2$
D	0	+1	0	$\mathbb{Z}_2$	$\mathbb{Z}$	0	0	0	$\mathbb{Z}$	0	$\mathbb{Z}_2$
DIII	-1	+1	+1	$\mathbb{Z}_2$	$\mathbb{Z}_2$	$\mathbb{Z}$	0	0	0	$\mathbb{Z}$	0
AII	-1	0	0	0	$\mathbb{Z}_2$	$\mathbb{Z}_2$	$\mathbb{Z}$	0	0	0	$\mathbb{Z}$
CII	-1	-1	+1	$\mathbb{Z}$	0	$\mathbb{Z}_2$	$\mathbb{Z}_2$	$\mathbb{Z}$	0	0	0
C	0	-1	0	0	$\mathbb{Z}$	0	$\mathbb{Z}_2$	$\mathbb{Z}_2$	$\mathbb{Z}$	0	0
CI	+1	-1	+1	0	0	$\mathbb{Z}$	0	$\mathbb{Z}_2$	$\mathbb{Z}_2$	$\mathbb{Z}$	0

Table 1: Le "tenfold way". Classification d'Altland-Zirnbauer des isolants (et supraconducteurs) topologiques [45, 46].

ainsi 9 classes d'hamiltoniens différentes basées sur ces deux symétries fondamentales. Dans certains cas, enfin, les hamiltoniens peuvent également ne posséder aucune des deux symétries $\mathcal{T}$ et $\mathcal{C}$ de manière indépendante, mais une combinaison des deux, connue sous le nom de symétrie chirale, ou symétrie de sous-réseau $\mathcal{S} = \mathcal{C}\mathcal{T}$, amenant à une troisième symétrie, et à une dixième classe d'hamiltoniens. Ces 10 classes, connues comme les 10 classes d'Altland-Zirnbauer (AZ), divisent la matière en 10 types fondamentalement différents. Ces 10 combinaisons de symétries sont représentées dans la partie gauche de la Table 1, dans laquelle la classe est indiquée par son indice de Cartan, et où un 0 signifie l'absence d'une symétrie, un 1 sa présence, et le signe $+$ ou $-$ la positivité ou négativité du carré de ladite symétrie.

Pour classer ces hamiltoniens selon qu'ils puissent présenter ou non des propriétés topologiques, Schnyder, Ryu, Furusaki et Ludwig ont remarqué qu'une phase topologique pouvait être vue précisément comme une phase dans laquelle il existait des états de bord qui échappent à la localisation d'Anderson [46, 56]. En effet, les états de bord étant conducteurs, c'est-à-dire délocalisés, et présentant une robustesse face au désordre, ils évitent la localisation. De cette façon, une phase topologique en dimension d peut être vue comme une phase de dimension $d-1$ évitant d'une certaine façon la localisation d'Anderson. C'est en suivant cette approche que le remplissage de la Table 1 a pu être réalisé pour la première fois [56], et le résultat est présenté dans sa partie droite, où les 8 colonnes indiquent la dimension considérée entre 1 et 8. Dans ce tableau, d'une part, un 0 indique l'absence d'une phase topologique pour l'hamiltonien dans une classe et une dimension donnée. D'autre part, lorsqu'une phase topologique est présente, elle est indiquée par l'ensemble mathématique auquel appartient son invariant topologique. Seulement deux types d'invariants topologiques sont possibles : soit des invariants $\mathbb{Z}$, qui peuvent prendre toute valeur entière, soit des invariants $\mathbb{Z}_2$, qui sont limités aux valeurs de 0 et 1. Enfin, il est intéressant de noter que seules les 8 premières dimensions potentielles du système sont représentées dans le tableau. Cela vient du fait qu'il existe une périodicité de dimension 8, un phénomène appelé "Bott Clock", de sorte que le tableau se répète à l'infini passée cette dimension. Cette à priori curieuse périodicité provient de la structure mathématique particulièrement profonde sous-jacente à cette classification [45].

Dans ce manuscrit de thèse, nous nous concentrons sur la physique topologique à une dimension. En particulier, notre étude tournera autour du modèle de Su-Schrieffer-Heeger (SSH) du polyacétylène [61], qui possède les trois symétries $\mathcal{T}$, $\mathcal{C}$ et $\mathcal{S}$. Selon les symétries que l'on considère pour assurer la robustesse des propriétés topologiques, le modèle SSH peut ainsi appartenir aux classes AIII ou BDI d'Altland-Zirnbauer (la classe D, elle, représente la chaîne de Kitaev, un supraconducteur topologique), et possède un invariant topologique $\mathbb{Z}$. Par sa simplicité apparente, le modèle SSH sert souvent d'exemple typique de topologie à une dimension.

De manière intéressante, tout comme la localisation d'Anderson, les phénomènes topologiques en physique ont leur origine sous-jacente dans des phénomènes fondamentalement non quantiques. Plus précisément, les propriétés topologiques proviennent d'effets de phases géométriques, qui peuvent être retrouvés dans de nombreux systèmes de physique des ondes, et plus particulièrement dans ceux où une onde se propage dans un milieu périodique, de sorte qu'une structure de bande puisse être définie [4]. En effet, pléthore de systèmes classiques possèdent des propriétés topologiques analogues à celles des isolants topologiques électroniques. Des états de bord topologiques ont notamment été observés dans des domaines aussi variés que l'acoustique [5], la mécanique [62], la matière active [63], l'océanographie [7], les mouvements coordonnés d'êtres humains (tels que la danse) [64], les atomes froids [10], la photonique [14], ainsi que dans la physique des polaritons [65, 66], que nous allons introduire dans la section suivante.

1.3 Le couplage fort lumière-matière

L'interaction entre la lumière et la matière, de par son omniprésence autour de nous, a été un important sujet de recherche scientifique depuis le début de la méthode scientifique il y a des siècles de celà. Une étape importante de sa compréhension eut lieu dans les années 1930, avec l'établissement de la théorie de l'électrodynamique quantique, qui offra un cadre théorique complet et précis permettant d'expliquer ses subtilités au niveau le plus fondamental. L'électrodynamique quantique permit notamment de comprendre des phénomènes aussi important que l'émission spontanée, cette dernière étant à l'origine de la grande majorité de la lumière que nous observons tous les jours autour de nous [67].

Alors que la lumière et la matière peuvent apparaître initialement comme des entités complètement différentes, il existe une situation où elles ont un comportement étroitement lié, connu sous le nom de régime de couplage fort lumière-matière. Dans ce régime, lumière et matière deviennent indistinguables et se comportent comme des excitations ou quasiparticules hybrides,

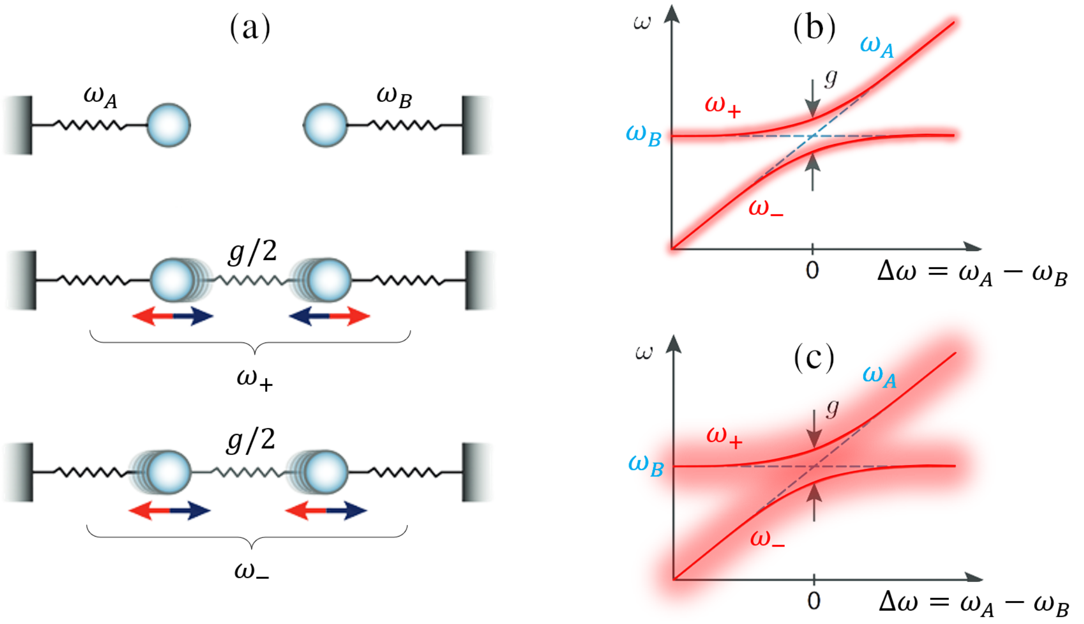

Figure 2: Analogie des oscillateurs couplés. (a) Schéma de deux oscillateurs de fréquence ω_A et ω_B. Une fois couplés par une constante de couplage $g/2$, le système présente deux modes propres de fréquences ω_+ et ω_-, qui constituent des excitations hybrides faites d'une combinaison des deux excitations découplées, tout comme les polaritons sont des excitations hybrides lumière-matière. (b)-(c) Schéma d'un croisement évité : (b) dans le régime de couplage fort, où les largeurs de bandes des excitations sont plus faibles que la séparation de Rabi g, et (c) dans le régime de couplage faible, où les largeurs de bandes sont plus grandes que la séparation de Rabi, de sorte que les deux excitations ne sont plus distinguables l'une de l'autre. Figures adaptées de la Ref. [77].

appelées polaritons. Ces quasiparticules, combinaisons linéaires de lumière et de matière, ont d'abord été introduites dans les années 1950 dans le contexte du couplage fort entre de la lumière et des excitations vibrationnelles, des phonons, résultant en des phonon-polaritons [68, 69]. Par la suite, des caractéristiques similaires ont été prédites dans le couplage entre de la lumière et des degrés de liberté électroniques comme des excitons – une combinaison entre un électron et un trou, liée par la force de Coulomb – donnant lieu à des exciton-polaritons [70, 71]. Depuis, le domaine n'a cessé de grandir et aujourd'hui plus de 70 différent types d'excitations polaritoniques ont été découvertes [72]. Parmi elles, les plasmon-polaritons, des excitations aux interfaces métal-isolant, ont beaucoup attiré l'attention, tout comme les excitons-polaritons. Ces derniers ont notamment été abondamment étudiés dans le contexte des puits quantiques intégrés dans des microcavités [73], ainsi que dans celui des films de semiconducteurs organiques dans des résonateurs optiques [74].

Le mécanisme sous-jacent à l'existence des polaritons peut être grossièrement compris à partir d'une simple perspective classique [75], notamment au travers de l'analogie des oscillateurs couplés, illustrée par la Fig. 2(a). Dans cette analogie, détaillée dans la Ref. [76], on considère deux oscillateurs mécaniques, tels que des systèmes masses-ressorts, ayant chacun une fréquence de résonance différente ω_A et ω_B. Une fois couplés linéairement avec une constante de couplage $g/2$, les modes propres originaux des deux oscillateurs découplés sont renormalisés en deux nouveaux modes propres du système combiné : une excitation en phase, de fréquence ω_+, et une excitation en opposition de phase, de fréquence ω_-. Dans le contexte du couplage fort lumière-matière, les oscillateurs A et B correspondent respectivement, par exemple, aux degrés de liberté photoniques et de matière. Le couplage $g/2$, quant à lui, dénote le taux d'échange d'énergie entre les deux systèmes. Les deux nouveaux modes propres peuvent être vus comme des excitations hybrides des deux oscillateurs originaux A et B, et sont donc les polaritons. De manière intéressante, dans de nombreux scénarios, à la fois les excitations de lumière et de matière peuvent être modélisées par des oscillateurs harmoniques, et leur couplage est linéaire, ce qui rend cette analogie à priori naïve plutôt réaliste [76].

Si nous étudions maintenant la variation des fréquences des modes propres couplés ω_+ et ω_- en fonction de la différence entre les deux fréquences originales, $\Delta\omega = \omega_A - \omega_B$, nous obtenons les tracés rouges de la Fig. 2(b). Dans cette figure, les deux lignes bleues en pointillé correspondent, elles, aux fréquences originales des oscillateurs A et B. On observe dans ce graphique ce qu'on appelle un schéma de croisement évité, à savoir la séparation des deux lignes bleues croisées en deux courbes rouges. C'est un phénomène typique de la physique des systèmes fortement couplés, qui est couramment observé dans la structure de bande des polaritons. On remarque notamment que lorsque la différence $\Delta\omega = 0$, c'est à dire lorsque les deux oscillateurs entrent en résonance, l'écart entre les deux fréquences renormalisées est exactement égal à g, à savoir deux fois la constante de couplage. Dans le contexte des polaritons, cet écart est appelé la séparation de Rabi.

Afin de décrire correctement un système physique, il est cependant nécessaire de prendre en compte l'effet de la dissipation du système, qui implique de considérer des excitations avec un temps de vie fini. Cette dissipation entraîne des pertes, que l'on note κ pour les photons (oscillateur A), et γ pour les excitations de matière (oscillateur B). Ces pertes induisent une largeur de bande aux excitations, qui est représentée sur la Fig. 2(b) comme un flou entourant les courbes. Pour être formellement dans le régime de couplage fort, il est alors essentiel que le taux d'échange d'énergie entre les deux oscillateurs excède leurs taux de pertes, de sorte qu'un transfert cohérent d'énergie puisse avoir lieu entre les deux oscillateurs. En d'autres termes, la largeur de bande des excitations doit être plus faible que la séparation de Rabi, et donc les deux courbes floues de la Fig. 2 doivent restées distinguables l'une de l'autre. Cela nous amène à définir le couplage fort lumière-matière via le critère $g > \kappa, \gamma$. Dans la Fig. 2(c), nous illustrons ensuite le cas d'un système avec plus de pertes, tel que $g < \kappa, \gamma$. Dans ce cas le système est dans le régime de couplage faible, les excitations étant perdues avant qu'elles ne puissent s'hybrider.

Afin d'atteindre expérimentalement le régime de couplage fort, les expérimentateurs emploient généralement des cavités miroirs de type Fabry-Pérot, qui confinent les modes électromagnétiques à l'intérieur d'un volume fini. Les miroirs réfléchissent les photons, augmentant leur interaction avec le matériau à l'intérieur de la cavité, et ainsi augmentant leurs effets sur les excitations de matière. À l'aide d'un ajustement fin de la cavité, il est possible de sélectionner la fréquence de résonance des photons à l'intérieur, de sorte qu'ils entrent en résonance avec les excitations de matière. Il est également possible d'optimiser le temps de vie des photons en ajustant le facteur de qualité des miroirs de la cavité. Dans le chapitre 2, nous introduirons notre cadre théorique permettant de décrire ce type de cavités optiques, qui seront au centre de ce manuscrit.

Les polaritons offrent de nombreux avantages et sont activement étudiés pour leurs propriétés mixtes lumière et matière. Ils promettent des percées technologiques et des avancées fondamentales dans de nombreux domaines, en permettant notamment l'étude de condensat de Bose-Einstein [78], de comportement hors équilibres universels [79], de technologies laser à température ambiante [80], de superfluidité [81], ou encore de manipuler et d'améliorer des réactions chimiques [82]. En plus de cela, une des caractéristiques clés des polaritons est leur capacité à réaliser du transport d'énergie à longue portée, via une propagation balistique.

Cette propriété de transport amena un grand nombre de propositions théoriques [83–95] et d'expériences utilisant notamment des semiconducteurs organiques moléculaires [96–110], des puits quantiques semiconducteurs [111], des plexcitons dans des réseaux de nanoparticules plasmoniques [112], ou encore des dichalcogénures de métaux de transitions [113–115], à utiliser le couplage fort lumière-matière pour améliorer le transport d'énergie ou de charge dans la matière, comme par exemple la conductivité électrique ou la photoconductivité [106], cette dernière étant particulièrement intéressante pour les technologies photovoltaïques. De façon intéressante, il a été démontré que les états sombres, c'est-à-dire les états de matière qui ne sont que faiblement hybridés aux degrés de libertés photoniques, ont également des caractéristiques de transport intéressantes induites par le couplage fort [87, 90, 91, 107].

Ces améliorations du transport sont attribuées à la nature hybride des excitations collectives polaritoniques, permettant leur délocalisation dans tout le système, le couplage fort induisant un couplage effectif à longue portée, médié par les photons, entre les excitations de matière. Ce transport amélioré par la cavité peut être particulièrement intéressant lorsqu'il est appliqué aux

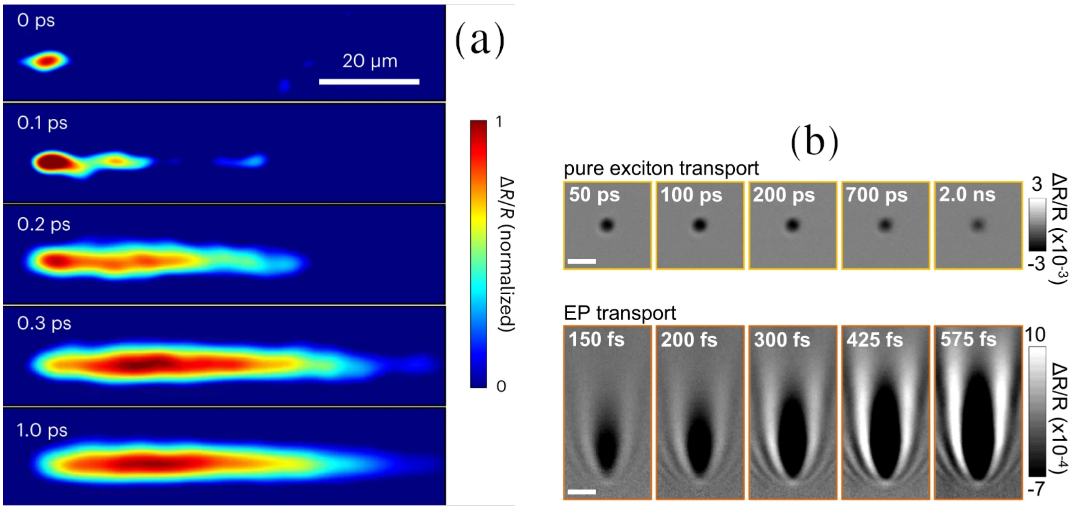

Figure 3: Transport polaritonique. Imagerie en temps réel du transport de polaritons, via une mesure différentielle de la réflectivité dans des expériences pompes-sondes. (a) Propagation rapide d'exciton-polaritons (EP) dans un film moléculaire de colorant placé à l'intérieur d'une cavité miroir. Figure reproduite de la Ref. [109]. (b) Comparaison entre le transport d'exciton purs (en haut) et d'EP (en bas) dans des couches minces de perovskites halogénées incorporées dans une cavité optique. Figure reproduite de la Ref. [110].

systèmes désordonnés, un scénario que nous étudierons en détails dans le chapitre 3.

Très récemment, des études expérimentales ont réussi à suivre de manière précise le transport à longue portée des polaritons, en utilisant des techniques de microscopie en temps réel et dans l'espace réel [109, 110]. Nous présentons ces résultats dans les figures 3(a)-(b), qui ont l'avantage de permettre une visualisation claire du phénomène de transport amélioré par la cavité. Ces expériences ont été réalisées à température ambiante, en utilisant des films bidimensionnels de matériaux excitoniques, placés entre deux réseaux de Bragg, des cavités optiques de type Fabry-Pérot constitués d'une alternance de couches de matériaux d'indices de réfraction différents. En utilisant une configuration de type pompe-sonde, la différence de l'intensité de réflexion entre le signal pompé et le signal sondé, ΔR, a été mesuré, puis normalisé par le signal pompé, R. Différents temps de délais entre la pompe et la sonde ont été utilisés pour suivre temporellement l'évolution de l'excitation.

Dans la Fig. 3(a), des films moléculaires de colorants de type “J-aggregates”, un semiconducteur organique, ont été utilisés. On observe très clairement la rapide propagation de l'excitation polaritonique, qui traverse plusieurs dizaines de micromètres en une picoseconde. Dans la Fig. 3(b), ce sont des couches minces de pérovskites halogénées, un semiconducteur particulièrement photosensible, qui ont été utilisées. Une comparaison entre la propagation d'excitons sans cavité (panneaux supérieurs) et avec cavité (panneaux inférieurs) permet de visualiser les avantages de transport permis par la cavité. Il est intéressant de constater que les films moléculaires utilisés dans ces deux expériences sont par nature amorphes, et donc fortement désordonnés. Ils permettent donc directement l'étude de l'interaction entre désordre et couplage fort, de sorte que nous reviendrons à ces expériences au début du chapitre 3.

Dans l'étude présentée dans le reste de ce manuscrit, nous allons démontrer que ces caractéristiques de propagation à longue portée des polaritons présentent un potentiel intéressant à la fois pour les systèmes désordonnés et pour les systèmes topologiques.

2 Modélisation du couplage lumière-matière

Dans ce chapitre, nous développons une théorie quantique microscopique, à partir de zéro, d'une chaîne d'émetteurs dipolaires couplés aux modes confinés d'un champ électromagnétique dans une cavité optique. Bien que les équations de Maxwell soient à priori suffisantes pour décrire l'interaction lumière-matière et également le régime de couplage fort, il est intéressant de construire un modèle quantique de cette interaction, en utilisant le formalisme hamiltonien. En effet, alors que résoudre directement les équations de Maxwell amènent généralement à l'utilisation d'algorithmes numériques complexes, un formalisme quantique nous permet d'utiliser les outils de l'optique quantique, et de bien souvent gagner en intuition physique sur le problème grâce à une théorie analytique transparente.

L'idée de départ de ce chapitre est de partir du potentiel vecteur $\mathbf{A}$ du champ électromagnétique qui, dans la jauge de Coulomb, est purement transverse,

$$\nabla \cdot \mathbf{A} = 0, \tag{1}$$

puis d'utiliser la seconde quantification pour quantifier le champ électromagnétique via une expansion en modes de Fourier du potentiel vecteur, de sorte qu'il s'écrive alors [120–122]

$$\mathbf{A}(\mathbf{r}) = \sum_{\mathbf{k},\hat{\lambda}_{\mathbf{k}}} \sqrt{\frac{2\pi\hbar c^2}{\omega_{\mathbf{k}}^{\mathrm{ph}}}} \left[\mathbf{f}_{\mathbf{k}}^{\hat{\lambda}_{\mathbf{k}}}(\mathbf{r}) c_{\mathbf{k}}^{\hat{\lambda}_{\mathbf{k}}} + \mathbf{f}_{\mathbf{k}}^{\hat{\lambda}_{\mathbf{k}}\,*}(\mathbf{r}) c_{\mathbf{k}}^{\hat{\lambda}_{\mathbf{k}}\,\dagger} \right]. \tag{2}$$

Dans cette équation, $\omega_{\mathbf{k}}^{\mathrm{ph}} = c|\mathbf{k}|$ représente la dispersion photonique, et les $\mathbf{f}_{\mathbf{k}}^{\hat{\lambda}_{\mathbf{k}}}(\mathbf{r})$ correspondent aux fonctions de modes du champ électromagnétique, évalué à la position $\mathbf{r}$. Ces fonctions de modes contiennent la dépendance spatiale du mode de champ ayant un vecteur d'onde $\mathbf{k}$ et une polarisation $\hat{\lambda}_{\mathbf{k}}$, et ils dépendent ainsi de la géométrie de l'espace dans lequel le champ est quantifié. Les opérateurs de champ bosoniques $c_{\mathbf{k}}^{\hat{\lambda}_{\mathbf{k}}}$ et $c_{\mathbf{k}}^{\hat{\lambda}_{\mathbf{k}}\,\dagger}$ apparaissant dans l'Eq. (2) respectivement annihilent et créent une excitation photonique de vecteur d'onde $\mathbf{k}$ et de polarisation $\hat{\lambda}_{\mathbf{k}}$.

On considère ensuite $\mathcal{M}$ émetteurs dipolaires sous-longueur d'ondes, polarisés dans la direction x, et alignés dans la direction z. On traite ces émetteurs comme des dipôles idéaux, c'est à dire sans degrés de libertés internes, de sorte qu'ils se comportent comme des dipôles oscillants classiques. Ce type d'émetteurs dipolaires peut représenter en réalité une large gamme de systèmes physiques dont le couplage principal est de nature dipolaire, et dont les propriétés sont gouvernées par l'électromagnétisme classique. En effet, ils peuvent modéliser des plateformes expérimentales aussi variées que des nanoparticules sous-longueur d'ondes plasmoniques, diélectriques ou SiC [19, 123–125], des microsphères magnoniques [126–128], des antennes micro-ondes [129], des excitons de semiconducteurs [130], ou encore des atomes froids [131–133] ainsi que tout autre système d'émetteurs à deux niveaux, ces derniers se comportant également comme des dipôles classiques dans le sous-espace d'excitation unique [134].

L'hamiltonien décrivant un ensemble de ces émetteurs dipolaires non-couplés s'écrit

$$H_{\mathrm{dp}}^{0} = \sum_{i=1}^{\mathcal{M}} \left[\frac{\mathbf{\Pi}_i^2}{2M} + \frac{M\omega_i \mathbf{h}_i^2}{2} \right], \tag{3}$$

où $\mathbf{\Pi}_i$ est l'impulsion conjuguée au déplacement $\mathbf{h}_i$ de la $i$ème excitation dipolaire, M la masse effective d'un émetteur, et ω_i sa fréquence de résonance.

Pour coupler ces dipôles au champ électromagnétique, on utilise le couplage minimal en substituant l'impulsion via [121]

$$\mathbf{\Pi}_i \to \mathbf{\Pi}_i + \frac{Q}{c}\mathbf{A}(\mathbf{r}_i), \tag{4}$$

où $-Q$ est la charge effective d'un émetteur et c la vitesse de la lumière dans le vide. Une telle substitution prend sont origine dans une théorie relativiste, par le remplacement dans l'hamiltonien libre des dérivées usuelles par les dérivées covariantes, $\partial_\mu \to D_\mu = \partial_\mu + (\mathrm{i}Q/c)A_\mu$, où A_μ est le quadrivecteur potentiel. Ce remplacement est nécessaire pour préserver la symétrie de jauge $U(1)$ de l'électromagnétisme [135].

Enfin, l'hamiltonien du champ électromagnétique s'écrit, en unités cgs,

$$\begin{aligned} H_{\mathrm{em}} &= \frac{1}{8\pi}\int \mathrm{d}^3\mathbf{r} \left[|\mathbf{E}_\perp + \mathbf{E}_\parallel|^2 + |\mathbf{B}|^2 \right] \\ &= \frac{1}{8\pi}\int \mathrm{d}^3\mathbf{r} \left[|\mathbf{E}_\perp|^2 + |\mathbf{B}|^2 \right] + \frac{1}{2}\int \mathrm{d}^3\mathbf{r}\, \rho\phi \\ &= H_{\mathrm{ph}} + V_{\mathrm{Coulomb}}^{\mathrm{dip-dip}} \end{aligned} \tag{5}$$

où l'on a séparé, via le théorème de décomposition de Helmholtz, le champ électrique en sa partie transverse $\mathbf{E}_\perp$ et sa partie longitudinale $\mathbf{E}_\parallel$, le champ magnétique étant lui purement transverse. Dans la jauge de Coulomb, le couplage lumière-matière est entièrement décrit par le potentiel vecteur et donc la partie transverse du champ électromagnétique, qui contient notamment tous les effets de retard du champ. La partie longitudinale du champ électromagnétique, amène quant à elle l'énergie potentielle d'interaction de Coulomb $V_{\text{Coulomb}}^{\text{dip}-\text{dip}}$, autrement dit le couplage dipolaire quasistatique entre les émetteurs, qui décroît avec le cube de la distance séparant les dipôles, et s'écrit en fonction du potentiel scalaire ϕ et de la densité de charge ρ.

Via les relations $\mathbf{B} = \nabla \times \mathbf{A}$ et $\mathbf{E}_{\perp} = -(1/c)\partial_t \mathbf{A}$, on obtient ensuite l'hamiltonien photonique en seconde quantification,

$$H_{\text{ph}} = \sum_{\mathbf{k},\hat{\lambda}_{\mathbf{k}}} \hbar\omega_{\mathbf{k}}^{\text{ph}} \left[{c_{\mathbf{k}}^{\hat{\lambda}_{\mathbf{k}}}}^{\dagger} c_{\mathbf{k}}^{\hat{\lambda}_{\mathbf{k}}} + \frac{1}{2} \right], \tag{6}$$

qui correspond à une somme d'oscillateurs harmoniques quantiques, un pour chaque mode photonique. Cela nous amène à l'hamiltonien total du système que nous considérons dans ce manuscrit de thèse :

$$H = \sum_{i=1}^{\mathcal{M}} \left[\frac{\left(\mathbf{\Pi}_i + \frac{Q}{c}\mathbf{A}(\mathbf{r}_i) \right)^2}{2M} + \frac{M\omega_i \mathbf{h}_i^2}{2} \right] + H_{\text{em}}. \tag{7}$$

En utilisant un formalisme de seconde quantification également pour les excitations dipolaires, via des opérateurs d'échelle bosoniques de création et d'annihilation d'excitations dipolaires $b_i^{\dagger}$ et b_i, on obtient l'hamiltonien sous sa forme quantifiée :

$$\begin{aligned} H = &\sum_{i=1}^{\mathcal{M}} \hbar\omega_i {b_i}^{\dagger} b_i \; + \sum_{\mathbf{k},\hat{\lambda}_{\mathbf{k}}} \hbar\omega_{\mathbf{k}}^{\text{ph}} {c_{\mathbf{k}}^{\hat{\lambda}_{\mathbf{k}}}}^{\dagger} c_{\mathbf{k}}^{\hat{\lambda}_{\mathbf{k}}} \\ &+ \sum_{\substack{i,j=1 \\ (i \neq j)}}^{\mathcal{M}} \frac{\hbar Q^2}{4M\sqrt{\omega_i \omega_j} |\mathbf{r}_i - \mathbf{r}_j|^3} \left({b_i}^{\dagger} + b_i \right) \left({b_j}^{\dagger} + b_j \right) \\ &+ \mathrm{i}\hbar \sum_{i=1}^{\mathcal{M}} \sum_{\mathbf{k},\hat{\lambda}_{\mathbf{k}}} \sqrt{\frac{\pi Q^2 \omega_i}{M\omega_{\mathbf{k}}^{\text{ph}}}} \left({b_i}^{\dagger} - b_i \right) \left[\mathbf{f}_{\mathbf{k}}^{\hat{\lambda}_{\mathbf{k}}}(\mathbf{r}_i) c_{\mathbf{k}}^{\hat{\lambda}_{\mathbf{k}}} + \text{H.c.} \right] \cdot \hat{x} \\ &+ \sum_{i=1}^{\mathcal{M}} \sum_{\substack{\mathbf{k},\hat{\lambda}_{\mathbf{k}} \\ \mathbf{k}',\hat{\lambda}'_{\mathbf{k}'}}} \frac{\hbar\pi Q^2}{M\sqrt{\omega_{\mathbf{k}}^{\text{ph}} \omega_{\mathbf{k}'}^{\text{ph}}}} \left[\mathbf{f}_{\mathbf{k}}^{\hat{\lambda}_{\mathbf{k}}}(\mathbf{r}_i) c_{\mathbf{k}}^{\hat{\lambda}_{\mathbf{k}}} + \text{H.c.} \right] \cdot \left[\mathbf{f}_{\mathbf{k}'}^{\hat{\lambda}'_{\mathbf{k}'}}(\mathbf{r}_i) c_{\mathbf{k}'}^{\hat{\lambda}'_{\mathbf{k}'}} + \text{H.c.} \right], \end{aligned} \tag{8}$$

qui sera au cœur de l'étude menée dans ce manuscrit. De façon importante, l'hamiltonien (8) représente le couplage d'émetteurs dipolaires à une cavité optique multimodale, ce qui va au-delà de la majorité de la littérature existante, qui considère le plus souvent des cavités optiques monomodales.

La suite de ce chapitre est alors dédié à la quantification précise du champ électromagnétique, afin de trouver la forme des fonctions de modes $\mathbf{f}_{\mathbf{k}}^{\hat{\lambda}_{\mathbf{k}}}$ – et donc la forme du couplage lumière-matière – à l'intérieur d'une cavité miroir

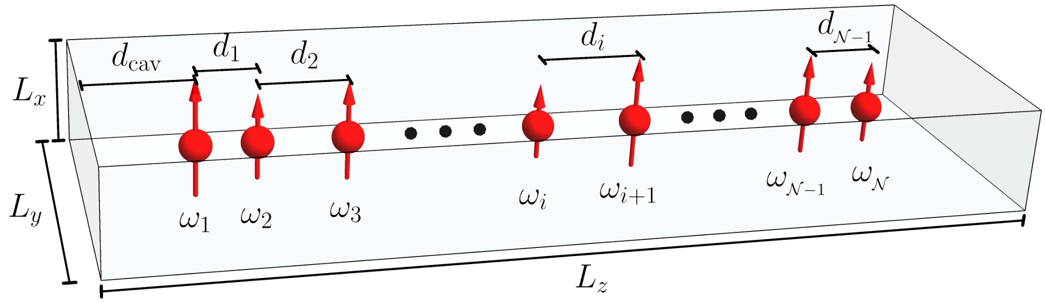

Figure 4: Chaîne désordonnée de dipôles dans une cavité. Schéma d'une chaîne de $\mathcal{N} \gg 1$ dipôles désordonnés, arrangés selon la direction z, et placés au milieu d'une cavité optique cuboïdale. Chaque dipôle i oscille à une fréquence de résonance aléatoire ω_i, et est séparé de son voisin de droite par une distance aléatoire d_i. La fréquence de résonance moyenne est ω_0, et la distance de séparation moyenne est d.

de forme allongée, d'abord infiniment allongée, puis de taille finie. On notera que dans tous les cas, on obtient un couplage lumière-matière proportionnel à $1/\sqrt{\mathcal{V}}$, avec $\mathcal{V}$ le volume de la cavité. Un ajustement précis du volume de la cavité, et notamment de ses dimensions transverses, nous permettra alors de modifier les fréquences de résonances de la cavité ainsi que le couplage lumière-matière, et d'amener – ou non – le système dans le régime de couplage fort. Ensuite, nous utilisons diverses approximations afin de simplifier l'hamiltonien (8) pour pouvoir l'étudier dans les chapitres suivants.

3 Désordre et polaritons

Dans le chapitre précédent, nous avons présenté un formalisme permettant de modéliser le couplage d'émetteurs dipolaires à des modes confinés du champ électromagnétique dans une cavité optique multimodale. L'objectif de ce présent chapitre est d'utiliser ce formalisme pour étudier l'interaction entre le désordre et le couplage fort lumière-matière. Comme présenté au chapitre 1, le couplage fort lumière-matière permet l'apparition d'excitations propres hybrides, appelées polaritons, ayant des propriétés uniques. En particulier, les excitations polaritoniques sont connues pour présenter des caractéristiques de transport d'énergie à longue portée. De façon intéressante, une grande partie des expériences conduites sur la propagation des polaritons s'est faite en utilisant des excitons dans des semiconducteurs moléculaires amorphes, des matériaux qui sont donc désordonnés par nature. L'étude de ces polaritons désordonnés est donc importante d'un point de vue expérimental, et elle a révélé des phénomènes inattendus, comme une robustesse des polaritons face au désordre, ce qui va au-delà de la théorie de la localisation d'Anderson. De manière surprenante, dans des études théoriques récentes de systèmes polaritoniques désordonnés, une amélioration des caractéristiques de transport a même été prédite en augmentant la force du désordre, au lieu de la suppression attendue.

Jusqu'à aujourd'hui, l'analyse théorique de ces expériences de transport de polaritons désordonnés, et notamment la prédiction de ce phénomène de transport amélioré par le désordre, a été réalisé en utilisant des modèles théoriques ne considérant qu'un seul mode photonique, tel que le modèle de Tavis-Cummings. Cependant, les cavités optiques utilisées dans ces expériences sont généralement multimodales, et il a été récemment pointé dans des études qu'il était indispensable de considérer des photons et un couplage dispersif, c'est-à-dire de modéliser une cavité multimodale, pour décrire correctement le transport de polaritons [17, 92, 94, 163–165].

Dans ce chapitre, nous utilisons alors les outils développés précédemment pour étudier les polaritons désordonnés au-delà du modèle monomode de Tavis-Cummings, en incorporant un couplage dipolaire quasistatique entre tous les émetteurs, et le couplage à une cavité multimode. Le système considéré dans ce chapitre est schématisé dans la Figure 4, à savoir $\mathcal{N}$ émetteurs dipolaires désordonnés – c'est à dire ayant des fréquences de résonance différentes, et des positions non régulières le long de la direction z – placés au cœur d'une cavité optique allongée de taille finie, comportant des miroirs métalliques parfaitement réfléchissants de tous les côtés.

Grâce à ce cadre théorique, nous démontrons dans ce chapitre de nombreux résultats intéressants. L'un d'entre eux est que le phénomène de transport amélioré par le désordre a pour origine l'hybridation entre les états propres sombres et polaritoniques du système. Cette hybridation se produit via l'augmentation de la largeur de bande des états sombres induite par le désordre – les polaritons étant eux non touchés par l'augmentation – qui permet de nouveaux couplages entre les états sombres et les photons. Ce mécanisme, lorsque le système est dans le régime de couplage fort lumière-matière, permet aux états sombres de se transformer en polaritons et donc d'hériter les caractéristiques de transport à longue portée de ces derniers.

Ce résultat est notamment visible sur la Figure 5, où nous avons utilisé un formalisme de Lindblad pour étudier le transport des excitations propres du système le long de la chaîne. Il est important de noter que nous considérons ici le système dans le régime de couplage fort lumière-matière, en ajustant la taille de la cavité de façon à ce que les photons résonnent avec les émetteurs dipolaires. L'expérience simulée est le forçage du système à l'aide de l'excitation sinusoïdale continue du premier site dipolaire, à une fréquence de forçage donnée $\omega_{\mathrm{d}}/\omega_0$. Des pertes du système ont été prises en compte, à la fois pour les dipôles et pour les miroirs de la cavité, et la quantité représentée dans la figure est l'amplitude du moment dipolaire $|p_i|$ d'un dipôle sur le site i le long de la chaîne, calculée dans le régime stationnaire. Sur la figure, la gauche des graphiques représente le début de la chaîne d'émetteurs, et la droite des graphiques sa fin. Une couleur noire signifie une faible amplitude

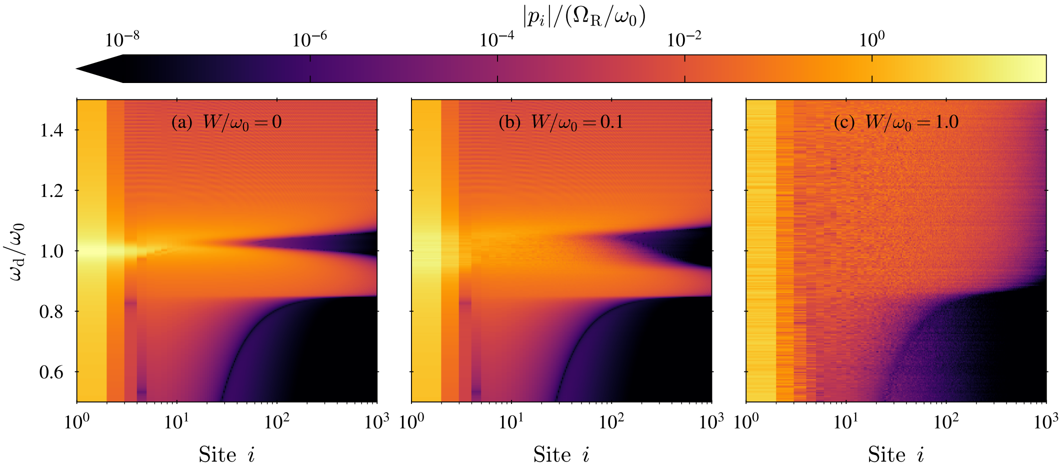

Figure 5: Transport amélioré par le désordre. Graphiques à deux dimensions de l'amplitude du moment dipolaire en régime stationnaire $|p_i|$, en unités de la fréquence réduite de Rabi $\Omega_\mathrm{R}/\omega_0$, en fonction d'à la fois le site i le long de la chaîne de dipôles et la fréquence de forçage utilisée $\omega_\mathrm{d}/\omega_0$. Trois cas sont présentés: (a) Sans désordre, (b) Désordre moyen $W/\omega_0 = 0.1$, et (c) Fort désordre $W/\omega_0 = 1$. Les pertes dipolaires considérées sont $\gamma/\omega_0 = 0.02$, celles de la cavité $\kappa/\omega_0 = 0.002$, le système est pris dans le régime de couplage fort, en choisissant une taille de cavité $L_x = 12a$ et $L_y = 3L_x$, et les données désordonnées ont été moyennées sur 100 configurations du désordre.

de moment dipolaire et donc une faible excitation à cet endroit de la chaîne, tandis qu'une couleur orangée ou jaune signifie une très forte amplitude.

On constate dans cette figure que l'augmentation du désordre conduit les états dipolaires non couplés, situés autour d'une fréquence de résonance de ω_0, à hériter les caractéristiques de transport à longue distance des polaritons, situés eux autours des fréquences de résonance $0.9\omega_0$ et au delà de ω_0. Ceci est en effet visible via le fait que la tâche noire présente sans désordre au milieu à droite de la Fig. 5(a), qui correspond à une mauvaise propagation à longue distance pour les états sombres, est remplacée à très fort désordre dans la Fig. 5(c) par des bandes oranges, qui correspondent à de bonnes propriétés de transport à longue distance.

En prenant en compte la dissipation dans le système, nous avons également montré que ce mécanisme de transport amélioré par le désordre est de plus en plus visible lorsque les dipôles considérés présentent plus de pertes. D'autres résultats de ce chapitre sont par exemple le fait que les états sombres héritant une partie photonique deviennent des états dénommés semi-localisés, qui, dans notre modèle de cavité multimode, ne présentent pas de propriétés multifractales, ou encore que la propagation des polaritons se réalise via une décroissance exponentielle, dont le taux de décroissance dépend directement du poids photonique de l'excitation propre considérée.

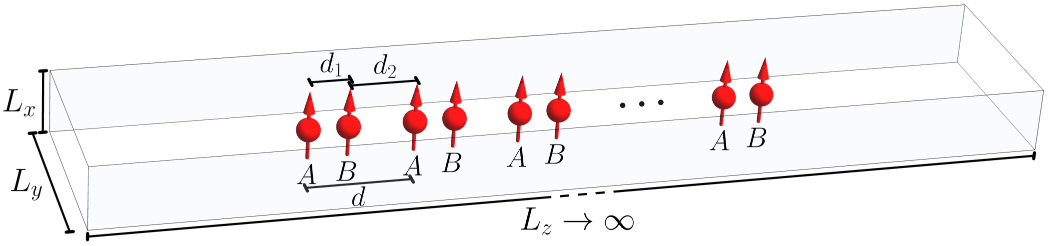

Figure 6: Chaîne SSH de dipôles dans une cavité guide d'onde. Schéma d'une chaîne dimérisée de dipôles oscillants placés au milieu d'une cavité optique guide d'onde n'ayant pas de miroirs dans la direction z, mais des miroirs parfaitement métalliques dans les directions x et y.

Ce dernier résultat implique notamment que le transport amélioré par la cavité, tout comme le transport amélioré par le désordre, n'est valable que pour certaines échelles de tailles du système.

De façon intéressante, depuis la publication de notre étude sur le sujet [17], plusieurs groupes expérimentaux ont été témoins des phénomènes mentionnés dans ce chapitre. En particulier, dans la référence [162], les auteurs ont démontré l'existence de transport amélioré par le désordre dans un ensemble d'atomes froids couplés fortement à une cavité optique. De plus, ils ont précisément observé le mécanisme d'hybridation induit par le désordre, en montrant une augmentation du poids photonique de certains états propres du système lorsque le désordre augmentait. Enfin, des phénomènes similaires d'hybridation induit par le désordre ont également été observés expérimentalement dans le contexte du couplage fort vibrationnel, dans des ensembles moléculaires [167].

4 Topologie et polaritons

Dans ce chapitre, nous utilisons le formalisme développé au Chapitre 2 pour étudier l'interaction entre le couplage fort lumière-matière et les phases topologiques de la matière. Comme présenté au Chapitre 1, les phases topologiques de la matière ont attiré beaucoup d'attention pour les états de bord robustes qu'elles peuvent héberger [36, 37]. Récemment, l'attrait pour ces états de bord, combiné aux progrès réalisés dans l'ingénierie du couplage lumière-matière, ont amené à un intérêt grandissant pour les phénomènes topologiques dans les systèmes photoniques [13–15]. La combinaison de la photonique topologique et de la physique du couplage fort lumière-matière en ce que nous appelons la polaritonique topologique est maintenant un nouveau domaine en développement, et sa compréhension, que nous nous efforçons d'améliorer via l'étude présentée dans ce chapitre, pourrait s'avérer essentielle à la mise en œuvre de technologies photoniques topologiques.

Comme nous l'avons vu précédemment, un effet direct du couplage fort lumière-matière est un couplage effectif à longue portée médié par les photons de la cavité, permettant aux excitations polaritoniques de présenter des propriétés attrayantes telles qu'une propagation accrue. De récents travaux expérimentaux ont souligné l'importance de ce couplage effectif sur les phénomènes topologiques, et plus précisément sur le comportement des états de bord [207]. De plus, une littérature très active a récemment été consacrée aux extensions des modèles topologiques unidimensionnels, tel que le célèbre modèle de Su-Schrieffer-Heeger (SSH) [61], en incorporant des couplages supplémentaires [124, 128, 136, 208–225]. Ce modèle présente l'intérêt particulier d'héberger une phase topologique non triviale, abritant des états de bord topologiques.

Dans ce chapitre, nous allons au-delà de cette littérature existante en étudiant l'influence du couplage fort entre une cavité optique multimode et une chaîne dimérisée d'émetteurs, comme schématisé sur la Fig. 6, réalisant ainsi ce que nous appelons un modèle SSH polaritonique. Comme au chapitre précédent, nous traitons les émetteurs comme des dipôles classiques idéaux et le couplage, dérivé du Chapitre 2, est multimodal, dispersif et dépendant de l'espace. Nous rappelons notamment que la prise en compte de modes photoniques multiples s'est avérée essentielle pour modéliser correctement les effets induits par les cavités [17, 92, 94, 163–165], et il s'agit ici d'un ingrédient clé de notre modèle.

Alors qu'une étude préliminaire du modèle SSH polaritonique a été réalisée dans la Ref. [136], mettant en évidence l'impact de la cavité sur les phases topologiques du système, nous nous concentrons ici sur le sort des états de bord du système. Pour ce faire, nous affinons le modèle dérivé dans la Ref. [136], en considérant notamment une cavité guide d'onde afin d'éviter tout effet de bords des miroirs de la cavité qui pourrait influencer les états de bord topologiques. De plus, en intégrant les degrés de liberté photoniques de la cavité à l'aide d'une transformation unitaire de Schrieffer-Wolff de l'hamiltonien, nous décrivons théoriquement le système par un modèle effectif à deux bandes de sorte qu'il imite très exactement une variation du modèle SSH avec un couplage effectif induit par la cavité. Grâce à ce nouveau formalisme théorique, nous sommes notamment en mesure d'extraire la dépendance du couplage effectif induit par la cavité avec les dimensions de cette dernière, et nous révélons sa décroissance exponentielle avec la distance.

Dans le régime de couplage fort lumière-matière, nous observons une forte renormalisation du spectre en énergie ainsi qu'une totale brisure de la symétrie chirale du système. Ceci conduit à la perte formelle des états de bord topologiques, ces derniers se fondant dans la bande d'états polaritoniques. Alors que cette perte formelle puisse à première vue sembler préjudiciable aux propriétés topologiques du système, nous démontrons ici que, de manière intéressante, les polaritons entrant en résonance avec les états de bord formellement perdus héritent d'une partie des propriétés de localisation sur les bords de ces derniers. Cette hybridation des états de bord dipolaires

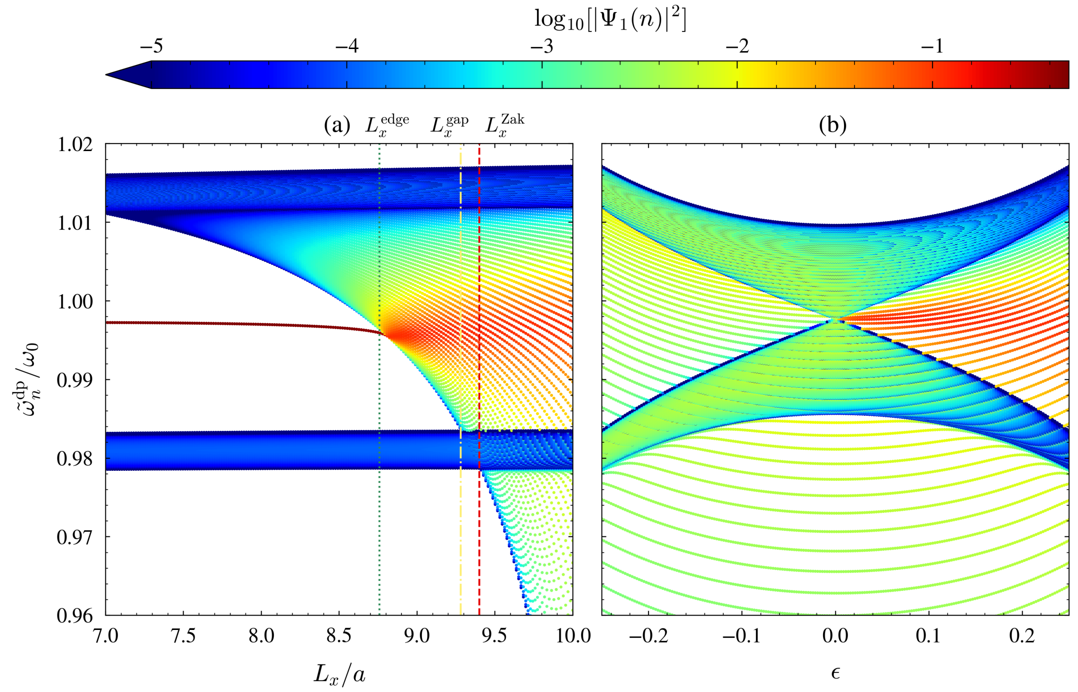

Figure 7: Spectre polaritonique dans l'espace réel. Fréquences propres polaritoniques $\tilde{\omega}_n^{\mathrm{dp}}/\omega_0$ en fonction (a) de la hauteur de la cavité L_x et (b) de la dimérisation de la chaîne ϵ. Le code couleur représente la densité de probabilité sur le premier site de chaque état propre du système.

avec les photons de la cavité amène de nombreux états mixtes, directement induits par la cavité, que nous appelons “états de bord polaritoniques”.

Ce résultat est notamment visible dans la Figure 7, qui présente le résultat d'une diagonalisation de l'hamiltonien du système donnant les fréquences propres polaritoniques $\tilde{\omega}_n^{\mathrm{dp}}/\omega_0$, pour une chaîne de $\mathcal{N} = 500$ dipôles. Sur la figure, le code couleur associé à chaque état propre n indique le logarithme de sa densité de probabilité sur le premier site $i = 1$ de la chaîne, de sorte que la couleur souligne la présence (en rouge) ou l'absence (en vert ou bleu) d'états de bord.

Dans le panneau (a), nous choisissons une dimérisation de la chaîne – caractérisée par le paramètre $\epsilon = (d_1 - d_2)/d$, où d_1, d_2 et d sont définis dans la Figure 6 – telle que le système sans cavité soit dans une phase topologique, et nous faisons varier la dimension L_x de la cavité, et donc le couplage lumière-matière. Sur la gauche de la figure, le système est dans un régime de couplage faible, et l'on observe distinctement en rouge les deux états de bord topologiques originaux, quasi-dégénérés, du modèle SSH. Lorsque le système entre dans le régime de couplage fort, sur la droite de la figure, ces deux états de bord originaux fusionnent avec les états polaritoniques, et l'on observe la diffusion des états de bord originaux en une multitude d'états de bord polaritoniques, dont nous voyons via le code couleur rouge qu'ils sont toujours très fortement localisés sur les bords de la chaîne. Dans le panneau (b), nous fixons les dimensions de la cavité afin d'être en régime de couplage fort, et nous faisons cette fois-ci varier la dimérisation de la chaîne. On observe ici un résultat analogue à celui du modèle SSH original, à savoir que les états de bord, ici polaritoniques, n'apparaissent que pour une dimérisation $\epsilon > 0$.

Dans le reste de ce chapitre, ces états de bord polaritonique sont étudiés en détails, et bien qu'ils ne soient pas entièrement localisés sur les bords, nous montrons qu'ils présentent des propriétés intéressantes et inhabituelles. En particulier, en raison de leur partie délocalisée due à leur nature polaritonique, ces multiples états de bord polaritoniques présentent des caractéristiques de propagation très efficaces notamment en configuration bord-à-bord, que nous révélons à l'aide de simulations de transport d'énergie sous forçage et dissipation. Par ailleurs, au lieu d'être dégénérés en énergie, ils occupent une grande partie du spectre, ce qui permet de les sonder dans une large gamme de fréquences de forçage. L'étude d'une chaîne dimérisée désordonnée nous permet également de dévoiler une forte tolérance des états de bord polaritoniques au désordre sur les positions des dipoles, bien qu'ils ne soient pas formellement protégés par la symétrie chirale. Ces effets de la cavité sur les états de bord d'un système topologique pourraient notamment faciliter la détection expérimentale de ces derniers. Enfin, d'autres résultats de ce chapitre sont l'étude des transitions de phases topologiques induites par la cavité à l'aide de notre modèle effectif à deux bandes, de l'influence de la taille de la longueur de la chaîne considérée sur les propriétés des états de bord polaritoniques, ou bien encore des effets importants de la distance entre les bords de la chaîne dipolaire et les miroirs de la cavité optique selon la direction z.

Conclusions et perspectives

Dans ce travail de thèse, nous nous sommes efforcés de contribuer à la compréhension de l'influence du régime de couplage fort lumière-matière sur deux domaines majeurs de la physique de la matière condensée : les systèmes désordonnés et les phases topologiques de la matière. À cette fin, nous avons étudié le couplage fort entre une cavité optique multimode et, premièrement, un système désordonné unidimensionnel dans le chapitre 3, et deuxièmement, un système topologique unidimensionnel hébergeant des états de bord topologiques dans le chapitre 4.

Dans les deux cas, nous avons mis en évidence un impact considérable du couplage fort lumière-matière sur les propriétés du système. En particulier, nous avons démontré l'importance de prendre en compte une cavité multimode et dispersive, et révélé que l'effet spécifique du couplage fort d'une chaîne d'émetteurs dipolaires à une telle cavité est un couplage dipôle-dipôle effectif, médié par les photons, qui décroît exponentiellement.

Ce couplage médié par les photons sert de mécanisme sous-jacent à la plupart des effets physiques induits par la cavité rapportés dans cette thèse. En effet, un tel couplage effectif est visible à travers les caractéristiques de transport le long du système sous la forme d'une décroissance exponentielle supplémentaire, qui suit la première induite par le couplage dipolaire quasi-statique de plus proches voisins. Plus important encore, son taux de décroissance est directement lié au couplage lumière-matière et à l'hybridation des états propres entre les degrés de liberté photoniques et dipolaires. Plus grande est la partie photonique de l'état propre polaritonique, plus mauvaise est sa propagation à courte portée, mais plus plate est cette décroissance exponentielle induite par la cavité, de sorte que le transport d'énergie sur de plus longues distances est rendu possible par le régime de couplage fort.

Dans le chapitre 3, c'est précisément ce régime supplémentaire de décroissance exponentielle qui permet le transport amélioré des polaritons par la cavité. Avec l'hybridation induite par le désordre des états sombres en polaritons, c'est également ce qui permet l'émergence d'un transport amélioré par le désordre. Dans le chapitre 4, la rupture prononcée de la symétrie chirale dans le système, qui conduit à une transition de phase topologique induite par la cavité caractérisée par un changement de l'invariant topologique du système, ainsi qu'à l'hybridation des états de bord originaux en états de bord polaritonique, est également réalisée grâce à un tel couplage effectif. En outre, cette décroissance médiée par les photons joue un rôle crucial dans l'amélioration des propriétés de transport des états de bord polaritoniques, résultant en un transport d'énergie bord-à-bord particulièrement efficace.

Pour conclure ce manuscrit, le travail réalisé au cours de cette thèse de doctorat a également ouvert des perspectives et soulevé de nouvelles questions.[1]

À cet égard, bien que notre étude se soit concentrée sur l'interaction individuelle entre le désordre et le couplage fort, et la topologie et le couplage fort, elle ne comporte pas d'étude de l'interaction complète entre le désordre et la topologie dans un système lumière-matière fortement couplé. Compte tenu du lien fascinant entre le désordre et la topologie, une étude spécifique des polaritons topologiques désordonnés serait particulièrement intéressante.

Une autre extension de notre étude consisterait à examiner l'effet de la dimensionnalité sur tous les phénomènes que nous avons théoriquement observés. En effet, bien que notre analyse se soit concentrée sur des systèmes unidimensionnels, il est bien établi dans la littérature que la localisation d'Anderson et les phases topologiques de la matière dépendent significativement de la dimensionnalité du système [22, 46].

Enfin, une importante limitation de notre étude est sa restriction au régime de couplage fort, notre modèle ne permettant pas l'analyse des régimes dits "ultra-fort" et "profondément-fort" [149, 151]. Ces régimes de couplage où l'interaction lumière-matière est encore plus prononcée peuvent en effet donner lieu à une pléthore de phénomènes intrigants, notamment dans le contexte des phases topologiques de la matière [207, 237, 242–244]. De plus, à la différence du régime de couplage fort, ceux-ci peuvent amener à des

---

[1] Pour citer John A. Wheeler : "Nous vivons sur une île entourée d'une mer d'ignorance. À mesure que notre île de connaissances grandit, le rivage de notre ignorance grandit aussi.".

phénomènes essentiellement quantiques. Le développement de notre cadre théorique afin d'incorporer ces régimes de couplage lumière-matière plus forts représente ainsi une autre perspective particulièrement attrayante, qui permettrait à la théorie quantique que nous employons dans le présent travail de thèse de libérer pleinement son potentiel.

BIBLIOGRAPHY

[1] A. Einstein, "Über einen die Erzeugung und Verwandlung des Lichtes betreffenden heuristischen Gesichtspunkt", Ann. Phys. (Berl.) **322**, 132 (1905) (cit. on pp. 1, 167).

[2] A. Einstein, "Die Plancksche Theorie der Strahlung und die Theorie der spezifischen Wärme", Ann. Phys. (Berl.) **327**, 180 (1907) (cit. on pp. 1, 167).

[3] P. Sheng, *Scattering and Localization of Classical Waves in Random Media* (World Scientific, Singapore, 1990) (cit. on pp. 1, 8, 167, 168, 171).

[4] F. Zangeneh-Nejad, A. Alù, and R. Fleury, "Topological wave insulators: a review", C. R. Phys. **21**, 467 (2020) (cit. on pp. 1, 12, 167, 174).

[5] Z. Yang, F. Gao, X. Shi, X. Lin, Z. Gao, Y. Chong, and B. Zhang, "Topological Acoustics", Phys. Rev. Lett. **114**, 114301 (2015) (cit. on pp. 1, 12, 168, 174).

[6] E. Guazzelli, E. Guyon, and B. Souillard, "On the localization of shallow water waves by a random bottom", J. Physique Lett. **44**, 837 (1983) (cit. on pp. 1, 8, 168, 171).

[7] P. Delplace, J. B. Marston, and A. Venaille, "Topological origin of equatorial waves", Science **358**, 1075 (2017) (cit. on pp. 1, 12, 168, 174).

[8] G. M. Graf, H. Jud, and C. Tauber, "Topology in Shallow-Water Waves: A Violation of Bulk-Edge Correspondence", Commun. Math. Phys. **383**, 731 (2021) (cit. on pp. 1, 168).

[9] J. Billy, V. Josse, Z. Zuo, A. Bernard, B. Hambrecht, P. Lugan, D. Clément, L. Sanchez-Palencia, P. Bouyer, and A. Aspect, "Direct observation of Anderson localization of matter waves in a controlled disorder", Nature **453**, 891 (2008) (cit. on pp. 1, 168).

[10] N. R. Cooper, J. Dalibard, and I. B. Spielman, "Topological bands for ultracold atoms", Rev. Mod. Phys. **91**, 015005 (2019) (cit. on pp. 1, 12, 168, 174).

[11] T. Schwartz, G. Bartal, S. Fishman, and M. Segev, "Transport and Anderson localization in disordered two-dimensional photonic lattices", Nature **446**, 52 (2007) (cit. on pp. 1, 8, 168, 171).

[12] L. Lu, J. D. Joannopoulos, and M. Soljačić, "Topological photonics", Nat. Photonics **8**, 821 (2014) (cit. on pp. 1, 168).

[13] M. S. Rider, S. J. Palmer, S. R. Pocock, X. Xiao, P. A. Huidobro, and V. Giannini, "A perspective on topological nanophotonics: Current status and future challenges", J. Appl. Phys. **125**, 120901 (2019) (cit. on pp. 1, 99, 168, 185).

[14] T. Ozawa, H. M. Price, A. Amo, N. Goldman, M. Hafezi, L. Lu, M. C. Rechtsman, D. Schuster, J. Simon, O. Zilberberg, and I. Carusotto, "Topological photonics", Rev. Mod. Phys. **91**, 015006 (2019) (cit. on pp. 1, 12, 89, 99, 168, 174, 185).

[15] M. S. Rider, À. Buendía, D. R. Abujetas, P. A. Huidobro, J. A. Sánchez-Gil, and V. Giannini, "Advances and Prospects in Topological Nanoparticle Photonics", ACS Photonics **9**, 1483 (2022) (cit. on pp. 1, 99, 168, 185).

[16] F. J. Garcia-Vidal, C. Ciuti, and T. W. Ebbesen, "Manipulating matter by strong coupling to vacuum fields", Science **373**, eabd0336 (2021) (cit. on pp. 2, 99, 168).

[17] T. F. Allard and G. Weick, "Disorder-enhanced transport in a chain of lossy dipoles strongly coupled to cavity photons", Phys. Rev. B **106**, 245424 (2022) (cit. on pp. 3, 43, 89, 99, 183, 185, 186).

[18] T. F. Allard and G. Weick, "Multiple polaritonic edge states in a Su-Schrieffer-Heeger chain strongly coupled to a multimode cavity", Phys. Rev. B **108**, 245417 (2023) (cit. on pp. 3, 97).

[19] T. F. Allard and G. Weick, "Quantum theory of plasmon polaritons in chains of metallic nanoparticles: From near- to far-field coupling regime", Phys. Rev. B **104**, 125434 (2021) (cit. on pp. 3, 20, 22, 33, 35, 180).

[20] P. A. Lee and T. V. Ramakrishnan, "Disordered electronic systems", Rev. Mod. Phys. **57**, 287 (1985) (cit. on p. 6).

[21] B. Kramer and A. MacKinnon, "Localization: theory and experiment", Rep. Prog. Phys. **56**, 1469 (1993) (cit. on p. 6).

[22] F. Evers and A. D. Mirlin, "Anderson transitions", Rev. Mod. Phys. **80**, 1355 (2008) (cit. on pp. 6, 45, 64, 67, 71, 164, 189).

[23] E. Abrahams, *50 Years of Anderson Localization* (World Scientific, 2010) (cit. on p. 6).

[24] A. Lagendijk, B. A. van Tiggelen, and D. S. Wiersma, "Fifty years of Anderson localization", Phys. Today **62**, 24 (2009) (cit. on p. 6).

[25] P. W. Anderson, "Absence of Diffusion in Certain Random Lattices", Phys. Rev. **109**, 1492 (1958) (cit. on pp. 6, 45, 49, 54, 169).

[26] D. Basko, I. Aleiner, and B. Altshuler, "Metal–insulator transition in a weakly interacting many-electron system with localized single-particle states", Ann. Phys. **321**, 1126 (2006) (cit. on p. 6).

[27] L. S. Levitov, "Delocalization of vibrational modes caused by electric dipole interaction", Phys. Rev. Lett. **64**, 547 (1990) (cit. on pp. 6, 45, 53).

[28] A. Aspect and M. Inguscio, "Anderson localization of ultracold atoms", Phys. Today **62**, 30 (2009) (cit. on pp. 7, 170).

[29] J. Perrin, “Mouvement brownien et réalité moléculaire”, Ann. Chim. Phys. **18**, 1 (1909) (cit. on pp. 6, 170).

[30] N. Mott and W. Twose, “The theory of impurity conduction”, Adv. Phys. **10**, 107 (1961) (cit. on pp. 6, 52).

[31] E. Abrahams, P. W. Anderson, D. C. Licciardello, and T. V. Ramakrishnan, “Scaling Theory of Localization: Absence of Quantum Diffusion in Two Dimensions”, Phys. Rev. Lett. **42**, 673 (1979) (cit. on p. 6).

[32] C. Guan and X. Guan, *A brief introduction to Anderson Localization* (available online, Dated: 18 May 2019) (cit. on p. 6).

[33] E. Larose, L. Margerin, B. A. van Tiggelen, and M. Campillo, “Weak Localization of Seismic Waves”, Phys. Rev. Lett. **93**, 048501 (2004) (cit. on pp. 8, 171).

[34] J. K. Asbóth, L. Oroszlány, and A. Pályi, *A Short Course on Topological Insulators* (Springer, Berlin, 2016) (cit. on pp. 8, 103, 126, 131, 138).

[35] J. Cayssol and J. N. Fuchs, “Topological and geometrical aspects of band theory”, J. Phys. Mater. **4**, 034007 (2021) (cit. on pp. 8, 102).

[36] M. Z. Hasan and C. L. Kane, “Colloquium: Topological insulators”, Rev. Mod. Phys. **82**, 3045 (2010) (cit. on pp. 8, 99, 171, 185).

[37] X.-L. Qi and S.-C. Zhang, “Topological insulators and superconductors”, Rev. Mod. Phys. **83**, 1057 (2011) (cit. on pp. 8, 99, 171, 185).

[38] J. E. Avron, D. Osadchy, and R. Seiler, “A Topological Look at the Quantum Hall Effect”, Phys. Today **56**, 38 (2003) (cit. on p. 8).

[39] X.-L. Qi and S.-C. Zhang, “The quantum spin Hall effect and topological insulators”, Phys. Today **63**, 33 (2010) (cit. on pp. 8, 9, 11).

[40] J. E. Moore, “The birth of topological insulators”, Nature **464**, 194 (2010) (cit. on p. 8).

[41] S.-Q. Shen, “The family of topological phases in condensed matter”, Natl. Sci. Rev. **1**, 49 (2013) (cit. on p. 8).

[42] K. von Klitzing, G. Dorda, and M. Pepper, “New Method for High-Accuracy Determination of the Fine-Structure Constant Based on Quantized Hall Resistance”, Phys. Rev. Lett. **45**, 494 (1980) (cit. on pp. 8, 171).

[43] B. I. Halperin, “Quantized Hall conductance, current-carrying edge states, and the existence of extended states in a two-dimensional disordered potential”, Phys. Rev. B **25**, 2185 (1982) (cit. on pp. 8, 171).

[44] R. Jackiw and C. Rebbi, “Solitons with fermion number ½”, Phys. Rev. D **13**, 3398 (1976) (cit. on pp. 8, 171).

[45] A. Kitaev, “Periodic table for topological insulators and superconductors”, AIP Conf. Proc. **1134**, 22 (2009) (cit. on pp. 9–11, 172–174).

[46] S. Ryu, A. P. Schnyder, A. Furusaki, and A. W. W. Ludwig, “Topological insulators and superconductors: Tenfold way and dimensional hierarchy”, New J. Phys. **12**, 065010 (2010) (cit. on pp. 9, 10, 104, 164, 172, 173, 189).

[47] L. Lepori and L. Dell’Anna, “Long-range topological insulators and weakened bulk-boundary correspondence”, New J. Phys. **19**, 103030 (2017) (cit. on p. 9).

[48] S. Rachel, "Interacting topological insulators: a review", Rep. Prog. Phys. **81**, 116501 (2018) (cit. on p. 9).

[49] K. Kawabata, K. Shiozaki, M. Ueda, and M. Sato, "Symmetry and Topology in Non-Hermitian Physics", Phys. Rev. X **9**, 041015 (2019) (cit. on p. 9).

[50] L. Fu and C. L. Kane, "Topological insulators with inversion symmetry", Phys. Rev. B **76**, 045302 (2007) (cit. on p. 9).

[51] L. Fu, "Topological Crystalline Insulators", Phys. Rev. Lett. **106**, 106802 (2011) (cit. on p. 9).

[52] T. L. Hughes, E. Prodan, and B. A. Bernevig, "Inversion-symmetric topological insulators", Phys. Rev. B **83**, 245132 (2011) (cit. on pp. 9, 124).

[53] F. Schindler, A. M. Cook, M. G. Vergniory, Z. Wang, S. S. P. Parkin, B. A. Bernevig, and T. Neupert, "Higher-order topological insulators", Sci. Adv. **4**, eaat0346 (2018) (cit. on p. 9).

[54] B. Bradlyn, L. Elcoro, J. Cano, M. G. Vergniory, Z. Wang, C. Felser, M. I. Aroyo, and B. A. Bernevig, "Topological quantum chemistry", Nature **547**, 298 (2017) (cit. on p. 9).

[55] A. Altland and M. R. Zirnbauer, "Nonstandard symmetry classes in mesoscopic normal-superconducting hybrid structures", Phys. Rev. B **55**, 1142 (1997) (cit. on pp. 9, 172).

[56] A. P. Schnyder, S. Ryu, A. Furusaki, and A. W. W. Ludwig, "Classification of topological insulators and superconductors in three spatial dimensions", Phys. Rev. B **78**, 195125 (2008) (cit. on pp. 10, 11, 173).

[57] E. Prodan, "Disordered topological insulators: a non-commutative geometry perspective", J. Phys. A: Math. Theor. **44**, 113001 (2011) (cit. on p. 11).

[58] J. Li, R.-L. Chu, J. K. Jain, and S.-Q. Shen, "Topological Anderson Insulator", Phys. Rev. Lett. **102**, 136806 (2009) (cit. on p. 11).

[59] B. Lapierre, T. Neupert, and L. Trifunovic, "Topologically Localized Insulators", Phys. Rev. Lett. **129**, 256401 (2022) (cit. on p. 11).

[60] B. A. Bernevig and S.-C. Zhang, "Quantum Spin Hall Effect", Phys. Rev. Lett. **96**, 106802 (2006) (cit. on p. 11).

[61] W. P. Su, J. R. Schrieffer, and A. J. Heeger, "Solitons in Polyacetylene", Phys. Rev. Lett. **42**, 1698 (1979) (cit. on pp. 11, 99, 100, 102, 174, 186).

[62] G. Ma, M. Xiao, and C. T. Chan, "Topological phases in acoustic and mechanical systems", Nat. Rev. Phys. **1**, 281 (2019) (cit. on pp. 12, 174).

[63] S. Shankar, A. Souslov, M. J. Bowick, M. C. Marchetti, and V. Vitelli, "Topological active matter", Nat. Rev. Phys. **4**, 380 (2022) (cit. on pp. 12, 174).

[64] M. Du, J. B. Pérez-Sánchez, J. A. Campos-Gonzalez-Angulo, A. Koner, F. Mellini, S. Pannir-Sivajothi, Y. R. Poh, K. Schwennicke, K. Sun, S. van den Wildenberg, D. Karzen, A. Barron, and J. Yuen-Zhou, "Chiral edge waves in a dance-based human topological insulator", arXiv:2301.08356 (cit. on pp. 12, 174).

[65] A. V. Nalitov, D. D. Solnyshkov, and G. Malpuech, “Polariton $\mathbb{Z}$ Topological Insulator”, Phys. Rev. Lett. **114**, 116401 (2015) (cit. on pp. 12, 174).

[66] S. Klembt, T. H. Harder, O. A. Egorov, K. Winkler, R. Ge, M. A. Bandres, M. Emmerling, L. Worschech, T. C. H. Liew, M. Segev, C. Schneider, and S. Höfling, “Exciton-polariton topological insulator”, Nature **562**, 552 (2018) (cit. on pp. 12, 174).

[67] P. W. Milonni, “Why spontaneous emission?”, Am. J. Phys. **52**, 340 (1984) (cit. on pp. 12, 174).

[68] K. Tolpygo, “Physical properties of a rock salt lattice made up of deformable ions”, Zh. eksp. teor. fiz **20**, 497 (1950) (cit. on pp. 12, 175).

[69] K. Huang, “Lattice Vibrations and Optical Waves in Ionic Crystals”, Nature **167**, 779 (1951) (cit. on pp. 12, 175).

[70] S. Pekar, “The theory of electromagnetic waves in a crystal in which excitons are produced”, J. Exptl. Theoret. Phys. (U.S.S.R.) **6**, 4 (1958) (cit. on pp. 12, 175).

[71] J. J. Hopfield, “Theory of the Contribution of Excitons to the Complex Dielectric Constant of Crystals”, Phys. Rev. **112**, 1555 (1958) (cit. on pp. 12, 39, 175).

[72] D. N. Basov, A. Asenjo-Garcia, P. J. Schuck, X. Zhu, and A. Rubio, “Polariton panorama”, Nanophotonics **10**, 549 (2021) (cit. on pp. 12, 175).

[73] C. Weisbuch, M. Nishioka, A. Ishikawa, and Y. Arakawa, “Observation of the coupled exciton-photon mode splitting in a semiconductor quantum microcavity”, Phys. Rev. Lett. **69**, 3314 (1992) (cit. on pp. 13, 175).

[74] D. G. Lidzey, D. D. C. Bradley, M. S. Skolnick, T. Virgili, S. Walker, and D. M. Whittaker, “Strong exciton–photon coupling in an organic semiconductor microcavity”, Nature **395**, 53 (1998) (cit. on pp. 13, 176).

[75] D. L. Mills and E. Burstein, “Polaritons: the electromagnetic modes of media”, Rep. Prog. Phys. **37**, 817 (1974) (cit. on pp. 13, 176).

[76] L. Novotny, “Strong coupling, energy splitting, and level crossings: A classical perspective”, Am. J. Phys. **78**, 1199 (2010) (cit. on pp. 13, 176).

[77] H. Gross, “Controlling Light-Matter Interaction between Localized Surface Plasmons and Quantum Emitters”, PhD thesis (Universität Würzburg, 2019) (cit. on pp. 14, 175).

[78] J. Kasprzak, M. Richard, S. Kundermann, A. Baas, P. Jeambrun, J. M. J. Keeling, F. M. Marchetti, M. H. Szymańska, R. André, J. L. Staehli, V. Savona, P. B. Littlewood, B. Deveaud, and L. S. Dang, “Bose–Einstein condensation of exciton polaritons”, Nature **443**, 409 (2006) (cit. on pp. 15, 177).

[79] Q. Fontaine, D. Squizzato, F. Baboux, I. Amelio, A. Lemaître, M. Morassi, I. Sagnes, L. Le Gratiet, A. Harouri, M. Wouters, I. Carusotto, A. Amo, M. Richard, A. Minguzzi, L. Canet, S. Ravets, and J. Bloch, “Kardar–Parisi–Zhang universality in a one-dimensional polariton condensate”, Nature **608**, 687 (2022) (cit. on pp. 15, 177).

[80] S. Christopoulos, G. B. H. von Högersthal, A. J. D. Grundy, P. G. Lagoudakis, A. V. Kavokin, J. J. Baumberg, G. Christmann, R. Butté, E. Feltin, J.-F. Carlin, and N. Grandjean, "Room-Temperature Polariton Lasing in Semiconductor Microcavities", Phys. Rev. Lett. **98**, 126405 (2007) (cit. on pp. 15, 177).

[81] A. Amo, J. Lefrère, S. Pigeon, C. Adrados, C. Ciuti, I. Carusotto, R. Houdré, E. Giacobino, and A. Bramati, "Superfluidity of polaritons in semiconductor microcavities", Nat. Phys. **5**, 805 (2009) (cit. on pp. 15, 177).

[82] J. A. Hutchison, T. Schwartz, C. Genet, E. Devaux, and T. W. Ebbesen, "Modifying Chemical Landscapes by Coupling to Vacuum Fields", Angew. Chem. Int. Ed. **51**, 1592 (2012) (cit. on pp. 15, 177).

[83] J. Feist and F. J. Garcia-Vidal, "Extraordinary Exciton Conductance Induced by Strong Coupling", Phys. Rev. Lett. **114**, 196402 (2015) (cit. on pp. 15, 45, 46, 177).

[84] J. Schachenmayer, C. Genes, E. Tignone, and G. Pupillo, "Cavity-Enhanced Transport of Excitons", Phys. Rev. Lett. **114**, 196403 (2015) (cit. on pp. 15, 45, 46, 177).

[85] C. Gonzalez-Ballestero, J. Feist, E. Gonzalo Badía, E. Moreno, and F. J. Garcia-Vidal, "Uncoupled Dark States Can Inherit Polaritonic Properties", Phys. Rev. Lett. **117**, 156402 (2016) (cit. on pp. 15, 45, 46, 177).

[86] D. Hagenmüller, J. Schachenmayer, S. Schütz, C. Genes, and G. Pupillo, "Cavity-Enhanced Transport of Charge", Phys. Rev. Lett. **119**, 223601 (2017) (cit. on pp. 15, 45, 46, 177).

[87] T. Botzung, D. Hagenmüller, S. Schütz, J. Dubail, G. Pupillo, and J. Schachenmayer, "Dark state semilocalization of quantum emitters in a cavity", Phys. Rev. B **102**, 144202 (2020) (cit. on pp. 15, 45, 46, 62, 63, 66, 67, 75, 88, 177).

[88] N. C. Chávez, F. Mattiotti, J. A. Méndez-Bermúdez, F. Borgonovi, and G. L. Celardo, "Disorder-Enhanced and Disorder-Independent Transport with Long-Range Hopping: Application to Molecular Chains in Optical Cavities", Phys. Rev. Lett. **126**, 153201 (2021) (cit. on pp. 15, 45–47, 62, 63, 72, 75, 81, 83, 177).

[89] K. Sun, C. Dou, M. F. Gelin, and Y. Zhao, "Dynamics of disordered Tavis-Cummings and Holstein-Tavis-Cummings models", J. Chem. Phys. **156**, 024102 (2022) (cit. on pp. 15, 45, 46, 61, 177).

[90] J. Dubail, T. Botzung, J. Schachenmayer, G. Pupillo, and D. Hagenmüller, "Large random arrowhead matrices: Multifractality, semilocalization, and protected transport in disordered quantum spins coupled to a cavity", Phys. Rev. A **105**, 023714 (2022) (cit. on pp. 15, 45–47, 62, 63, 67, 70–72, 75, 177).

[91] G. Engelhardt and J. Cao, "Unusual dynamical properties of disordered polaritons in microcavities", Phys. Rev. B **105**, 064205 (2022) (cit. on pp. 15, 45–47, 72, 177).

[92] R. F. Ribeiro, "Multimode polariton effects on molecular energy transport and spectral fluctuations", Commun. Chem. **5**, 48 (2022) (cit. on pp. 15, 45, 46, 58, 99, 177, 183, 186).

[93] T. Gera and K. L. Sebastian, "Effects of disorder on polaritonic and dark states in a cavity using the disordered Tavis-Cummings model", J. Chem. Phys. **156**, 194304 (2022) (cit. on pp. 15, 45, 46, 177).

[94] G. Engelhardt and J. Cao, "Polariton Localization and Dispersion Properties of Disordered Quantum Emitters in Multimode Microcavities", Phys. Rev. Lett. **130**, 213602 (2023) (cit. on pp. 15, 45, 46, 99, 177, 183, 186).

[95] G. J. R. Aroeira, K. T. Kairys, and R. F. Ribeiro, "Theoretical Analysis of Exciton Wave Packet Dynamics in Polaritonic Wires", J. Phys. Chem. Lett. **14**, 5681 (2023) (cit. on pp. 15, 45, 46, 177).

[96] K. Takazawa, J.-i. Inoue, K. Mitsuishi, and T. Takamasu, "Fraction of a Millimeter Propagation of Exciton Polaritons in Photoexcited Nanofibers of Organic Dye", Phys. Rev. Lett. **105**, 067401 (2010) (cit. on pp. 15, 45, 177).

[97] G. H. Lodden and R. J. Holmes, "Long-Range, Photon-Mediated Exciton Hybridization in an All-Organic, One-Dimensional Photonic Crystal", Phys. Rev. Lett. **109**, 096401 (2012) (cit. on pp. 15, 45, 177).

[98] G. Lerario, A. Cannavale, D. Ballarini, L. Dominici, M. D. Giorgi, M. Liscidini, D. Gerace, D. Sanvitto, and G. Gigli, "Room temperature Bloch surface wave polaritons", Opt. Lett. **39**, 2068 (2014) (cit. on pp. 15, 45, 177).

[99] E. Orgiu, J. George, J. A. Hutchison, E. Devaux, J. F. Dayen, B. Doudin, F. Stellacci, C. Genet, J. Schachenmayer, C. Genes, G. Pupillo, P. Samorì, and T. W. Ebbesen, "Conductivity in organic semiconductors hybridized with the vacuum field", Nat. Mater. **14**, 1123 (2015) (cit. on pp. 15, 45, 177).

[100] X. Zhong, T. Chervy, S. Wang, J. George, A. Thomas, J. A. Hutchison, E. Devaux, C. Genet, and T. W. Ebbesen, "Non-Radiative Energy Transfer Mediated by Hybrid Light-Matter States", Angew. Chem. Int. Ed. **55**, 6202 (2016) (cit. on pp. 15, 45, 177).

[101] G. Lerario, D. Ballarini, A. Fieramosca, A. Cannavale, A. Genco, F. Mangione, S. Gambino, L. Dominici, M. De Giorgi, G. Gigli, and D. Sanvitto, "High-speed flow of interacting organic polaritons", Light Sci. Appl. **6**, e16212 (2017) (cit. on pp. 15, 45, 177).

[102] X. Zhong, T. Chervy, L. Zhang, A. Thomas, J. George, C. Genet, J. A. Hutchison, and T. W. Ebbesen, "Energy Transfer between Spatially Separated Entangled Molecules", Angew. Chem. Int. Ed. **56**, 9034 (2017) (cit. on pp. 15, 45, 177).

[103] G. G. Rozenman, K. Akulov, A. Golombek, and T. Schwartz, "Long-Range Transport of Organic Exciton-Polaritons Revealed by Ultrafast Microscopy", ACS Photonics **5**, 105 (2018) (cit. on pp. 15, 45, 177).

[104] R. Su, J. Wang, J. Zhao, J. Xing, W. Zhao, C. Diederichs, T. C. H. Liew, and Q. Xiong, "Room temperature long-range coherent exciton polariton condensate flow in lead halide perovskites", Sci. Adv. **4**, eaau0244 (2018) (cit. on pp. 15, 45, 177).

[105] S. Hou, M. Khatoniar, K. Ding, Y. Qu, A. Napolov, V. M. Menon, and S. R. Forrest, "Ultralong-Range Energy Transport in a Disordered

Organic Semiconductor at Room Temperature Via Coherent Exciton-Polariton Propagation", Adv. Mater. **32**, 2002127 (2020) (cit. on pp. 15, 45, 177).

[106] K. Nagarajan, J. George, A. Thomas, E. Devaux, T. Chervy, S. Azzini, K. Joseph, A. Jouaiti, M. W. Hosseini, A. Kumar, C. Genet, N. Bartolo, C. Ciuti, and T. W. Ebbesen, "Conductivity and Photoconductivity of a p-Type Organic Semiconductor under Ultrastrong Coupling", ACS Nano **14**, 10219 (2020) (cit. on pp. 15, 45, 177).

[107] R. Pandya, A. Ashoka, K. Georgiou, J. Sung, R. Jayaprakash, S. Renken, L. Gai, Z. Shen, A. Rao, and A. J. Musser, "Tuning the Coherent Propagation of Organic Exciton-Polaritons through Dark State Delocalization", Adv. Sci. **9**, 2105569 (2022) (cit. on pp. 15, 45, 47, 177).

[108] A. M. Berghuis, R. H. Tichauer, L. M. A. de Jong, I. Sokolovskii, P. Bai, M. Ramezani, S. Murai, G. Groenhof, and J. Gómez Rivas, "Controlling Exciton Propagation in Organic Crystals through Strong Coupling to Plasmonic Nanoparticle Arrays", ACS Photonics **9**, 2263 (2022) (cit. on pp. 15, 45, 177).

[109] M. Balasubrahmaniyam, A. Simkhovich, A. Golombek, G. Sandik, G. Ankonina, and T. Schwartz, "From enhanced diffusion to ultrafast ballistic motion of hybrid light–matter excitations", Nat. Mater. **22**, 338 (2023) (cit. on pp. 15, 16, 45–47, 177, 178).

[110] D. Xu, A. Mandal, J. M. Baxter, S.-W. Cheng, I. Lee, H. Su, S. Liu, D. R. Reichman, and M. Delor, "Ultrafast imaging of polariton propagation and interactions", Nat. Commun. **14**, 3881 (2023) (cit. on pp. 15, 16, 45, 177, 178).

[111] D. M. Myers, S. Mukherjee, J. Beaumariage, D. W. Snoke, M. Steger, L. N. Pfeiffer, and K. West, "Polariton-enhanced exciton transport", Phys. Rev. B **98**, 235302 (2018) (cit. on pp. 15, 45, 177).

[112] Y. Zakharko, M. Rother, A. Graf, B. Hähnlein, M. Brohmann, J. Pezoldt, and J. Zaumseil, "Radiative Pumping and Propagation of Plexcitons in Diffractive Plasmonic Crystals", Nano Lett. **18**, PMID: 29995428, 4927 (2018) (cit. on pp. 15, 45, 177).

[113] P. Bhatt, K. Kaur, and J. George, "Enhanced Charge Transport in Two-Dimensional Materials through Light–Matter Strong Coupling", ACS Nano **15**, 13616 (2021) (cit. on pp. 15, 45, 177).

[114] M. Wurdack, E. Estrecho, S. Todd, T. Yun, M. Pieczarka, S. K. Earl, J. A. Davis, C. Schneider, A. G. Truscott, and E. A. Ostrovskaya, "Motional narrowing, ballistic transport, and trapping of room-temperature exciton polaritons in an atomically-thin semiconductor", Nat. Commun. **12**, 5366 (2021) (cit. on pp. 15, 45, 177).

[115] Q. Guo, B. Wu, R. Du, J. Ji, K. Wu, Y. Li, Z. Shi, S. Zhang, and H. Xu, "Boosting Exciton Transport in WSe2 by Engineering Its Photonic Substrate", ACS Photonics **9**, 2817 (2022) (cit. on pp. 15, 45, 177).

[116] A. F. Koenderink and A. Polman, "Complex response and polariton-like dispersion splitting in periodic metal nanoparticle chains", Phys. Rev. B **74**, 033402 (2006) (cit. on pp. 20, 49).

[117] V. A. Markel and A. K. Sarychev, "Propagation of surface plasmons in ordered and disordered chains of metal nanospheres", Phys. Rev. B **75**, 085426 (2007) (cit. on pp. 20, 49, 75, 77).

[118] C.-R. Mann, S. A. R. Horsley, and E. Mariani, "Tunable pseudo-magnetic fields for polaritons in strained metasurfaces", Nat. Photonics **14**, 669 (2020) (cit. on p. 20).

[119] J. D. Jackson, *Classical Electrodynamics*, 3rd ed. (Wiley, New York, 2007) (cit. on pp. 20, 73, 135, 151).

[120] D. P. Craig and T. Thirunamachandran, *Molecular Quantum Electrodynamics* (Academic Press, London, Nov. 1984) (cit. on pp. 20, 21, 23, 24, 179).

[121] P. W. Milonni, *The Quantum Vacuum* (Academic Press, 1994) (cit. on pp. 20, 21, 23, 24, 179, 180).

[122] D. A. Steck, *Quantum and Atom Optics* (available online, revision 0.13.20, 2 May 2023) (cit. on pp. 20, 21, 23, 179).

[123] A. P. Slobozhanyuk, A. N. Poddubny, A. E. Miroshnichenko, P. A. Belov, and Y. S. Kivshar, "Subwavelength Topological Edge States in Optically Resonant Dielectric Structures", Phys. Rev. Lett. **114**, 123901 (2015) (cit. on pp. 22, 180).

[124] B. X. Wang and C. Y. Zhao, "Topological phonon polaritons in one-dimensional non-Hermitian silicon carbide nanoparticle chains", Phys. Rev. B **98**, 165435 (2018) (cit. on pp. 22, 99, 135, 180, 186).

[125] Y. Zhang, R. P. H. Wu, L. Shi, and K. H. Fung, "Second-Order Topological Photonic Modes in Dipolar Arrays", ACS Photonics **7**, 2002 (2020) (cit. on pp. 22, 180).

[126] F. Pirmoradian, B. Zare Rameshti, M. Miri, and S. Saeidian, "Topological magnon modes in a chain of magnetic spheres", Phys. Rev. B **98**, 224409 (2018) (cit. on pp. 22, 180).

[127] B. Zare Rameshti, S. Viola Kusminskiy, J. A. Haigh, K. Usami, D. Lachance-Quirion, Y. Nakamura, C.-M. Hu, H. X. Tang, G. E. W. Bauer, and Y. M. Blanter, "Cavity Magnonics", Phys. Rep. **979**, 1 (2022) (cit. on pp. 22, 180).

[128] F. Pirmoradian, M. Miri, B. Zare Rameshti, and S. Saeidian, "Topological magnon modes of a chain of magnetic spheres in a waveguide", Phys. Rev. B **107**, 064401 (2023) (cit. on pp. 22, 99, 180, 186).

[129] C. R. Mann, T. J. Sturges, G. Weick, W. L. Barnes, and E. Mariani, "Manipulating type-I and type-II Dirac polaritons in cavity-embedded honeycomb metasurfaces", Nat. Commun. **9**, 2194 (2018) (cit. on pp. 22, 37, 135, 180).

[130] J. Yuen-Zhou, S. K. Saikin, T. Zhu, M. C. Onbasli, C. A. Ross, V. Bulovic, and M. A. Baldo, "Plexciton Dirac points and topological modes", Nat. Commun. **7**, 11783 (2016) (cit. on pp. 22, 45, 180).

[131] A. Browaeys, D. Barredo, and T. Lahaye, "Experimental investigations of dipole-dipole interactions between a few Rydberg atoms", J. Phys. B **49**, 152001 (2016) (cit. on pp. 22, 180).

[132] J. Perczel, J. Borregaard, D. E. Chang, H. Pichler, S. F. Yelin, P. Zoller, and M. D. Lukin, “Topological Quantum Optics in Two-Dimensional Atomic Arrays”, Phys. Rev. Lett. **119**, 023603 (2017) (cit. on pp. 22, 180).

[133] B. X. Wang and C. Y. Zhao, “Topological photonic states in one-dimensional dimerized ultracold atomic chains”, Phys. Rev. A **98**, 023808 (2018) (cit. on pp. 22, 180).

[134] A. Asenjo-Garcia, H. J. Kimble, and D. E. Chang, “Optical waveguiding by atomic entanglement in multilevel atom arrays”, Proc. Natl. Acad. Sci. U.S.A. **116**, 25503 (2019) (cit. on pp. 22, 40, 180).

[135] M. D. Schwartz, *Quantum Field Theory and the Standard Model* (Cambridge University Press, Cambridge, 2013) (cit. on pp. 24, 180).

[136] C. A. Downing, T. J. Sturges, G. Weick, M. Stobińska, and L. Martín-Moreno, “Topological Phases of Polaritons in a Cavity Waveguide”, Phys. Rev. Lett. **123**, 217401 (2019) (cit. on pp. 27, 29, 99, 110, 117, 120, 122, 123, 125, 127, 141–143, 145–148, 186).

[137] K. Kakazu and Y. S. Kim, “Quantization of electromagnetic fields in cavities and spontaneous emission”, Phys. Rev. A **50**, 1830 (1994) (cit. on pp. 28, 38).

[138] C. A. Downing, E. Mariani, and G. Weick, “Retardation effects on the dispersion and propagation of plasmons in metallic nanoparticle chains”, J. Phys. Condens. Matter **30**, 025301 (2018) (cit. on pp. 33, 49, 75).

[139] C. Schäfer, M. Ruggenthaler, V. Rokaj, and A. Rubio, “Relevance of the Quadratic Diamagnetic and Self-Polarization Terms in Cavity Quantum Electrodynamics”, ACS Photonics **7**, 975 (2020) (cit. on p. 36).

[140] R. H. Dicke, “Coherence in Spontaneous Radiation Processes”, Phys. Rev. **93**, 99 (1954) (cit. on pp. 36, 40).

[141] K. Rzążewski, K. Wódkiewicz, and W. Żakowicz, “Phase Transitions, Two-Level Atoms, and the A^2 Term”, Phys. Rev. Lett. **35**, 432 (1975) (cit. on p. 36).

[142] I. Bialynicki-Birula and K. Rzążewski, “No-go theorem concerning the superradiant phase transition in atomic systems”, Phys. Rev. A **19**, 301 (1979) (cit. on p. 36).

[143] P. Nataf and C. Ciuti, “No-go theorem for superradiant quantum phase transition in cavity QED and counter-example in circuit QED”, Nat. Commun. **1**, 72 (2010) (cit. on p. 36).

[144] A. Vukics and P. Domokos, “Adequacy of the Dicke model in cavity QED: A counter-no-go statement”, Phys. Rev. A **86**, 053807 (2012) (cit. on p. 36).

[145] A. Vukics, T. Grießer, and P. Domokos, “Elimination of the A-Square Problem from Cavity QED”, Phys. Rev. Lett. **112**, 073601 (2014) (cit. on p. 36).

[146] P. Nataf, T. Champel, G. Blatter, and D. M. Basko, “Rashba Cavity QED: A Route Towards the Superradiant Quantum Phase Transition”, Phys. Rev. Lett. **123**, 207402 (2019) (cit. on p. 36).

[147] O. D. Stefano, A. Settineri, V. Macrì, L. Garziano, R. Stassi, S. Savasta, and F. Nori, “Resolution of gauge ambiguities in ultrastrong-coupling

cavity quantum electrodynamics", Nat. Phys. **15**, 803 (2019) (cit. on p. 36).

[148] C. Cohen-Tannoudji, J. Dupont-Roc, and G. Grynberg, *Atom-Photon Interactions: Basic Processes and Applications* (Wiley, New York, Mar. 1992) (cit. on p. 36).

[149] P. Forn-Díaz, L. Lamata, E. Rico, J. Kono, and E. Solano, "Ultrastrong coupling regimes of light-matter interaction", Rev. Mod. Phys. **91**, 025005 (2019) (cit. on pp. 36, 93, 148, 164, 189).

[150] S. Y. Park and D. Stroud, "Surface-plasmon dispersion relations in chains of metallic nanoparticles: An exact quasistatic calculation", Phys. Rev. B **69**, 125418 (2004) (cit. on pp. 37, 49).

[151] A. F. Kockum, A. Miranowicz, S. De Liberato, S. Savasta, and F. Nori, "Ultrastrong coupling between light and matter", Nat. Rev. Phys. **1**, 19 (2019) (cit. on pp. 40, 94, 148, 164, 189).

[152] I. I. Rabi, "Space Quantization in a Gyrating Magnetic Field", Phys. Rev. **51**, 652 (1937) (cit. on p. 40).

[153] E. Jaynes and F. Cummings, "Comparison of quantum and semiclassical radiation theories with application to the beam maser", Proc. IEEE **51**, 89 (1963) (cit. on p. 40).

[154] M. Tavis and F. W. Cummings, "Exact Solution for an N-Molecule—Radiation-Field Hamiltonian", Phys. Rev. **170**, 379 (1968) (cit. on p. 40).

[155] R. Houdré, R. P. Stanley, and M. Ilegems, "Vacuum-field Rabi splitting in the presence of inhomogeneous broadening: Resolution of a homogeneous linewidth in an inhomogeneously broadened system", Phys. Rev. A **53**, 2711 (1996) (cit. on pp. 45, 60, 87, 138).

[156] V. M. Agranovich, M. Litinskaia, and D. G. Lidzey, "Cavity polaritons in microcavities containing disordered organic semiconductors", Phys. Rev. B **67**, 085311 (2003) (cit. on p. 45).

[157] P. Michetti and G. C. La Rocca, "Polariton states in disordered organic microcavities", Phys. Rev. B **71**, 115320 (2005) (cit. on pp. 45, 87, 138).

[158] A. D. Mirlin, Y. V. Fyodorov, F.-M. Dittes, J. Quezada, and T. H. Seligman, "Transition from localized to extended eigenstates in the ensemble of power-law random banded matrices", Phys. Rev. E **54**, 3221 (1996) (cit. on pp. 45, 53).

[159] A. Rodríguez, V. A. Malyshev, G. Sierra, M. A. Martín-Delgado, J. Rodríguez-Laguna, and F. Domínguez-Adame, "Anderson Transition in Low-Dimensional Disordered Systems Driven by Long-Range Nonrandom Hopping", Phys. Rev. Lett. **90**, 027404 (2003) (cit. on pp. 45, 53).

[160] F. A. B. F. de Moura, A. V. Malyshev, M. L. Lyra, V. A. Malyshev, and F. Domínguez-Adame, "Localization properties of a one-dimensional tight-binding model with nonrandom long-range intersite interactions", Phys. Rev. B **71**, 174203 (2005) (cit. on pp. 45, 53).

[161] X. Deng, V. E. Kravtsov, G. V. Shlyapnikov, and L. Santos, "Duality in Power-Law Localization in Disordered One-Dimensional Systems", Phys. Rev. Lett. **120**, 110602 (2018) (cit. on pp. 45, 53).

[162] N. Sauerwein, F. Orsi, P. Uhrich, S. Bandyopadhyay, F. Mattiotti, T. Cantat-Moltrecht, G. Pupillo, P. Hauke, and J.-P. Brantut, “Engineering random spin models with atoms in a high-finesse cavity”, Nat. Phys. (2023) (cit. on pp. 46, 47, 89, 185).

[163] R. H. Tichauer, J. Feist, and G. Groenhof, “Multi-scale dynamics simulations of molecular polaritons: The effect of multiple cavity modes on polariton relaxation”, J. Chem. Phys. **154**, 104112 (2021) (cit. on pp. 46, 99, 183, 186).

[164] A. Mandal, D. Xu, A. Mahajan, J. Lee, M. Delor, and D. R. Reichman, “Microscopic Theory of Multimode Polariton Dispersion in Multilayered Materials”, Nano Lett. **23**, PMID: 37103998, 4082 (2023) (cit. on pp. 46, 99, 183, 186).

[165] R. H. Tichauer, I. Sokolovskii, and G. Groenhof, “Tuning the Coherent Propagation of Organic Exciton-Polaritons through the Cavity Q-factor”, Adv. Sci., 2302650 (2023) (cit. on pp. 46, 99, 183, 186).

[166] M. Baghdad, P.-A. Bourdel, S. Schwartz, F. Ferri, J. Reichel, and R. Long, “Spectral engineering of cavity-protected polaritons in an atomic ensemble”, Nat. Phys. (2023) (cit. on pp. 46, 47).

[167] B. Cohn, S. Sufrin, A. Basu, and L. Chuntonov, “Vibrational Polaritons in Disordered Molecular Ensembles”, J. Phys. Chem. Lett. **13**, 8369 (2022) (cit. on pp. 47, 89, 185).

[168] J. R. Krenn, A. Dereux, J. C. Weeber, E. Bourillot, Y. Lacroute, J. P. Goudonnet, G. Schider, W. Gotschy, A. Leitner, F. R. Aussenegg, and C. Girard, “Squeezing the Optical Near-Field Zone by Plasmon Coupling of Metallic Nanoparticles”, Phys. Rev. Lett. **82**, 2590 (1999) (cit. on pp. 49, 88).

[169] S. A. Maier, M. L. Brongersma, P. G. Kik, and H. A. Atwater, “Observation of near-field coupling in metal nanoparticle chains using far-field polarization spectroscopy”, Phys. Rev. B **65**, 193408 (2002) (cit. on pp. 49, 88).

[170] S. A. Maier, P. G. Kik, H. A. Atwater, S. Meltzer, E. Harel, B. E. Koel, and A. A. G. Requicha, “Local detection of electromagnetic energy transport below the diffraction limit in metal nanoparticle plasmon waveguides”, Nat. Mater. **2**, 229 (2003) (cit. on pp. 49, 88).

[171] A. F. Koenderink, R. de Waele, J. C. Prangsma, and A. Polman, “Experimental evidence for large dynamic effects on the plasmon dispersion of subwavelength metal nanoparticle waveguides”, Phys. Rev. B **76**, 201403(R) (2007) (cit. on pp. 49, 60, 88).

[172] K. B. Crozier, E. Togan, E. Simsek, and T. Yang, “Experimental measurement of the dispersion relations of the surface plasmon modes of metal nanoparticle chains”, Opt. Express **15**, 17482 (2007) (cit. on pp. 49, 88).

[173] A. Apuzzo, M. Février, R. Salas-Montiel, A. Bruyant, A. Chelnokov, G. Lérondel, B. Dagens, and S. Blaize, “Observation of Near-Field Dipolar Interactions Involved in a Metal Nanoparticle Chain Waveguide”, Nano Lett. **13**, 1000 (2013) (cit. on pp. 49, 60, 88).

[174] S. J. Barrow, D. Rossouw, A. M. Funston, G. A. Botton, and P. Mulvaney, "Mapping Bright and Dark Modes in Gold Nanoparticle Chains using Electron Energy Loss Spectroscopy", Nano Lett. **14**, 3799 (2014) (cit. on pp. 49, 88).

[175] A. Brandstetter-Kunc, G. Weick, C. A. Downing, D. Weinmann, and R. A. Jalabert, "Nonradiative limitations to plasmon propagation in chains of metallic nanoparticles", Phys. Rev. B **94**, 205432 (2016) (cit. on pp. 49, 75–77, 83, 135).

[176] R. J. Bell and P. Dean, "Atomic vibrations in vitreous silica", Discuss. Faraday Soc. **50**, 55 (1970) (cit. on p. 51).

[177] D. Thouless, "Electrons in disordered systems and the theory of localization", Phys. Rep. **13**, 93 (1974) (cit. on pp. 51, 52).

[178] K. Ishii, "Localization of Eigenstates and Transport Phenomena in the One-Dimensional Disordered System", Prog. Theor. Phys. Suppl. **53**, 77 (1973) (cit. on p. 52).

[179] C. A. Downing and L. Martín-Moreno, "Polaritonic Tamm states induced by cavity photons", Nanophotonics **10**, 513 (2021) (cit. on pp. 54, 93, 145).

[180] S. Richter, T. Michalsky, L. Fricke, C. Sturm, H. Franke, M. Grundmann, and R. Schmidt-Grund, "Maxwell consideration of polaritonic quasi-particle Hamiltonians in multi-level systems", Appl. Phys. Lett. **107**, 231104 (2015) (cit. on p. 58).

[181] M. Balasubrahmaniyam, C. Genet, and T. Schwartz, "Coupling and decoupling of polaritonic states in multimode cavities", Phys. Rev. B **103**, L241407 (2021) (cit. on p. 58).

[182] K. Georgiou, K. E. McGhee, R. Jayaprakash, and D. G. Lidzey, "Observation of photon-mode decoupling in a strongly coupled multimode microcavity", J. Chem. Phys. **154**, 124309 (2021) (cit. on p. 58).

[183] F. J. Dyson, "The Dynamics of a Disordered Linear Chain", Phys. Rev. **92**, 1331 (1953) (cit. on p. 59).

[184] G. G. Kozlov, V. A. Malyshev, F. Domínguez-Adame, and A. Rodríguez, "Zero-energy peak of the density of states and localization properties of a one-dimensional Frenkel exciton: Off-diagonal disorder", Phys. Rev. B **58**, 5367 (1998) (cit. on p. 59).

[185] M. Petrov, "Disorder-induced Purcell enhancement in nanoparticle chains", Phys. Rev. A **91**, 023821 (2015) (cit. on p. 59).

[186] N. S. Mueller, Y. Okamura, B. G. M. Vieira, S. Juergensen, H. Lange, E. B. Barros, F. Schulz, and S. Reich, "Deep strong light-matter coupling in plasmonic nanoparticle crystals", Nature **583**, 780 (2020) (cit. on pp. 60, 164).

[187] C. Sönnichsen, T. Franzl, T. Wilk, G. von Plessen, J. Feldmann, O. Wilson, and P. Mulvaney, "Drastic Reduction of Plasmon Damping in Gold Nanorods", Phys. Rev. Lett. **88**, 077402 (2002) (cit. on p. 60).

[188] C. Sönnichsen, T. Franzl, T. Wilk, G. von Plessen, and J. Feldmann, "Plasmon resonances in large noble-metal clusters", New J. Phys. **4**, 93 (2002) (cit. on p. 60).

[189] S. Berciaud, L. Cognet, P. Tamarat, and B. Lounis, “Observation of Intrinsic Size Effects in the Optical Response of Individual Gold Nanoparticles”, Nano Lett. **3**, 515 (2005) (cit. on p. 60).

[190] S. Roy, I. M. Khaymovich, A. Das, and R. Moessner, “Multifractality without fine-tuning in a Floquet quasiperiodic chain”, SciPost Phys. **4**, 025 (2018) (cit. on p. 67).

[191] L. Levitov, “Critical Hamiltonians with long range hopping”, Ann. Phys. (Berl.) **511**, 697 (1999) (cit. on p. 67).

[192] X. Deng, B. L. Altshuler, G. V. Shlyapnikov, and L. Santos, “Quantum Levy Flights and Multifractality of Dipolar Excitations in a Random System”, Phys. Rev. Lett. **117**, 020401 (2016) (cit. on p. 67).

[193] V. Oganesyan and D. A. Huse, “Localization of interacting fermions at high temperature”, Phys. Rev. B **75**, 155111 (2007) (cit. on p. 69).

[194] Y. Y. Atas, E. Bogomolny, O. Giraud, and G. Roux, “Distribution of the Ratio of Consecutive Level Spacings in Random Matrix Ensembles”, Phys. Rev. Lett. **110**, 084101 (2013) (cit. on pp. 69, 70).

[195] E. Tarquini, G. Biroli, and M. Tarzia, “Critical properties of the Anderson localization transition and the high-dimensional limit”, Phys. Rev. B **95**, 094204 (2017) (cit. on p. 69).

[196] E. J. Torres-Herrera, J. A. Méndez-Bermúdez, and L. F. Santos, “Level repulsion and dynamics in the finite one-dimensional Anderson model”, Phys. Rev. E **100**, 022142 (2019) (cit. on pp. 69, 70).

[197] J. Šuntajs, T. Prosen, and L. Vidmar, “Spectral properties of three-dimensional Anderson model”, Ann. Phys. (N. Y.) **435**, 168469 (2021) (cit. on p. 69).

[198] E. B. Bogomolny, U. Gerland, and C. Schmit, “Models of intermediate spectral statistics”, Phys. Rev. E **59**, R1315 (1999) (cit. on p. 70).

[199] Y. Y. Atas, E. Bogomolny, O. Giraud, P. Vivo, and E. Vivo, “Joint probability densities of level spacing ratios in random matrices”, J. Phys. A **46**, 355204 (2013) (cit. on p. 70).

[200] K. H. Fung, R. C. H. Tang, and C. T. Chan, “Analytical properties of the plasmon decay profile in a periodic metal-nanoparticle chain”, Opt. Lett. **36**, 2206 (2011) (cit. on pp. 75, 77).

[201] T. J. Sturges, T. Repän, C. A. Downing, C. Rockstuhl, and M. Stobińska, “Extreme renormalisations of dimer eigenmodes by strong light–matter coupling”, New J. Phys. **22**, 103001 (2020) (cit. on p. 85).

[202] G. S. Agarwal, “Rotating-Wave Approximation and Spontaneous Emission”, Phys. Rev. A **4**, 1778 (1971) (cit. on p. 94).

[203] G. S. Agarwal, “Rotating-Wave Approximation and Spontaneous Emission”, Phys. Rev. A **7**, 1195 (1973) (cit. on p. 94).

[204] B. J. West and K. Lindenberg, “On the rotating wave approximation”, Phys. Lett. A **102**, 189 (1984) (cit. on p. 94).

[205] G. W. Ford and R. F. O’Connell, “The rotating wave approximation (RWA) of quantum optics: serious defect”, Physica A **243**, 377 (1997) (cit. on p. 94).

[206] C. Fleming, N. I. Cummings, C. Anastopoulos, and B. L. Hu, “The rotating-wave approximation: consistency and applicability from an

open quantum system analysis", J. Phys. A **43**, 405304 (2010) (cit. on p. 94).

[207] F. Appugliese, J. Enkner, G. L. Paravicini-Bagliani, M. Beck, C. Reichl, W. Wegscheider, G. Scalari, C. Ciuti, and J. Faist, "Breakdown of topological protection by cavity vacuum fields in the integer quantum Hall effect", Science **375**, 1030 (2022) (cit. on pp. 99, 164, 186, 189).

[208] M. Di Liberto, D. Malpetti, G. I. Japaridze, and C. Morais Smith, "Ultracold fermions in a one-dimensional bipartite optical lattice: Metal-insulator transitions driven by shaking", Phys. Rev. A **90**, 023634 (2014) (cit. on pp. 99, 125, 186).

[209] S. Longhi, "Probing one-dimensional topological phases in waveguide lattices with broken chiral symmetry", Opt. Lett. **43**, 4639 (2018) (cit. on pp. 99, 125, 186).

[210] C. A. Downing and G. Weick, "Topological plasmons in dimerized chains of nanoparticles: Robustness against long-range quasistatic interactions and retardation effects", Eur. Phys. J. B **91**, 253 (2018) (cit. on pp. 99, 107, 109, 186).

[211] B. Pérez-González, M. Bello, Á. Gómez-León, and G. Platero, "Interplay between long-range hopping and disorder in topological systems", Phys. Rev. B **99**, 035146 (2019) (cit. on pp. 99, 125, 186).

[212] S. R. Pocock, P. A. Huidobro, and V. Giannini, "Bulk-edge correspondence and long-range hopping in the topological plasmonic chain", Nanophotonics **8**, 1337 (2019) (cit. on pp. 99, 125, 186).

[213] M. Bello, G. Platero, J. I. Cirac, and A. González-Tudela, "Unconventional quantum optics in topological waveguide QED", Sci. Adv. **5**, eaaw0297 (2019) (cit. on pp. 99, 186).

[214] M. Malki, L. Müller, and G. S. Uhrig, "Absence of localized edge modes in spite of a non-trivial Zak phase in $\mathrm{BiCu_2PO_6}$", Phys. Rev. Res. **1**, 033197 (2019) (cit. on pp. 99, 125, 186).

[215] W. Nie and Y. Liu, "Bandgap-assisted quantum control of topological edge states in a cavity", Phys. Rev. Res. **2**, 012076 (2020) (cit. on pp. 99, 186).

[216] L. Lin, S. Kruk, Y. Ke, C. Lee, and Y. Kivshar, "Topological states in disordered arrays of dielectric nanoparticles", Phys. Rev. Res. **2**, 043233 (2020) (cit. on pp. 99, 186).

[217] H.-C. Hsu and T.-W. Chen, "Topological Anderson insulating phases in the long-range Su-Schrieffer-Heeger model", Phys. Rev. B **102**, 205425 (2020) (cit. on pp. 99, 186).

[218] W. Nie, T. Shi, F. Nori, and Y. Liu, "Topology-Enhanced Nonreciprocal Scattering and Photon Absorption in a Waveguide", Phys. Rev. Appl. **15**, 044041 (2021) (cit. on pp. 99, 186).

[219] Z.-Q. Jiao, S. Longhi, X.-W. Wang, J. Gao, W.-H. Zhou, Y. Wang, Y.-X. Fu, L. Wang, R.-J. Ren, L.-F. Qiao, and X.-M. Jin, "Experimentally Detecting Quantized Zak Phases without Chiral Symmetry in Photonic Lattices", Phys. Rev. Lett. **127**, 147401 (2021) (cit. on pp. 99, 125, 130, 186).

[220] R. G. Dias and A. M. Marques, "Long-range hopping and indexing assumption in one-dimensional topological insulators", Phys. Rev. B **105**, 035102 (2022) (cit. on pp. 99, 186).

[221] B. Pérez-González, Á. Gómez-León, and G. Platero, "Topology detection in cavity QED", Phys. Chem. Chem. Phys. **24**, 15860 (2022) (cit. on pp. 99, 186).

[222] C. McDonnell and B. Olmos, "Subradiant edge states in an atom chain with waveguide-mediated hopping", Quantum **6**, 805 (2022) (cit. on pp. 99, 186).

[223] J. Wei, "Cavity-controlled exciton transport of the Su-Schrieffer-Heeger chain", Phys. Rev. A **106**, 033710 (2022) (cit. on pp. 99, 134, 136, 186).

[224] O. Dmytruk and M. Schirò, "Controlling topological phases of matter with quantum light", Commun. Phys. **5**, 271 (2022) (cit. on pp. 99, 186).

[225] À. Buendía, J. A. Sánchez-Gil, and V. Giannini, "Exploiting Oriented Field Projectors to Open Topological Gaps in Plasmonic Nanoparticle Arrays", ACS Photonics **10**, 464 (2023) (cit. on pp. 99, 186).

[226] C. A. Downing and G. Weick, "Topological collective plasmons in bipartite chains of metallic nanoparticles", Phys. Rev. B **95**, 125426 (2017) (cit. on pp. 101, 104, 109).

[227] J.-N. Fuchs and F. Piéchon, "Orbital embedding and topology of one-dimensional two-band insulators", Phys. Rev. B **104**, 235428 (2021) (cit. on pp. 102, 104).

[228] W. Shockley, "On the Surface States Associated with a Periodic Potential", Phys. Rev. **56**, 317 (1939) (cit. on p. 102).

[229] C. Bourne, J. Kellendonk, and A. Rennie, "The K-Theoretic Bulk–Edge Correspondence for Topological Insulators", Ann. Henri Poincaré **18**, 1833 (2017) (cit. on p. 104).

[230] G. van Miert, C. Ortix, and C. Morais Smith, "Topological origin of edge states in two-dimensional inversion-symmetric insulators and semimetals", 2D Mater. **4**, 015023 (2016) (cit. on pp. 109, 124).

[231] J. R. Schrieffer and P. A. Wolff, "Relation between the Anderson and Kondo Hamiltonians", Phys. Rev. **149**, 491 (1966) (cit. on p. 113).

[232] J. Zak, "Berry's phase for energy bands in solids", Phys. Rev. Lett. **62**, 2747 (1989) (cit. on p. 124).

[233] P. Delplace, D. Ullmo, and G. Montambaux, "Zak phase and the existence of edge states in graphene", Phys. Rev. B **84**, 195452 (2011) (cit. on p. 124).

[234] H.-X. Wang, G.-Y. Guo, and J.-H. Jiang, "Band topology in classical waves: Wilson-loop approach to topological numbers and fragile topology", New J. Phys. **21**, 093029 (2019) (cit. on p. 124).

[235] R. D. King-Smith and D. Vanderbilt, "Theory of polarization of crystalline solids", Phys. Rev. B **47**, 1651(R) (1993) (cit. on p. 125).

[236] Y. Chang, N. D. R. Torres, S. F. Manrique, R. A. R. Robles, V. C. Silalahi, C. Wu, G. Wang, G. Marcucci, L. Pilozzi, C. Conti, R. Lee, and W. Kuo, "Probing topological protected transport in finite-sized Su-Schrieffer-Heeger chains", arXiv:2004.09282 (cit. on p. 134).

[237] K. Masuki and Y. Ashida, "Berry phase and topology in ultrastrongly coupled quantum light-matter systems", Phys. Rev. B **107**, 195104 (2023) (cit. on pp. 148, 164, 189).

[238] E. A. Power and T. Thirunamachandran, "Quantum electrodynamics in a cavity", Phys. Rev. A **25**, 2473 (1982) (cit. on p. 152).

[239] S. Velury, B. Bradlyn, and T. L. Hughes, "Topological crystalline phases in a disordered inversion-symmetric chain", Phys. Rev. B **103**, 024205 (2021) (cit. on p. 164).

[240] E. J. Meier, F. A. An, A. Dauphin, M. Maffei, P. Massignan, T. L. Hughes, and B. Gadway, "Observation of the topological Anderson insulator in disordered atomic wires", Science **362**, 929 (2018) (cit. on p. 164).

[241] S. Lamowski, C. R. Mann, F. Hellbach, E. Mariani, G. Weick, and F. Pauly, "Plasmon polaritons in cubic lattices of spherical metallic nanoparticles", Phys. Rev. B **97**, 125409 (2018) (cit. on p. 164).

[242] G. Scalari, C. Maissen, D. Turčinková, D. Hagenmüller, S. D. Liberato, C. Ciuti, C. Reichl, D. Schuh, W. Wegscheider, M. Beck, and J. Faist, "Ultrastrong Coupling of the Cyclotron Transition of a 2D Electron Gas to a THz Metamaterial", Science **335**, 1323 (2012) (cit. on pp. 164, 189).

[243] X. Wang, E. Ronca, and M. A. Sentef, "Cavity quantum electrodynamical Chern insulator: Towards light-induced quantized anomalous Hall effect in graphene", Phys. Rev. B **99**, 235156 (2019) (cit. on pp. 164, 189).

[244] V. Rokaj, M. Penz, M. A. Sentef, M. Ruggenthaler, and A. Rubio, "Polaritonic Hofstadter butterfly and cavity control of the quantized Hall conductance", Phys. Rev. B **105**, 205424 (2022) (cit. on pp. 164, 189).

Thomas ALLARD

Disorder and topology in strongly coupled light-matter systems

Résumé

Cette thèse explore sur le plan théorique l'influence du couplage fort lumière-matière sur deux domaines majeurs de la physique de la matière condensée : les systèmes désordonnés et les phases topologiques de la matière. Nous y étudions le couplage fort entre une cavité optique multimode et, d'abord, une chaîne d'émetteurs dipolaires désordonnée, puis, une chaîne topologique d'émetteurs dipolaires. Dans les deux cas, nous révélons un impact considérable du couplage fort lumière-matière sur les propriétés du système. En étudiant une chaîne désordonnée, nous révélons entre autres que l'augmentation du désordre conduit les états sombres du système à acquérir une partie photonique leur permettant d'hériter de caractéristiques de transport polaritoniques à longue portée. En considérant une chaîne topologique dite de Su-Schrieffer-Heeger, nous révélons notamment l'hybridation des états de bord en états de bord polaritoniques présentant des propriétés de transport bord-à-bord efficaces.

Mots clés : Couplage fort lumière-matière, polaritons, localisation d'Anderson, phases topologiques de la matière, modèle de Su-Schrieffer-Heeger

Résumé en anglais (abstract)

This thesis explores theoretically the fate of Anderson localization, as well as of topological phases of matter, in the strong light-matter coupling regime. We analyze the properties of one-dimensional systems made of dipolar emitters strongly-coupled to a multimode optical cavity. By studying a disordered chain of emitters, we find notably that, in the strong-coupling regime, increasing disorder leads almost uncoupled dark states to acquire a photonic part, allowing them to inherit polaritonic long-range transport characteristics. Investigating a dimerized chain of emitters, we study a variation of the Su-Schrieffer-Heeger model of polyacetylene, with the addition of an effective, cavity-induced, dipole-dipole coupling. We unveil the hybridization of the original topological edge states into polaritonic edge states that present unusual properties, such as efficient edge-to-edge transport characteristics.

Keywords: Strong light-matter coupling, polaritons, Anderson localization, topological phases of matter, Su-Schrieffer-Heeger model